Exploiting Rotaxane and Pseudorotaxane Inter-component Interactions for Synthesis, Sensing and Catalysis

Jamie T. Wilmore

Trinity College

A thesis submitted for the degree of Doctor of Philosophy.

Hilary Term 2024

Exploiting Rotaxane and Pseudorotaxane Inter-component Interactions for Synthesis, Sensing and Catalysis

Jamie T. Wilmore, Trinity College

Abstract of Thesis Submitted for the Degree of Doctor of Philosophy
Hilary Term 2024

This thesis describes the exploitation of non-covalent interactions between components of supramolecular systems, principally rotaxanes and pseudorotaxane assemblies, to enhance the synthesis of mechanically interlocked molecules (MIMs) and for sensing and catalysis applications.

Chapter One introduces supramolecular chemistry and the non-covalent interactions typically exploited within the field, in particular in the context of anion recognition and sensing. The synthesis of MIM architectures is discussed and their advantages as highly preorganised hosts for the recognition and sensing of charged guests, and in catalysis applications, is discussed through examples from the literature.

Chapter Two describes the high yielding synthesis of a series of Zn(II) metalloporphyrin [2]- and [3]-rotaxanes. The inter-component macrocycle pyridyl···Zn(II) metalloporphyrin axle interaction is investigated by variable temperature ^{1}H NMR spectroscopy and by rotaxane transmetallation studies. The binding of neutral or anionic competing guest ligands, and the resultant change in the metalloporphyrin optical spectra, is investigated and a [2]rotaxane congener with a heteroditopic macrocycle synthesised to investigate the effects of rotaxane co-conformational dynamism on ion-pair binding.

Chapter Three describes the use of pillar[5]arene host-guest chemistry to form pseudorotaxanes as a potential route to higher order [3]- or [4]-rotaxanes and for facile stoppering by a phosphaalkyne-azide click reaction to form organometallic-containing [2]rotaxanes. The effect of the mechanical bond to stabilise air- and moisture-sensitive

organometallic species is investigated. Furthermore, the ability of a hydrophobic pillar[5]arene host system functionalised with halogen bonding motifs and an optical reporter group to sense neutral and anionic environmental pollutants is explored.

Chapter Four presents a series of transition metal salen complexes in [2]rotaxane MIM and non-interlocked frameworks, and investigates the potential of supramolecular non-covalent interactions to catalyse the synthesis of sustainable polyester and polycarbonate polymers.

Chapter Five presents the main conclusions of this thesis.

Chapter Six details the experimental procedures used in the work in this thesis and presents the full characterisation of all novel compounds.

Acknowledgements

First and foremost, I would like to thank Prof. Paul Beer for all the words of support over the past few years, from the challenges of starting in the lab mid-pandemic to helping me secure an EPSRC Doctoral Prize and postdoc position. I have been incredibly fortunate to work with a supervisor who is so supportive and offers so many 'baroque' ideas for collaborations in his group and beyond. I am also hugely grateful for the support of Prof. Charlotte Williams, not only for acting as my co-supervisor, but also for supporting me through my undergraduate degree and giving me my first taste of research in her group back in Summer 2018.

I am especially grateful for the support of Dr Andrew Docker whose patience and guidance as the CRL reopened in the summer of 2020, when his own research time was limited, was invaluable for helping me move from organometallic to supramolecular chemistry. To all of the Beer, Williams and Langton groups, thank you for making the past four years such an enjoyable experience. I would like to particularly thank Prof. Jose Goicoechea, Dr Richard Tse, Andrew Taylor and Alex Mapp, with whom I have collaborated, and Dr Heike Kuhn and Hui Min Tay for their advice on crystallography.

It is not possible to name all of the people whose work behind the scenes made this research possible, but I would like to particularly acknowledge Dr Nick Rees and the NMR team for all their help and advice, Dr Victor Mikhailov for his efforts trying to get some of my more elusive compounds to fly by ESI-MS and all of the support team, not least for the many times they have come to my aid fixing my rotavap.

My A-level Chemistry teacher, Dr Rob Spink, warned me that if I studied chemistry at university, I would end up doing a PhD. If he was trying to put me off, he failed. Only

time will tell if his warning was warranted — thus far, it has been a great journey. I would like to thank Dr Spink and all who contributed to building up my passion for chemistry and bringing me to this point in my academic career.

Eight-and-a-half years in Oxford has given me many great friends and experiences. I would like to thank everyone who has left a mark on my time here, especially friends at the Newman Society, fellow volunteers with the Companions, the Chaplaincy team and the Fathers and Brothers of the Oratory for their continued friendship and spiritual guidance.

Above all, I would like to thank my family for all their love and support, particularly Anna who has been a daily support over the past three years.

J.T.W.

Oxford, HT 24

Non nobis Domine, non nobis, sed nomini tuo da gloriam – Ps. CXIII:ix

Abbreviations

Abbreviation	Meaning
[2.2.2]-crypt	4,7,13,16,21,24-Hexaoxa-1,10-diazabicyclo[8.8.8]hexacosane
°	Degrees
°C	Degrees Celsius
1-D	One dimensional
2-D	Two dimensional
3-D	Three dimensional
Å	Angstrom (10^{-10} m)
A^-	Anion
AMT	Active metal templated
App.	Apparent
ATP	Adenosine triphosphate
a.u.	Arbitrary units
Ax	Axle
B15C5	Benzo-15-crown-5
$BAr^F{}_4^-$	Tetrakis(3,5-bis(trifluoromethyl)phenyl)borate
Bn	Benzyl
BODIPY	Boron-dipyrromethene (4,4-difluoro-4-bora-3a,4a-diaza-s-indacene)
Bu	Butyl
c.	*circa*
CCD	Charge-coupled device
CCDC	Cambridge Crystallographic Data Centre
CEES	2-Chloroethyl ethyl sulfide

CHO	Cyclohexene oxide
conc.	Concentrated
CuAAC	Copper(I)-catalysed azide-alkyne cycloaddition
CWA	Chemical warfare agent
Cy	Cyclohexyl
d	Doublet
d	Deuterated
DB18C6	Dibenzo-18-crown-6
DB24C8	Dibenzo-24-crown-8
DCA	Dicarboxylic Acid
DCB	Dicarboxylate
DCE	1,2-Dichloroethane
DCM	Dichloromethane
dd	Doublet of doublets
DDQ	2,3-Dichloro-5,6-dicyano-1,4-benzoquinone
DFT	Density functional theory
DIBAL-H	Diisobutylaluminium hydride
DIPEA	*N*,*N*-Diisopropylethylamine
DMAP	4-Dimethylaminopyridine
DMF	*N*,*N*-Dimethylformamide
DMSO	Dimethyl sulfoxide
DNA	Deoxyribonucleic acid
e^-	Electron
EDTA	Ethylenediaminetetraacetic acid

ee	Enantiomeric excess
e.g.	*Exempli gratia*
Eq	Equivalents
ESI-MS	Electrospray ionisation mass spectrometry
Et	Ethyl
et al.	*Et alia*
EtOAc	Ethyl acetate
ex	Excitation
Fc	Ferrocene
FLP	Frustrated Lewis pair
g	Gram
G	Gibbs' free energy
G_{hyd}	Gibbs' free energy of hydration
h	Planck constant
h	Hour
H	Enthalpy
HB	Hydrogen bonding
HEPES	2-[4-(2-Hydroxyethyl)piperazin-1-yl]ethane-1-sulfonic acid
HOMO	Highest occupied molecular orbital
Hz	Hertz (s^{-1})
I.e.	*Id est*
IR	Infrared
J	Joule
J	Coupling constant

k	Kilo (10^3)
k	Rate constant
K	Kelvin
K_a	Association constant
LO	Limonene oxide
LUMO	Lowest unoccupied molecular orbital
M	Molar (mol dm^{-3}), molecular ion
m	*meta*
m	Multiplet, metre
Max	Maximum
MALDI-ToF	Matrix-assisted laser desorption/ionisation-time of flight
Me	Methyl
MeCN	Acetonitrile
MeOH	Methanol
Mes	Mesityl (2,4,6-trimethylphenyl)
MIM	Mechanically interlocked molecule
MLCT	Metal-to-ligand charge transfer
mol	Mole
MS	Mass spectrometry
MW	Microwave irradiation
m/z	Mass-to-charge ratio
n	Nano (10^{-9})
NHC	*N*-Heterocyclic carbene
NIS	*N*-Iodosuccinimide

NMR	Nuclear Magnetic Resonance
o	*ortho*
OAc	Acetate
o/n	Overnight
p	*para*
p	Pentet
P[*n*]A	Pillar[*n*]arene
P5A	Pillar[5]arene
P6A	Pillar[6]arene
PET	Photoinduced electron transfer
PFA	Paraformaldehyde
pH	$-\log_{10}[H^+]$
Ph	Phenyl
pK_a	$-\log_{10}[K_a]$
PO	Propylene oxide
ppm	Parts per million
PPN	Bis(triphenylphosphine)iminium
Py	Pyridine
q	Quartet
RCM	Ring-closing metathesis
R	Chemical substituent, gas constant
R_f	Retention factor
RNA	Ribonucleic acid
ROCOP	Ring-opening co-polymerisation

ROP	Ring-opening polymerisation
rt, RT	Room temperature
S	Entropy
s	Singlet, second
Sept.	Septet
Syn	*Syn*-periplanar
T	Tesla
t, *tert*	*Tertiary*
$t_{1/2}$	Half-life
TBA	Tetra-*n*-butylammonium
TBTA	Tris(benzyltriazolylmethyl)amine
^{t}Bu	*Tert*-butyl
td	Triplet of doublets
TFA	Trifluoroacetic acid
THF	Tetrahydrofuran
TLC	Thin layer chromatography
TMS	Trimethylsilyl
Tolyl	$-C_6H_4CH_3$
Ts, tosyl	*p*-Toluenesulfonyl
UV	Ultraviolet
v/v	Volume-to-volume ratio
vdW	Van der Waals' Interactions
Vis.	Visible
vs.	Versus

VX	*S*-{2-[Di(propan-2-yl)amino]ethyl} *O*-ethyl methylphosphonothioate
Wt	Weight
w/*w*	Weight-to-weight ratio
X	Halogen atom/halide
XB	Halogen bonding
XRD	X-ray diffraction
δ	Chemical shift
Δ	Change in [physical quantity]
λ	Wavelength
λ_{ex}	Excitation wavelength
μ	Micro (10^{-6})

Previously Published Work

Some of the work presented in this thesis has previously been published in the following peer-reviewed journal articles:

'Exploiting the Mechanical Bond Effect for Enhanced Molecular Recognition and Sensing'
J. T. Wilmore and P. D. Beer, *Adv. Mater.* **2024**, 2309098.

'Dynamic Metalloporphyrin-Based [2]Rotaxane Molecular Shuttles Stimulated by Neutral Lewis Base and Anion Coordination'
J. T. Wilmore, Y. Cheong Tse, A. Docker, C. Whitehead, C. K. Williams and P. D. Beer, *Chem. Eur. J.* 2023, **29**, e202300608.

'An Inorganic Click Reaction for the Synthesis of Interlocked Molecules'
A. Mapp, J. T. Wilmore, P. D. Beer and J. M. Goicoechea, *Angew. Chem. Int. Ed.* 2023, **62**, e202309211.

Table of Contents

Abstract ..... **i**

Acknowledgements ..... **iii**

Abbreviations ..... **v**

Previously Published Work ..... **xii**

Table of Contents ..... **xiii**

1 Introduction **1**

1.1 Supramolecular Host-Guest Chemistry **2**

1.1.1 Supramolecular Chemistry 2

1.1.2 Non-covalent Interactions 4

1.1.2.1 Electrostatic Interactions 4

1.1.2.2 π Interactions 5

1.1.2.3 Hydrogen Bonding 6

1.1.2.4 Halogen Bonding 7

1.1.2.5 Dispersion Interactions 8

1.1.2.6 Hydrophobic Effects 9

1.1.3 Principles of Supramolecular Host Design 10

1.1.3.1 Host-Guest Recognition 10

1.1.3.2 Complementarity 10

1.1.3.3 Preorganisation 12

1.2 Supramolecular Anion Recognition **13**

1.2.1 The Importance of Anions 13

1.2.2 Challenges of Anion Recognition 15

1.2.3 Synthetic Anion Receptors 17

1.2.3.1 Positively Charged Receptors 17

1.2.3.2 Neutral HB Receptors 20

1.2.3.3 Neutral XB Receptors 23

1.3 Ion-Pair Recognition **25**

1.4 Mechanically Interlocked Molecules **29**

1.4.1 MIM Synthesis 30

1.4.2 MIMs for Charged Guest Recognition and Sensing 34

1.4.2.1 Cation Recognition MIMs 35
1.4.2.2 Anion Recognition MIMs 37
1.4.2.3 Ion-Pair Recognition MIMs 42
1.4.3 MIMs for Guest Sensing 46
1.4.3.1 MIM Sensors for Charged Guests 46
1.4.3.2 Dynamic MIM Sensors 51
1.4.4 MIMs for Catalysis 53
1.5 Thesis Aims 56
1.6 References 58

2 Dynamic Zn(II) Metalloporphyrin Rotaxanes for Anion and Ion-Pair Recognition and Sensing 65
2.1 Introduction 66
2.1.1 The Porphyrin Moiety 66
2.1.2 Optical Properties of Porphyrins 67
2.1.3 Porphyrins for Anion Sensing 68
2.1.4 Porphyrin-containing MIMs 69
2.1.5 Project Aims 71
2.2 Synthesis of First-generation Pyridyl Macrocycle-porphyrin Axle [*n*]Rotaxanes 72
2.2.1 Synthesis of Bis-azido Functionalised Metalloporphyrins 73
2.2.2 Active Metal Templated Synthesis of Initial Rotaxanes 75
2.2.3 UV-visible and Fluorescence Optical Characterisation 81
2.3 Investigation of Rotaxane Inter-component Interactions 83
2.3.1 Effect of a Competing Solvent 83
2.3.2 Effect of a Competing Ligand 85
2.3.3 Synthesis of Demetallated [2]Rotaxanes 87
2.3.4 Variation of Metalloporphyrin Metal Centre 90
2.3.5 Quantification of Macrocycle Shuttling Activation Parameters 92
2.3.6 Calculation of Co-conformational Bias 95
2.4 Anion Binding Studies 97
2.5 Preliminary Ion-Pair Binding Studies 102
2.6 Synthesis of a Heteroditopic Ion-Pair Binding Rotaxane 105

2.6.1 Synthesis of a Halogen Bonding Heteroditopic Macrocycle 106
2.6.2 Synthesis of an Ion-Pair Receptor [2]Rotaxane with a Heteroditopic Macrocycle 108
2.6.3 Preliminary Anion Binding Studies 112
2.7 Ion-Pair Binding Studies 113
2.7.1 Lithium Cation Binding Studies 113
2.7.2 Lithium Halide Ion-Pair Binding Studies 116
2.8 Conclusions and Future Work 120
2.9 References 123

3 Exploiting Pillar[5]arene Host-Guest Chemistry for Rotaxane Assembly and Enhanced Optical Sensing of Biologically Relevant Substrates 126
3.1 Pillar[5]arenes: Neutral Supramolecular Hosts 127
3.1.1 The Pillar[5]arene Moiety 127
3.1.2 P5As as Supramolecular Hosts 128
3.1.3 Mechanically Interlocked P5A Assemblies 130
3.1.4 Project Aims 131
3.2 Towards Active Metal Synthesis of Higher Order [*n*]Rotaxanes 133
3.2.1 Synthesis of a P5A [2]Rotaxane 133
3.2.2 Attempted Synthesis of Higher Order Rotaxanes 136
3.2.3 Conclusions and Future Work 139
3.3 Synthesis of Interlocked Molecules by an Inorganic Click Reaction 141
3.3.1 Introduction 141
3.3.2 Synthesis of First Generation [2]Rotaxane 142
3.3.3 Synthesis of a [2]Rotaxane by a Stoichiometric Inorganic Click Reaction 147
3.3.4 Conclusions and Future Work 151
3.4 Halogen-Bonding BODIPY-Appended P5As for Optical Sensing of Dicarboxylates and a Chemical Warfare Agent Simulant 152
3.4.1 Introduction 152
3.4.2 Synthesis of an XB BODIPY-appended P5A 155
3.4.3 Optical Sensing of Dicarboxylates 158
3.4.4 Optical Dicarboxylate Sensing in Aqueous-organic Media 161

3.4.5 Sensing of a Chemical Warfare Agent Simulant 162
3.4.6 Limit of Detection of CWA Simulant 164
3.4.7 Conclusions and Future Work 166
3.5 References 167

4 Towards Supramolecular Metal Salen Complexes for Ring Opening Polymerisation 171
4.1 Introduction 172
4.1.1 The Salen Ligand 172
4.1.2 Ring-opening Polymerisation 173
4.1.3 Ring-opening Polymerisation Catalysis 174
4.1.4 Co-catalysts for ROCOP 176
4.1.5 Rotaxanes for Ring-opening Polymerisation 177
4.1.6 Project Aims 177
4.2 Salen-containing Rotaxanes for Polymerisation Catalysis 178
4.2.1 Synthesis of Axle Precursor Synthons 178
4.2.2 Synthesis of a Novel XB Macrocycle 181
4.2.3 Synthesis of Ni(II) Salen-containing [2]Rotaxanes 183
4.2.4 Preliminary ROCOP Testing 187
4.2.5 Attempted Synthesis of Co(III) [2]Rotaxane Congeners 188
4.3 Crown Ether-appended Salen Complexes for Cation and Ion-Pair Recognition 191
4.3.1 Synthesis of Crown Ether Pendant Salen Complexes 191
4.3.2 Alkali Metal Cation Binding Studies of a Salen Nickel Complex with B15C5 Pendants 193
4.3.3 Preliminary Ion-Pair Recognition Studies 194
4.3.4 Attempted Synthesis of an XB-functionalised Ni Salen Complex for Enhanced Ion-Pair Recognition 195
4.3.5 Synthesis of a Co(III) Congener for ROCOP Catalysis 199
4.4 Halogen Bonding Acyclic Salen Complexes for Co-catalyst Binding 200
4.4.1 Synthesis of XB Acyclic Salen Receptors 200
4.4.2 Preliminary Anion Binding Studies 201
4.5 Conclusions and Future Work 203

4.6 References 205

5 Conclusions 208

6 Experimental 214

6.1 General Experimental Procedures 215

6.1.1 Reagents and Instrumentation 215

6.1.2 General Method for ^{1}H NMR Binding Titrations 216

6.1.3 General Method for Optical Binding Titrations 217

6.2 Synthesis and Characterisation of Novel Compounds in Chapter 2 218

6.3 Synthesis and Characterisation of Novel Compounds in Chapter 3 233

6.4 Synthesis and Characterisation of Novel Compounds in Chapter 4 246

6.5 Single Crystal X-ray Diffraction Data 267

6.6 References 268

Chapter One

Introduction

1 Introduction

1.1 Supramolecular Host-Guest Chemistry

1.1.1 Supramolecular Chemistry

The chemistry of everyday life relies heavily on the interactions between molecules. Hydrogen bonding networks between water molecules give rise to the unique properties of aqueous media, and biology relies greatly on the dynamic formation and breaking of weak intermolecular interactions. Perhaps the best-known example of this is the double helix of DNA, where the ability to replicate genetic material *in vivo* arises from the ability to separate the two strands of DNA, with Watson-Crick base pairing facilitating DNA replication through specific hydrogen bonding patterns.[1]

In the 1960s, Pedersen's pioneering work on crown ethers, which displayed strong alkali metal cation binding capabilities,[2] opened up the field of supramolecular chemistry which targets the construction of molecular systems to exploit 'chemistry beyond the molecule'[3] either for self-assembly or to facilitate 'host-guest chemistry', wherein designed hosts selectively bind charged or neutral guest species through non-covalent interactions.[4] Building on Pedersen's crown ether work, Lehn and Cram,[3, 5-7] respectively, synthesised macrobicyclic cryptand and spherand host molecules which displayed enhanced alkali metal cation selectivity and binding affinities through increased preorganisation of the host binding cavity (see Section 1.1.3.3). The three supramolecular chemists were recognised with the 1987 Nobel Prize in Chemistry 'for their development and use of molecules with structure-specific interactions of high selectivity' (Figure 1.1).[8]

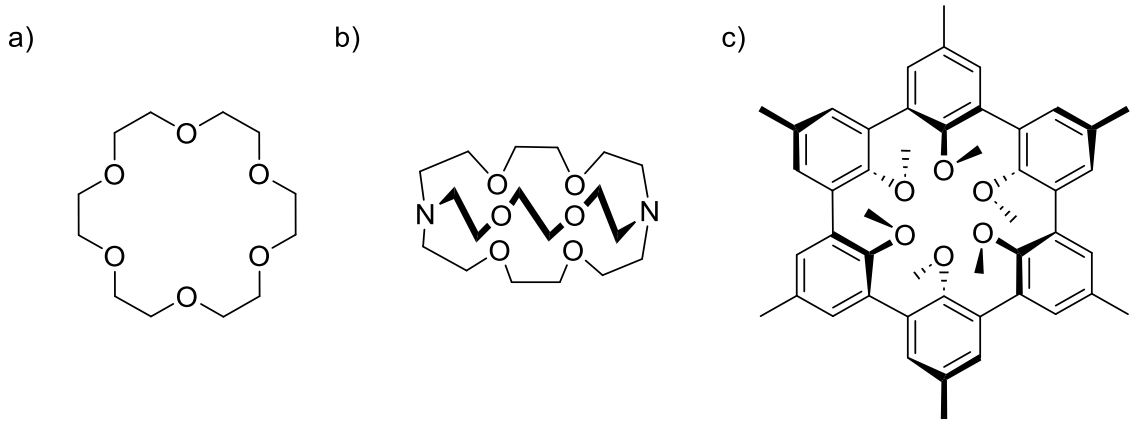

Figure 1.1. Initial classes of supramolecular host systems for alkali metal cation complexation: a) Pedersen's 18-crown-6 ether, b) Lehn's 2.2.2-cryptand (2.2.2-crypt), and c) Cram's spherand.

During the following three or so decades, supramolecular chemistry emerged as a growing interdisciplinary field in which dynamic non-covalent interactions between molecular species are employed for a myriad of applications. Just to highlight a few, these include the detection of charged species,[9-12] extraction of environmental pollutants,[13-15] drug delivery and transmembrane ion transport,[16-20] catalysis,[21, 22] and the production of functional and self-healing materials.[23-27]

With the vast array of potential applications of supramolecular chemistry in mind, this thesis seeks to deploy supramolecular chemistry for the construction of mechanically interlocked host molecules for anion and ion-pair recognition, and as potential polymerisation catalysts. This introductory chapter seeks to review the various host design strategies utilised in selective charged guest binding, before introducing mechanically interlocked molecules (MIMs) and highlighting their superior host-guest recognition behaviour over non-interlocked acyclic and macrocyclic receptor analogues. Finally, the aims of the novel work presented in this thesis will be outlined in light of the discussed supramolecular literature.

1.1.2 Non-covalent Interactions

In contrast to synthetic organic chemistry, in which molecular systems are typically prepared through the irreversible formation and cleavage of permanent covalent bonds, supramolecular chemistry exploits weaker, reversible, non-covalent interactions in order to achieve dynamic self-assembly and host-guest binding. While individual non-covalent interactions are typically much weaker than conventional covalent bond strengths (Figure 1.2), the combination of multiple weak supramolecular interactions, discussed in the following sections, can achieve strong overall association between two or more molecular components.

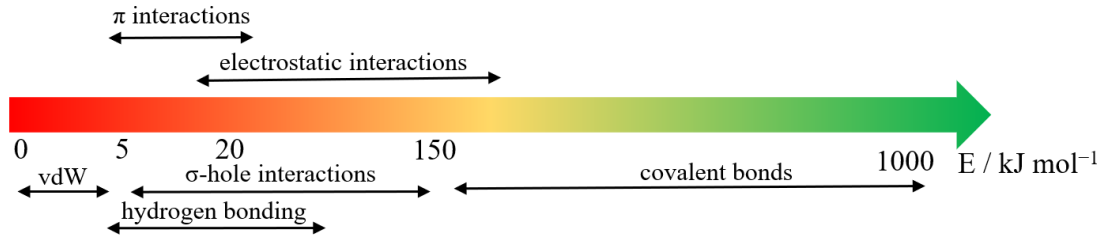

Figure 1.2. Relative strengths of covalent and non-covalent interactions.[4]

1.1.2.1 Electrostatic Interactions

Electrostatic interactions are the attractive Coulombic interactions between ions or dipoles of opposite charge, and the repulsive interactions between like-charged species. Accordingly, they can be characterised, in order of decreasing strength, as ion-ion, ion-dipole and dipole-dipole interactions (Figure 1.3).

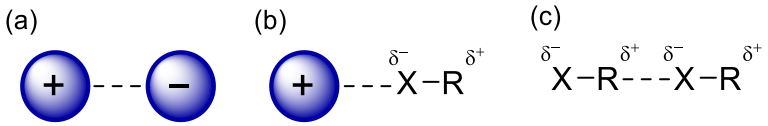

Figure 1.3. Types of electrostatic non-covalent interactions: a) ion-ion interactions, b) ion-dipole interactions, c) dipole-dipole interactions.

While ion-ion interactions are the strongest, on account of their permanent charge, their observance of Coulomb's law leads to a distance dependence ($E \propto r^{-1}$), and a lack of directionality. Ion-dipole and dipole-dipole interactions are more directional, due to the

directionality of the dipole partial charge. However, they have a stronger distance dependence ($E \propto r^{-2}$ and $E \propto r^{-3}$, respectively), and are comparatively weaker due to the lower charge magnitude of dipoles.[28] Due to their strong charge dependence when employed in supramolecular assemblies, electrostatic interactions are typically employed for the binding of charged guest species and can function even in highly polar solvents, including aqueous media.

1.1.2.2 π Interactions

Weaker than the aforementioned electrostatic interactions, π interactions are a further class of non-covalent interactions which arise between aromatic systems, or between an aromatic motif and an ion.[29] The former are responsible for the herringbone crystal structure of solid benzene,[30] and the weak dynamic nature of π interactions between graphite layers is responsible for the material's lubricating properties.[31]

The placement of a cation close to an electron-rich π aromatic system can result in polarisation of the π electron cloud, resulting in a favourable electrostatic attraction between the polarising cation and polarised π electron cloud. Such systems are well-known in biology where cation-π interactions are essential in the recognition of a range of neurotransmitters such as acetylcholine···tryptophan associations, which play a key role in the functioning of the parasympathetic nervous system.[32]

Conversely, the placement of an anion in close proximity to electron-deficient π aromatic molecules results in an analogous polarisation and attractive electrostatic interactions. Due to the need for anion-induced polarisation of the aromatic system, anion-π interactions are typically strongest for charge-dense anions such as fluoride. In 2012, Li *et al.* reported a triazine- and perfluorinated arene-containing macrocycle (Figure 1.4) which demonstrated strong and selective anion-π binding of fluoride over other, less

charge dense, halides, with $K_a > 10^3$ M^{-1} determined by UV-visible spectroscopic titration experiments in acetonitrile.[33]

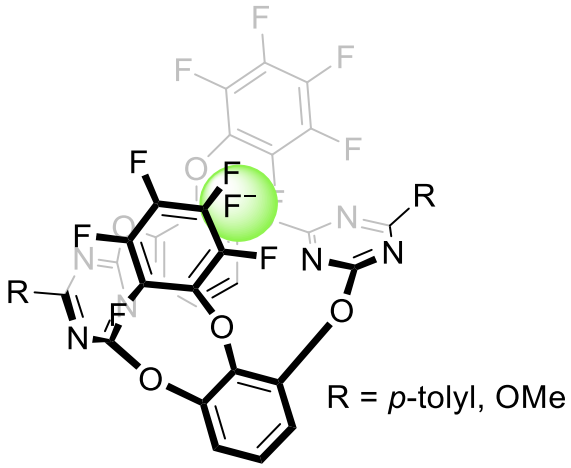

Figure 1.4. Triazine and perfluorinated arene-containing macrocyclic fluoride receptor reported by Li *et al*.

1.1.2.3 Hydrogen Bonding

Hydrogen bonding (HB) interactions occur when a hydrogen atom is covalently bound to a more electronegative atom, R–H, where R is typically N, O or F. The resulting polarisation of the R–H bond creates an electron-deficient H atom.[34] Such HB donors may interact with the lone pair of an electron-rich HB acceptor atom, E, or with anions. HB interactions exhibit directionality, brought about by a combination of electrostatics and orbital contributions. Consequently, hydrogen bonds are strongest when R–H···E bond angles approach 180°, however a range of bond lengths and angles are observed.[35] While individual HB interactions are relatively weak, with typical bond enthalpies of < 50 kJ mol^{-1},[36] their additive nature can lead to significant intermolecular association effects, accounting for the high boiling point of water and the stability of Watson-Crick base pairs in DNA.[37] Such HB arrays have also been exploited in designed abiotic systems, for example by Leigh's heterodimeric quadruple HB arrays which employed N–H···N and C–H···N HB interactions with $K_a > 10^7$ M^{-1} in DCM (Figure 1.5),[38] with

dimer molecular association displaying on/off switchability via protonation and deprotonation of the HB donor components.

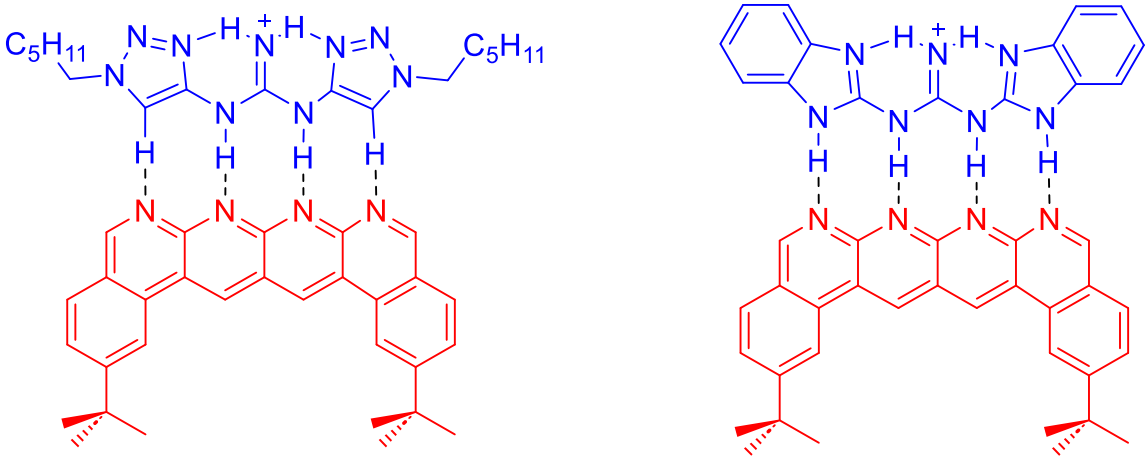

Figure 1.5. Quadruple HB arrays reported by Leigh and co-workers.

1.1.2.4 Halogen Bonding

Halogen bonding (XB) is a class of sigma-hole interaction resulting from the polarisation of a heavy halogen atom, X, typically iodine, when covalently bound to an electronegative group, R, to form an electron-deficient region at the halogen atom's pole position. This σ-hole can form highly directional attractive associations with Lewis basic species at a 180° angle to the R−X bond. The magnitude or depth of the σ-hole is dependent on the polarisability, and hence size, of the halogen atom. Thus, the strength of XB interactions increases upon descending the halogen group (Figure 1.6).[39, 40]

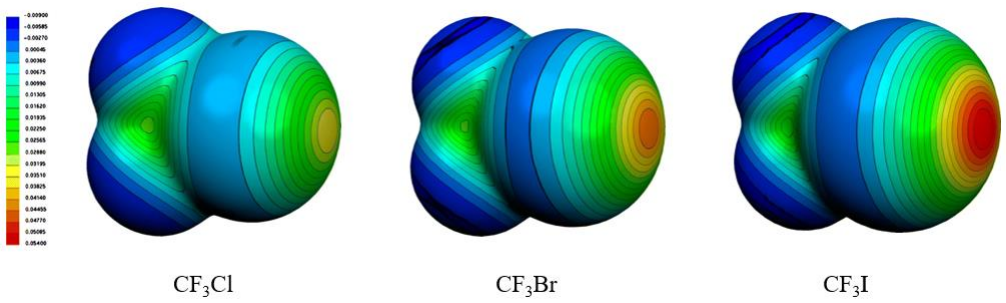

Figure 1.6. Electrostatic molecular potentials of halomethanes in hartrees at 0.001 electrons bohr^{-3} isodensity surface. Copyright 2007, Springer Nature, reproduced with permission.[39]

As a result of the stringent linear directionality of the σ-hole (Figure 1.7), projecting along the R–X bond axis, and reports of XB interactions exceeding HB strengths in aqueous media, XB systems demonstrate the potential for enhanced solution phase anion binding over HB analogues.[41-44] In particular, they are desirable as they avoid the complex protonation equilibria, and hence pH dependence, of HB systems.[45]

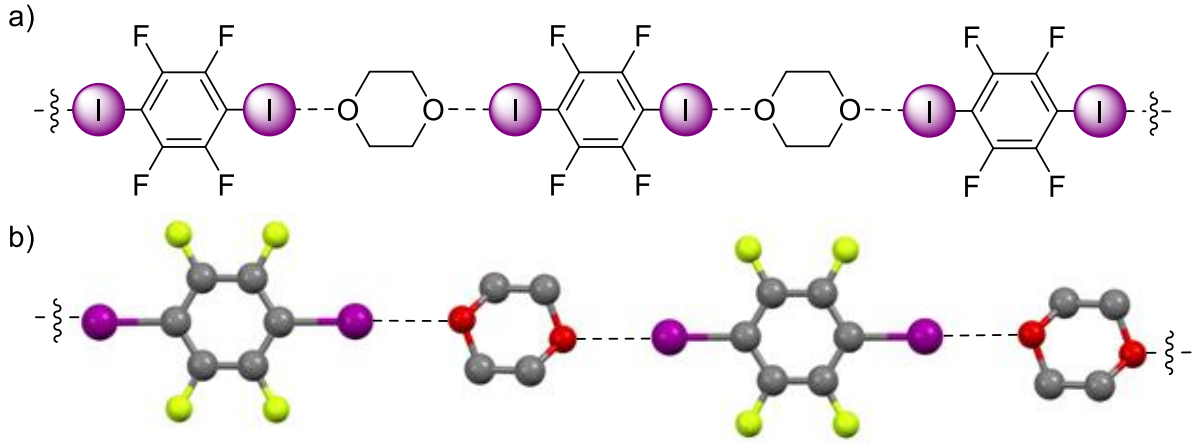

Figure 1.7. a) XB supramolecular polymeric structure with 1,4-diiodotetrafluorobenzene and dioxane. b) Solid state structure determined by x-ray diffraction, demonstrating the linearity of XB interactions, as reported by Jones and co-workers.[46]

1.1.2.5 Dispersion Interactions

Van der Waals forces or London dispersion interactions are the very weak transient associations which arise between the instantaneous dipoles which form in the electronic distributions of molecules. Although rarely employed as the principal non-covalent interaction in supramolecular systems, their ability to be a determining factor in the behaviour of molecular and supramolecular systems has been powerfully demonstrated in the attempted preparation of the hypothetical organic small molecule hexaphenylethane.[47, 48] While this species remains synthetically unknown, with the triphenylmethyl radical instead dimerising to form Gomberg's dimer, the all-*meta tert*-butyl substituted congener, hexakis(3,5-di-*tert*-butylphenyl)ethane, can be prepared, with an unusually long central C—C bond (r = 1.64 Å). The apparent stability of this molecule

has been attributed to the cumulative effect of dispersion interactions between the multiple *tert*-butyl groups stabilising the weak C—C bond (Figure 1.8).[49]

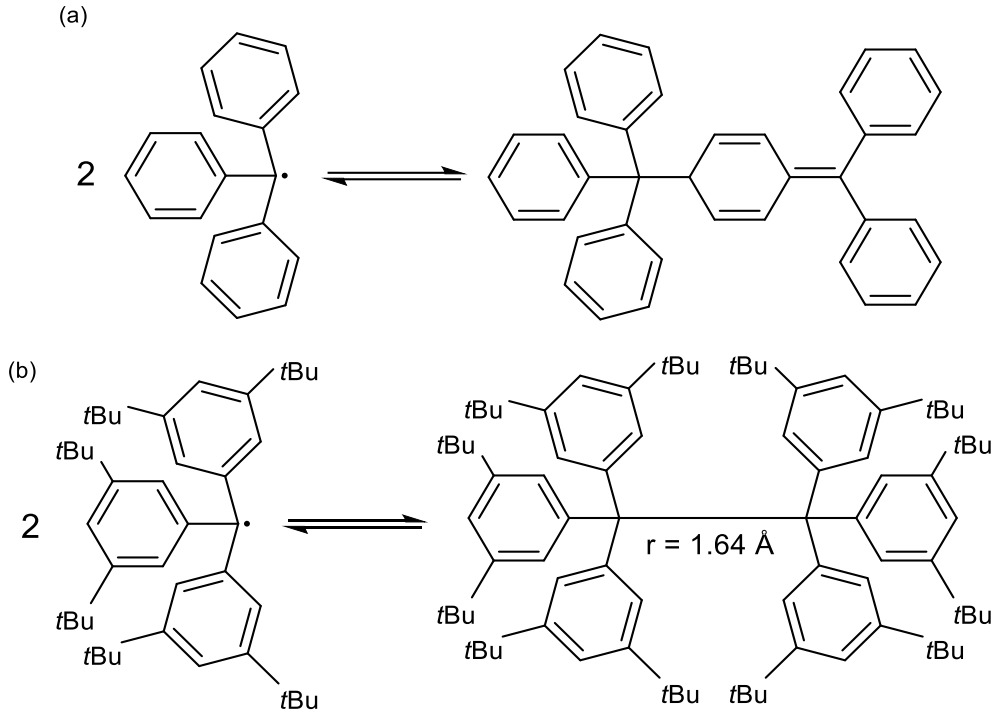

Figure 1.8. a) Reaction of two triphenyl radicals to form Gomberg's dimer, b) dimerisation of two tri(3,5-di-*tert*-butyl phenyl) radicals.

1.1.2.6 Hydrophobic Effects

The tendency of hydrophobic molecules to associate in aqueous media, to the exclusion of water molecules, is readily apparent in biological systems. The three-dimensional structures of proteins fold in such a manner that amino acids with hydrophobic side-chains cluster inside the protein, forming a hydrophobic core which serves to stabilise the protein structure.[50] The classical driving force for the hydrophobic effect is the entropic gain upon the displacement of HB-ordered water molecules by an apolar guest, which results in the release of disordered water molecules into the bulk medium.[51] However, reports such as those by Diederich *et al*. have demonstrated systems in which enthalpy is the dominant driving force, wherein the released water molecules can maximise HB interactions with bulk water molecules leading to continued interest in so-called 'non-classical' hydrophobic effects.[52, 53]

1.1.3 Principles of Supramolecular Host Design

1.1.3.1 Host-Guest Recognition

Supramolecular chemistry, as 'the chemistry of the intermolecular bond',[3] seeks to exploit non-covalent interactions to form larger, more complex, structures. Such efforts may be broadly categorised into two concepts: i) *host-guest recognition*, in which a host molecule selectively binds a smaller guest molecule (Figure 1.9 a) and ii) *self-assembly*, in which small molecules spontaneously form larger, higher order, structures through the formation of dynamic bonds (Figure 1.9 b). This section will discuss the design principles applied by supramolecular chemists to maximise the association of the components of supramolecular systems.

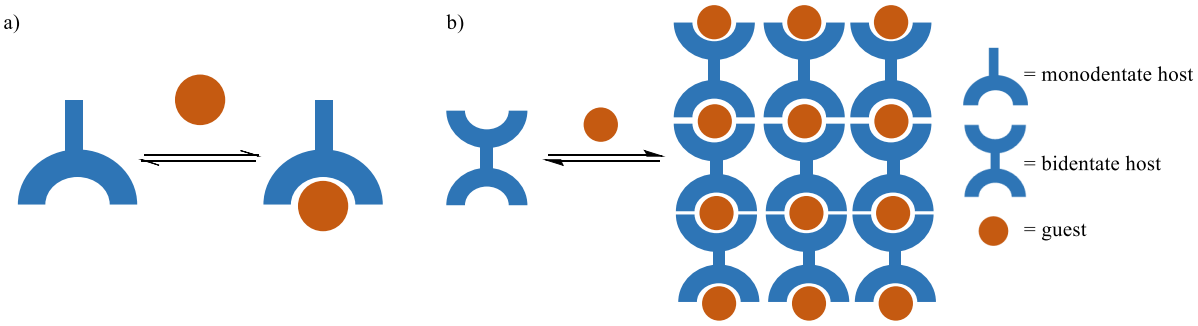

Figure 1.9. Schematic depiction of the supramolecular concept of a) host-guest chemistry, b) self-assembly.

1.1.3.2 Complementarity

The design of receptors with complementary host-guest size- and shape-matching exploits the directionality of non-covalent interactions in order to maximise host-guest association, engendering selectivity for the recognition of a target guest. Emil Fischer coined the concept of 'lock-and-key' complementarity in enzyme-substrate association in 1894,[54] in which the enzyme active site acts like a lock, such that only a specific substrate, of precise complementary shape to the active site, can act as a 'key' and bind to the enzyme. This theory was subsequently refined to give the 'induced-fit' model which recognises the unbound enzyme may not be a precise fit for the substrate, but that

a small degree of low energy conformational change may occur upon binding (Figure 1.10).[55]

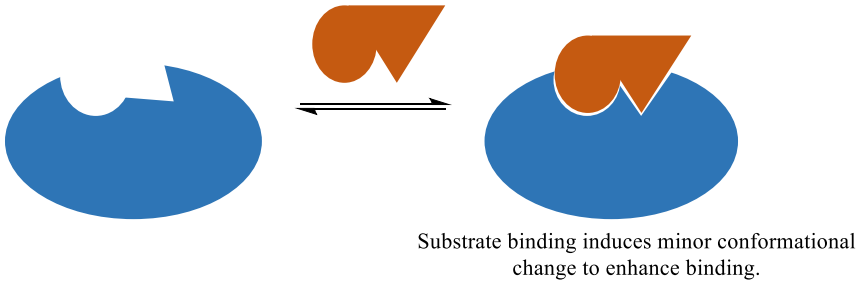

Figure 1.10. Schematic depiction of the 'induced fit' model of enzyme-substrate binding.

Size-shape complementarity has been exploited in synthetic systems, as demonstrated by Flood's triazolophane macrocycle, which preferentially binds chloride over the other halides.[56] Whereas fluoride is too small and iodide too large to be bound by the eight C−H HB donors in the macrocycle, chloride is an appropriate size to be bound in the centre of the cavity resulting in association constant values of 40- and 80-times larger magnitude than those obtained for fluoride and iodide, respectively, in DCM solution (Figure 1.11).[57]

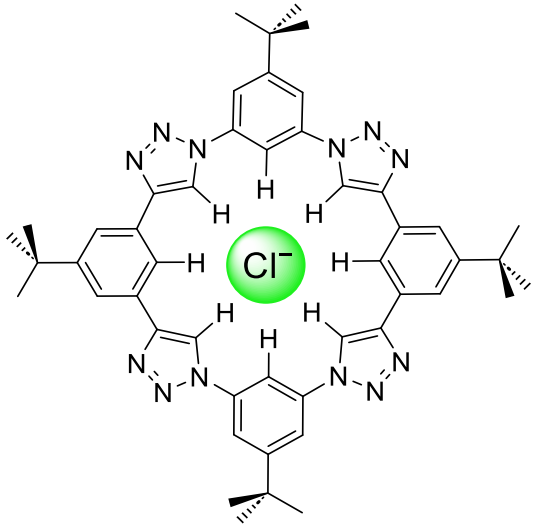

Figure 1.11. Size-specific chloride binding macrocycle reported by Flood and co-workers.

1.1.3.3 Preorganisation

A supramolecular host will typically have a given conformation which is most conducive to strong host-guest association. Thus, minimising the enthalpic and entropic penalties upon adopting this conformation enhances supramolecular association by reducing the associated thermodynamic penalties upon guest binding. Cram's principle of preorganisation states 'the more highly hosts and guests are organised for binding and low solvation prior to their complexation, the more stable will be their complexes'.[6] The enhancement of host-guest binding upon increasing preorganisation is demonstrated by a series of 'effects', which were first discovered in transition metal coordination chemistry, where multidentate ligands were introduced to augment the strength of transition metal complexation.

The chelate effect describes the observation of the significantly greater thermodynamic stability of metal cation complexes with chelating polydentate ligands, over the equivalent number of non-chelating monodentate ligands.[58] Such an increase is both entropic and enthalpic in nature. Increasing entropic favourability, the binding of a multidentate ligand displaces a greater number of solvent molecules per ligand bound from the metal ion's coordination sphere compared with monodentate ligand binding, which does not result in a net increase of free solvent molecules. Furthermore, the enthalpic penalty for bringing together electron-rich Lewis basic donor atoms such as nitrogen and oxygen, and the electrostatic repulsion of the donor atom lone pairs, is partially overcome during ligand synthesis, resulting in a more favourable enthalpic change upon ligand coordination.

Compared to their analogous acyclic chelating ligands, macrocycles typically exhibit greater binding affinities for guests – the macrocyclic effect – which also arises due to a

combination of enthalpic and entropic factors. As cyclic species are conformationally more preorganised compared to their acyclic analogues, there is a reduced entropic loss upon binding to a metal ion, while macrocyclic species are typically more poorly solvated than acyclic ligands, leading to a diminished desolvation penalty upon binding. The macrocyclic effect can be further extended by formation of a more preorganised three-dimensional structure, for example a cryptand. Such is the driving force of the 'cryptate effect', disproportionation of sodium is observed with 2.2.2-crypt in triethylamine, forming the sodide (Na^-) anion in order to enable binding of Na^+ by the cryptand (Figure 1.12).[59]

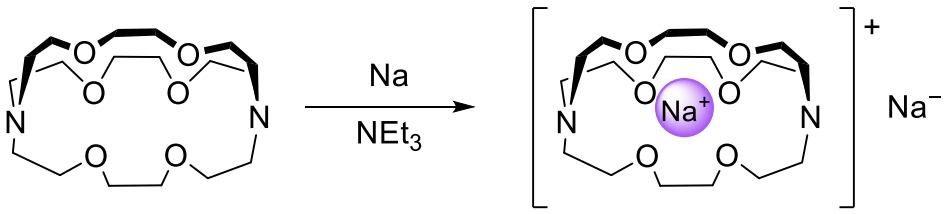

Figure 1.12. Synthesis of sodide complex by reaction of Na with 2.2.2-crypt.

1.2 Supramolecular Anion Recognition

1.2.1 The Importance of Anions

The inspiration for the design of selective anion recognition systems primarily stems from an appreciation of the fundamental importance of anions in biology. Indeed, the majority of enzyme substrates and co-factors are anionic at physiological pH, thus biological systems have evolved the ability to effect exquisite selectivity for anion binding in aqueous media. The three-dimensional binding cavities of the phosphate and sulfate binding proteins are highly preorganised for selective binding of their respective oxoanion guest species. The protein structure spatially arranges multiple HB donor groups for convergent guest binding in a highly solvent-excluded cavity, minimising competing solvent interactions and maximising binding affinities.[60, 61]

The moderation of even simple spherical chloride and iodide halide anions is essential for human health. Cystic fibrosis, a hereditary life-limiting disease, is caused by defects in cell membrane ion channels, which result in misregulation of intercellular chloride transport,[62] while normal thyroid functioning is dependent upon regulation of iodide to enable synthesis of essential hormones.[63] Furthermore, adenosine triphosphate (ATP), exists in anionic form (either as ATP^{4-}, or as an anionic salt) at physiological pH.[64] In addition to its well-known role as an energy source for all cell types, ATP functions as an extracellular messenger molecule thus regulation of transport of ATP-derived anions across cell membranes is essential for correct functioning of biological processes.

In addition to naturally occurring anions, the monitoring of anionic anthropogenic environmental pollutants is an area of increasing concern. The pertechnetate species, $^{99}TcO_4^-$, is one of the most hazardous components of nuclear waste streams, due to its extremely long half-life ($t_{1/2}$ = 2.13 x 10^5 years) and high water solubility.[65] In addition the mining of precious metals exploits the highly toxic cyanide anion to form soluble salt complexes with the target metal, enabling metal extraction from their ores.[66] Furthermore, leaching of the toxic non-target contents of metal ores, such as arsenate anions, can result in significant ground water pollution.[67] Indeed, toxic arsenic acid derivatives have been detected in groundwater globally and the removal of this oxoanion from contaminated watercourses is extremely challenging.[68] Clearly, the industrial production of toxic anions leads to an imperative to develop methods for their detection and remediation to prevent significant environmental damage.

In addition to threats to human health, anthropogenic anions pose a significant threat to ecosystems. The move to increasingly intense arable farming over the past 80 years has resulted in the deployment of synthetic nitrate and phosphate fertilisers at scale on

agricultural land to increase crop yields.[69] While the implementation of such farming technologies has enabled the scaling of farming in the face of ever-increasing global food demand, the leaching of excess nutrients into local watercourses has resulted in eutrophication, which can result in excessive growth of phytoplankton and algae, and the formation of hypoxic aquatic environments.[70] Thus, there has been immense interest in the deployment of the supramolecular toolkit for the selective recognition of anions for anion transport,[20, 43, 71] sensing,[72-74] and environmental remediation.[75]

1.2.2 Challenges of Anion Recognition

Anions typically possess larger ionic radii than their isoelectronic cations (Table 1.1).[4, 76, 77] As a result, anions possess relatively lower charge densities and hence their electrostatic interactions are inherently weaker than for the analogous cations. Furthermore, for a host to bind an ion, the guest must be at least partly desolvated. As anions are typically more strongly-solvated than cations with comparable radii, particularly in polar protic solvents, there is a correspondingly larger desolvation enthalpic barrier to be overcome for anion binding, reducing the thermodynamic drive for host-guest recognition.

Anion	Ionic Radius (Å)	ΔG_{hyd} (kJ mol^{-1})	Cation	Ionic Radius (Å)	ΔG_{hyd} (kJ mol^{-1})
F^-	1.33	−465	Na^+	1.02	−365
Cl^-	1.81	−340	K^+	1.38	−295
Br^-	1.96	−315	Rb^+	1.57	−275
I^-	2.20	−275	Cs^+	1.67	−250

Table 1.1. Effective ionic radii of 6-coordinate group 7 anions and isoelectronic group 1 cations. [4, 76, 77]

In aqueous media, the degree of anion hydrophilicity, and hence hydration, is indicated by the Hofmeister series (Table 1.2).[78] Thus, in aqueous media, hydrophobic anions, such as iodide or perchlorate, typically display the highest host-guest binding affinities due to a reduced desolvation penalty upon binding.[79, 80]

More Hydrophobic
Weakly Hydrated

More Hydrophilic
Strongly Hydrated

Organic anions > ClO_4^- > I^- > SCN^- > ClO_3^- > Br^- > Cl^- > F^- > CO_3^{2-} > HPO_4^{2-} > SO_4^{2-} > citrate^{3-}

Table 1.2. The Hofmeister series of anion hydration.[4]

As many anions are conjugate bases and so protonate at low pH, anion recognition is generally highly dependent upon solvent pH. Furthermore, many anion receptors, such as polyammonium systems (Section 1.2.3.1) are susceptible to deprotonation at high pH. Thus, anion binding can only function within a narrow 'pH window' in which the receptor is protonated, while the anion is deprotonated (Figure 1.13).[81]

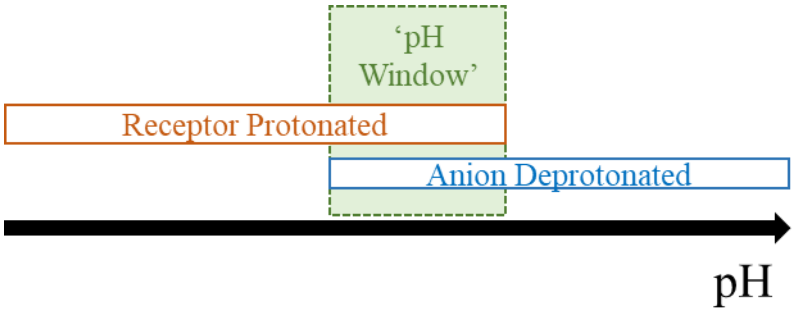

Figure 1.13. Schematic depiction of the pH-dependency of anion host-guest chemistry.

A further consideration in anion binding is the wide range of geometries adopted by even simple inorganic anions (Figure 1.14). Consideration of the target guest geometry is essential to ensure complementarity between the anionic guest and the host binding site. For geometrically complex molecular anions, this can pose a particular challenge.[80]

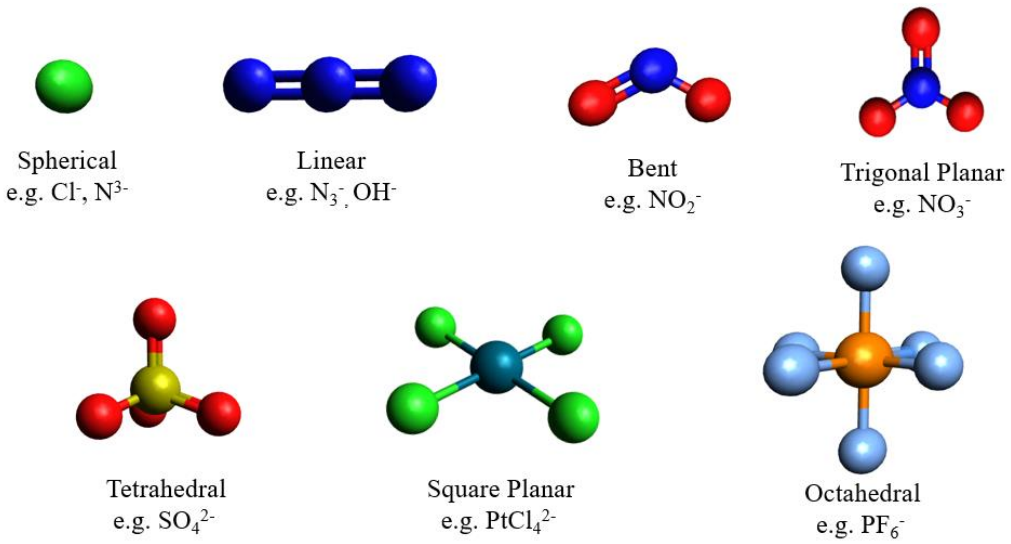

Figure 1.14. Commonly occurring anion geometries.

1.2.3 Synthetic Anion Receptors

Inspired by the range of biotic receptors, such as the phosphate- and sulfate-binding proteins, which employ highly solvent-excluding three-dimensional cavities for strong and selective anion recognition in aqueous media,[82] for the past four decades or so supramolecular chemists have sought to design a variety of positively charged and neutral host systems for the strong and selective binding of target anions. Initial attempts focused on highly positively charged receptors employing multiple HB interactions for recognition in aqueous media, with neutral systems for binding in organic media being subsequently reported.

1.2.3.1 Positively Charged Receptors

The field of supramolecular anion recognition was pioneered in the late 1960s to early 1980s by the seminal works of Park and Simmons, Lehn, and Schmidtchen. Park and Simmons reported a lipophilic cryptand-like ammonium macrobicyclic receptor which was capable of binding halide anions in acidic aqueous media (Figure 1.15 a).[83] The length of the alkyl spacer between N atoms dictates the pK_a of the secondary amines. Thus, the introduction of a propyl or longer linker chain length enables full protonation

of the polyamine host at physiological pH, facilitating strong binding of biotic anions such as phosphate esters at pH = 7.5, reminiscent of the biotic spermine and spermidine species.[84] A systematic study in 1982 by Yatsunami and co-workers found a macrocycle with propyl and butyl spacers gave rise to a fully protonated host, and hence the strongest binding of ATP^{4-} in aqueous buffer (Figure 1.15 b).[85] Related hexaprotonated polyammonium macrocycles of complementary sizes for selective dicarboxylate (DCB) anion binding were reported by Lehn and co-workers (Figure 1.15 c), and an octaprotonated cryptand described by Lehn and co-workers demonstrated selectivity for the azide anion due to the complementarity of the cryptate cavity for the linear anion (Figure 1.15 d).[86]

In 1977 Schmidtchen constructed macrotricyclic quaternary ammonium cage-like receptors, wherein, without HB donors, the pH-independent tetracationic hosts bound halide anions via strong electrostatic interactions (Figure 1.15 e).[87]

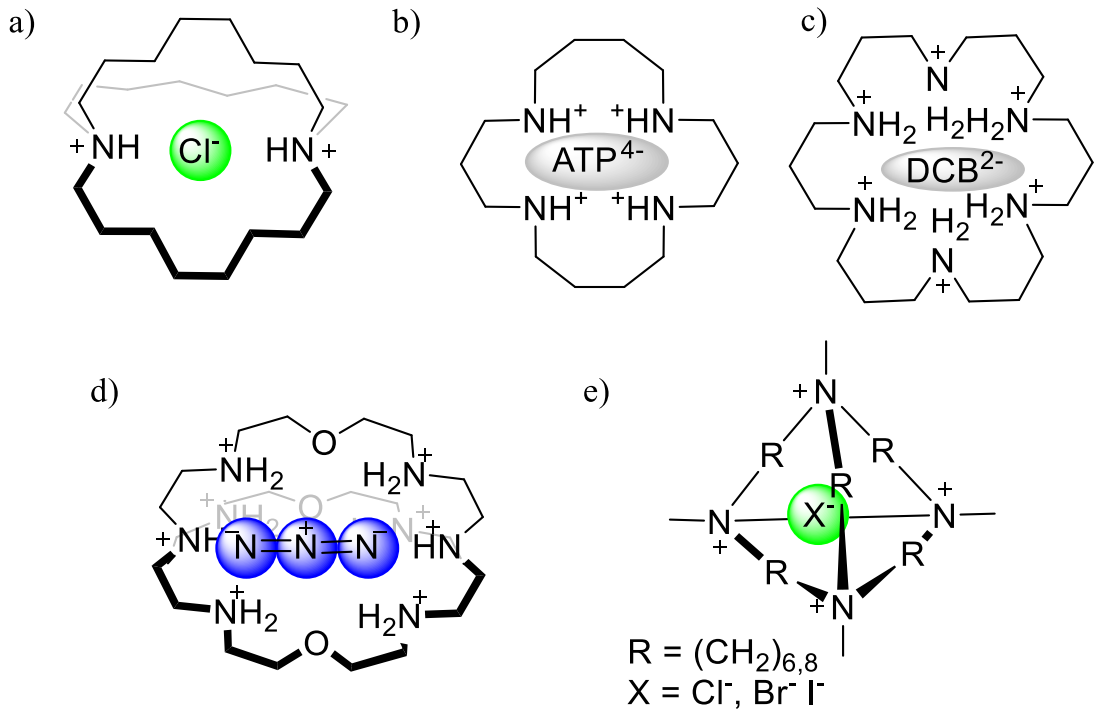

Figure 1.15. Initially reported cationic ammonium anion receptors.

Despite these promising preliminary results, in the ensuing years the field took a surprising time to fully emerge, with reports of incorporation of a range of HB donor cationic motifs into various acyclic and macrocyclic structural host frameworks. (Figure 1.16).[88]

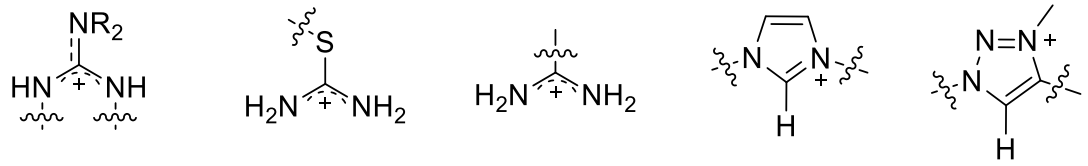

Figure 1.16. Selection of positively charged HB anion binding motifs.

Of these receptor motifs, the guanidinium motif attracted interest due to its high pK_a of *c.* 12–13, depending upon substituents, enabling it to act as a bidentate HB donor over a wide pH range.[89] The first examples of guanidinium-containing receptors were the series of phosphate binding macrocycles reported by Lehn and co-workers,[90] which were capable of anion recognition in water, however the binding constants were relatively weak (K_a < 250 M^{-1}) which was attributed to the delocalisation of the positive charge in the guanidinium motif (Figure 1.17 a). In 1992, Hamilton and co-workers demonstrated exploitation of intramolecular HB interactions to preorganise a bis-guanidinium receptor which demonstrated strong binding of the diphenylphosphate anion (K_a > 10^4 M^{-1} in MeCN) (Figure 1.17 b).[91]

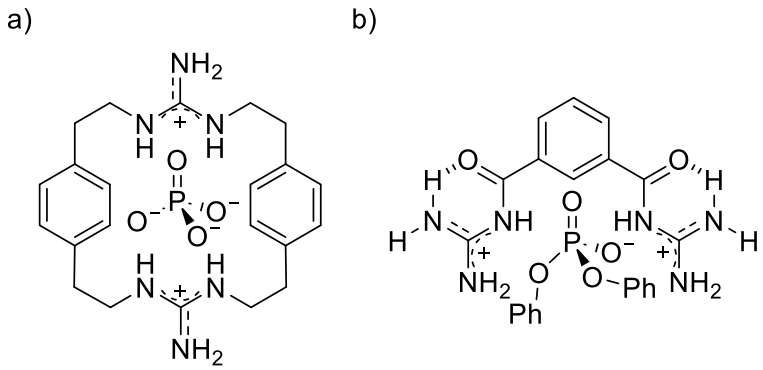

Figure 1.17. Guanidinium HB anion receptors reported by a) Lehn and co-workers, b) Hamilton and co-workers.

Similarly, imidazolium and triazolium motifs offer pH independent electrostatic binding, in these cases augmented by charge-assisted C−H HB donation to anionic guest species.[92] In 2005, Kim and co-workers demonstrated selective fluoride binding by the convergent charge assisted C−H HB interactions of a calix[4]imidazolium[2]pyridine anion receptor, in both acetonitrile and DMSO (Figure 1.18 a).[93] The first reported use of a triazolium motif for anion binding came in 2007, when Kumar and Pandey reported a bis-triazolium receptor which displayed selectivity for dihydrogen phosphate over halides in chloroform (Figure 1.18 b).[94] The use of charge led to highly polarised iodotriazolium XB donors by Beer and co-workers who demonstrated highly linear binding of halides, consistent with the binding occurring through stringently linear XB interactions (Figure 1.18 c).[95] Such XB interactions have been subsequently exploited for a range of non-interlocked and MIM hosts for enhanced anion recognition and selectivity (*vide infra*).

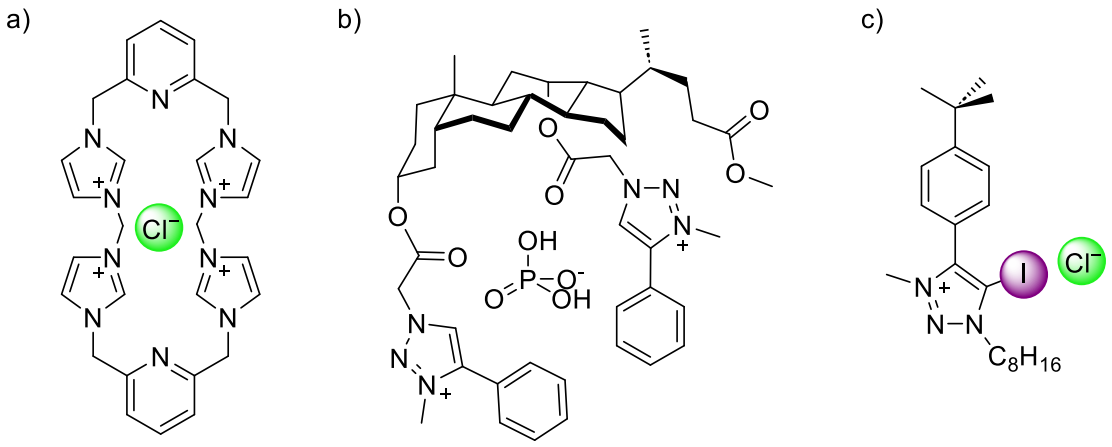

Figure 1.18. Charge-assisted HB donors reported by a) Kim and co-workers, b) Kumar and Pandey, and c) XB donor reported by Beer and co-workers.

1.2.3.2 Neutral HB Receptors

While initial reports of supramolecular anion hosts typically employed charge-assisted HB interactions, as discussed above, the non-directional nature of electrostatic interactions, particularly dominant in highly positively charged receptor systems, led to the expected directionality of HB interactions being compromised, and the necessity of

the target anion guest competing with the cationic receptor's counterion reduces binding affinities. Furthermore, electrostatic interactions frequently result in selectivity trends which mirror the overall charge of anions, thus highly charged receptors typically favour the binding of ATP^{4-}, over adenosine di- or mono-phosphate, which possess charges of 3^- and 2^- respectively.[96, 97] Thus, efforts moved towards the development of potent neutral HB donor motifs for anion recognition. These initially reported neutral anion receptors were primarily designed to perform in polar aprotic organic solvent media and were dominated by amide and urea HB donor containing systems.

In 1997, Crabtree and co-workers reported a seminal neutral bis-amide isophthalamide HB donor receptor which exhibited strong binding of halides in DCM-d_2 (Cl^- K_a = 6.1 x 10^4 M^{-1}), with association constants following the charge density of the halides (Cl^- > Br^- > I^-).[98] The receptor binds halides through convergent binding by both amide HB donors through an unusual *syn-syn* amide conformation (Figure 1.19 a). In 2005, Gale and co-workers demonstrated a related bis-urea containing neutral HB receptor which demonstrated selectivity for carboxylates in DMSO-d_6 solution, with single crystal XRD studies revealing binding of the anion through four convergent HB interactions with the carboxylate guest in the solid-state (Figure 1.19 b).[99]

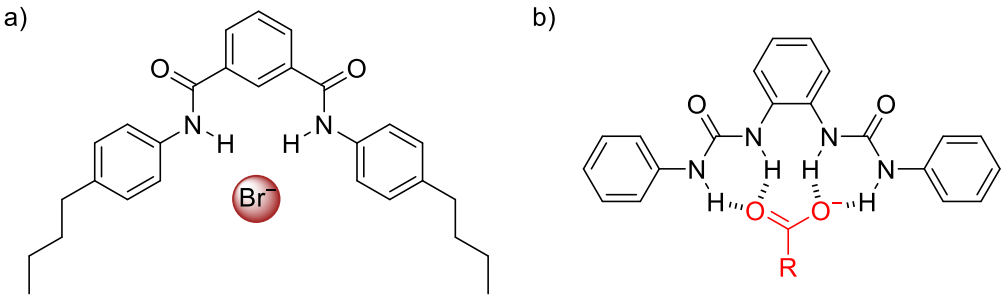

Figure 1.19. Neutral amide-based HB anion receptors reported by a) Crabtree and co-workers, b) Gale and co-workers.

Potent neutral pyrrole HB donor macrocycles, calix[4]pyrroles, have been pioneered for anion recognition by Sessler and co-workers.[92] Such systems demonstrated noteworthy

selectivity for fluoride binding over the larger halides in DCM and MeCN, due to size complementarity between the host cavity and the halide guest.[100] Upon fluorination of the pyrrole backbone to enhance HB potency by Sessler and co-workers in 2000, a seven-fold enhancement in the binding constant for dihydrogen phosphate in acetonitrile-d_3 with 0.5% *v/v* D_2O compared with the all-proto analogue was observed (Figure 1.20 a).[101]

As seen in the earlier discussed work of Flood and co-workers (Figure 1.11), recent work has employed the highly polarised C−H bond in the 1,2,3-triazole moiety as an HB donor in neutral anion recognition motifs.[92] Such interactions, particularly when multiple triazole HB motifs act in concert for binding of an anionic guest, can give rise to strong anion binding. For example, in 2008, Craig reported a tetra-triazole foldamer which underwent helical folding upon binding of halides, showing strong binding ($K_a > 10^4$ M^{-1} for Cl^- and Br^- in acetone-d_6), which 2-D NMR experiments confirmed arise through the folded conformer enabling tetradentate convergent HB binding (Figure 1.20 b).[102]

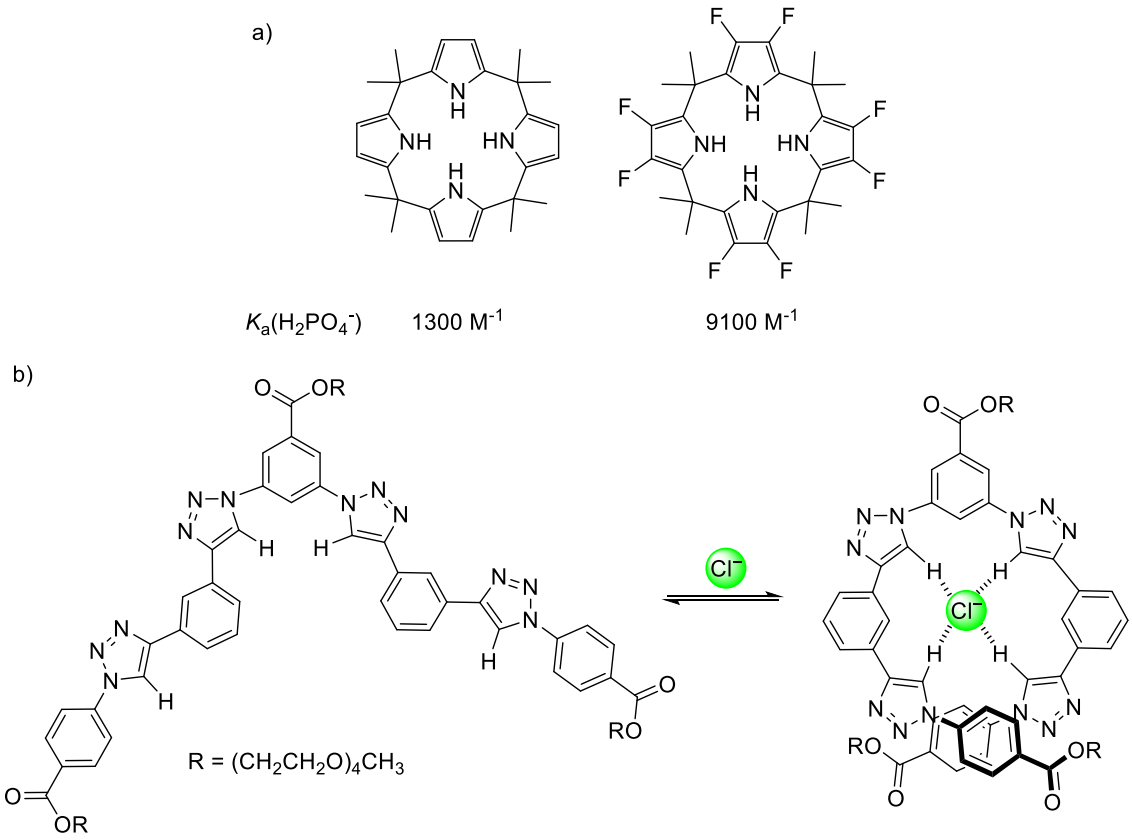

Figure 1.20. a) Calix[4]pyrrole anion receptors reported by Sessler and co-workers. b) Neutral HB foldamer formation upon chloride binding, as reported by Craig and co-workers.

1.2.3.3 Neutral XB Receptors

Given their stringent linearity and pH independence,[103] there is growing interest in the synthesis of highly potent neutral XB anion receptors. The first report of XB anion recognition was made by Metrangolo, Resnati and co-workers in 2005, who described a heteroditopic neutral XB receptor for sodium halides.[104] The inclusion of electron-withdrawing fluorine atoms onto the iodobenzene motif afforded a potent XB binding interaction which resulted in strong iodide binding as evidenced by ^{1}H NMR spectroscopic binding studies in $CDCl_3$. XRD studies confirmed the highly linear nature of the halogen bond (∠C–I···I = 177°), while the ethylene glycol base of the tripod effectively bound the sodium cation. (Figure 1.21).

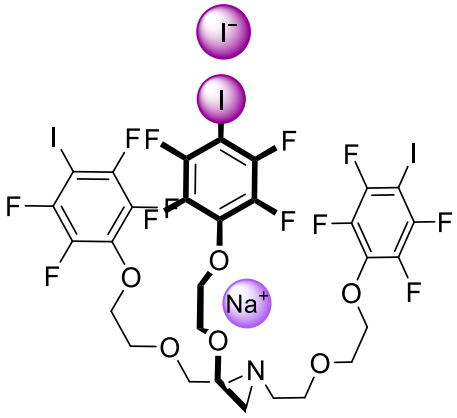

Figure 1.21. The first neutral XB anion receptor, reported by Metrangolo, Resnati and co-workers.

Five years later, in 2010, Taylor and co-workers reported a series of mono-, bi- and tri-dentate acyclic XB receptors capable of solution phase halide anion binding in deuterated acetone, which could be monitored by ^{19}F NMR spectroscopy (Figure 1.22).[105] Predictably, the tripodal receptor demonstrated the greatest halide binding affinity, with selectivity following the charge density of the halides ($Cl^- > Br^- > I^-$).

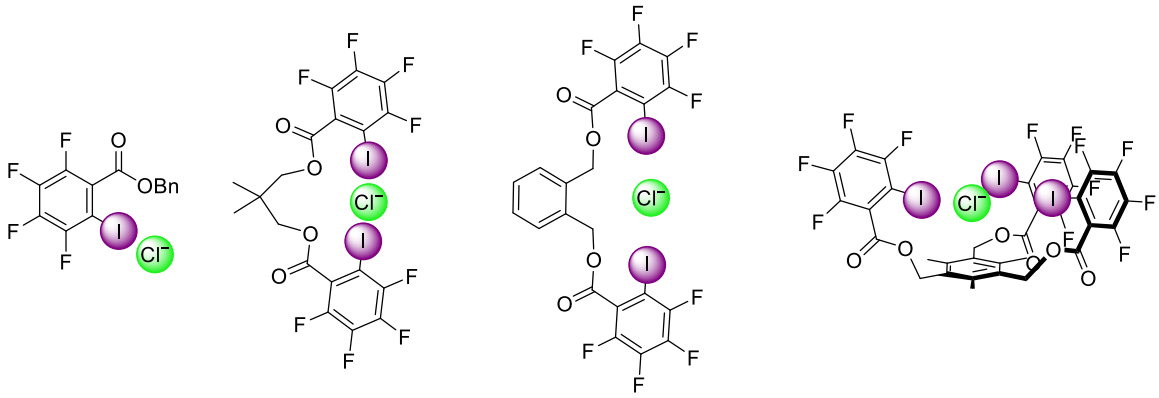

Figure 1.22. Series of iodo fluorobenzene based neutral XB anion receptors, reported by Taylor and co-workers.

More recently, iodo-1,2,3-triazoles have emerged as an XB donor motif of choice due to their ease of incorporation into a range of structures by a copper(I)-catalysed azide-alkyne cycloaddition (CuAAC) 'click' reaction between an iodoalkyne and an azide. In 2015, Schubert and co-workers reported an indolocarbazole-linked bis-iodotriazole XB receptor,[106] which demonstrated relatively strong binding of bromide in THF (K_a = 1.58

x 10^3 M^{-1}). Incorporation of judiciously positioned hydroxyl groups, such that HB interactions between the triazole N atom and hydroxyl proton enabled the preorganisation of the XB donor site in a conformation for convergent binding, resulted in a *c.* 2.5-fold increase in bromide binding constant (Figure 1.23 a). In a systematic 2021 study, Docker *et al*. further demonstrated marked increases in potency in iodo-1,2,3-triazole systems through the appendage of inductively electron withdrawing aryl groups to the triazole motif, further polarising the halogen atom and hence increasing the magnitude of the σ-hole, affording significantly enhanced halide anion binding by neutral XB hosts in competitive 2.5:97.5 *v/v* D_2O:acetone-d_6 (Figure 1.23 b).

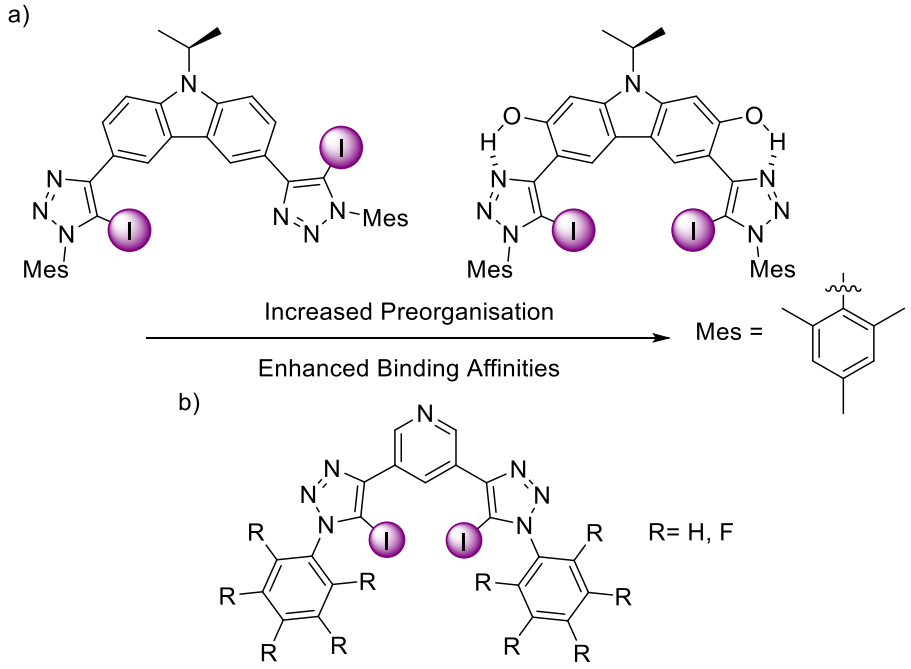

Figure 1.23. Examples of neutral XB receptors which exhibit enhanced halide binding affinities via a) increased preorganisation and b) electron withdrawing aryl group substituents.

1.3 Ion-Pair Recognition

The need to separate an ion from its counterion upon binding by a monotopic receptor gives rise to a significant energetic penalty, especially in organic media. Thus, supramolecular chemists historically employed highly non-coordinating lipophilic counterions to reduce this barrier, typically the tetrakis(3,5-

bis(trifluoromethyl)phenyl)borate ($BAr^{F}{}_{4}^{-}$) or hexafluorophosphate (PF_6^-) anions for cation binding, and the tetra-*n*-butylammonium (TBA^+) cation for anion binding. Such a requirement for complex counterions reduces the utility of host-guest systems in the sensing and remediation of the previously discussed anthropogenic environmental pollutants, which typically exist as simple alkali metal, or halide or oxoanion salts. Hence, there is growing interest in the binding of *both* a cation and anion by a single receptor, known as ion-pair recognition. Such heteroditopic host systems have the potential to unlock a range of challenging recognition applications, including salt extraction for precious metal mining,[107, 108] lithium salt recovery for battery development and sustainability,[109-111] environmental cleansing, such as the remediation of anthropogenically polluted water,[69, 70] and membrane transport of sodium and potassium salts for biomedical applications.[112-115]

Various modes of ion-pair binding are possible, commonly including: i) the formation of a contact ion-pair, in which the two bound ions are in direct contact (Figure 1.24 a); ii) host-separated ion-pair binding in which the two recognition sites are distinctly apart from one another (Figure 1.24 b) and iii) solvent separated ion-pair binding, in which solvent molecules coordinate to one or both bound ions in the space between them (Figure 1.24 c).[107, 116] Through judicious heteroditopic host design, positive cooperative ion-pair binding is sought after, arising from favourable electrostatic interactions between the proximally bound oppositely charged ions, and potential conformational allosteric effects.

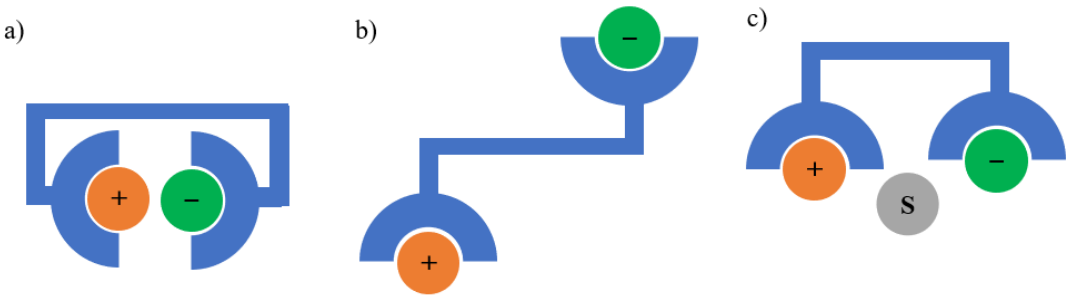

Figure 1.24. Schematic depiction of a) a contact ion-pair, b) a host-separated ion-pair, c) a solvent-separated ion-pair.

While contact ion-pair complexes are common in nature, for example in the cascade binding of anionic substrates between two Zn^{2+} centres in alkaline phosphatases,[28] in general recent research efforts have focused on heteroditopic receptor synthesis (i.e. receptors with two distinct binding motifs).[108]

The interplay of electrostatic and allosteric effects in heteroditopic ion-pair recognition were explored by Flood and co-workers, who produced a series of neutral heteroditopic macrocycles for the binding of sodium halide ion-pairs (Figure 1.25 a).[117] Extensive cation, anion and ion-pair binding studies in 4:1 *v/v* CD_2Cl_2:CD_3CN, coupled with density functional theory (DFT) computational studies, demonstrated favourable cooperative contact ion-pair electrostatic contributions, which are dictated by ionic radii, to be dominant. Thus, sodium halide ion-pairs were noted to exhibit a greater degree of cooperativity than $NaClO_4$.

The ability of XB anion recognition sites to effect ion-pair binding in heteroditopic receptor systems was powerfully demonstrated in 2020 by Docker *et al*. who reported a series of 3,5-bis-proto- and iodo-triazole pyridyl receptors appended by benzo-15-crown-5 (B15C5) substituents (Figure 1.25 b).[118] While binding of halides in the absence of co-bound Na^+ was weak for both HB and XB systems in 10% *v/v* DMSO-d_6 in $CDCl_3$ (K_a < 50 M^{-1} in all cases), Na^+ crown ether complexation led to an effective switch-on response in anion binding, with ion-pair binding constants for bromide and iodide an order of

magnitude larger for the XB receptor over the HB analogue (Br^-, $K_{a(XB)}$ = 5060, $K_{a(HB)}$ 380 M^{-1}). Such a marked increase was attributed to proximal electrostatic interactions and inductive through-bond increased polarisation of the XB iodine donor atoms by the B15C5 co-bound sodium cations. In 2023, Taylor *et al*. extended this work with an XB ion-pair receptor which exploited positive allosteric effects induced by co-bound bis-B15C5 K^+ sandwich complexation, resulting in a 10,000-fold increase in the magnitude of the halide binding constants in 1:1 *v/v* $CDCl_3$:CD_3CN (Figure 1.25 c).[119]

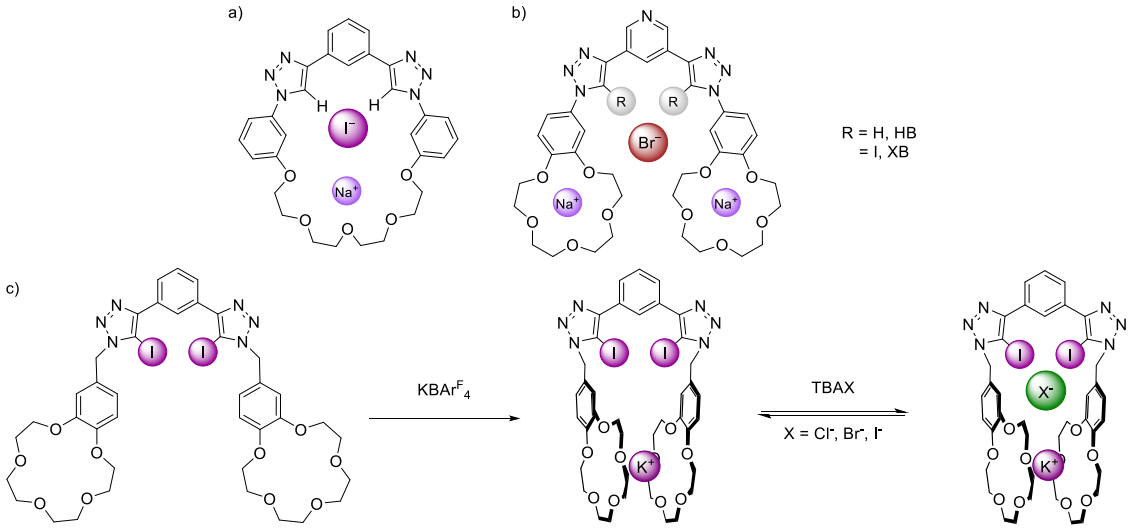

Figure 1.25. a) Flood's ion-pair macrocycle, b) crown-ether appended XB receptor for sodium halide ion-pair recognition by Docker *et al*. c) Positive allosteric effect inducing ion-pair binding, by Taylor *et al*.

Such ion-pair systems have also been used to prepare functional materials. Romański and Piątek incorporated a heteroditopic receptor into a polymethacrylate material, in which the polymer lipophilicity resulted in enhanced sodium nitrite ion-pair binding over the free receptor in $CDCl_3$ (Figure 1.26 a).[120] Importantly, as polymeric materials can be recycled via washing, such materials provide a reusable platform for extraction of contaminants from solution. In related work, the same group functionalised polymeric resin beads with a similar thiourea-aza crown ether ion-pair receptor to extract sodium nitrite from acetonitrile, but was unable to bind NO_2^- in $TBANO_2$ MeCN solutions, highlighting the importance of cation binding for cooperative anion binding (Figure 1.26

b).[121] In addition to these non-interlocked receptors, mechanically interlocked receptors have been exploited for powerful ion-pair binding, capable of the extraction of alkali metal salts into organic media and the binding of transition metal salts (see Section 1.4.2.3).

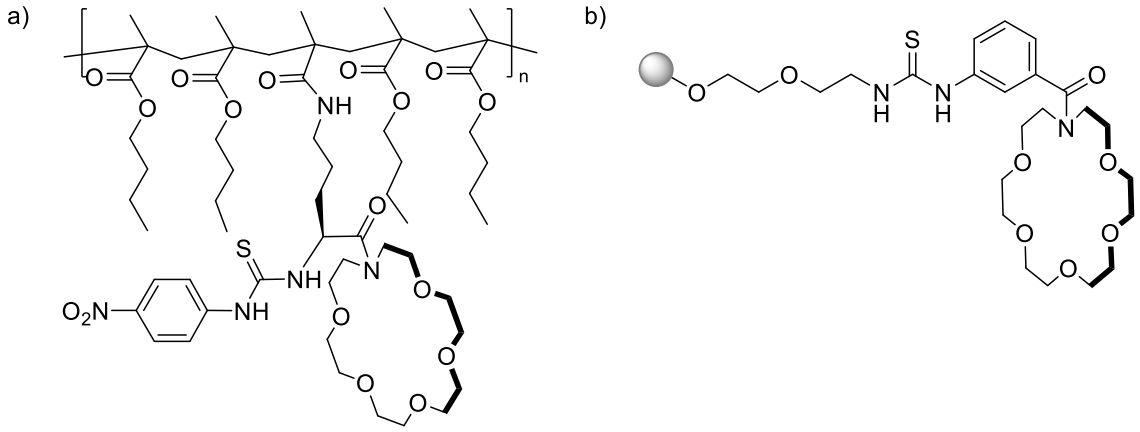

Figure 1.26. a) Polymethacrylate-incorporated ion-pair receptor, as reported by Romański and Piątek, b) Romański and co-workers' ion-pair receptor functionalised polymer resins as a recyclable extractant of sodium nitrite.

1.4 Mechanically Interlocked Molecules

Mechanically interlocked molecules (MIMs) are a class of topologically constrained molecules formed by linking two or more components such that the components are not directly connected by conventional covalent bonding, but nevertheless cannot be separated without the cleavage of covalent bonds. The components of such systems may be said to be joined by 'mechanical bonding'. The two major classes of MIMs are [*n*]rotaxanes and [*n*]catenanes, where *n* denotes the number of mechanically interlocked components. [*n*]Rotaxanes consist of an assembly whereby a macrocycle is threaded by an axle, with axle-appended bulky stopper groups preventing macrocycle dethreading (Figure 1.27 a). [*n*]Catenanes are a second class of MIMs in which one or more macrocycles are threaded through the aperture of each other, creating a topologically complex molecule in which the macrocycles resemble links in a chain (Figure 1.27 b).

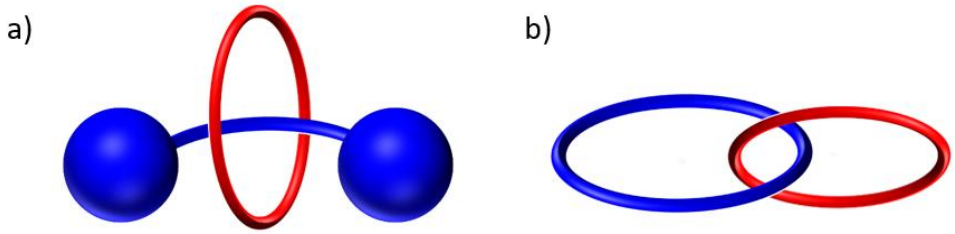

Figure 1.27. Schematic depiction of a) a [2]rotaxane, b) a [2]catenane.

Over the past 40 years, the development of novel template-based synthetic methodologies for accessing MIM architectures in pragmatic yields has enabled the mechanical bond to be exploited for a range of applications. This section will briefly review MIM synthesis from the formation of trace quantities in the 1960s to contemporary templated methods, before discussing the advantages of MIMs over non-interlocked analogues for applications such as molecular recognition, sensing and catalysis.

1.4.1 MIM Synthesis

Initial attempts to exploit the potential unique properties of MIMs were impeded by the difficulty of synthesising MIMs in appreciable yields, due to the challenge of forming mechanically interlocked products. The first reported MIM synthesis, in the 1960s by Wasserman and co-workers, afforded a 0.0001% yield of a [2]catenane by an acyloin condensation (Scheme 1.1).[122, 123] The exceptionally low yield and lack of direct experimental observation of the [2]catenane, relying instead on the detection of deuterium in the product by IR spectroscopy, led to debate as to the veracity of the report,[124] with direct experimental evidence for Wasserman's catenane only being reported in 2023 by Leigh and co-workers.[125]

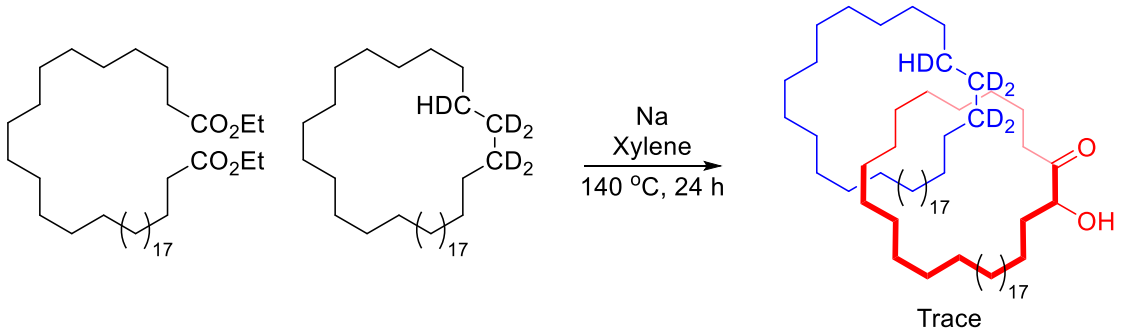

Scheme 1.1. Wasserman's statistical [2]catenane synthesis.

A transformative step-change development in MIM synthesis came in 1983 with the Nobel Prize-winning work of Sauvage and co-workers who reported a seminal Cu(I)-templated synthesis of metallo[2]catenanes,[126] wherein the catenane precursors are orthogonally arranged in a homoleptic bis-phenanthroline complex around a Cu(I)-templating cation. Subsequent double ring closure by a Williamson ether synthesis afforded the target [2]catenane in 27% yield (Scheme 1.2), significantly higher than Wasserman's statistical synthesis. A second route, in which the Cu(I) template was used to form a pseudorotaxane (a non-mechanically bonded interpenetrated assembly) between a phenanthroline-containing macrocycle and a phenanthroline ligand with subsequent ring closing by the same Williamson ether synthesis, produced the [2]catenane in improved 42% yield (Scheme 1.2). Transition metal templation has since proved an efficient MIM synthetic method, using square planar, octahedral and linear metal templation stereochemical preferences.[127-131]

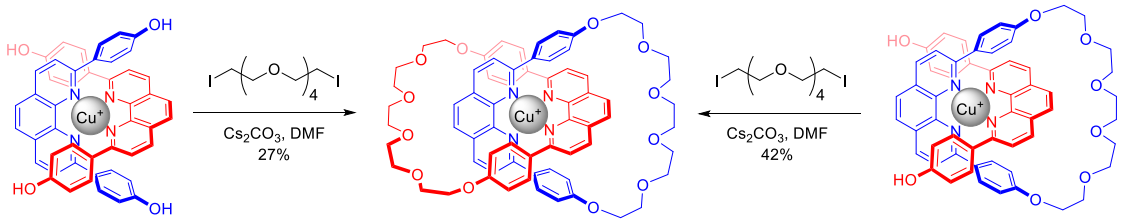

Scheme 1.2. Routes to Cu(I)-templated [2]catenanes with passive metal templation reported by Sauvage and co-workers.

Alkali metal and lanthanide cations have also proved to be powerful templates for MIM construction.[132-135] Over the past decade, Chiu and co-workers have utilised the strong binding of alkali metal cations by oligo-polyether chains to template the formation of pseudorotaxanes which can be stoppered to form [2]rotaxanes or ring-closed to form [2]catenanes (Scheme 1.3).[136-139]

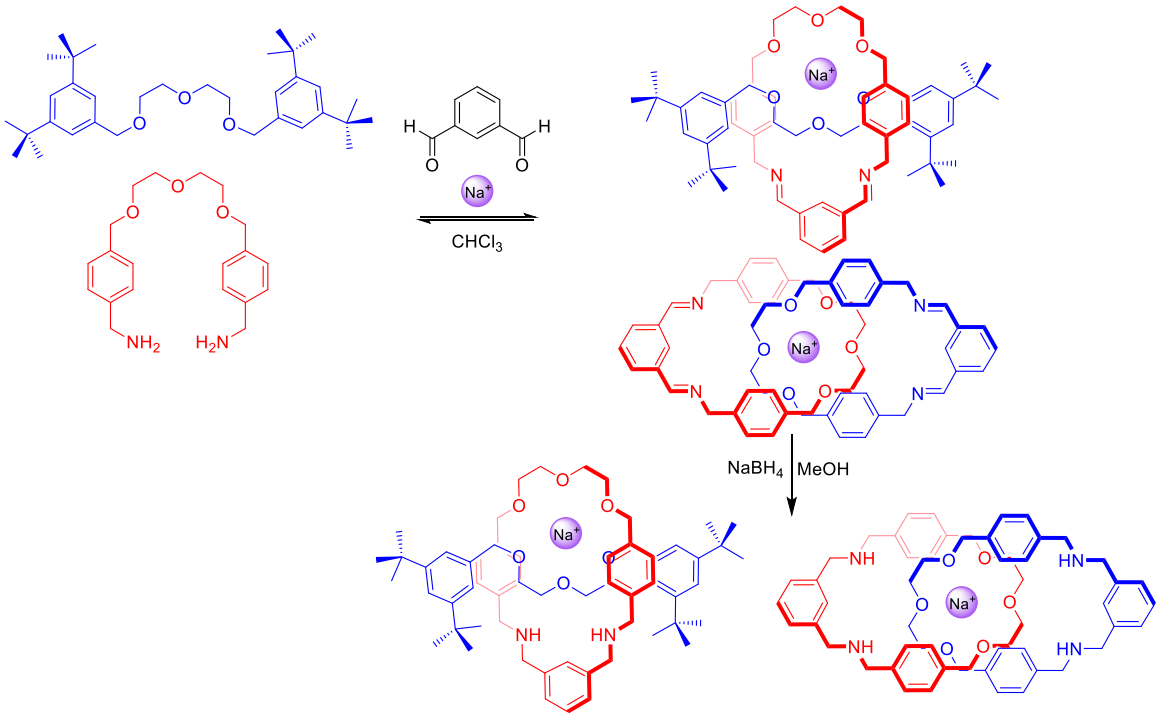

Scheme 1.3. Chiu's alkali metal MIM synthesis methodology.

In 2002 Beer and co-workers demonstrated discrete anion-templated MIM synthesis through a chloride anion templated orthogonal assembly between a 3,5-bis-amido-*N*-methylpyridinium axle and an isophthalamide containing macrocycle precursor,[140] which upon a Grubbs' catalysed ring-closing metathesis (RCM) reaction gave the desired [2]rotaxane in 47% yield (Scheme 1.4). Such an approach has since been demonstrated for a range of discrete inorganic anion templates, including bromide, sulfate, nitrate and nitrite, for a range of MIM architectures.[141-143]

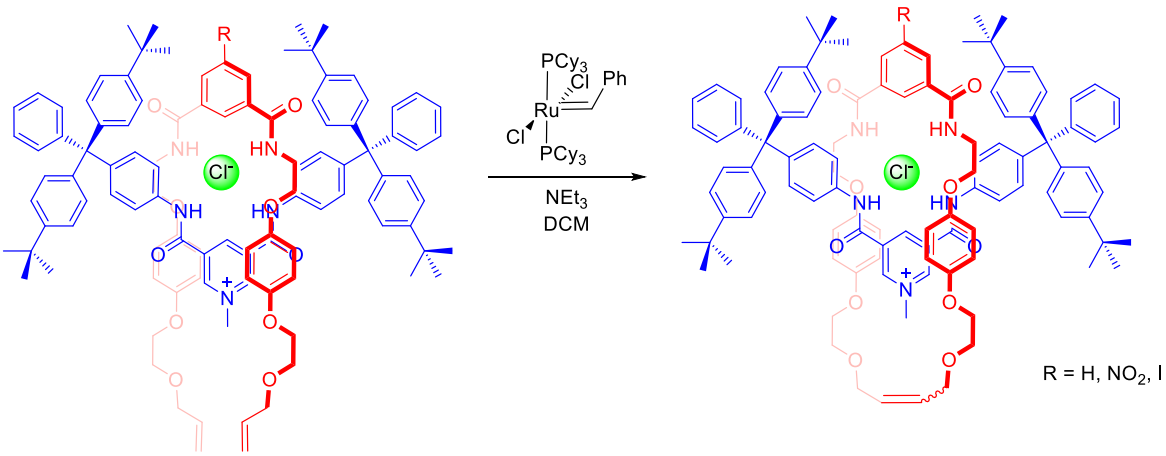

Scheme 1.4. Beer and co-workers' chloride anion-templated [2]rotaxane synthesis.

In all the above templation strategies, the cation or anion acts as a 'passive' template, facilitating the stereochemically preorganised arrangement of the non-interlocked components for subsequent MIM-forming reactions in which the template plays no further role. In 2006, Leigh and co-workers reported a seminal active metal templated (AMT) MIM synthesis methodology, wherein endotopic coordination of a Cu(I) catalyst within a macrocycle cavity affords a tetrahedral Cu(I) complex which not only preorganises the components for MIM formation, but also catalyses the subsequent mechanical bond forming CuAAC 'click' reaction, to obtain [2]rotaxane products in good yields (Figure 1.28). [144-147] The scope of AMT methodology has since been expanded to include a range of metal-catalysed reactions including copper(II)-catalysed homo- and hetero-couplings and palladium catalysed Heck reactions and Michael additions.[148-151]

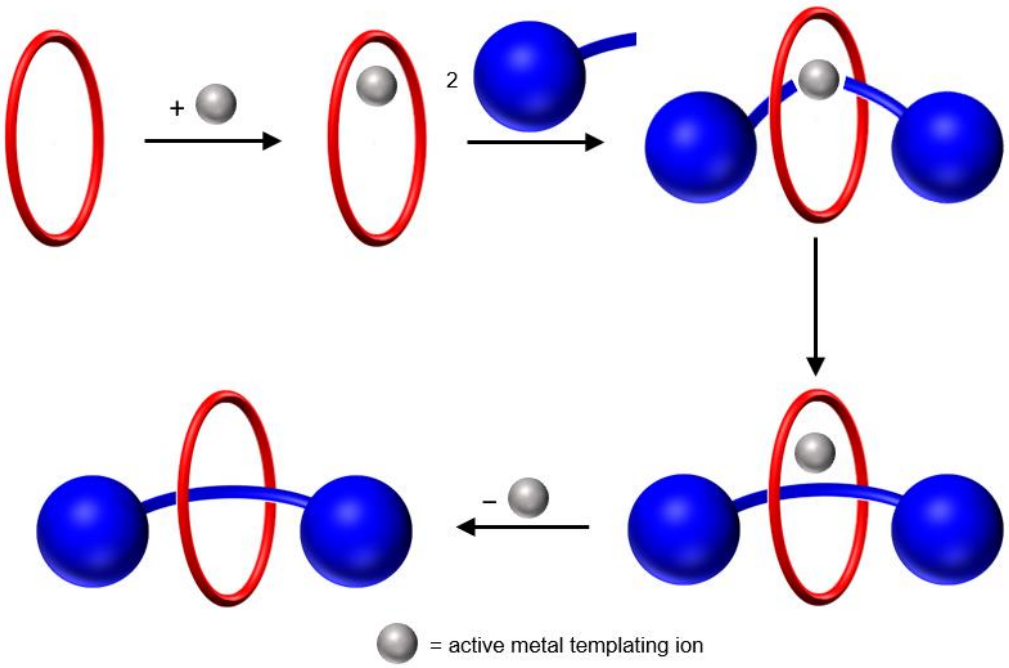

Figure 1.28. Schematic depiction of AMT [2]rotaxane synthesis.

The topological solvent-excluding, highly preorganised three-dimensional cavities of MIMs can be decorated with complementary non-covalent binding sites for recognition and sensing applications which makes them ideal candidates for supramolecular hosts, displaying superior binding selectivities and affinities compared with non-interlocked analogues. Furthermore, the inter-component interactions, and controllable inter-component co-conformational dynamism has enabled MIM use in sensing and stimuli-responsive on/off switchable catalysis applications.

1.4.2 MIMs for Charged Guest Recognition and Sensing

The mechanical bond spatially constrains MIM components, enforcing their proximity, and so non-covalent interactions between the components are substantially enhanced over their non-interlocked analogues. Thus, MIM architectures commonly display enhanced binding over the previously discussed non-interlocked supramolecular receptors, demonstrating a further 'mechanical bond effect' enhancement in both binding selectivity and affinities by MIM hosts (Figure 1.29).[152]

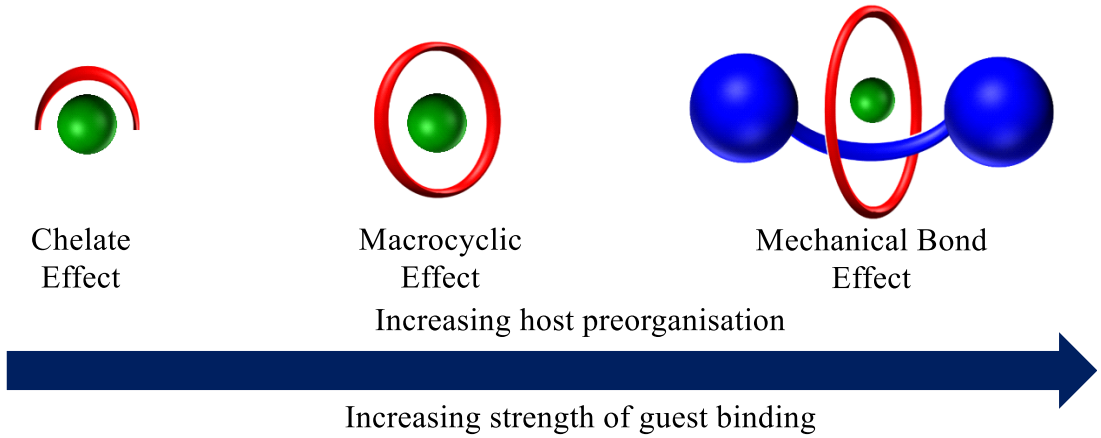

Figure 1.29. Schematic depiction of increasing host preorganisation from multidentate ligands to MIM hosts.

1.4.2.1 Cation Recognition MIMs

Following Sauvage's seminal Cu(I)-templated [2]catenane synthesis, an interesting property of MIMs became apparent: removal of the Cu(I) templating cation from the catenane cavity was substantially more challenging than Cu(I) sequestration from the non-interlocked precursor bis-phenanthroline complex. Sauvage termed this stabilisation the 'catenand' effect, with this report offering an initial insight into the unique ion recognition capabilities of MIMs.[126]

The co-conformational dynamism of MIMs, in which the relative position of the two components gives rise to distinct, controllable, inter-component motion, has previously been exploited for the recognition of charged guests. In 2007, Chiu and co-workers demonstrated the ability of a [2]rotaxane system to enable the identification of alkali and alkaline earth metal cations by ^{1}H NMR spectroscopy (Figure 1.30).[153] Subtle differences in metal cation binding kinetics and binding-induced MIM co-conformational changes resulted in guest-dependent perturbations in the rotaxane host's ^{1}H NMR spectrum in CD_3CN, enabling NMR spectroscopic identification of the metal ions present in the rotaxane-analyte solution.

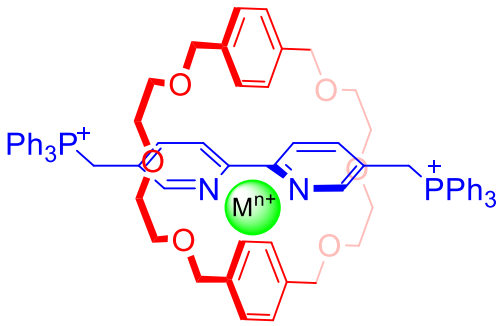

Figure 1.30. Chiu's [2]rotaxane for s-block metal recognition.

The binding of a cationic guest can also induce more marked co-conformational changes in MIM systems. Cheng, Chiu and co-workers reported two [2]rotaxanes with short amide-containing axles and polyether/amine macrocycles (Figure 1.31).[154] In the absence of a bound guest, the dominant co-conformer contained the polyether participating in HB interactions with the amide proton. However, upon addition of Na^+ to a solution of the rotaxane in toluene-d_8, pirouetting of the macrocycle relative to the axle was observed, such that the macrocycle was bound convergently between the carbonyl oxygen and the polyether oxygen atoms. This Na^+-bound co-conformer displayed catalytic activity for the Michael addition of diethyl malonate to *β*-nitrostyrene, arising due to activation of the nitro-olefin by HB donation by a protonated macrocycle amine group, demonstrating the ability of MIM co-conformational changes to give rise to on/off switchable organocatalysis (see Section 1.4.4).

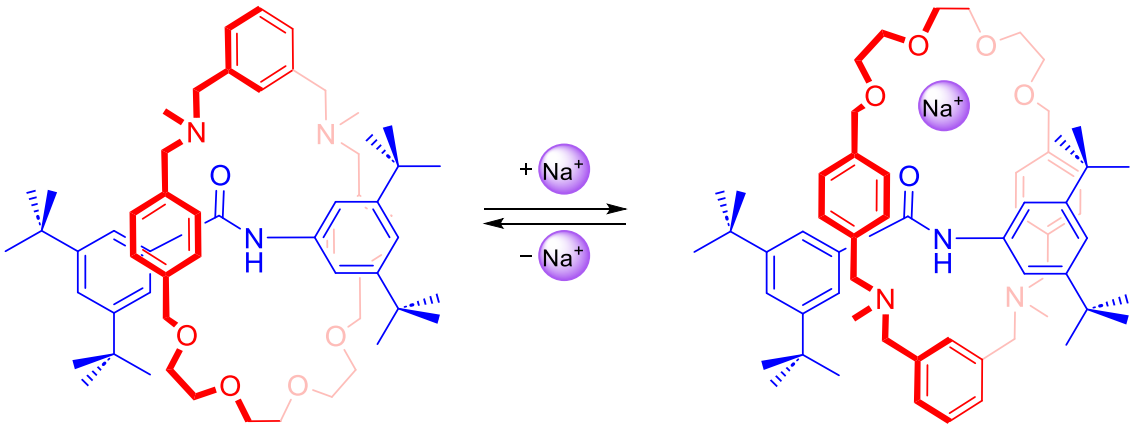

Figure 1.31. Cation binding-induced macrocycle circumrotation in a [2]rotaxane upon Na^+ binding, as reported by Cheng, Chiu and co-workers.

In addition to the initial reports of stimuli-responsive MIM macrocycle component pirouetting between two co-conformers, Baggi and Loeb reported a [2]rotaxane with three co-conformers, with the co-conformational dynamism able to discriminate between the identity of the cationic guest though differences in the preferred host-guest binding mode (Figure 1.32 a).[155] Addition of Li^+ to the free rotaxane induced pirouetting such that the Li^+ was preferentially bound by the macrocycle ethylene glycol (Figure 1.32 b), whereas addition of Cu^+ resulted in further circumrotation to enable participation of the macrocycle alkene bond in coordination of the transition metal cation (Figure 1.32 c). The preferred binding modes of each guest were elucidated by single-crystal XRD studies and observable by 2-D NMR spectroscopy, providing a spectroscopic method for identification of the cationic metal guest.

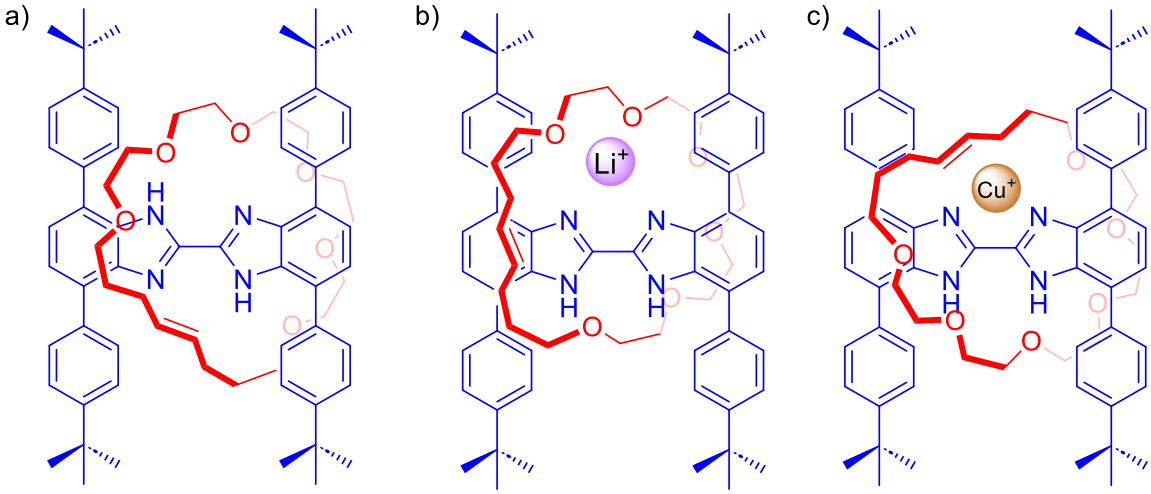

Figure 1.32. Baggi and Loeb's [2]rotaxane with stimuli-responsive dynamism between three co-conformers.

1.4.2.2 Anion Recognition MIMs

Building upon their previously discussed initial report of a discrete anion-templated [2]rotaxane synthesis in 2002 (Scheme 1.4),[140] in 2004 Beer and co-workers reported the first anion templated synthesis of a [2]catenane in high (45%) yield with a chloride-templated catenane synthesis by RCM (Scheme 1.5).[156] While the non-interlocked pyridinium bis-alkene macrocycle precursor was selective for acetate binding over halide

binding in 1:1 *v/v* CD_3OD:$CDCl_3$, after post-synthetic removal of the templating chloride anion, the [2]catenane was selective for chloride over acetate, the mechanical bond serving to reverse the anion selectivity by enabling the formation of a size-complementary binding cavity for the chloride anion, to the exclusion of larger anions, as confirmed by single crystal XRD. Furthermore, the chloride binding constant for the [2]catenane was an order of magnitude higher compared to the non-interlocked axle alone, demonstrating the mechanical bond effect not only increases selectivity, but also affinity, for anion binding. Recent computational studies by Pereira Orenha *et al.* corroborate the experimental conclusions, confirming the preorganised HB donor functionalised MIM cavity as the origin of the marked shift in anion binding selectivity and affinity.[157]

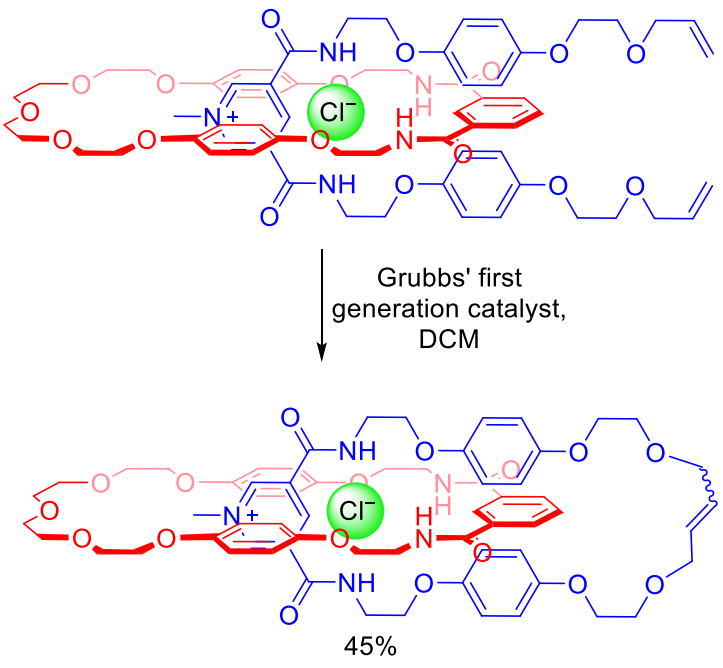

Scheme 1.5. Discrete chloride anion-templated [2]catenane synthesis, reported by Beer and co-workers.

Motivated by the increased directionality and anion recognition potency of XB donor motifs, demonstrated in previous reports of non-interlocked XB host structures,[105, 158-163] recent years have seen efforts to introduce XB anion recognition sites into MIMs to

further enhance their anion binding abilities. The first XB anion templated rotaxane synthesis was reported by Beer and co-workers in 2010,[95] with a report of a [2]rotaxane containing an XB iodo-triazolium donor axle and an isophthalamide macrocycle (Figure 1.33 a). The rotaxane demonstrated impressive halide anion binding performance in the competitive 45:45:10 *v/v* $CDCl_3$:CD_3OD:D_2O organic-aqueous solvent mixture, with binding constants an order of magnitude larger than the HB rotaxane analogue. Interestingly, the rotaxane demonstrated marked selectivity for iodide over the smaller, more charge-dense halides, likely due to the weaker solvation of the larger halide anions. In 2015, Kennepohl, Beer and co-workers described the synthesis of a bis-pyridinium XB [2]catenane (Figure 1.33 b),[164] which showed a similar halide selectivity. Interestingly, K-edge x-ray absorption spectroscopic studies for the chloride and bromide bound species demonstrated intense pre-edge features indicating substantial covalency in the XB-halide interactions, which DFT studies suggest show a similar degree of covalency to transition metal complexes.

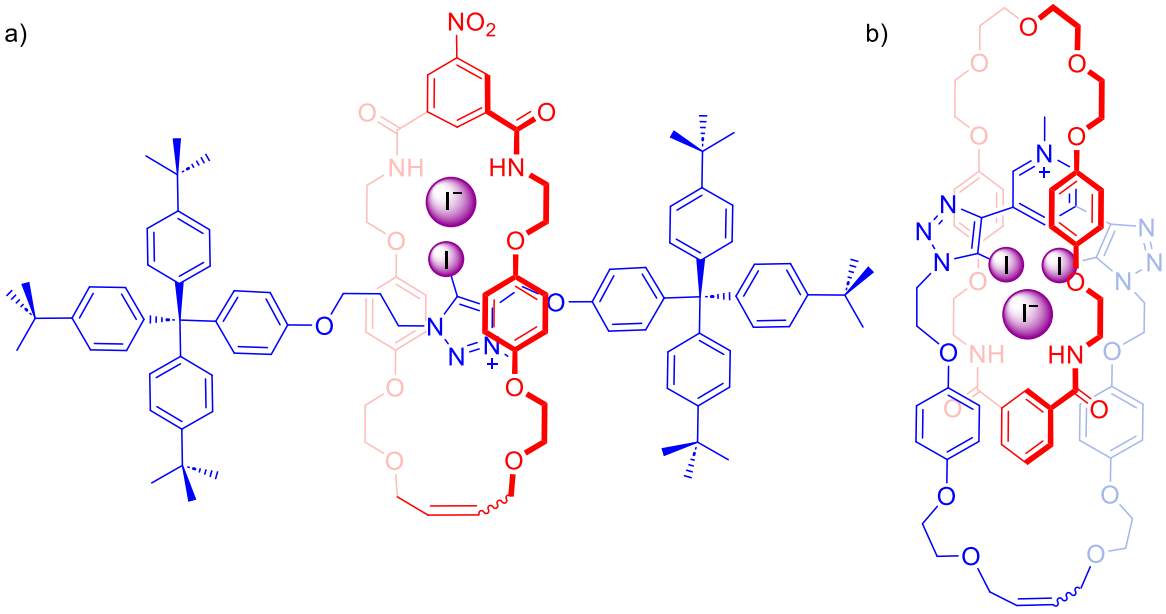

Figure 1.33. Charge-assisted XB/HB mixed a) [2]rotaxane, b) [2]catenane, for anion recognition, reported by Beer and co-workers.

In 2014, Langton *et al*. provided the first report of XB anion recognition in pure water with a [2]rotaxane stoppered with water-solubilising *per*-methylated *β*-cyclodextrin stoppers (Figure 1.34), containing a pyridinium bis-amide macrocycle and pyridinium bis-iodotriazole axle.[45] The XB rotaxane demonstrated significantly enhanced halide binding strengths over the HB analogue, with Hofmeister biased selectivity for iodide. Thermodynamic analysis revealed that the binding of iodide by the XB rotaxane is enthalpically favoured and entropically disfavoured, in contrast to the HB analogue where entropic contributions were the main factor. This is consistent with strong halide binding by XB interactions and the exclusion of water molecules from the binding cavity by the lipophilic iodine XB donor atoms, causing the expulsion of fewer water molecules from the cavity upon guest binding by the XB rotaxane over the HB congener. Here the three-dimensional binding site of the MIM creates a hydrophobic binding pocket, giving rise to a significantly enhanced hydrophobic component to binding, in contrast to the non-interlocked axle, reminiscent of the highly solvent excluding cavities of biological binding proteins.[82]

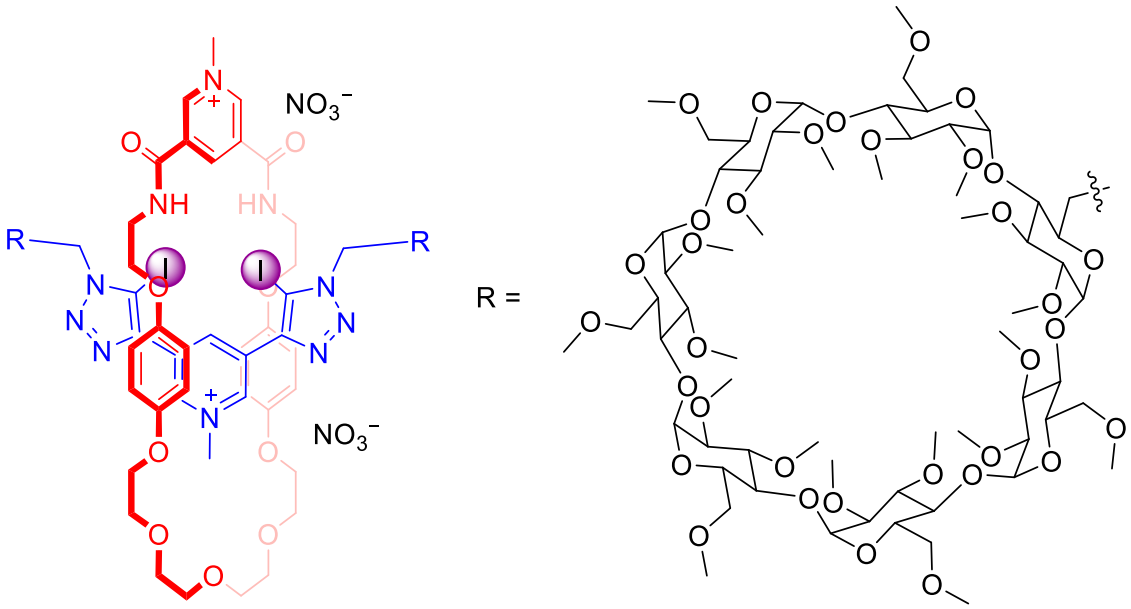

Figure 1.34. The first water-soluble XB anion binding [2]rotaxane, reported by Langton *et al.*

In addition to halide selective MIM systems, judicious interlocked host design enables the synthesis of anion binding systems which exhibit selectivity for other, non-spherical, anions. In 2013, Duckworth, Langton and Beer reported a nitrate-templated [2]rotaxane preparation (Figure 1.35 a),[165] facilitated through strategic exploitation of an axle group with two isophthalamide HB donor moieties and an isophthalamide-containing macrocycle. The resulting rotaxane contained three complementary bidentate HB sites, preorganised for the convergent binding of the trigonal planar nitrate anion (Figure 1.35 c), and demonstrated selectivity for the recognition of nitrate over the more basic acetate and dihydrogen phosphate oxoanions in aqueous-organic 45:45:10 *v/v* $CDCl_3$:CD_3OD:D_2O solvent media. Hence, exemplifying the power of the mechanical bond to engineer selective three-dimensional binding sites which would otherwise prove synthetically challenging to achieve. In 2015, Langton and Beer utilised the strategy further in the synthesis of the first nitrate-templated [2]catenane (Figure 1.35 b),[166] which displayed the same nitrate selectivity trend as the [2]rotaxane under analogous solvent conditions.

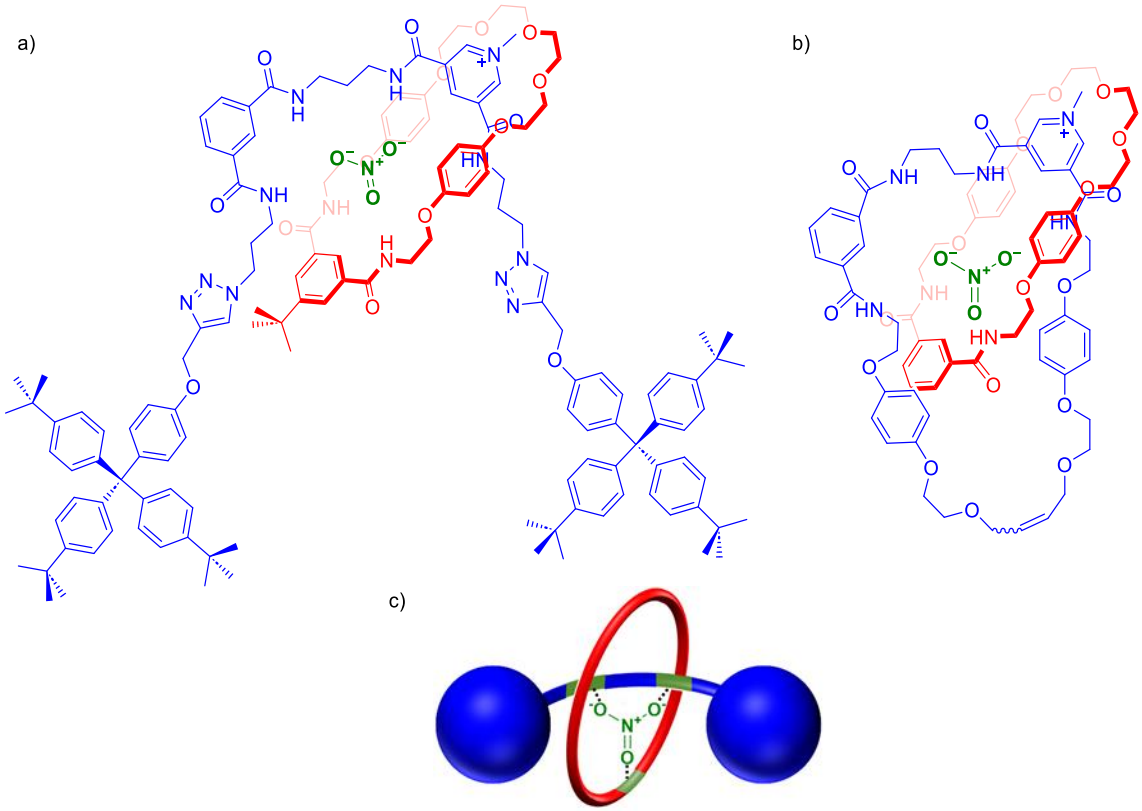

Figure 1.35. Nitrate selective a) [2]rotaxane, b) [2]catenane, reported by Beer and co-workers, c) schematic depiction of [2]rotaxane preorganisation for binding the trigonal planar nitrate anion.

1.4.2.3 Ion-Pair Recognition MIMs

In the field of ion-pair recognition, MIMs present an exciting framework as the introduction of a heteroditopic macrocycle into the MIM architecture enables the exploitation of the enhanced preorganisation afforded by the mechanical bond, coupled with the functionality of a heteroditopic macrocycle, to give rise to superior binding affinities and selectivities in ion-pair recognition.

The foundations for MIM ion-pair recognition were reported by Smith and co-workers in their 2002 report of a [2]rotaxane with a heteroditopic macrocycle containing both an isophthalamide anion binding motif and a dibenzo-18-crown-6 (DB18C6) ring for cation binding (Figure 1.36 a).[167, 168] ^{1}H NMR binding titrations demonstrated ion-pair binding of K^{+} and Cl^{-} in competitive 3:1 *v/v* DMSO-d_6:CD_3CN solvent media, however no

enhancement in chloride binding affinity was observed upon co-binding of K^+ by the [2]rotaxane. Cooperative ion-pair binding was demonstrated by the 2014 report of Beer and co-workers of a [2]rotaxane containing a calix[4]diquinone functionalised macrocycle (Figure 1.36 b).[169] In this system, the pirouetting motion of the macrocycle is arrested upon Na^+ binding, preorganising a convergent tetradentate HB anion binding cavity for chloride binding, resulting in a 15-fold enhancement of chloride binding upon co-complexation of sodium in 4:1 *v/v* $CDCl_3$:CD_3OD.

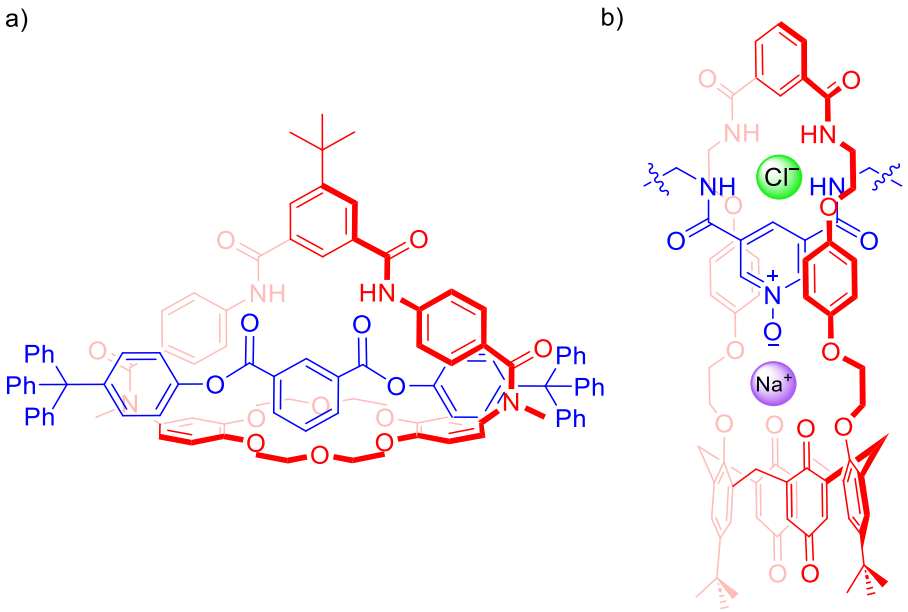

Figure 1.36. Initially reported ion-pair recognition [2]rotaxanes by a) Smith and co-workers, b) Beer and co-workers.

Stabilisation of lithium halide ion-pairs poses a particular challenge due to the high lattice enthalpies of lithium halide salts.[109] Nevertheless, LiX ion-pair binding is of considerable industrial interest due to potential applications in the extraction of lithium salts in the development of battery technologies.[110, 111] Recently, Beer and co-workers reported the incorporation of a heteroditopic XB macrocycle, containing a bis-iodotriazole XB donor group and a pyridyl macrocycle, into a [2]rotaxane with an iodotriazole-containing axle (Figure 1.37 a).[170] In CD_3CN:$CDCl_3$ solvent mixtures, the sequential addition of $LiClO_4$ and TBAX (X = Br^- and I^-) to the macrocycle alone resulted in LiX salt recombination

as the macrocycle ion-pair binding affinity is insufficient to overcome the high LiX lattice enthalpy. In contrast, addition of the TBAX salt to an equivalent solution of the [2]rotaxane pre-complexed with one equivalent of Li^+ led to the observation of strong binding of Br^- and I^- (K_a > 10^4 and 10^3 M^{-1}) respectively. The ion-pair binding enhancement was attributed to a positive allosteric effect, in which addition of Li^+ induces a co-conformational shift to facilitate cooperative cation binding between the pyridyl macrocycle and the axle triazole N donor atom, resulting in preorganisation of a convergent tridentate XB anion binding site. Computational DFT studies confirmed Li^+ binding leads to polarisation of the axle iodotriazole motif, leading to enhanced axle XB donor potency.

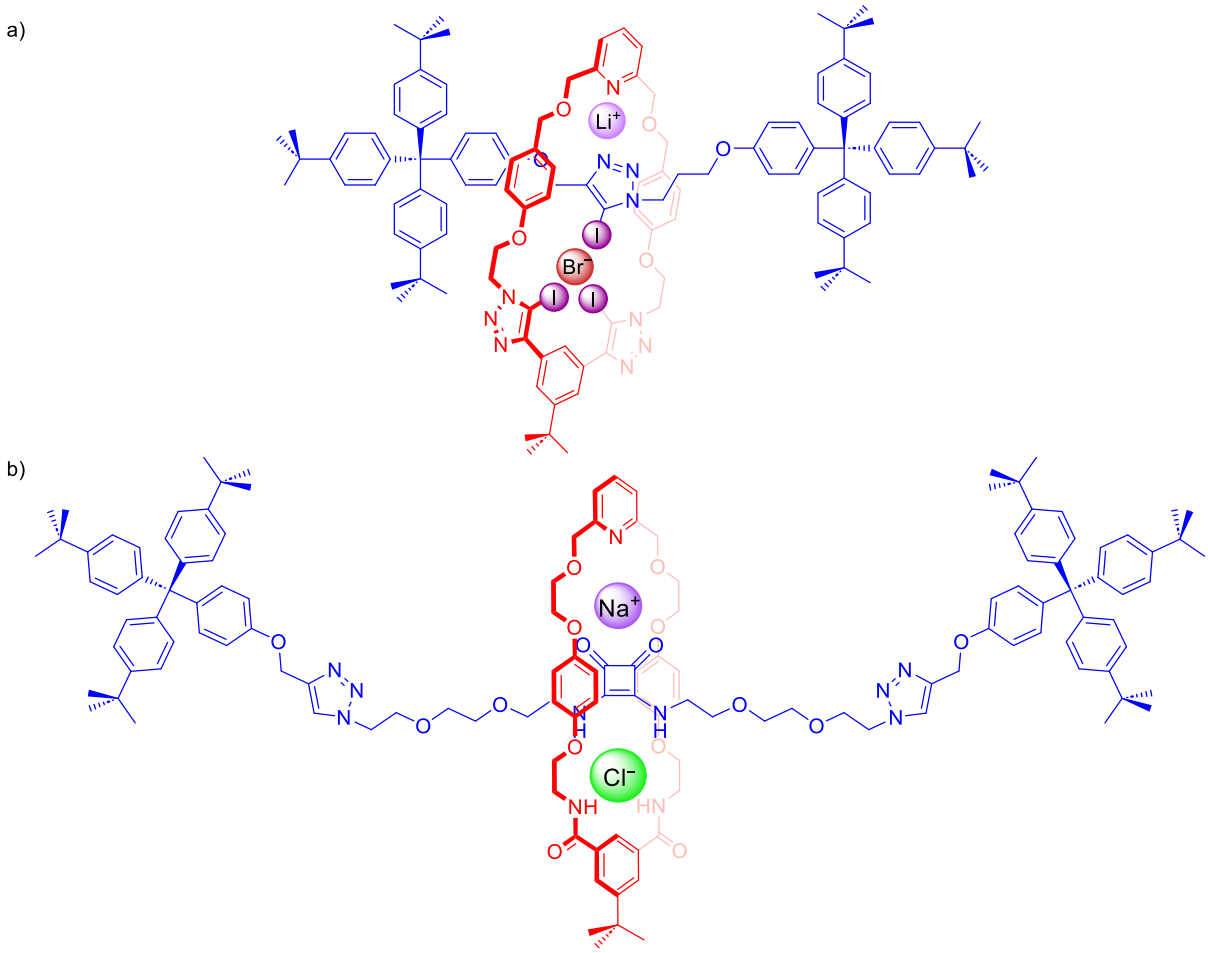

Figure 1.37. a) XB heteroditopic [2]rotaxane for lithium halide ion-pair recognition. b) Squaramide-containing [2]rotaxane for NaCl recognition and extraction.

In 2023, Arun *et al*. reported the exploitation of mechanical bonding to facilitate solid-liquid extraction of sodium halide salts, NaX (X = Br, I), into $CDCl_3$ with a heteroditopic pyridyl cation binding and isopthalamide anion binding macrocycle and squaramide axle-containing [2]rotaxane (Figure 1.37 b).[171] Na^+ binding afforded a positive allosteric affect for halide anion binding, as cooperative binding of the cation between the axle squaramide carbonyl oxygens and the macrocycle pyridyl preorganised a tetradentate convergent binding site between the isopthalamide and squaramide NH HB donor moiteties.

Exploiting Chiu's alkali metal cation-templated MIM synthesis methodology,[136] in 2023, Tay, Beer and co-workers reported a series of NaX/KX ion-pair binding [2]catenanes (Figure 1.38 a).[172] Alkali metal cation binding induced a marked enhancement in halide affinity in 1:1 *v/v* CD_3CN:$CDCl_3$, attributed to favourable proximal electrostatic interactions between the bound ions, with the catenane host ion-pair binding mode confirmed by single crystal XRD studies (Figure 1.38 b). Stoppering the pseudorotaxane intermediate of the [2]catenane synthesis enabled the isolation of the 'mechanical bond isomeric' [2]rotaxanes (Figure 1.38 c).[173] The [2]rotaxanes displayed dramatically enhanced halide binding affinitites in the presence of either pre-complexed Na^+ or K^+, attributed to binding of the alkali metal cation between the ethylene glycol chains of each component, preorganising a tetradentate all-XB donor anion binding site. While quantitative binding constant data could not be determined due to the complex equilbria present in ion pair binding, it was apparent that the rotaxanes demonstrated greater cooperativity than their 'mechanical bond isomeric' catenane analogues, demonstrating the importance of MIM topology in achieving mechanical bond enhancments in binding affinity and selectivity in ion-pair receptors.

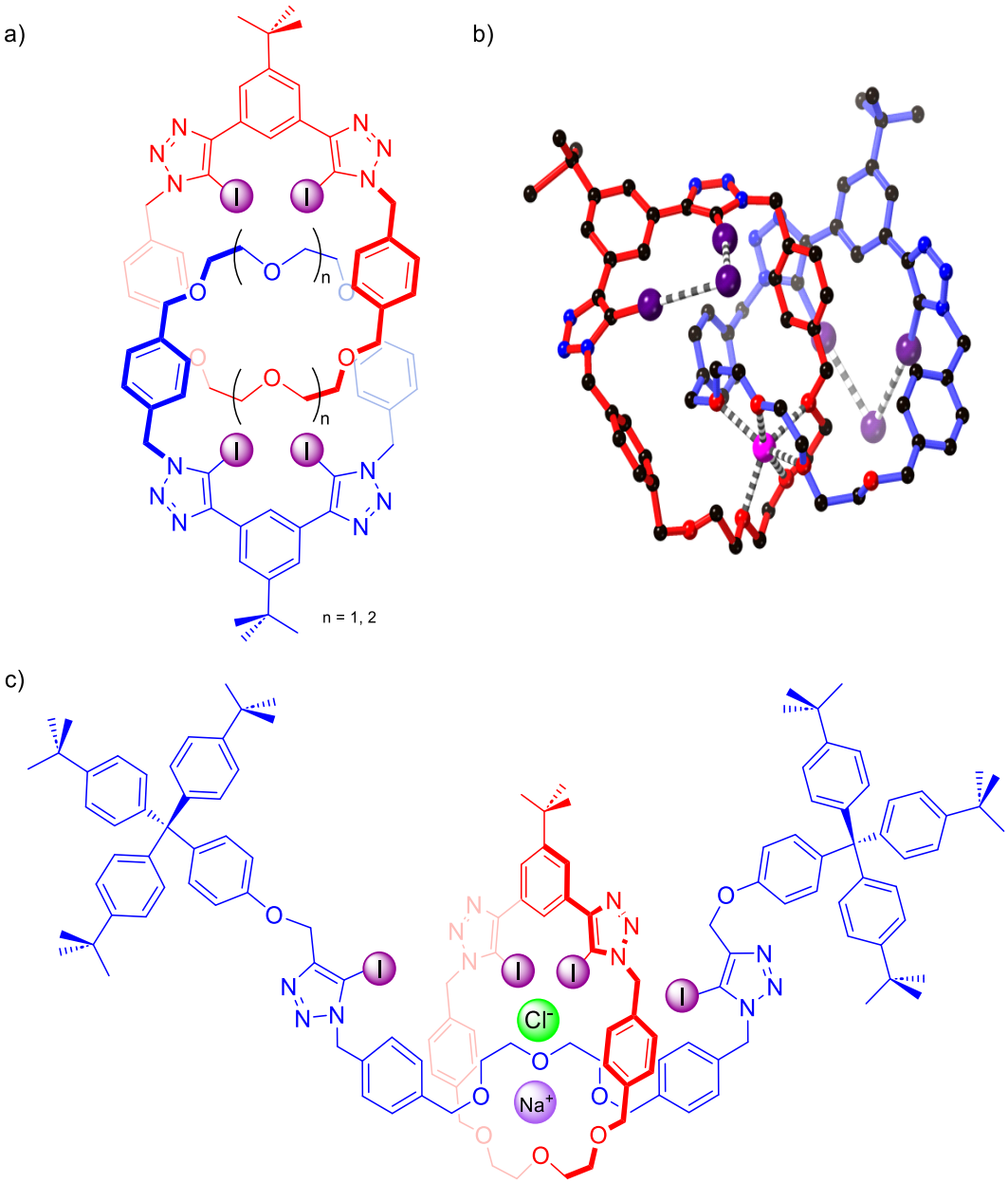

Figure 1.38. Ion-pair binding MIMs reported by Tay *et al*. a) [2]catenane prepared by alkali metal templation for ion-pair binding. b) XRD structure of catenane depicted in (a) with bound Na^+ / I^- ion-pair. c) 'Mechanical bond isomeric' [2]rotaxane.

1.4.3 MIMs for Guest Sensing

1.4.3.1 MIM Sensors for Charged Guests

Given the powerful charged guest recognition properties of MIM host systems, it is perhaps unsurprising that there has been considerable research interest in the incorporation of photo- or redox-active reporter groups into MIM architectures to provide

optical and electrochemical signal transduction mechanisms for MIM host-guest recognition events.

The first report of an interlocked ion sensor was made by Swager and co-workers in 1996, with their electrically conducting thiophene-containing polyrotaxane (Figure 1.39).[174] The binding of Cu^{+} or Zn^{2+} cations within the poly(MIM) cavities afforded marked increases in polymer conductivity, coupled with a bathochromically red-shifted UV-visible metal-to-ligand charge transfer (MLCT) absorption in MeCN solution. Washing of the bound polyrotaxane solution with ethylenediamine solution sequestered the metal ion, leading to observation of the metal-free absorption spectrum, affording a reversible sensing capability. Importantly, the non-interlocked polymer did not demonstrate any sensing ability, demonstrating the mechanical bond enables the sensing capability.

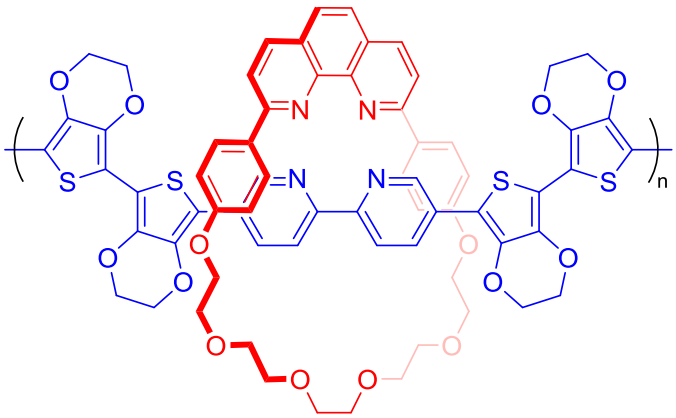

Figure 1.39. Transition metal sensing polyrotaxane, reported by Swager and co-workers.

A range of optical reporting groups have since been incorporated into cation recognition MIMs. In 2016, Lin and co-workers described a tetraphenylethylene- and phenanthroimidazole-containing rotaxane (Figure 1.40 a).[175] Addition of Fe^{3+} in aqueous-DMSO solvent mixtures resulted in quenching of fluorescence from both groups. Such dual quenching behaviour was observed only for Fe^{3+} and was not observed with other transition metal ions tested, including Fe^{2+}, demonstrating a sensor capable of the

impressive discrimination between biotoxic haemin (containing Fe(III)) and non-toxic haem (containing Fe(II)).

In 2019, Leung and co-workers reported anthracene- and BODIPY-stoppered [2]rotaxanes which demonstrated strong and selective optical responses to Au^{3+} ($K_a > 10^4$ M^{-1} in 50:50 *v/v* MeCN:H_2O solvent media) (Figure 1.40 b), with the observed fluorescence intensity being proportional to the concentration of Au^{3+}.[176] The BODIPY stoppered rotaxane proved capable of sensing Au^{3+} in HeLa cells at 2.0 μM without a significant effect on cell viability, indicating potential future applications of MIM sensing for *in vivo* applications.

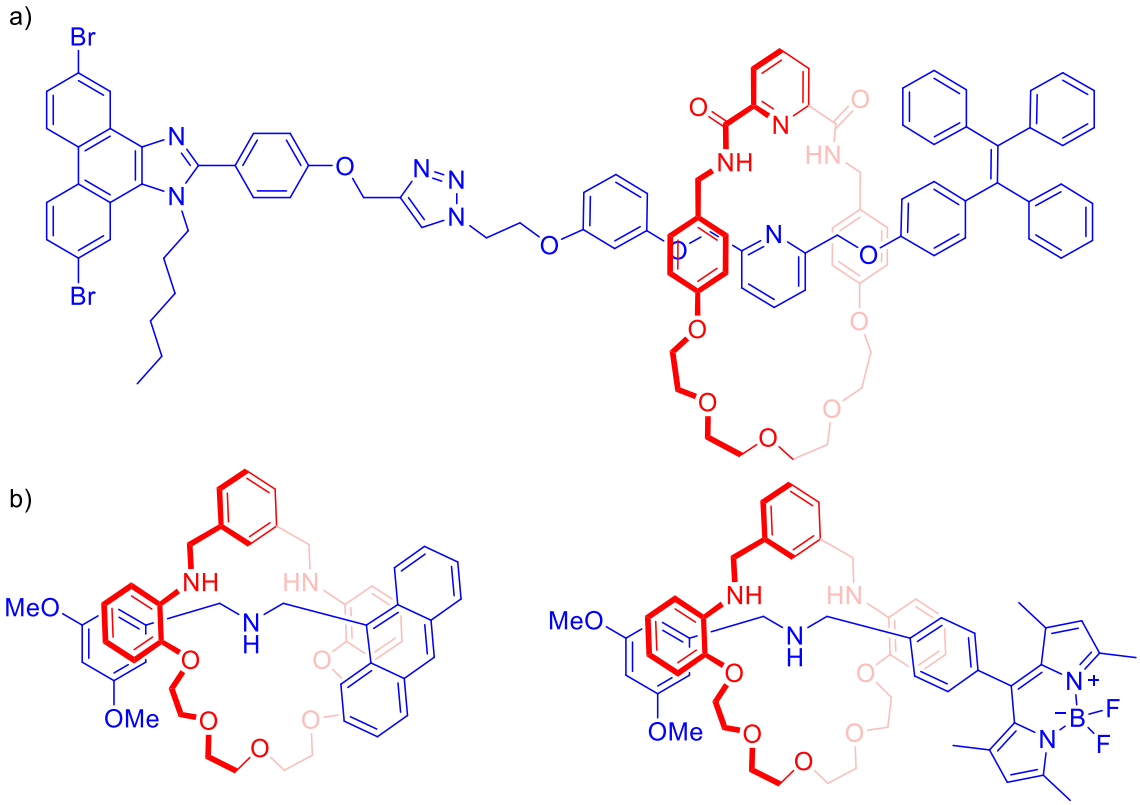

Figure 1.40. a) Transition metal sensing polyrotaxane, reported by Swager and co-workers. b) Au^{3+} sensing [2]rotaxanes reported by Leung and co-workers.

In 2012, Beer and co-workers incorporated Re(I) and Ru(II) bipyridyl complex-functionalised macrocycles into pyridinium [2]rotaxanes (Figure 1.41 a).[177] Both rotaxanes displayed marked selectivity for chloride over larger oxoanions in up to 30%

aqueous media. Significant perturbations in the respective rotaxane's transition metal MLCT luminescence facilitated optical sensing of the halide anion. Subsequent work enabled the selective optical sensing of iodide in water exploiting *β*-cyclodextrin stoppers to afford water solubility on a related [2]rotaxane which incorporated a pyridinium bis-XB axle for anion binding and a Ru^{2+} chromophore for MLCT signal transduction of the binding event (Figure 1.41 b).[178]

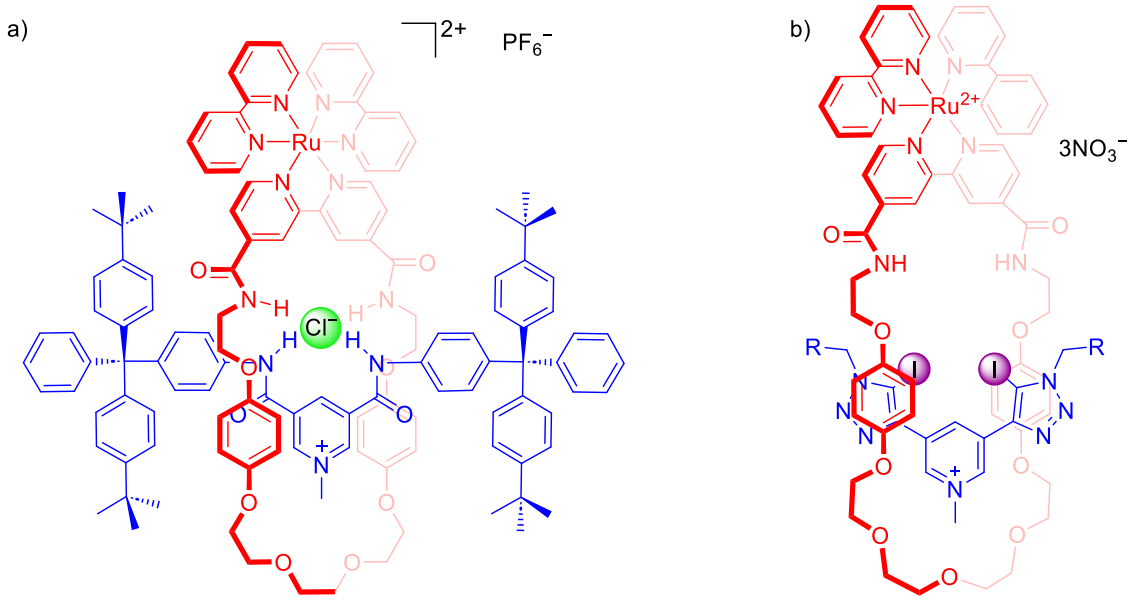

Figure 1.41. Ru(II) luminophore-containing [2]rotaxanes for optical sensing of anions, reported by Beer and co-workers.

The integration of redox reporter groups such as ferrocene (Fc) into the rotaxane host scaffold can afford an electrochemical sensing response to guest binding events. In 2010, Evans and Beer demonstrated an anion binding-induced significant cathodic shift for the (Fc/Fc^+) redox couple upon chloride binding by a [2]rotaxane containing a Fc-tethered isophthalamide macrocycle (Figure 1.42 a).[179] In 0.1 M $TBAPF_6$/MeCN electrolyte, the rotaxane demonstrated a ten-fold increase in halide binding constant over the non-interlocked axle alone, and demonstrated the maximum cathodic shift (−0.20 mV) after addition of only one equivalent of chloride. Subsequent studies demonstrated

incorporation of Fc into the stopper group of [2]rotaxanes (Figure 1.42 b),[180] or into a [2]catenane (Figure 1.42 c),[181] affords similarly significant chloride-binding induced Fc/Fc^+ redox potential cathodic shifts.

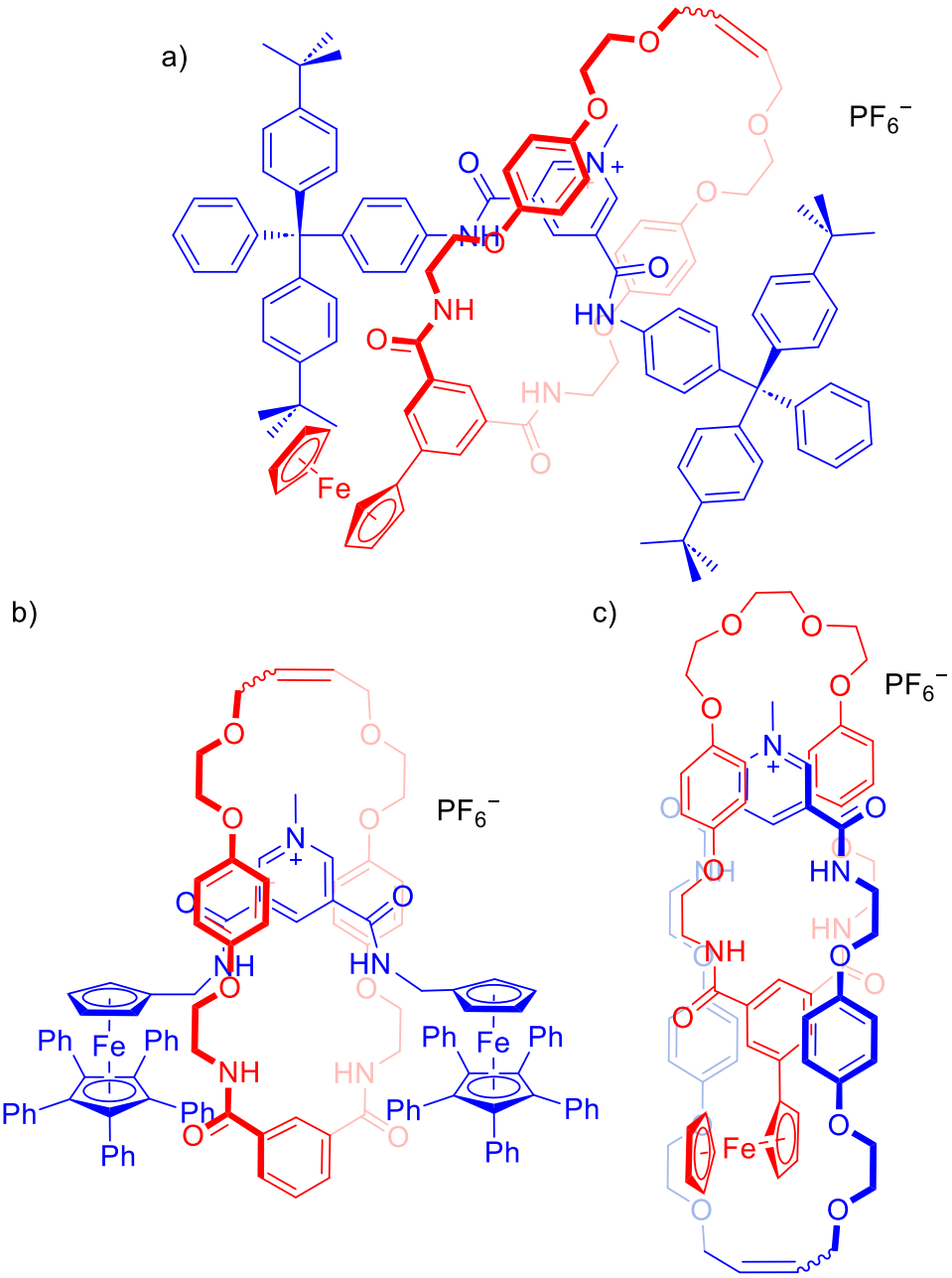

Figure 1.42. HB anion binding MIMs with appended ferrocene reporter groups for anion sensing.

1.4.3.2 Dynamic MIM Sensors

The co-conformational dynamism of MIM systems can also be exploited to give rise to marked sensing responses. In the case of a [2]rotaxane with marked host-guest co-conformational changes, the macrocycle may translocate along the axle randomly, by Brownian motion (Figure 1.43 a). In this case, binding of an exogeneous guest may serve to bias the macrocycle in one co-conformation to enable convergent binding of the guest by the macrocycle and axle, eliciting a sensing response. In a second case (Figure 1.43 b), the macrocycle is already bound at one axle station, which may be a photoactive station, and subsequent guest binding results in macrocycle translocation to the binding site, affording an optical response.[182, 183]

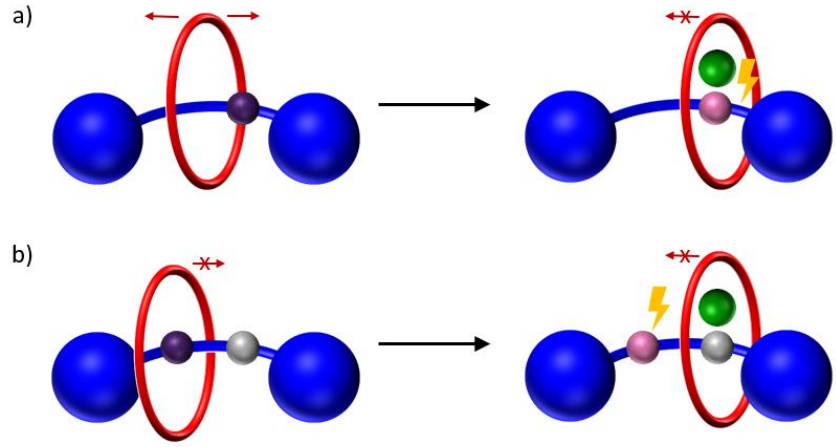

Figure 1.43. Schematic depiction of host-guest binding-induced co-conformational changes in a [2]rotaxane.

In 2010, Smith and co-workers reported a squaraine axle [2]rotaxane wherein, in the absence of a bound guest, the macrocycle preferentially resides over the squaraine station, quenching the squaraine fluorescence (Figure 1.44 a).[184] Binding of a chloride guest in $CHCl_3$ induced macrocycle translocation to the axle triazole moiety, removing the quenching interaction with the squaraine and resulting in a naked eye visible colour change.

In 2016, Beer and co-workers reported a nitrate sensing [3]rotaxane (Figure 1.44 b),[185] forming a 1:1 stoichiometric host-guest complex in which nitrate binding induces dynamic shuttling motion from the macrocycle NDI stations, such that the macrocycles reside over the axle triazolium moieties and bind nitrate in a pincer-like sandwich complex between the two macrocycles. The binding-induced shuttling induces similar optical changes to Smith's chloride sensing [2]rotaxane, enabling colourimetric nitrate sensing in chloroform with selectivity over other more basic anions such as acetate.

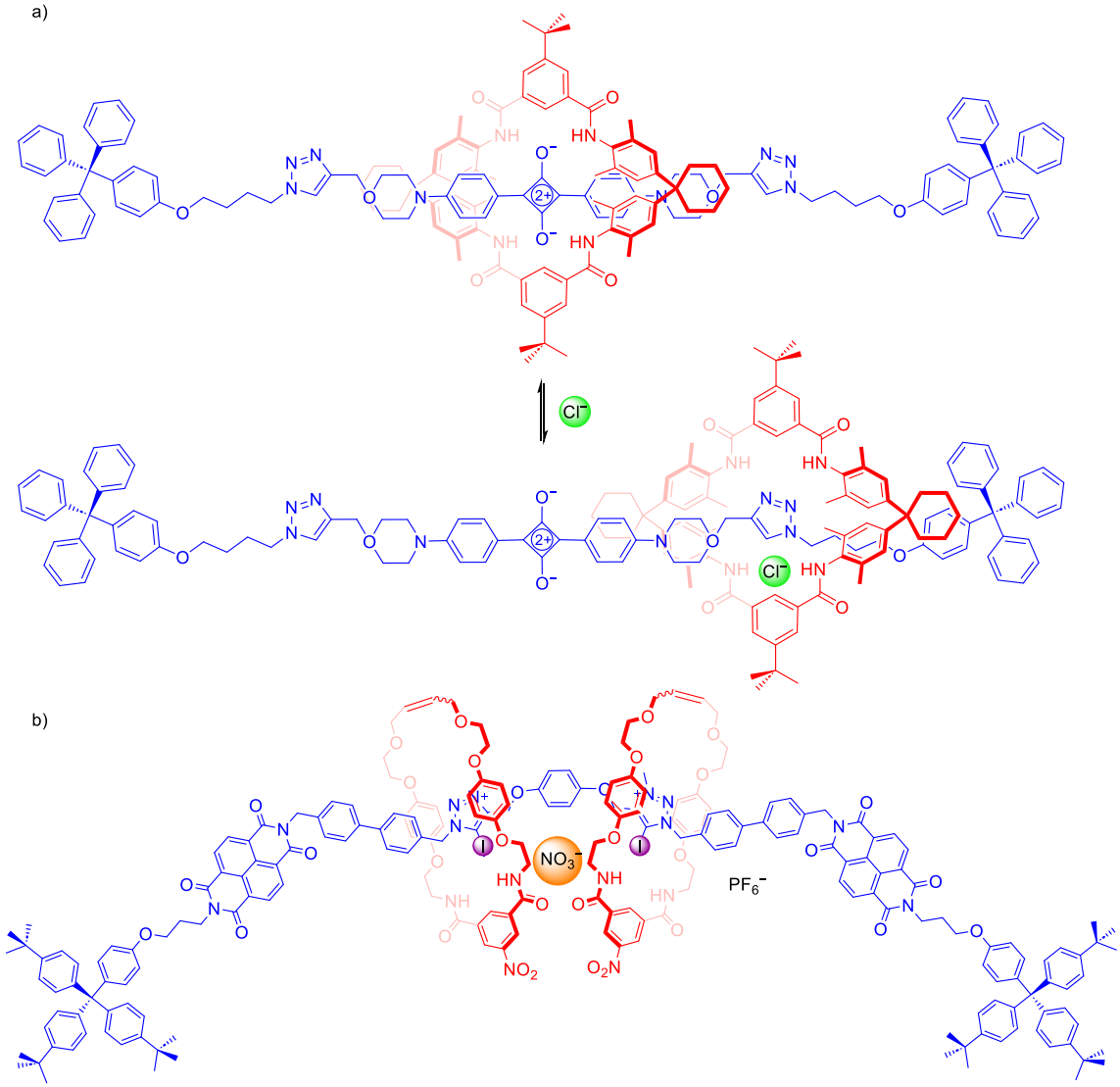

Figure 1.44. a) Initially reported colourimetric chloride sensing [2]rotaxanes, b) [3]rotaxane for colourimetric sensing of nitrate.

1.4.4 MIMs for Catalysis

In addition to affording high degrees of host preorganisation, the spatial constraints of the mechanical bond, and the unquenched reactivity of reactive groups integrated into MIM architectures, can provide routes to unusual reactivity. A profound example of the ability of mechanical bonding to enable activation of substrates is the activation of H_2 by a [2]rotaxane and a Lewis acid as reported in 2013 by Loeb, Stephan and co-workers (Scheme 1.6).[186] The formation of a rotaxane with a secondary ammonium axle and a 22-crown-6 macrocycle restricted exposure of the axle basic nitrogen atom, preventing Lewis adduct formation upon addition of a borane with bulky aryl substituents, $B(C_6F_5)_3$, resulting in the formation of a frustrated Lewis pair (FLP). The formation of an active FLP was demonstrated by utilising its unquenched reactivity in the heterolytic cleavage of H_2 to form the protonated rotaxane and $[B(C_6F_5)_3H]^-$, consistent with the reactivity of conventional FLPs.[187] The conventional route to FLP production is the direct covalent attachment of sterically bulky substituents to the Lewis acidic and basic atoms which can adversely affect the Lewis potency of the centre, restricting their end use.[188] Here, mechanical bonding allowed the use of a sterically unencumbered Lewis base for FLP behaviour, without covalent modification. Subsequent work has demonstrated the exploitation of the mechanical bond to dramatically stabilise ammonium species such that their deprotonation affords neutral rotaxanes with remarkably high proton affinities, demonstrating ‘super base’ behaviours.[189] Thus, the mechanical bond demonstrates great potential in the generation of highly reactive systems from relatively synthetically accessible MIM-precursors.

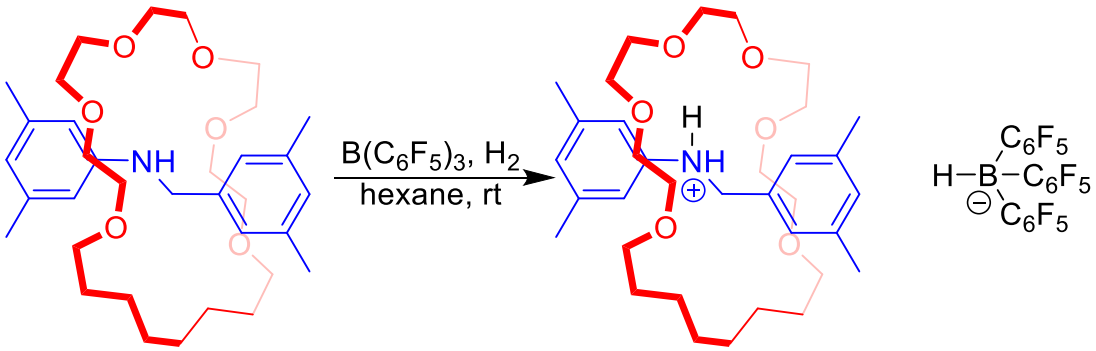

Scheme 1.6. Reaction of a MIM FLP with H_2, as reported by Loeb, Stephan and co-workers.

The use of rotaxanes to preorganise multifunctional catalysts and enable control of the relative position of active sites was demonstrated in 2011 by Osakada and co-workers who used a [3]rotaxane as a dinuclear Pd(II) catalyst to effect ring-closures through a Mizoroki–Heck reaction.[190] By utilising a rotaxane with a rigid, unsaturated axle containing two secondary ammonium stations where each acts as a binding station for a [$PdCl_2$] 1,2-bis(pyridylethynyl)benzene-containing crown either macrocycle (Figure 1.45), the relative position of the Pd(II) active sites could be fixed. This was subsequently exploited in the catalysis of ring-closing Mizoroki–Heck reactions using bifunctional alkenes and aryl halides. Such a reaction has competing macrocycle-forming ring closure and oligomerisation pathways. The reaction rate and yield of macrocyclic product were improved with the bifunctional rotaxane catalyst when compared with the conventional catalyst $Pd(OAc)_2$ as the rigid rotaxane structure could act as a template for macrocycle formation.[191]

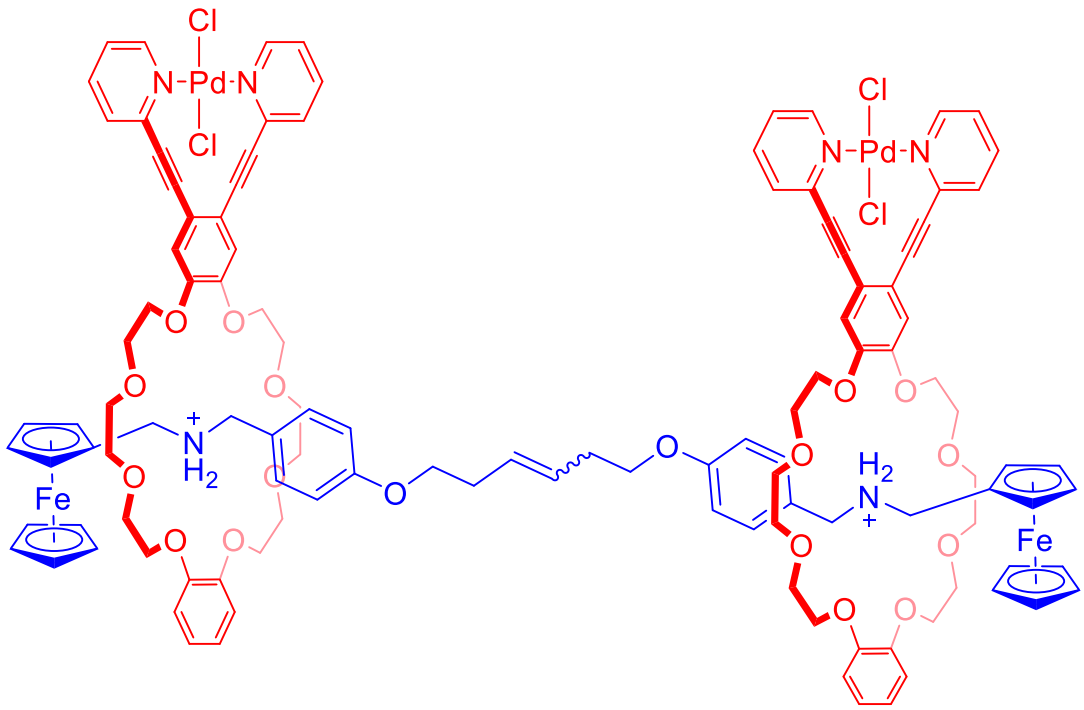

Figure 1.45. Osakada's [3]rotaxane with Pd-containing macrocycles, which acts as a binuclear catalyst for the Mizoroki–Heck reaction.

Stimuli-driven responses of MIMs have also been exploited in switchable catalysis – catalysis in which the system changes its reactivity upon the application of an external stimulus. Such systems are ubiquitous in nature, where enzymes catalysing metabolic processes are stimulated according to physiological need.[192] The simplest form of switchable catalysis uses an 'on/off' switch in which catalysis can be selectively activated and deactivated. In 2012, Leigh and co-workers reported a switchable [2]rotaxane catalyst which could be stimulated for a range of Michael addition reactions (Figure 1.46 a).[193] Switchable behaviour was achieved with a bifunctional axle containing ammonium/secondary amine and triazolium macrocycle binding stations with a dibenzo-24-crown-8 macrocycle (DB24C8), exploiting the relative hydrogen-bonding affinities of the macrocycle for the stations: 2˚ ammonium > triazolium > 2˚ amine. The catalyst was demonstrated to be active for the addition of an aliphatic thiol to *trans*-cinnamaldehyde. Under acidic conditions, the axle amine was protonated and the macrocycle preferentially located above the ammonium cation, sterically inhibiting the

approach of cinnamaldehyde to the cation, switching off catalysis. Upon deprotonation of the ammonium cation, the dominant co-conformer is the macrocycle bound at the triazolium site, enabling catalysis (Figure 1.46 b).

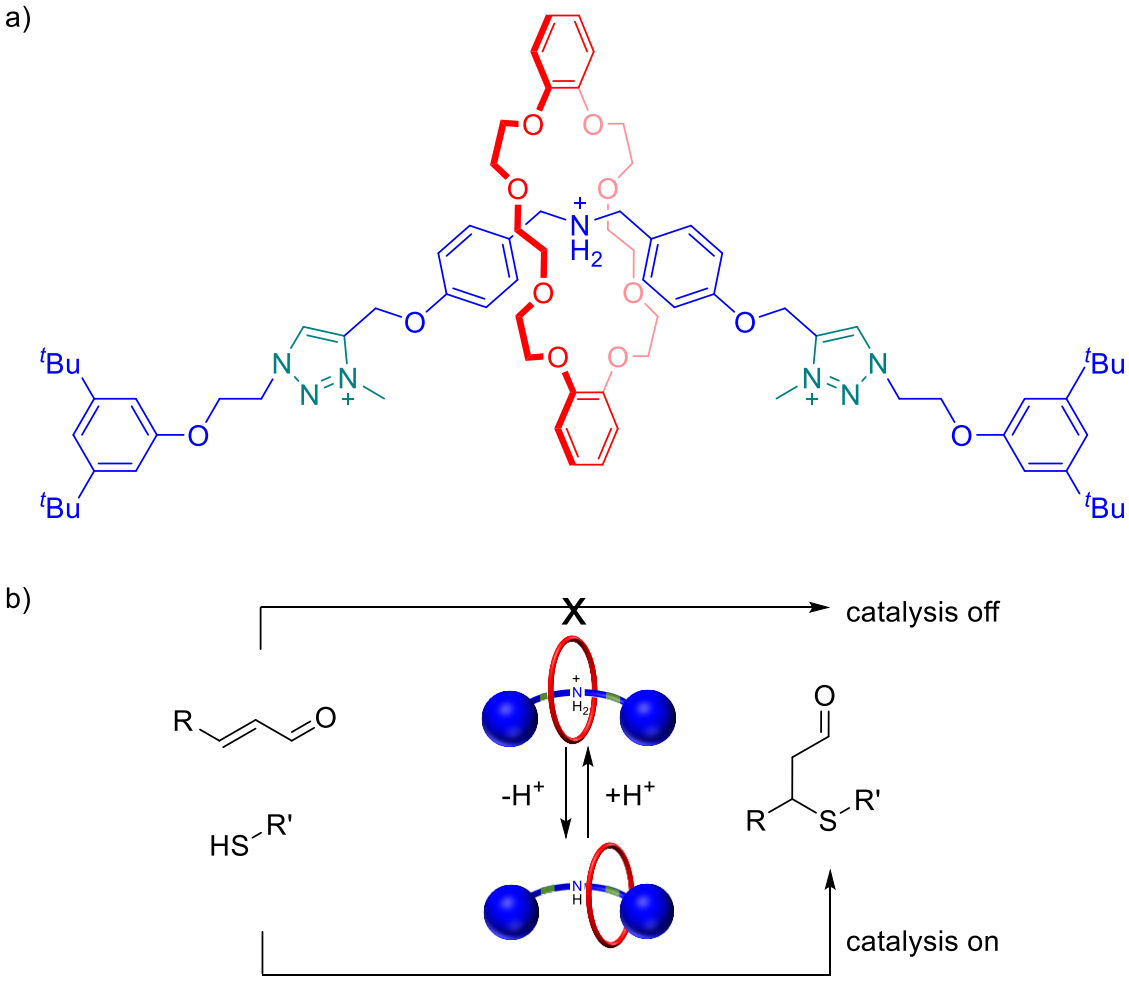

Figure 1.46 a) [2]Rotaxane with pH induced shuttling of the macrocycle reported by Leigh and co-workers. b) Schematic representation of the rotaxane displaying on/off switchable Michael addition catalysis.

1.5 Thesis Aims

This thesis describes the strategic integration of a range of supramolecular interactions into MIM and pseudo-MIM molecular architectures, in particular highlighting the potential of the exploitation of inter-component interactions in judiciously designed MIM and supramolecular systems for high yielding MIM synthesis, ion-pair recognition, sensing, and potential catalysis applications.

Chapter Two describes the synthesis of a series of metalloporphyrin-axle containing [2]- and [3]-rotaxanes, in which coordination of the metalloporphyrin by a macrocycle pyridyl motif forms an inter-component, intramolecular, transition metal complex. Extensive ^{1}H NMR and optical studies demonstrate that disruption of this complex by addition of a competing neutral or anionic Lewis base ligand displaces the macrocycle, inducing a reversible co-conformational change detectable by perturbation of the metalloporphyrin optical absorption spectrum, demonstrating a novel MIM signal transduction mechanism. Subsequent incorporation of a heteroditopic macrocycle achieved an ion-pair binding [2]rotaxane for the binding of lithium halide ion-pairs.

Chapter Three describes the exploitation of the facile formation of pillar[5]arene based pseudo[2]rotaxanes for a range of supramolecular applications. The synthesis of pillar[5]arene-containing [2]rotaxanes with organometallic stopper groups is discussed, in which the mechanical bond imparts air- and moisture-stability to the stopper groups. The synthesis of a pillar[5]arene functionalised with XB binding sites and BODIPY chromophores affords a sensor for a range of biologically relevant molecules including dicarboxylates and a chemical warfare agent simulant, in both organic and mixed organic-aqueous media.

Chapter Four targets the design and synthesis of [2]rotaxane catalysts for the ring-opening co-polymerisation (ROCOP) of epoxides with carbon dioxide to form sustainable polycarbonate polymers. The incorporation of Ni(II) and Co(III) salen complexes into MIM architectures seeks to exploit supramolecular interactions to afford superior catalytic activity over previously reported systems. Following synthesis and characterisation, high pressure CO_2 ROCOP reactions will be attempted and

supramolecular host-guest binding studies conducted to explore the potential of a supramolecular approach in the design of superior polymerisation catalysts.

1.6 References

1. F. H. C. Crick, J. D. Watson and W. L. Bragg, *Proc. R. Soc. A*, 1954, **223**, 80-96.
2. C. J. Pedersen, *J. Am. Chem. Soc.*, 1967, **89**, 7017-7036.
3. J.-M. Lehn, *Angew. Chem. Int. Ed. Engl.*, 1988, **27**, 89-112.
4. J. W. Steed and J. L. Atwood, *Supramolecular Chemistry*, Wiley, 3rd edn., 2022.
5. J.-M. Lehn, *Acc. Chem. Res.*, 1978, **11**, 49-57.
6. D. J. Cram, *Angew. Chem. Int. Ed. Engl.*, 1988, **27**, 1009-1020.
7. D. J. Cram and G. M. Lein, *J. Am. Chem. Soc.*, 1985, **107**, 3657-3668.
8. Nobel Prize Outreach AB, The Novel Prize in Chemistry 1987, https://www.nobelprize.org/prizes/chemistry/1987/press-release, (accessed 8th February 2024).
9. G. Fukuhara, *J. Photochem. Photobiol. C*, 2020, **42**, 100340.
10. N. Busschaert, C. Caltagirone, W. Van Rossom and P. A. Gale, *Chem. Rev.*, 2015, **115**, 8038-8155.
11. K. M. Bąk, K. Porfyrakis, J. J. Davis and P. D. Beer, *Mater. Chem. Front.*, 2020, **4**, 1052-1073.
12. S. Lim, Y. Kuang and H. A. M. Ardoña, *Front. Chem.*, 2021, **9**, 723111.
13. Z. Chen, A. K.-W. Chan, V. C.-H. Wong and V. W.-W. Yam, *J. Am. Chem. Soc.*, 2019, **141**, 11204-11211.
14. L. A. Malik, A. Bashir, A. Qureashi and A. H. Pandith, *Environ. Chem. Lett.*, 2019, **17**, 1495-1521.
15. B. O. Okesola and D. K. Smith, *Chem. Soc. Rev.*, 2016, **45**, 4226-4251.
16. A. Tamura and N. Yui, *Chem. Commun.*, 2014, **50**, 13433-13446.
17. M. J. Webber and R. Langer, *Chem. Soc. Rev.*, 2017, **46**, 6600-6620.
18. K. Kataoka, A. Harada and Y. Nagasaki, *Adv. Drug Deliv. Rev.*, 2001, **47**, 113-131.
19. A. Docker and M. J. Langton, *Trends Chem.*, 2023, **5**, 792-794.
20. L. E. Bickerton, T. G. Johnson, A. Kerckhoffs and M. J. Langton, *Chem. Sci.*, 2021, **12**, 11252-11274.
21. G. Olivo, G. Capocasa, D. Del Giudice, O. Lanzalunga and S. Di Stefano, *Chem. Soc. Rev.*, 2021, **50**, 7681-7724.
22. M. Raynal, P. Ballester, A. Vidal-Ferran and P. W. N. M. van Leeuwen, *Chem. Soc. Rev.*, 2014, **43**, 1660-1733.
23. T. Takata, *ACS. Cent. Sci.*, 2020, **6**, 129-143.
24. T. Takata, *Bull. Chem. Soc. Jpn.*, 2018, **92**, 409-426.
25. T. Ogawa, N. Usuki, K. Nakazono, Y. Koyama and T. Takata, *Chem. Commun.*, 2015, **51**, 5606-5609.
26. Y. Sagara, M. Karman, A. Seki, M. Pannipara, N. Tamaoki and C. Weder, *ACS. Cent. Sci.*, 2019, **5**, 874-881.
27. T. Muramatsu, Y. Okado, H. Traeger, S. Schrettl, N. Tamaoki, C. Weder and Y. Sagara, *J. Am. Chem. Soc.*, 2021, **143**, 9884-9892.
28. P. D. Beer, T. A. Barendt and J. Y. C. Lim, *Supramolecular Chemistry: Fundamentals and Applications*, Oxford University Press, 2022.
29. C. A. Hunter and J. K. M. Sanders, *J. Am. Chem. Soc.*, 1990, **112**, 5525-5534.

30. M. J. Langton, O. A. Blackburn, T. Lang, S. Faulkner and P. D. Beer, *Angew. Chem. Int. Ed.*, 2014, **53**, 11463-11466.
31. T. F. Headen, C. A. Howard, N. T. Skipper, M. A. Wilkinson, D. T. Bowron and A. K. Soper, *J. Am. Chem. Soc.*, 2010, **132**, 5735-5742.
32. D. L. Beene, G. S. Brandt, W. Zhong, N. M. Zacharias, H. A. Lester and D. A. Dougherty, *Biochemistry*, 2002, **41**, 10262-10269.
33. S. Li, S.-X. Fa, Q.-Q. Wang, D.-X. Wang and M.-X. Wang, *J. Org. Chem.*, 2012, **77**, 1860-1867.
34. E. Arunan, G. R. Desiraju, R. A. Klein, J. Sadlej, S. Scheiner, I. Alkorta, D. C. Clary, R. H. Crabtree, J. J. Dannenberg, P. Hobza, H. G. Kjaergaard, A. C. Legon, B. Mennucci and D. J. Nesbitt, *Pure Appl. Chem.*, 2011, **83**, 1637-1641.
35. P. A. Wood, F. H. Allen and E. Pidcock, *CrystEngComm*, 2009, **11**, 1563-1571.
36. A. Klamt, J. Reinisch, F. Eckert, J. Graton and J.-Y. Le Questel, *Phys. Chem. Chem. Phys.*, 2013, **15**, 7147-7154.
37. S. C. Zimmerman, T. J. Murray, A. J. Kirby and D. H. Williams, *Philos. Trans. R. Soc. A*, 1997, **345**, 49-56.
38. D. A. Leigh, C. C. Robertson, A. M. Z. Slawin and P. I. T. Thomson, *J. Am. Chem. Soc.*, 2013, **135**, 9939-9943.
39. T. Clark, M. Hennemann, J. S. Murray and P. Politzer, *J. Mol. Model.*, 2007, **13**, 291-296.
40. G. R. Desiraju, P. S. Ho, L. Kloo, A. C. Legon, R. Marquardt, P. Metrangolo, P. Politzer, G. Resnati and K. Rissanen, *Pure Appl. Chem.*, 2013, **85**, 1711-1713.
41. M. Saccone, G. Cavallo, P. Metrangolo, A. Pace, I. Pibiri, T. Pilati, G. Resnati and G. Terraneo, *CrystEngComm*, 2013, **15**, 3102-3105.
42. S. C. Patrick, R. Hein, A. Docker, P. D. Beer and J. J. Davis, *Chem. Eur. J.*, 2021, **27**, 10201-10209.
43. T. G. Johnson, A. Docker, A. Sadeghi-Kelishadi and M. J. Langton, *Chem. Sci.*, 2023, **14**, 5006-5013.
44. J. Pancholi and P. D. Beer, *Coord. Chem. Rev.*, 2020, **416**, 213281.
45. M. J. Langton, S. W. Robinson, I. Marques, V. Félix and P. D. Beer, *Nat. Chem.*, 2014, **6**, 1039-1043.
46. D. Cinčić, T. Friščić and W. Jones, *Chem. Eur. J.*, 2008, **14**, 747-753.
47. M. Gomberg, *J. Am. Chem. Soc.*, 1900, **22**, 757-771.
48. H. A. Staab, H. Brettschneider and H. Brunner, *Chem. Ber.*, 1970, **103**, 1101-1106.
49. S. Rösel, C. Balestrieri and P. R. Schreiner, *Chem. Sci.*, 2017, **8**, 405-410.
50. C. N. Pace, B. A. Shirley, M. McNutt and K. Gajiwala, *The FASEB Journal*, 1996, **10**, 75-83.
51. A. J. Metherell, W. Cullen, N. H. Williams and M. D. Ward, *Chem. Eur. J.*, 2018, **24**, 1554-1560.
52. S. B. Ferguson, E. M. Seward, F. Diederich, E. M. Sanford, A. Chou, P. Inocencio-Szweda and C. B. Knobler, *J. Org. Chem.*, 1988, **53**, 5593-5595.
53. M. Fernández-Vidal, S. H. White and A. S. Ladokhin, *J. Membr. Biol.*, 2011, **239**, 5-14.
54. E. Fischer, *Dtsch. Chem. Ges*, 1894, **27**, 2984-2993.
55. D. E. Koshland, *Proc. Natl. Acad. Sci. U.S.A.*, 1958, **44**, 98-104.
56. Y. Li and A. H. Flood, *J. Am. Chem. Soc.*, 2008, **130**, 12111-12122.
57. A. H. Flood, *Beilstein J. Org. Chem.*, 2016, **12**, 611-627.
58. D. K. Cabbiness and D. W. Margerum, *J. Am. Chem. Soc.*, 1969, **91**, 6540-6541.
59. J. L. Dye, *Angew. Chem. Int. Ed. Engl.*, 1979, **18**, 587-598.

60. J. W. Pflugrath and F. A. Quiocho, *Nature*, 1985, **314**, 257-260.
61. M. Hirshberg, K. Henrick, L. Lloyd Haire, N. Vasisht, M. Brune, J. E. T. Corrie and M. R. Webb, *Biochemistry*, 1998, **37**, 10381-10385.
62. M. P. Anderson, R. J. Gregory, S. Thompson, D. W. Souza, S. Paul, R. C. Mulligan, A. E. Smith and M. J. Welsh, *Science*, 1991, **253**, 202-205.
63. F. Delange, *Thyroid*, 1994, **4**, 107-128.
64. R. Z. Sabirov and Y. Okada, *Purinergic Signal.*, 2005, **1**, 311-328.
65. D. Banerjee, D. Kim, M. J. Schweiger, A. A. Kruger and P. K. Thallapally, *Chem. Soc. Rev.*, 2016, **45**, 2724-2739.
66. M. D. Rao, K. K. Singh, C. A. Morrison and J. B. Love, *RSC Adv.*, 2020, **10**, 4300-4309.
67. R. Eisler, in *Reviews of Environmental Contamination and Toxicology*, Springer New York, New York, NY, 2004, DOI: 10.1007/0-387-21729-0_3, pp. 133-165.
68. A. Mukherjee, M. K. Sengupta, M. A. Hossain, S. Ahamed, B. Das, B. Nayak, D. Lodh, M. M. Rahman and D. Chakraborti, *J Health Popul Nutr*, 2006, **24**, 142-163.
69. W. Werner, in *Ullmann's Encyclopedia of Industrial Chemistry*, Wiley, 2009, DOI: https://doi.org/10.1002/14356007.n10_n05.
70. V. H. Smith, G. D. Tilman and J. C. Nekola, *Environ. Pollut.*, 1999, **100**, 179-196.
71. P. A. Gale, J. T. Davis and R. Quesada, *Chem. Soc. Rev.*, 2017, **46**, 2497-2519.
72. H. M. Tay and P. D. Beer, *Org. Biomol. Chem.*, 2021, **19**, 4652-4677.
73. R. Hein, P. D. Beer and J. J. Davis, *Chem. Rev.*, 2020, **120**, 1888-1935.
74. P. A. Gale and C. Caltagirone, *Chem. Soc. Rev.*, 2015, **44**, 4212-4227.
75. C. R. Rice, C. Slater, R. A. Faulkner and R. L. Allan, *Angew. Chem. Int. Ed.*, 2018, **57**, 13071-13075.
76. R. Shannon, *Acta Crystallogr. A* . 1976, **32**, 751-767.
77. L. H. Ahrens, *Geochim. Cosmochim. Acta*, 1952, **2**, 155-169.
78. F. Hofmeister, *Arch. Exp. Path. Pharm.*, 1888, **24**, 247-260.
79. A. Docker, Y. C. Tse, H. M. Tay, A. J. Taylor, Z. Zhang and P. D. Beer, *Angew. Chem. Int. Ed.*, 2022, **134**, e202214523.
80. D. Lichosyt, S. Wasiłek, P. Dydio and J. Jurczak, *Chem. Eur. J.*, 2018, **24**, 11683-11692.
81. P. D. Beer and P. A. Gale, *Angew. Chem. Int. Ed.*, 2001, **40**, 486-516.
82. P. Chakrabarti, *J. Mol. Biol.*, 1993, **234**, 463-482.
83. C. H. Park and H. E. Simmons, *J. Am. Chem. Soc.*, 1968, **90**, 2431-2432.
84. A. E. Hargrove, S. Nieto, T. Zhang, J. L. Sessler and E. V. Anslyn, *Chem Rev*, 2011, **111**, 6603-6782.
85. E. Kimura, M. Kodama and T. Yatsunami, *J. Am. Chem. Soc.*, 1982, **104**, 3182-3187.
86. B. Dietrich, J. Guilhem, J.-M. Lehn, C. Pascard and E. Sonveaux, *Helv. Chim. Acta*, 1984, **67**, 91-104.
87. F. P. Schmidtchen, *Angew. Chem. Int. Ed. Engl.*, 1977, **16**, 720-721.
88. J. L. Sessler, P. Gale and W.-S. Cho, *Anion Receptor Chemistry*, The Royal Society of Chemistry, 2006.
89. P. Blondeau, M. Segura, R. Pérez-Fernández and J. de Mendoza, *Chem. Soc. Rev.*, 2007, **36**, 198-210.
90. B. Dietrich, T. M. Fyles, J.-M. Lehn, L. G. Pease and D. L. Fyles, *J. Chem. Soc., Chem. Commun.*, 1978, 934-936.

91. R. P. Dixon, S. J. Geib and A. D. Hamilton, *J. Am. Chem. Soc.*, 1992, **114**, 365-366.
92. J. Cai and J. L. Sessler, *Chem. Soc. Rev.*, 2014, **43**, 6198-6213.
93. K. Chellappan, N. J. Singh, I.-C. Hwang, J. W. Lee and K. S. Kim, *Angew. Chem. Int. Ed.*, 2005, **44**, 2899-2903.
94. A. Kumar and P. S. Pandey, *Org. Lett.*, 2008, **10**, 165-168.
95. N. L. Kilah, M. D. Wise, C. J. Serpell, A. L. Thompson, N. G. White, K. E. Christensen and P. D. Beer, *J. Am. Chem. Soc.*, 2010, **132**, 11893-11895.
96. P. P. Neelakandan, M. Hariharan and D. Ramaiah, *Org. Lett.*, 2005, **7**, 5765-5768.
97. D. Maity, M. Li, M. Ehlers and C. Schmuck, *Chem. Commun.*, 2017, **53**, 208-211.
98. K. Kavallieratos, S. R. de Gala, D. J. Austin and R. H. Crabtree, *J. Am. Chem. Soc.*, 1997, **119**, 2325-2326.
99. S. J. Brooks, P. A. Gale and M. E. Light, *Chem. Commun.*, 2005, 4696-4698.
100. C. B. Black, B. Andrioletti, A. C. Try, C. Ruiperez and J. L. Sessler, *J. Am. Chem. Soc.*, 1999, **121**, 10438-10439.
101. P. Anzenbacher, A. C. Try, H. Miyaji, K. Jursíková, V. M. Lynch, M. Marquez and J. L. Sessler, *J. Am. Chem. Soc.*, 2000, **122**, 10268-10272.
102. H. Juwarker, J. M. Lenhardt, D. M. Pham and S. L. Craig, *Angew. Chem. Int. Ed.*, 2008, **47**, 3740-3743.
103. J. Grant Hill and A. C. Legon, *Phys. Chem. Chem. Phys.*, 2015, **17**, 858-867.
104. A. Mele, P. Metrangolo, H. Neukirch, T. Pilati and G. Resnati, *J. Am. Chem. Soc.*, 2005, **127**, 14972-14973.
105. M. G. Sarwar, B. Dragisic, S. Sagoo and M. S. Taylor, *Angew. Chem. Int. Ed.*, 2010, **49**, 1674-1677.
106. R. Tepper, B. Schulze, H. Görls, P. Bellstedt, M. Jäger and U. S. Schubert, *Org. Lett.*, 2015, **17**, 5740-5743.
107. S. K. Kim and J. L. Sessler, *Chem. Soc. Rev.*, 2010, **39**, 3784-3809.
108. A. J. McConnell, A. Docker and P. D. Beer, *ChemPlusChem*, 2020, **85**, 1824-1841.
109. Y. C. Tse, A. Docker, Z. Zhang and P. D. Beer, *Chem. Commun.*, 2021, **57**, 4950-4953.
110. Q. He, N. J. Williams, J. H. Oh, V. M. Lynch, S. K. Kim, B. A. Moyer and J. L. Sessler, *Angew. Chem. Int. Ed.*, 2018, **57**, 11924-11928.
111. B. Akhuli and P. Ghosh, *Chem. Commun.*, 2015, **51**, 16514-16517.
112. J. Zhu, X.-D. Wang, J. Luo, Y.-F. Ao, Q.-Q. Wang and D.-X. Wang, *Org. Biomol. Chem.*, 2021, **19**, 8586-8590.
113. J. H. Lee, J. H. Lee, Y. R. Choi, P. Kang, M.-G. Choi and K.-S. Jeong, *J. Org. Chem.*, 2014, **79**, 6403-6409.
114. I.-W. Park, J. Yoo, B. Kim, S. Adhikari, S. K. Kim, Y. Yeon, C. J. E. Haynes, J. L. Sutton, C. C. Tong, V. M. Lynch, J. L. Sessler, P. A. Gale and C.-H. Lee, *Chem. Eur. J.*, 2012, **18**, 2514-2523.
115. G. Grauwels, H. Valkenier, A. P. Davis, I. Jabin and K. Bartik, *Angew. Chem. Int. Ed.*, 2019, **58**, 6921-6925.
116. B. D. Smith, in *Macrocyclic Chemistry: Current Trends and Future Perspectives*, ed. K. Gloe, Springer Netherlands, Dordrecht, 2005, DOI: 10.1007/1-4020-3687-6_9, pp. 137-151.
117. B. Qiao, A. Sengupta, Y. Liu, K. P. McDonald, M. Pink, J. R. Anderson, K. Raghavachari and A. H. Flood, *J. Am. Chem. Soc.*, 2015, **137**, 9746-9757.

118. T. Bunchuay, A. Docker, U. Eiamprasert, P. Surawatanawong, A. Brown and P. D. Beer, *Angew. Chem. Int. Ed.*, 2020, **59**, 12007-12012.
119. A. J. Taylor, A. Docker and P. D. Beer, *Chem. Asian J.*, 2023, **18**, e202201170.
120. J. Romanski and P. Piątek, *Chem. Commun.*, 2012, **48**, 11346-11348.
121. K. Ziach, M. Karbarz and J. Romański, *Dalton Trans.*, 2016, **45**, 11639-11643.
122. E. Wasserman, *J. Am. Chem. Soc.*, 1960, **82**, 4433-4434.
123. E. Wasserman, *Scientific American*, 1962, **207**, 94-106.
124. R. Brückner, *Eur. J. Org. Chem.*, 2019, **2019**, 3289-3319.
125. A. S. Baluna, A. Galan, D. A. Leigh, G. D. Smith, J. T. J. Spence, D. J. Tetlow, I. J. Vitorica-Yrezabal and M. Zhang, *J. Am. Chem. Soc.*, 2023, **145**, 9825-9833.
126. C. O. Dietrich-Buchecker, J. P. Sauvage and J. P. Kintzinger, *Tetrahedron Lett.*, 1983, **24**, 5095-5098.
127. D. A. Leigh, P. J. Lusby, R. T. McBurney, A. Morelli, A. M. Z. Slawin, A. R. Thomson and D. B. Walker, *J. Am. Chem. Soc.*, 2009, **131**, 3762-3771.
128. S. M. Goldup, D. A. Leigh, P. J. Lusby, R. T. McBurney and A. M. Z. Slawin, *Angew. Chem. Int. Ed.*, 2008, **47**, 6999-7003.
129. J. P. Sauvage and M. Ward, *Inorg. Chem.*, 1991, **30**, 3869-3874.
130. A.-M. L. Fuller, D. A. Leigh, P. J. Lusby, A. M. Z. Slawin and D. B. Walker, *J. Am. Chem. Soc.*, 2005, **127**, 12612-12619.
131. A.-M. Fuller, D. A. Leigh, P. J. Lusby, I. D. H. Oswald, S. Parsons and D. B. Walker, *Angew. Chem. Int. Ed.*, 2004, **43**, 3914-3918.
132. G. Kaiser, T. Jarrosson, S. Otto, Y.-F. Ng, A. D. Bond and J. K. M. Sanders, *Angew. Chem. Int. Ed.*, 2004, **43**, 1959-1962.
133. G. Zhang, G. Gil-Ramírez, A. Markevicius, C. Browne, I. J. Vitorica-Yrezabal and D. A. Leigh, *J. Am. Chem. Soc.*, 2015, **137**, 10437-10442.
134. J.-F. Ayme, G. Gil-Ramírez, D. A. Leigh, J.-F. Lemonnier, A. Markevicius, C. A. Muryn and G. Zhang, *J. Am. Chem. Soc.*, 2014, **136**, 13142-13145.
135. F. Zapata, O. A. Blackburn, M. J. Langton, S. Faulkner and P. D. Beer, *Chem. Commun.*, 2013, **49**, 8157-8159.
136. A. Inthasot, S.-T. Tung and S.-H. Chiu, *Acc. Chem. Res.*, 2018, **51**, 1324-1337.
137. S.-T. Tung, C.-C. Lai, Y.-H. Liu, S.-M. Peng and S.-H. Chiu, *Angew. Chem. Int. Ed.*, 2013, **52**, 13269-13272.
138. Y.-H. Lin, C.-C. Lai, Y.-H. Liu, S.-M. Peng and S.-H. Chiu, *Angew. Chem. Int. Ed.*, 2013, **52**, 10231-10236.
139. K.-D. Wu, Y.-H. Lin, C.-C. Lai and S.-H. Chiu, *Org. Lett.*, 2014, **16**, 1068-1071.
140. J. A. Wisner, P. D. Beer, M. G. B. Drew and M. R. Sambrook, *J. Am. Chem. Soc.*, 2002, **124**, 12469-12476.
141. A. Brown, M. J. Langton, N. L. Kilah, A. L. Thompson and P. D. Beer, *Chem. Eur. J.*, 2015, **21**, 17664-17675.
142. M. D. Lankshear, N. H. Evans, S. R. Bayly and P. D. Beer, *Chem. Eur. J.*, 2007, **13**, 3861-3870.
143. M. R. Sambrook, P. D. Beer, M. D. Lankshear, R. F. Ludlow and J. A. Wisner, *Org. Biomol. Chem.*, 2006, **4**, 1529-1538.
144. J. D. Crowley, S. M. Goldup, A.-L. Lee, D. A. Leigh and R. T. McBurney, *Chem. Soc. Rev.*, 2009, **38**, 1530-1541.
145. V. Aucagne, J. Berná, J. D. Crowley, S. M. Goldup, K. D. Hänni, D. A. Leigh, P. J. Lusby, V. E. Ronaldson, A. M. Z. Slawin, A. Viterisi and D. B. Walker, *J. Am. Chem. Soc.*, 2007, **129**, 11950-11963.
146. S. M. Goldup, D. A. Leigh, T. Long, P. R. McGonigal, M. D. Symes and J. Wu, *J. Am. Chem. Soc.*, 2009, **131**, 15924-15929.

147. V. Aucagne, K. D. Hänni, D. A. Leigh, P. J. Lusby and D. B. Walker, *J. Am. Chem. Soc.*, 2006, **128**, 2186-2187.
148. J. D. Crowley, K. D. Hänni, A.-L. Lee and D. A. Leigh, *J. Am. Chem. Soc.*, 2007, **129**, 12092-12093.
149. S. M. Goldup, D. A. Leigh, P. J. Lusby, R. T. McBurney and A. M. Z. Slawin, *Angew. Chem. Int. Ed.*, 2008, **47**, 3381-3384.
150. J. Berná, S. M. Goldup, A.-L. Lee, D. A. Leigh, M. D. Symes, G. Teobaldi and F. Zerbetto, *Angew. Chem. Int. Ed.*, 2008, **47**, 4392-4396.
151. J. Berná, J. D. Crowley, S. M. Goldup, K. D. Hänni, A.-L. Lee and D. A. Leigh, *Angew. Chem. Int. Ed.*, 2007, **46**, 5709-5713.
152. J. T. Wilmore and P. D. Beer, *Adv. Mater.*, 2024, DOI: https://doi.org/10.1002/adma.202309098, 2309098.
153. N.-C. Chen, P.-Y. Huang, C.-C. Lai, Y.-H. Liu, Y. Wang, S.-M. Peng and S.-H. Chiu, *Chem. Commun.*, 2007, DOI: 10.1039/B706461F, 4122-4124.
154. Y.-J. Lee, K.-S. Liu, C.-C. Lai, Y.-H. Liu, S.-M. Peng, R. P. Cheng and S.-H. Chiu, *Chem. Eur. J.*, 2017, **23**, 9756-9760.
155. G. Baggi and S. J. Loeb, *Angew. Chem. Int. Ed.*, 2016, **55**, 12533-12537.
156. M. R. Sambrook, P. D. Beer, J. A. Wisner, R. L. Paul and A. R. Cowley, *J. Am. Chem. Soc.*, 2004, **126**, 15364-15365.
157. R. Pereira Orenha, S. S. Pereira Furtado, A. Muñoz-Castro, M. Jeomar Piotrowski, G. Finoto Caramori and R. L. Tame Parreira, *Chem. Eur. J.*, 2023, **29**, e202203905.
158. A. C. Legon, *Phys. Chem. Chem. Phys.*, 2010, **12**, 7736-7747.
159. L. C. Gilday, N. G. White and P. D. Beer, *Dalton Trans.*, 2013, **42**, 15766-15773.
160. C. Loy, J. M. Holthoff, R. Weiss, S. M. Huber and S. V. Rosokha, *Chem. Sci.*, 2021, **12**, 8246-8251.
161. A. Borissov, J. Y. C. Lim, A. Brown, K. E. Christensen, A. L. Thompson, M. D. Smith and P. D. Beer, *Chem. Commun.*, 2017, **53**, 2483-2486.
162. R. Tepper, B. Schulze, M. Jäger, C. Friebe, D. H. Scharf, H. Görls and U. S. Schubert, *J. Org. Chem.*, 2015, **80**, 3139-3150.
163. F. Ostler, D. G. Piekarski, T. Danelzik, M. S. Taylor and O. García Mancheño, *Chem. Eur. J.*, 2021, **27**, 2315-2320.
164. S. W. Robinson, C. L. Mustoe, N. G. White, A. Brown, A. L. Thompson, P. Kennepohl and P. D. Beer, *J. Am. Chem. Soc.*, 2015, **137**, 499-507.
165. M. J. Langton, L. C. Duckworth and P. D. Beer, *Chem. Commun.*, 2013, **49**, 8608-8610.
166. M. J. Langton and P. D. Beer, *Chem. Commun.*, 2014, **50**, 8124-8127.
167. M. J. Deetz, M. Shang and B. D. Smith, *J. Am. Chem. Soc.*, 2000, **122**, 6201-6207.
168. M. J. Deetz, R. Shukla and B. D. Smith, *Tetrahedron*, 2002, **58**, 799-805.
169. R. C. Knighton and P. D. Beer, *Chem. Commun.*, 2014, **50**, 1540-1542.
170. V. K. Munasinghe, J. Pancholi, D. Manawadu, Z. Zhang and P. D. Beer, *Chem. Eur. J.*, 2022, **28**, e202201209.
171. A. Arun, A. Docker, H. M. Tay and P. D. Beer, *Chem. Eur. J.*, 2023, **29**, e202301446.
172. H. M. Tay, Y. C. Tse, A. Docker, C. Gateley, A. L. Thompson, H. Kuhn, Z. Zhang and P. D. Beer, *Angew. Chem. Int. Ed.*, 2023, **62**, e2022147.
173. H. M. Tay, A. Docker, Y. Cheong Tse and P. D. Beer, *Chem. Eur. J.*, 2023, **29**, e202301316.

174. S. S. Zhu, P. J. Carroll and T. M. Swager, *J. Am. Chem. Soc.*, 1996, **118**, 8713-8714.
175. T. Shukla, A. K. Dwivedi, R. Arumugaperumal, C.-M. Lin, S.-Y. Chen and H.-C. Lin, *Dyes Pigm.*, 2016, **131**, 49-59.
176. S.-M. Chan, F.-K. Tang, C.-S. Kwan, C.-Y. Lam, S. C. K. Hau and K. C.-F. Leung, *Mater. Chem. Front.*, 2019, **3**, 2388-2396.
177. L. M. Hancock, E. Marchi, P. Ceroni and P. D. Beer, *Chem. Eur. J.*, 2012, **18**, 11277-11283.
178. M. J. Langton, I. Marques, S. W. Robinson, V. Félix and P. D. Beer, *Chem. Eur. J.*, 2016, **22**, 185-192.
179. N. H. Evans and P. D. Beer, *Org. Biomol. Chem.*, 2011, **9**, 92-100.
180. N. H. Evans, C. J. Serpell, N. G. White and P. D. Beer, *Chem. Eur. J.*, 2011, **17**, 12347-12354.
181. N. H. Evans, H. Rahman, A. V. Leontiev, N. D. Greenham, G. A. Orlowski, Q. Zeng, R. M. J. Jacobs, C. J. Serpell, N. L. Kilah, J. J. Davis and P. D. Beer, *Chem. Sci.*, 2012, **3**, 1080-1089.
182. S.-Y. Hsueh, C.-C. Lai and S.-H. Chiu, *Chem. Eur. J.*, 2010, **16**, 2997-3000.
183. T. Iijima, S. A. Vignon, H.-R. Tseng, T. Jarrosson, J. K. M. Sanders, F. Marchioni, M. Venturi, E. Apostoli, V. Balzani and J. F. Stoddart, *Chem. Eur. J.*, 2004, **10**, 6375-6392.
184. J. J. Gassensmith, S. Matthys, J.-J. Lee, A. Wojcik, P. V. Kamat and B. D. Smith, *Chem. Eur. J.*, 2010, **16**, 2916-2921.
185. T. A. Barendt, A. Docker, I. Marques, V. Félix and P. D. Beer, *Angew. Chem. Int. Ed.*, 2016, **55**, 11069-11076.
186. C. B. Caputo, K. Zhu, V. N. Vukotic, S. J. Loeb and D. W. Stephan, *Angew. Chem. Int. Ed.*, 2013, **52**, 960-963.
187. G. C. Welch and D. W. Stephan, *J. Am. Chem. Soc.*, 2007, **129**, 1880-1881.
188. D. W. Stephan and G. Erker, *Angew. Chem. Int. Ed.*, 2010, **49**, 46-76.
189. M. J. Power, D. T. J. Morris, I. J. Vitorica-Yrezabal and D. A. Leigh, *J. Am. Chem. Soc.*, 2023, **145**, 8593-8599.
190. Y. Suzaki, K. Shimada, E. Chihara, T. Saito, Y. Tsuchido and K. Osakada, *Org. Lett.*, 2011, **13**, 3774-3777.
191. R. F. Heck and J. P. Nolley, *J. Org. Chem.*, 1972, **37**, 2320-2322.
192. T. W. Traut, *Allosteric Regulatory Enzymes*, Springer US, 2007.
193. V. Blanco, A. Carlone, K. D. Hänni, D. A. Leigh and B. Lewandowski, *Angew. Chem. Int. Ed.*, 2012, **51**, 5166-5169.

Chapter Two

Dynamic Zn(II) Metalloporphyrin Rotaxanes for Anion and Ion-Pair Recognition and Sensing

2 Dynamic Zn(II) Metalloporphyrin Rotaxanes for Anion and Ion-Pair Recognition and Sensing

2.1 Introduction

2.1.1 The Porphyrin Moiety

Derived from substitution of the heterocyclic molecule porphine, $C_{20}H_{14}N_4$, porphyrins consist of four pyrrole-like rings linked by methine groups to form a large aromatic macrocycle. Porphyrins are of vital importance to aerobic lifeforms, notably as the base scaffold for the haem protein, essential for mammalian respiration, and chlorophyll, the protein enabling harvesting of light by plants in photosynthesis (Figure 2.1).[1] The regulation of porphyrins in the body is essential as many chronic diseases are caused by their deficiencies: low haemoglobin levels lead to anaemia, while build-up of excess porphyrin in the liver leads to porphyria.[2] Many other biological processes are dependent upon porphyrin-containing biomolecules including cytochrome *c* (a vital enzyme in the electron transport chain), vitamin B_{12} (cobalamin, metabolic pathway) and myoglobin (an oxygen storage protein).[3-5]

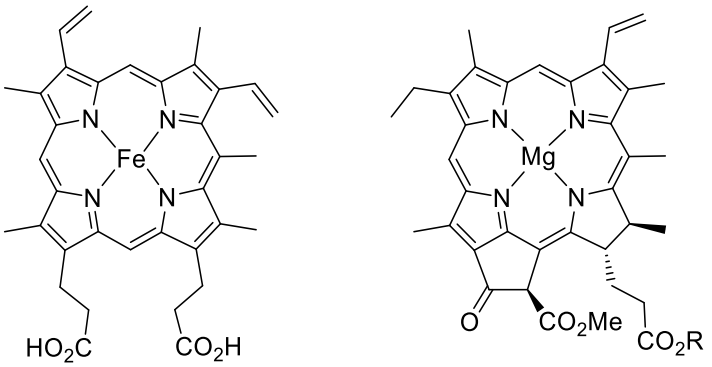

Figure 2.1. Structure of a) Fe-porphyrin subunit of haem *b*,[6] b) chlorophyll *a*.[7]

To the synthetic chemist, porphyrins also display vast diversity in function, with an easily functionalised base unit (Figure 2.2). Porphyrins are Hückel aromatic, with 18 of the 26 π-electrons delocalised, obeying the *4n+2* rule for aromaticity.[8] The most common

modifications to porphyrins include substitution of the *β*- or *meso*- protons, and metalation of the porphyrin, which can act as a chelating tetradentate dianionic ligand. Such metalloporphyrins can then bind additional species through the vacant axial coordination sites of the metal.[9]

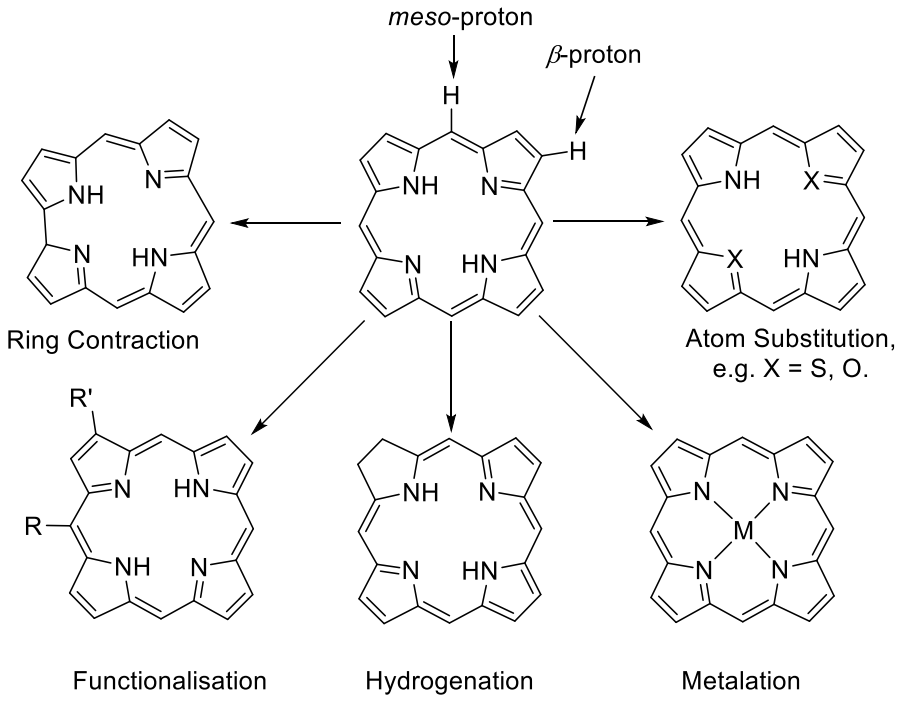

Figure 2.2. The porphine macrocycle and possible modification routes.

2.1.2 Optical Properties of Porphyrins

The etymology of 'porphyrin' can be attributed to the deep purple colour characteristic of porphyrins, with the roots of the name stemming from the Greek *πορφύρα*, *porphyra*, meaning 'purple'.[10] The UV-visible spectra of porphyrins are typically dominated by a sharp, intense (fully allowed) Soret band, from which arises their deep colouration, and less intense (quasi-allowed) Q-bands at longer wavelengths (Figure 2.3 a). The transitions observed in each band can be identified by Gouterman's four orbital model, which considers the electronic transitions between the two highest energy occupied molecular orbitals (HOMOs) and the two lowest energy unoccupied molecular orbitals (LUMOs) (Figure 2.3 b).[11] The relative energies of these transitions are highly sensitive to the ring

substituents and the identity of the porphyrin metal centre.[12] In addition, free-base porphyrins and metalloporphyrins with closed shell metal centres, e.g. Zn(II), d^{10}, Mg(II), s^0, display characteristic emission spectra.[13, 14]

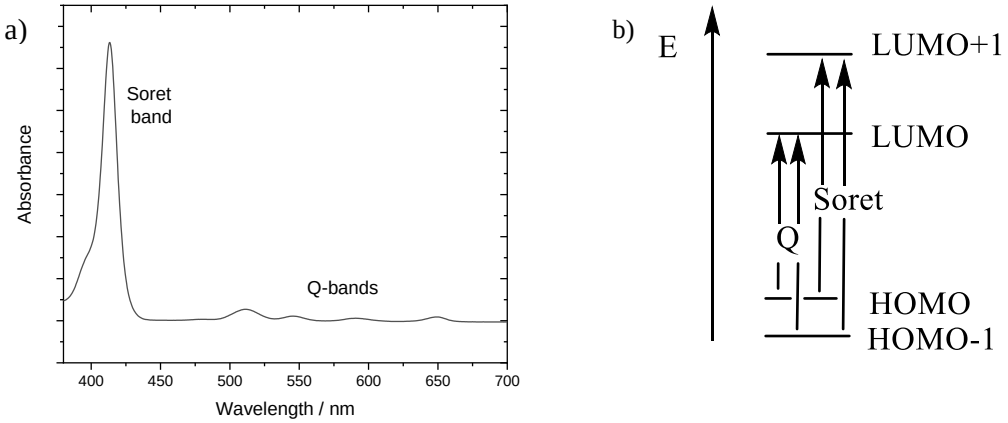

Figure 2.3. a) UV-visible spectrum of 1 mM solution of tetraphenylporphyrin in acetone**.** b) Electronic levels of porphyrins showing Soret and Q-band transitions.

2.1.3 Porphyrins for Anion Sensing

The Lewis acidity of the metal centre of metalloporphyrins has been exploited for anion binding and recognition. The first report on the effects of halide anion binding on tetraphenylporphyrin zinc to form five-coordinate complexes was made by Hinman and Pavelich in 1988,[15] who demonstrated halide sensing by binding-induced shifts in the metalloporphyrin oxidation potential. The ability of porphyrins to produce an optical response to anion binding has also received attention. In 2001, Hong and co-workers reported a Zn(II) porphyrin derivative with urea HB donors for anion binding, which exhibited high selectivity for acetate binding in MeCN, with sensing enabled by shifts in the Soret-band absorption of the metalloporphyrin unit (Figure 2.4 a).[16] Similar behaviour was reported by Starnes *et al*. in 2002, in which a porphyrin chromophore was appended to a disulfonamide anion binding site through a conjugated spacer (Figure 2.4 b).[17] In 2013, Beer and co-workers reported a picket fence Zn(II) porphyrin sensor containing

XB iodo-triazole anion binding-moieties, which bound anions cooperatively with the Lewis acidic Zn(II) centre in chloroform (Figure 2.4 c).[18]

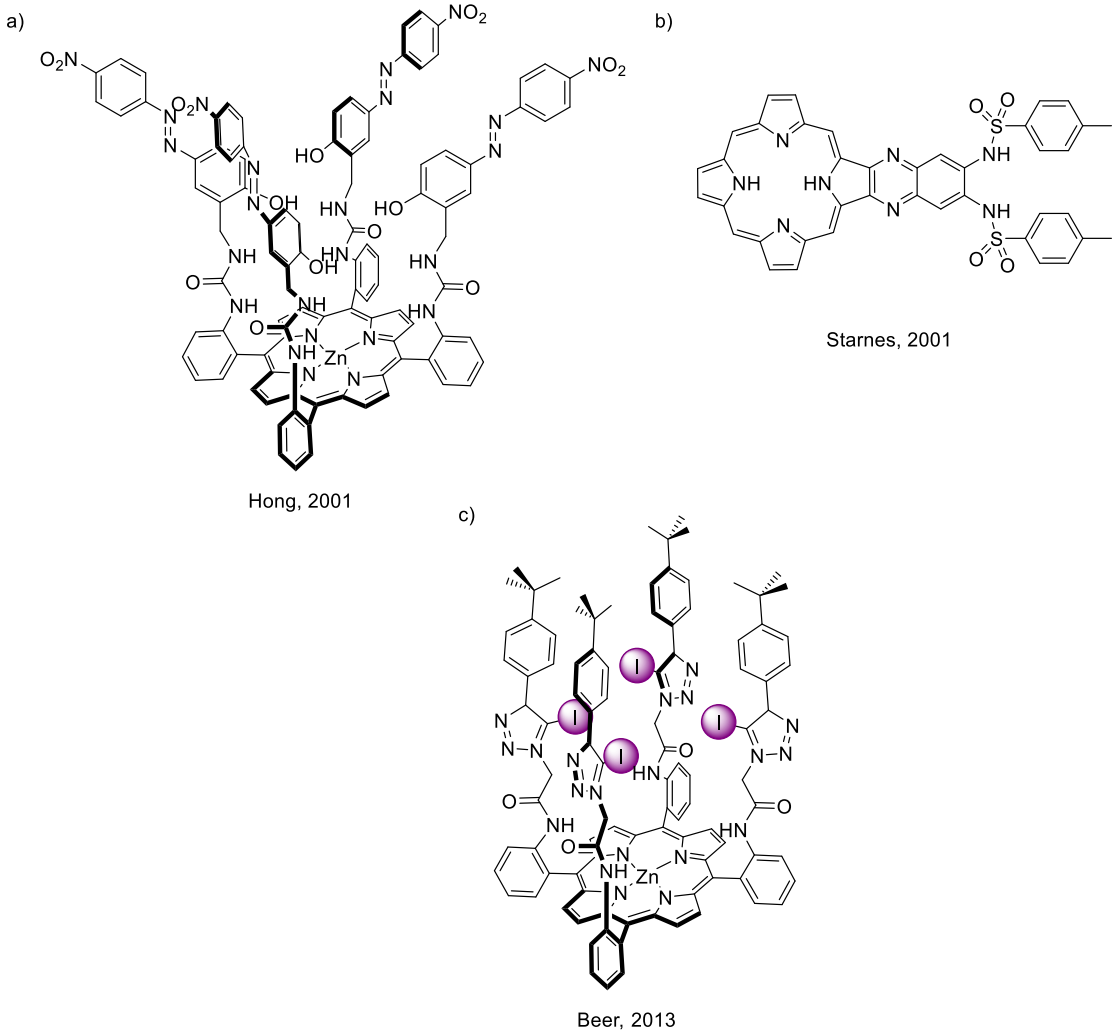

Figure 2.4. Previously reported non-interlocked porphyrin-based anion binding receptors.

2.1.4 Porphyrin-containing MIMs

The sensing capability of porphyrins has previously been exploited in [2]rotaxanes wherein the mechanical bond enables dynamic motion and through-space sensing of binding events at one of the rotaxane's axle or macrocycle components by a porphyrin on the other interlocked component. The innate shuttling motion of rotaxanes was exploited elegantly by Ma and co-workers, who reported a pH-dependent [2]rotaxane molecular shuttle, in which the shuttling motion could be probed optically (Figure 2.5 a).[19] In this system the proximity of a Pt(II) metalloporphyrin functionalised dibenzo-24-

crown-8 (DB24C8) macrocycle to a stopper anthracene group could be controlled by protonation of an axle amine, to form an ammonium cation. At low pH, the porphyrin was held in close proximity to the anthracene moiety, enabling room temperature phosphorescence of the porphyrin upon excitation of the anthracene due to a through-space energy transfer process. At high pH, the macrocycle preferentially resides at the bipyridinium moiety, increasing distance to the anthracene, impeding the energy transfer process and turning off room temperature fluorescence.

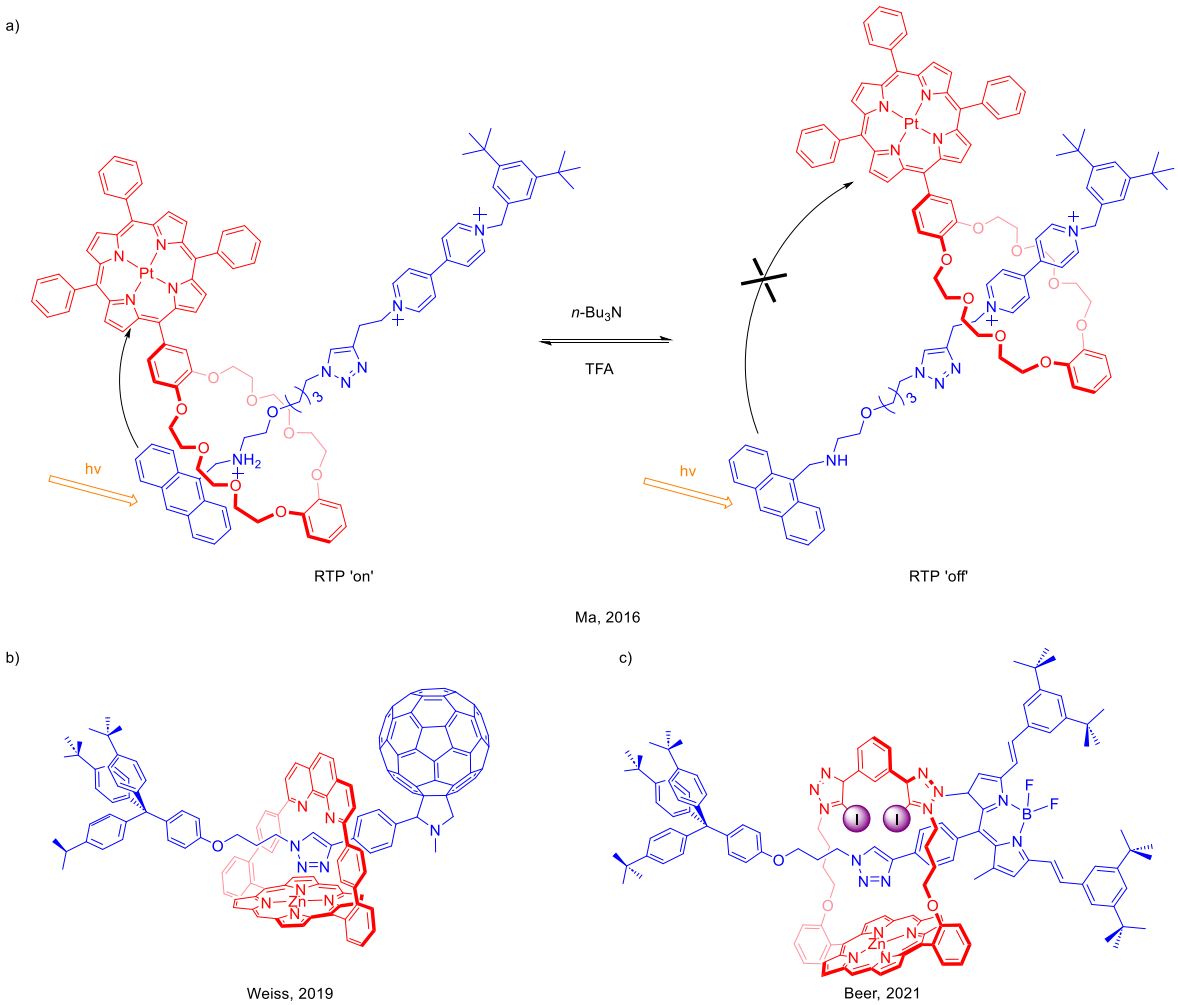

Figure 2.5. Previously reported [2]rotaxanes containing porphyrin moieties for chemical sensing.[19-21]

More recently, [2]rotaxanes containing strapped Zn(II) metalloporphyrin macrocycles have been reported. In 2019, Weiss and co-workers described a fullerene-stoppered

[2]rotaxane, in which the presence or absence of a competing external ligand, namely pyridine, controlled the location of the macrocycle by moderating coordination of the Zn(II) centre by the axle triazole moiety (Figure 2.5 b).[20] Thus, macrocycle shuttling could be probed by the detection of the charge-separated state formed between the fullerene and the porphyrin upon light excitation. In 2021, our group reported an XB strapped Zn(II) metalloporphyrin containing rotaxane with a BODIPY stopper for dual optical and electrochemical anion sensing (Figure 2.5 c).[21] This system, the first example of the incorporation of XB functionality into a porphyrin rotaxane, enabled the dual-signal transduction of anion binding via inter-component anion recognition between the Zn(II) coordinated triazole axle and macrocycle XB motif, in 98:2 *v/v* acetone:water and in DCM — the porphyrin enabled redox sensing, while the stopper BODIPY group gave rise to an optical fluorescence quenching response upon binding.

2.1.5 Project Aims

Despite the ability of porphyrins to act as optical and electrochemical signal transducers for binding events, their incorporation into mechanically interlocked molecules remains comparatively rare. This project seeks to design [2]rotaxanes in which a marked inter-component interaction — coordination of an axle metalloporphyrin motif by a macrocycle pyridyl group (Figure 2.6 a) — modulates the co-conformational dynamism of the system. Introducing a competing Lewis basic neutral or anionic ligand would be expected to displace the macrocycle (Figure 2.6 b), inducing a marked optical response. Furthermore, the introduction of a competing metal cationic guest which is preferentially bound by the macrocycle pyridyl, thus removing the inter-component interaction (Figure 2.6 c), should both elicit an optical response and increase the availability of the metalloporphyrin centre, facilitating ion-pair binding. The equilibria for the inter-component interaction will be probed by optical and ^{1}H NMR spectroscopy,

demonstrating charged guest-competition interruption of MIM host inter-component interactions in [2]rotaxanes to provide an optical signal transduction mechanism for binding events and understanding the co-conformational dynamism of MIM architectures.

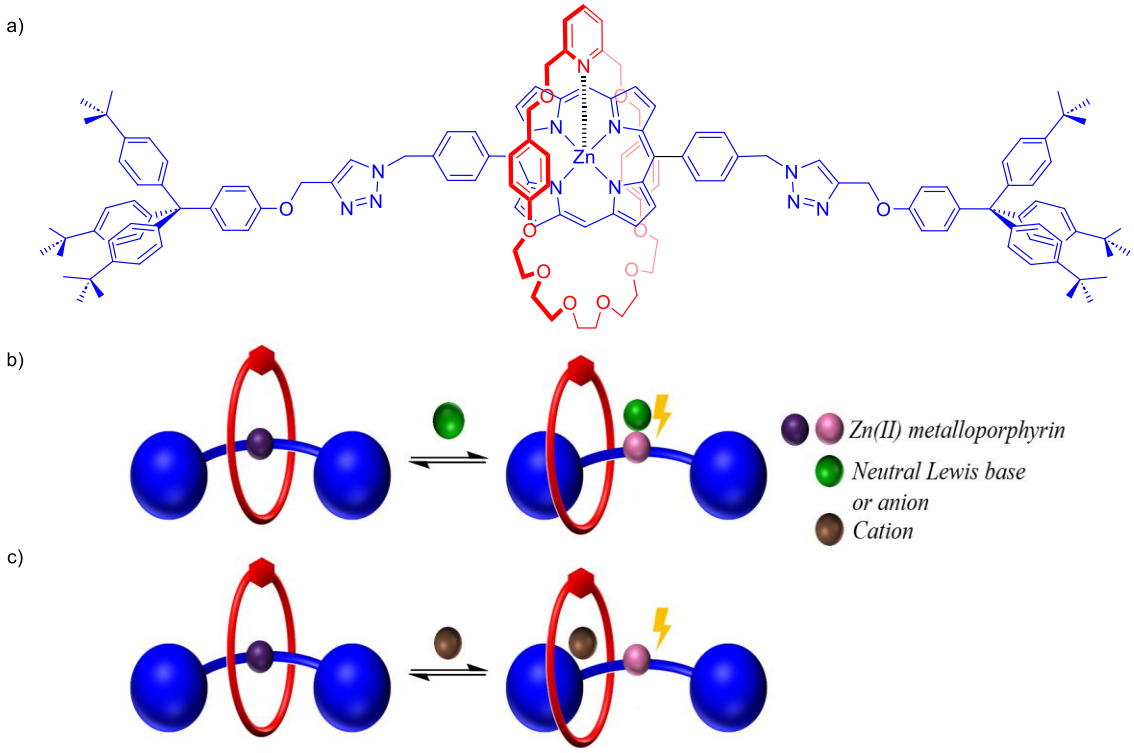

Figure 2.6. a) Representative structure of a target [2]rotaxane, cartoon representations of a Zn(II) metalloporphyrin-based [2]rotaxane exhibiting b) Lewis base or anion and c) Lewis acid mediated MIM molecular motion and photochemical response.

2.2 Synthesis of First-generation Pyridyl Macrocycle-porphyrin Axle [*n*]Rotaxanes[a]

Initial synthetic efforts targeted Zn(II) metalloporphyrin [2]rotaxanes, due to the known anion binding affinity of Zn(II) porphyrins and the diamagnetic, non-aggregating nature

[a] *The initial synthesis of the rotaxanes described in Section 2.2 was undertaken by final year undergraduate Part II project student Caspar Whitehead, under the supervision of Dr Richard Tse. These synthetic procedures were modified and optimised, and unless stated otherwise, all other syntheses and studies presented in this chapter were performed by my own hands.*

of these complexes. Initial efforts targeted [2]rotaxane synthesis through an active-metal templated CuAAC reaction, requiring the synthesis of porphyrin bis-azide and bulky stopper alkyne axle precursors, and a pyridyl macrocycle capable of endotopic coordination of the Cu(I) catalyst.

2.2.1 Synthesis of Bis-azido Functionalised Metalloporphyrins

Two regioisomeric *para*- and *meta*-bis-azido functionalised zinc(II) metalloporphyrin axle precursors were synthesised (Scheme 2.1). The appropriate 3- and 4-bromomethyl benzaldehyde compounds were prepared by reduction of the corresponding benzonitrile precursors with diisobutylaluminium hydride (DIBAL-H), according to modified literature procedures.[22, 23] The bromomethyl products were substituted by an S_N2 reaction with sodium azide to form 3- and 4-azidomethyl benzaldehyde. The Brønsted acid-promoted condensation of the corresponding aldehyde with 1,1-di(pyrrol-1-yl)methane in the presence of catalytic trifluoroacetic acid (TFA),[24] followed by stoichiometric oxidation with 2,3-dichloro-5,6-dicyano-1,4-benzoquinone (DDQ), afforded the *para*- and *meta*-azido-functionalised porphyrins, *p*-**2.1·H₂** and *m*-**2.2·H₂** respectively, in good yields, which could, pleasingly, be isolated by precipitation from a saturated DCM solution by addition of methanol.

Complexation of the free-base porphyrins with zinc(II) acetate dihydrate in 1:1 *v/v* DCM:MeOH afforded the target metalloporphyrins *p*-**2.1·Zn** and *m*-**2.2·Zn** in quantitative yields. Complete metalation of the ligand was confirmed by high-resolution ESI mass spectrometry (HR-ESI-MS) and by the absence of the characteristic porphyrin free base ^{1}H NMR resonance at *c.* -3 ppm in the spectra of the metalloporphyrins (Figure 2.7).[25]

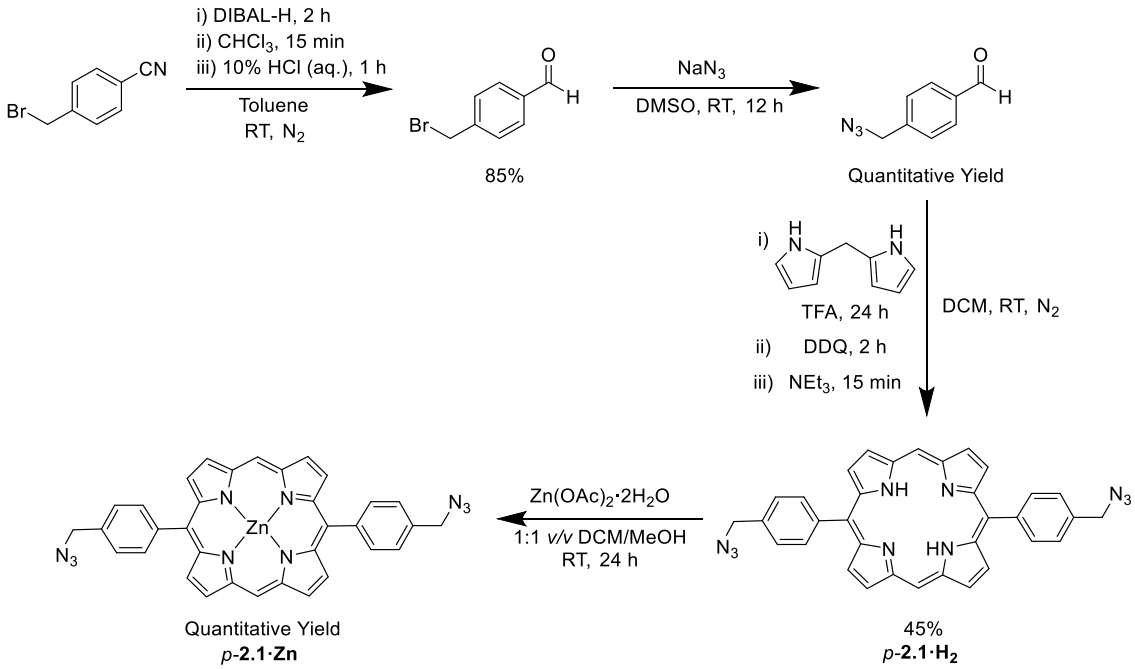

Scheme 2.1. Synthesis of *p*-**2.1·Zn**. The same methodology applied to 3-bromomethyl benzonitrile affords *m*-**2.2·Zn** with similar yields in each step.

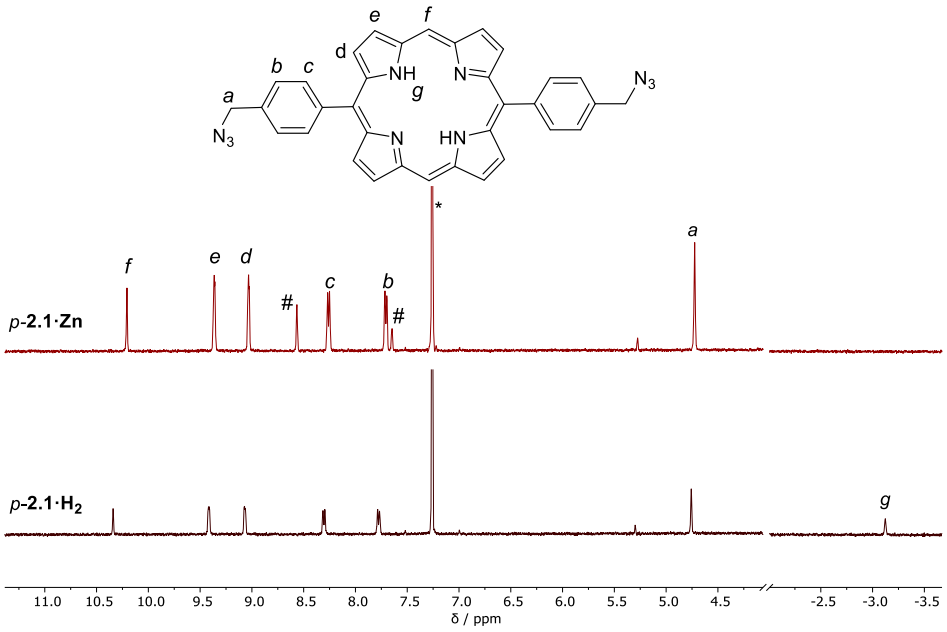

Figure 2.7. ^{1}H NMR (400 MHz, $CDCl_3$, 298 K) spectra of *p*-**2.1·Zn** and *p*-**2.1·H$_2$** showing the aromatic and free base proton regions. Pyridine-d_5 added to *p*-**2.1·Zn** to inhibit solution-phase aggregation. Residual protio solvent resonances denoted: $CDCl_3$: *, pyridine-d_5: #.

2.2.2 Active Metal Templated Synthesis of Initial Rotaxanes

To confirm the ability of the bis-azide functionalised metalloporphyrins *p*-**2.1·Zn** and *m*-**2.2·Zn** to form interlocked structures through a CuAAC active metal templation approach, their incorporation into rotaxane structural frameworks was explored by AMT reaction with the pyridyl macrocycle **2.3**. The macrocycle **2.3** was prepared by the reaction of 4-hydroxybenzyl alcohol with pentaethylene glycol ditosylate under basic acetonitrile solution conditions, followed by pseudo high-dilution Williamson ether synthesis ring-closing reaction with 2,6-bis-bromomethylpyridine in the presence of the strong base NaH to form the target macrocycle **2.3** in 38% yield, following purification by column chromatography (Scheme 2.2).

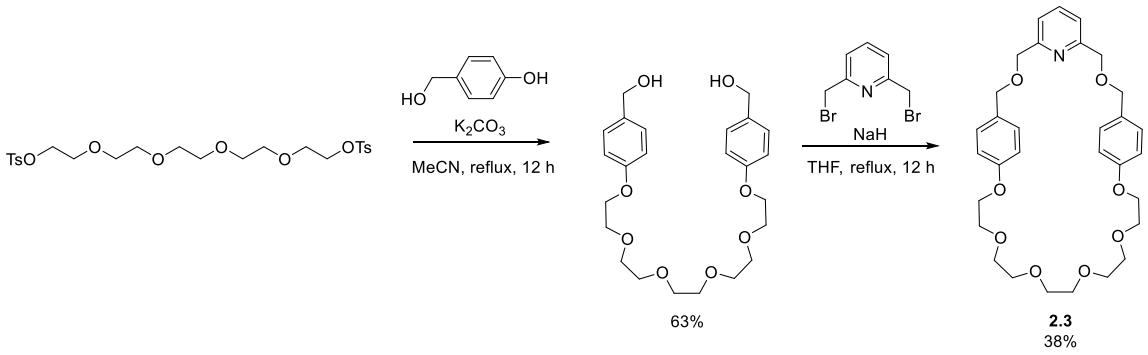

Scheme 2.2. Synthesis of pyridyl macrocycle **2.3**.

With the target metalloporphyrin azides and pyridyl macrocycle in hand, the AMT rotaxane synthesis was performed (Scheme 2.3). In a typical reaction, one equivalent of the Cu(I) catalyst, $[Cu(MeCN)_4]PF_6$, was precomplexed with macrocycle **2.3** by stirring in 1,2-dichloroethane (DCE) for 15 min. The resulting solution was added to a DCE solution containing a three-fold excess of the corresponding bis-azido metalloporphyrin and a six-fold excess of the sterically bulky terphenyl stopper-alkyne **2.4**,[26] at 60 °C under an N_2 atmosphere. Monitoring of the reaction by thin layer chromatography (TLC) confirmed complete consumption of the azide starting material after 3 days, and the formation of three new porphyrin-containing bands, identified by their purple

colouration, visible to the naked eye on the TLC plate. The Cu^{I} metal ion was sequestered from the products by washing with aqueous basic EDTA, and the three porphyrin-containing compounds isolated by repeated preparative TLC. ESI-MS identified the three porphyrin components as the non-interlocked axle, the target [2]rotaxane and serendipitously formed [3]rotaxane, in which two macrocycle units were threaded onto a single axle.

All three novel products were fully characterised by 1-D ^{1}H and $^{13}C\{^{1}H\}$ and 2-D ^{1}H-^{1}H NMR spectroscopy and by HR-ESI-MS, with HR-ESI-MS used to confirm the identity of the [2] and [3]rotaxanes (Figure 2.8).

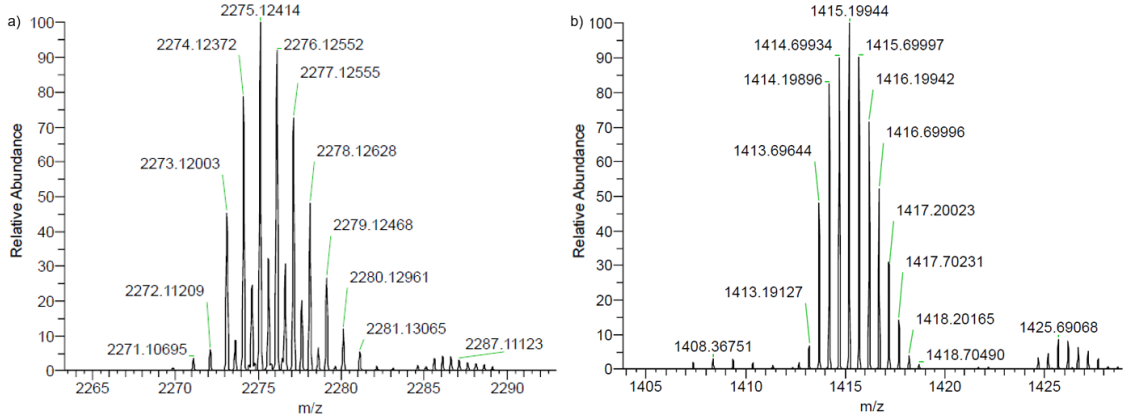

Figure 2.8. HR-ESI-MS spectra of a) ***p*-2·5a·Zn** and b) ***p*-2·5b·Zn**.
***p*-2·5a**: *m/z* calculated for $[C_{145}H_{154}N_{11}O_{10}Zn]^{+}$, $[M + H]^{+}$: 2274.1200, *m/z* found: 2274.1237.
***p*-2·5b**: *m/z* calculated for $[C_{176}H_{194}N_{12}O_{18}Zn]^{2+}$, $[M + 2H]^{2+}$: 1414.1974, *m/z* found: 1414.1990.
Minor peaks in a) likely due to the detection of doubly charged dimers.

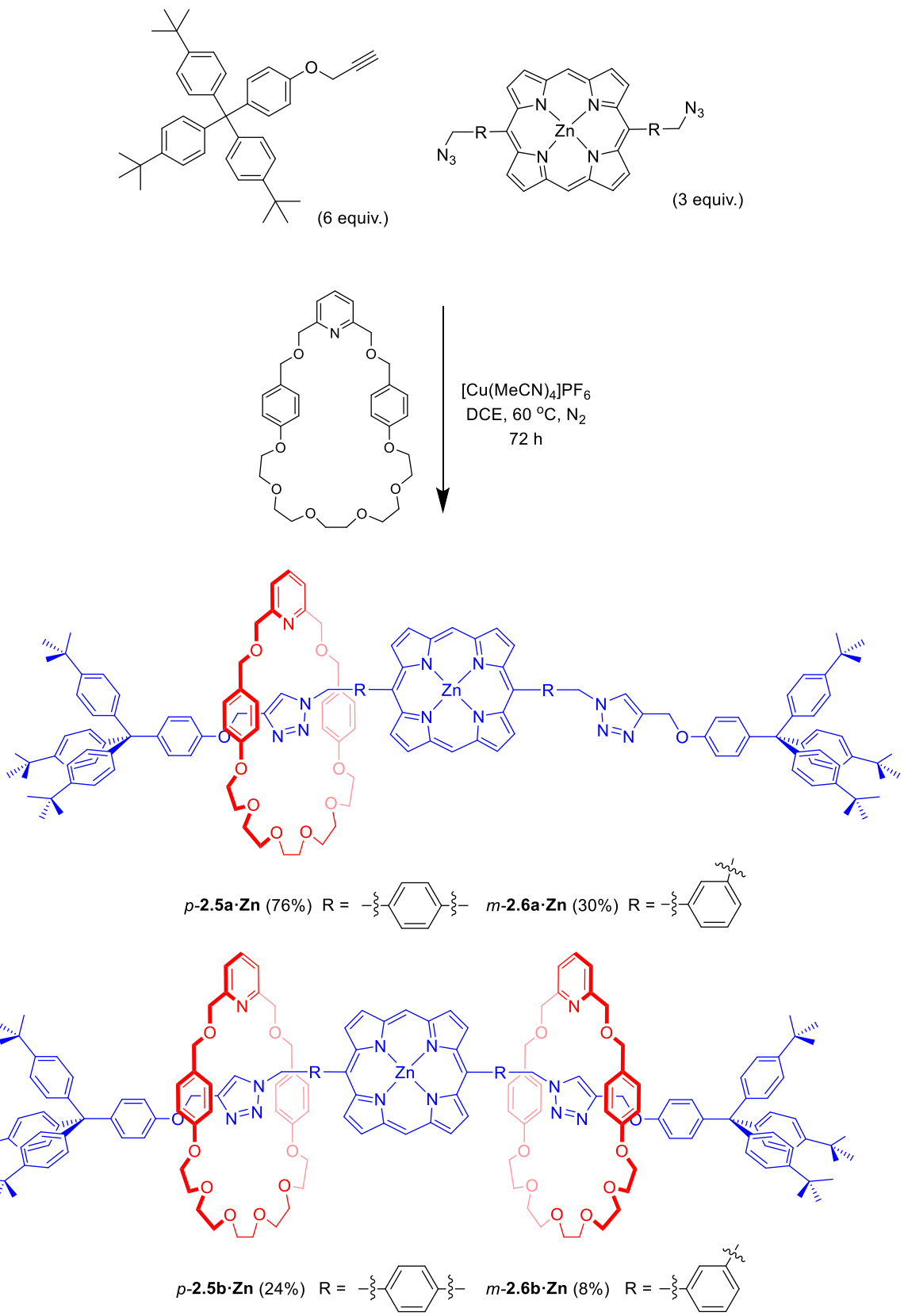

Scheme 2.3. Synthesis of [2]rotaxanes *p*-**2.5a·Zn** and *m*-**2.6a·Zn**, and [3]rotaxanes *p*-**2.5b·Zn** and *m*-**2.6b·Zn**.

The interlocked nature of the rotaxanes *p*-**2.5a·Zn** and *p*-**2.5b·Zn** was confirmed by comparison of their ^{1}H NMR spectra with those of the non-interlocked axle component *p*-**2.5c·Zn** and the macrocycle **2.3**.

The ^{1}H NMR spectrum of the *para*-[2]rotaxane *p*-**2.5a·Zn** possesses several significant changes relative to the non-interlocked axle component, strongly evidencing rotaxane formation (Figure 2.9). Notably, the axle phenyl protons *4* and *5* possess significant downfield shifts in the [2]rotaxane compared to the free axle. Such an effect is likely observed as a result of interactions between these protons and the aromatic ring currents of the macrocycle phenyl groups. Correspondingly, the aromatic macrocycle protons *e* and *f* both possess a significant upfield shift ($\Delta\delta \approx 0.25$ ppm), consistent with shielding due to π-π interactions between the interlocked components. The significant broadening of the axle methylene signals *6* and *8*, and the disappearance of the triazole signal *7*, are indicative of translocation of the macrocycle along the axle. The overall spectrum is consistent with C_s molecular symmetry, indicating this shuttling to be in fast-exchange with respect to the NMR timescale. As a result of these data, further studies were performed on the dynamics of the interlocked systems (*vide infra*).

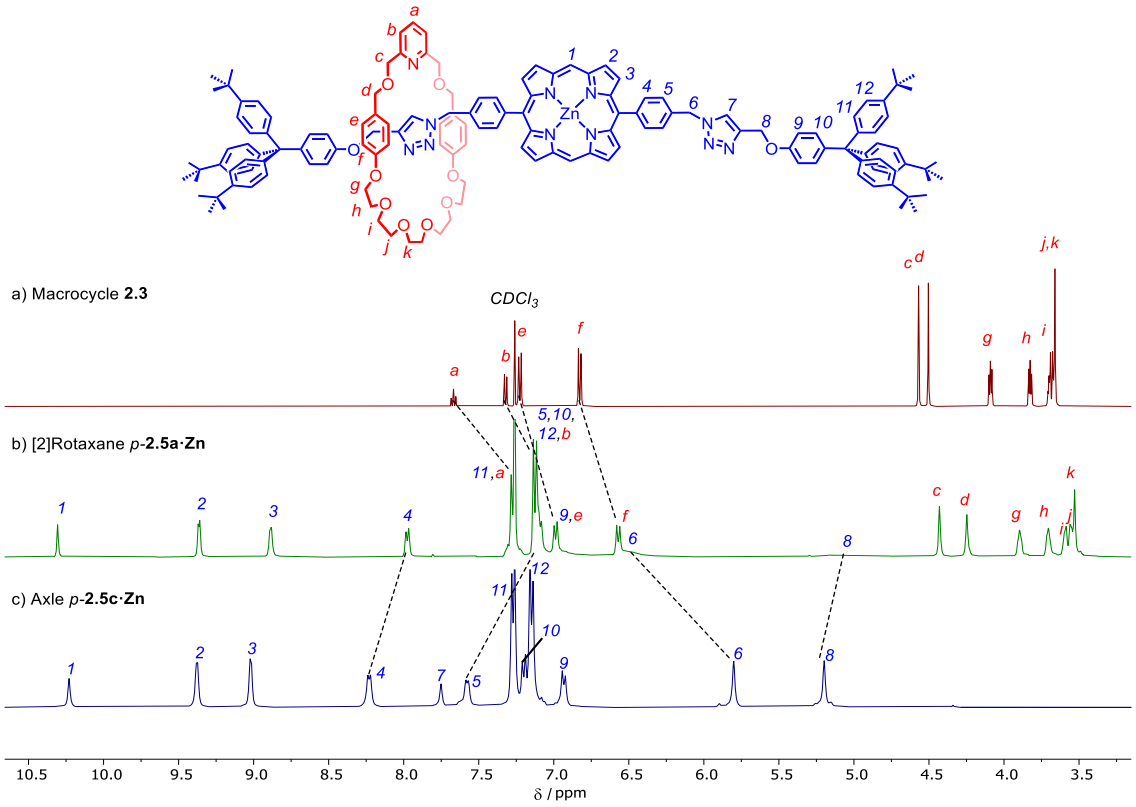

Figure 2.9. Stacked ^{1}H NMR spectra (400 MHz, $CDCl_3$, 298 K) of a) macrocycle **2.3**, b) [2]rotaxane *p*-**2.5a·Zn** and c) non-interlocked axle *p*-**2.5c·Zn**.

Similar diagnostic changes were observed in the ^{1}H spectrum of the *para*-[3]rotaxane *p*-**2.5b·Zn** (Figure 2.10). In contrast to the [2]rotaxane spectrum, the axle methylene signals *6* and *8*, and triazole signal *7*, are all sharp and resolved. This is consistent with more limited dynamic behaviour as translocation of the macrocycle over the central porphyrin is now inhibited by the presence of a second macrocycle. Macrocycle protons *d*, *g* and *h* have complex multiplicities due to the mutual effect of one macrocycle on the other. Of particular note is the remarkable 100% overall interlocked product yield for the synthesis of *p*-**2.5a·Zn** and *p*-**2.5b·Zn**, which is significantly higher than previously reported AMT reactions (*vide infra*).[27-29]

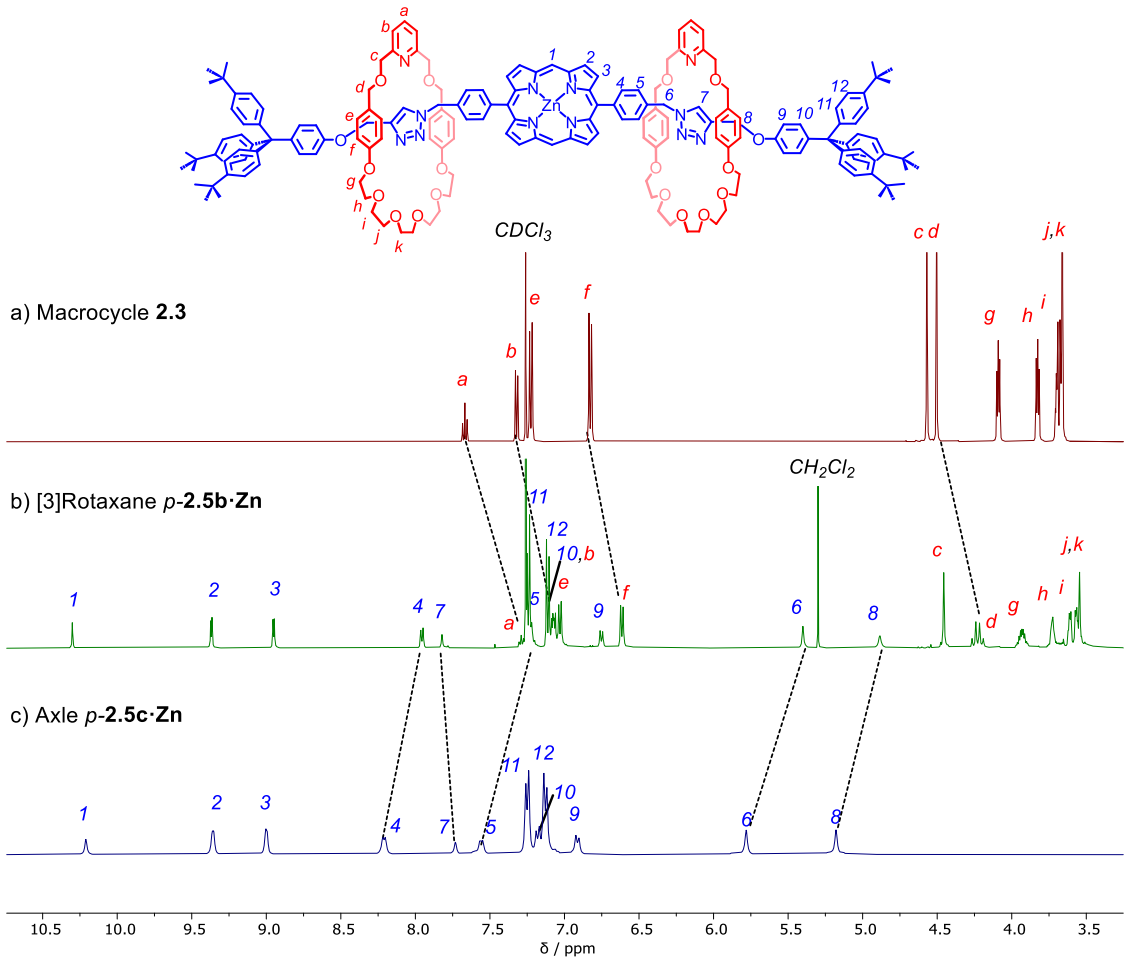

Figure 2.10. Stacked ^{1}H NMR spectra (400 MHz, $CDCl_3$, 298 K) of a) macrocycle **2.3**, b) [3]rotaxane *p*-**2.5b·Zn** and c) non-interlocked axle *p*-**2.5c·Zn**.

The *meta*-analogue of the [2]rotaxane, *m*-**2.6a·Zn**, displayed a similar ^{1}H NMR spectrum indicating dynamic behaviour; however, the macrocycle resonances *e* and *f* were split into complex multiplets, indicating significant desymmetrisation (Figure 2.11). It is postulated this desymmetrisation arises from a greater kinetic barrier to shuttling. The *meta*-[3]rotaxane, *m*-**2.6b·Zn**, displayed a highly asymmetric ^{1}H spectrum, likely due to the adoption of multiple co-conformations and the mutual perturbation of each macrocycle on the other's chemical environment.

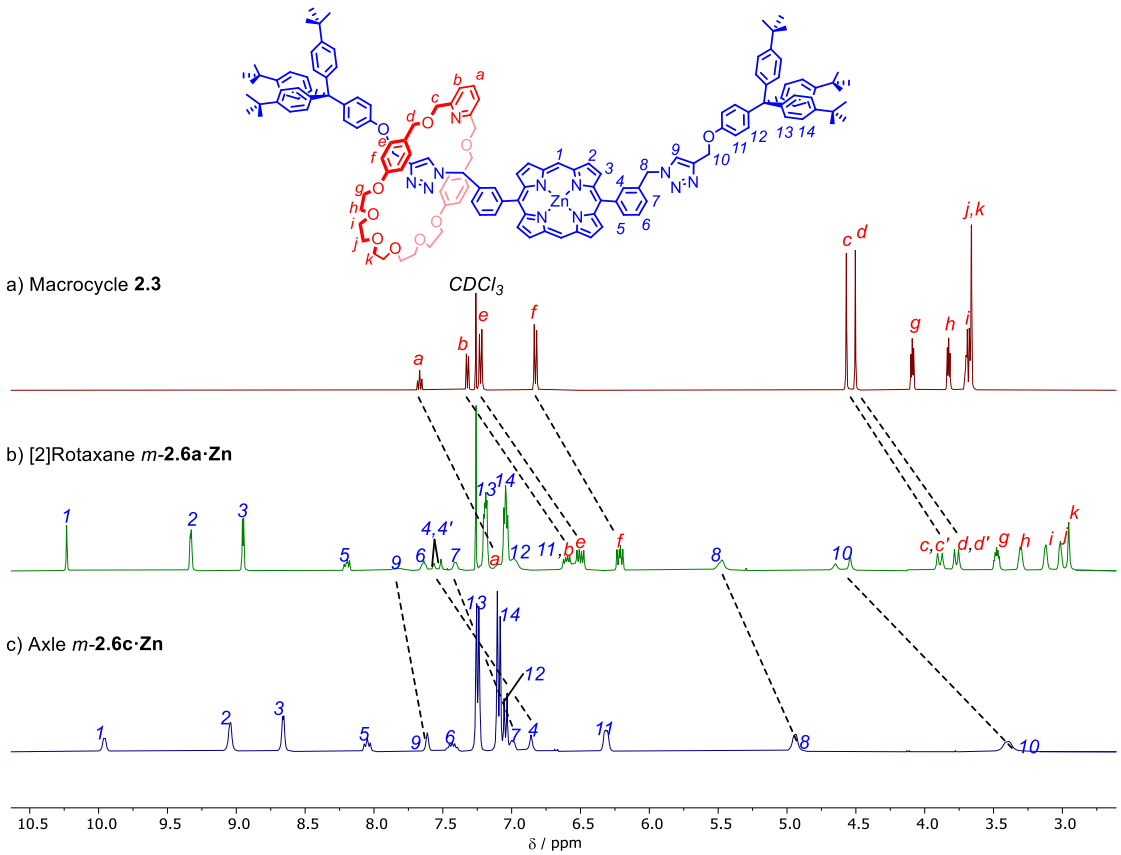

Figure 2.11. Stacked ^{1}H NMR spectra (400 MHz, $CDCl_3$, 298 K) of a) macrocycle **2.3**, b) [2]rotaxane *m*-**2.6a·Zn** and c) non-interlocked axle *m*-**2.6c·Zn**.

2.2.3 UV-visible and Fluorescence Optical Characterisation

The UV-visible and fluorescence spectral properties of [2]rotaxane and non-interlocked axle products *p*-**2.5a·Zn** and *p*-**2.5c·Zn** were determined in acetone. In the UV-visible absorption spectra, both compounds displayed the expected pattern of a sharp Soret-band peak and two broader Q-bands, consistent with a metalloporphyrin species.[30] The Soret-band of the rotaxane displayed a marked bathochromic shift compared to the free axle, consistent with the presence of a MIM inter-component axial interaction between the macrocycle pyridyl ligand and the Lewis acidic Zn(II) centre (Figure 2.12).

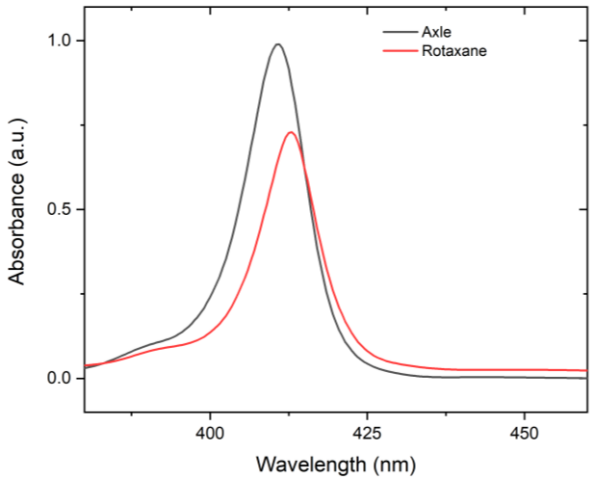

Figure 2.12. UV-visible spectra of the Soret absorption region of 2 μM solutions of [2]rotaxane *p*-**2.5a·Zn** and non-interlocked axle *p*-**2.5c·Zn** in acetone.

Given the apparent inter-component interaction demonstrated by the Soret band bathochromic shift in the UV-visible spectrum of *p*-**2.5a·Zn**, it was expected that the emission intensity of the [2]rotaxane should be lower than the free axle, consistent with axle coordination by the macrocycle pyridyl group leading to partial quenching of the fluorescence. Indeed, this expected trend was observed in the non-competitive solvent acetone (Figure 2.13 a).

Surprisingly, in 1:1 *v/v* acetonitrile:chloroform, the non-interlocked axle displayed lower fluorescence than the [2]rotaxane. This is strongly indicative that the axial-coordination of the porphyrin by the macrocycle is severely disrupted in this solvent system (Figure 2.13 b), likely due to the ability of acetonitrile to compete with the macrocycle in coordinating to the Zn(II) centre.[31]

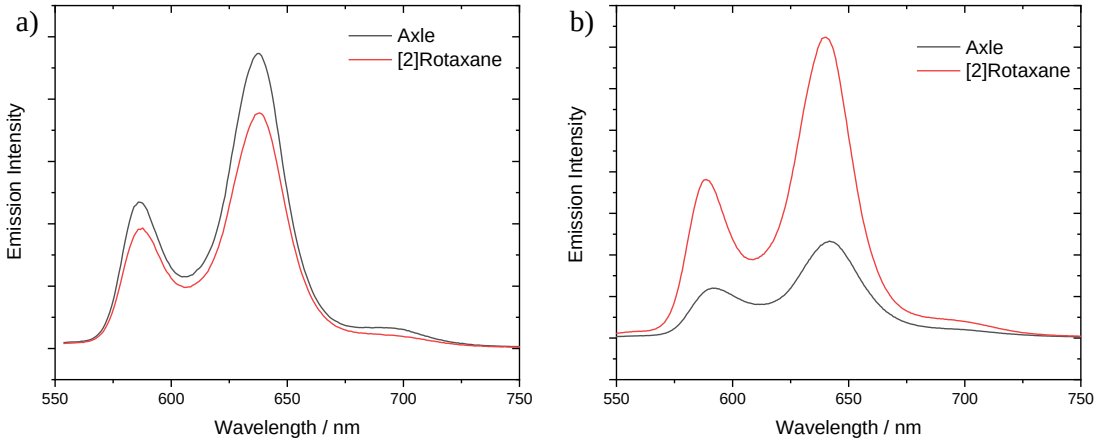

Figure 2.13. Emission (10 μM) spectra of solutions of [2]rotaxane *p*-**2.5a·Zn** and non-interlocked axle *p*-**2.5c·Zn** in a) acetone b) 1:1 *v/v* chloroform:acetonitrile. Excitation at the Soret band peak.

2.3 Investigation of Rotaxane Inter-component Interactions

The effect of the significant inter-component interaction of the macrocycle pyridyl nitrogen with the axle Lewis acidic Zn(II) metalloporphyrin centre, as demonstrated by the preliminary optical studies of the rotaxanes and axles, was further studied with a view to understanding the effects of this interaction on MIM co-conformational dynamic behaviour.

2.3.1 Effect of a Competing Solvent

As the fluorescence spectra measured in 1:1 *v/v* acetonitrile:chloroform suggested significant solvent-Zn(II) metalloporphyrin interaction, the ^{1}H NMR spectra of *p*-**2.5a·Zn** and *m*-**2.6a·Zn** in solutions of varying $CDCl_3$:CD_3CN ratios were recorded to elucidate the effects of competitive solvent binding on the [2]rotaxane co-conformational dynamism. It was expected that the ability of acetonitrile-d_3 to interact with the Zn(II) centre would attenuate the macrocycle-axle interaction and result in faster shuttling motion on the NMR timescale and improved resolution of the axle proton resonances. Increasing the proportion of CD_3CN to 50% *v/v* for *p*-**2.5a·Zn** led to the axle resonance

8 becoming visible and beginning to sharpen (Figure 2.14). Unfortunately, the poor solubility of *p*-**2.5a·Zn** in acetonitrile prevented studies at higher acetonitrile proportions.

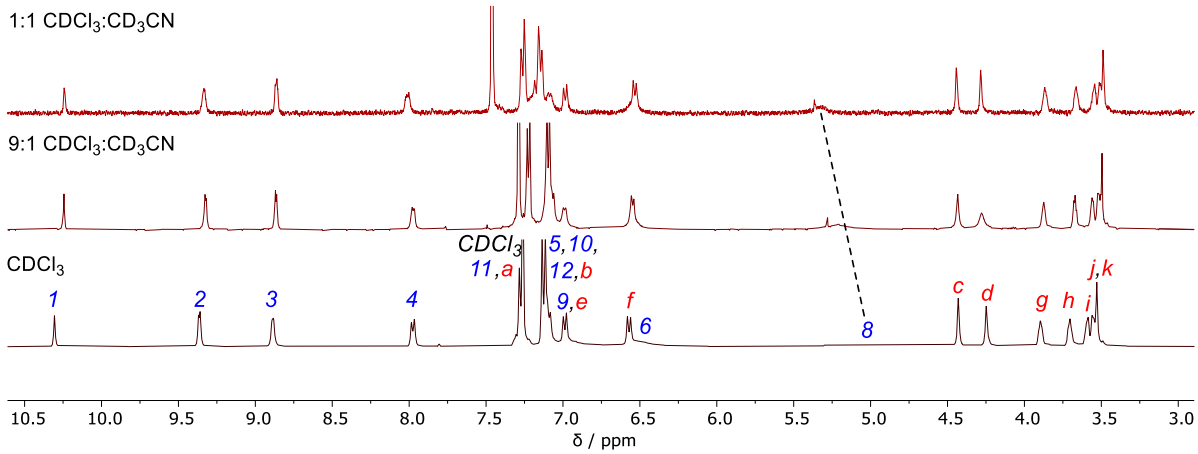

Figure 2.14. ^{1}H NMR (500 MHz, 298 K) spectra of *p*-**2.5a·Zn** measured in varying solvent systems. All ratios expressed as *v/v* ratios.

The increased solubility of the *meta*-[2]rotaxane *m*-**2.6a·Zn** enabled studies with in to 70% CD_3CN (Figure 2.15). As for the *para* isomer, the NMR spectra were consistent with faster macrocycle translocation at increasing acetonitrile concentration. This was particularly pronounced in the case of macrocycle resonances *c* and *d*, which coalesce into singlets at high percentage CD_3CN composition. The importance of the Zn(II)···pyridyl interaction (or lack thereof) for the inter-component dynamics is highlighted by the changes seen even at the axle periphery of the rotaxane molecule, with signal *15*, corresponding to the axle ^{t}Bu groups, coalescing at high CD_3CN concentration.

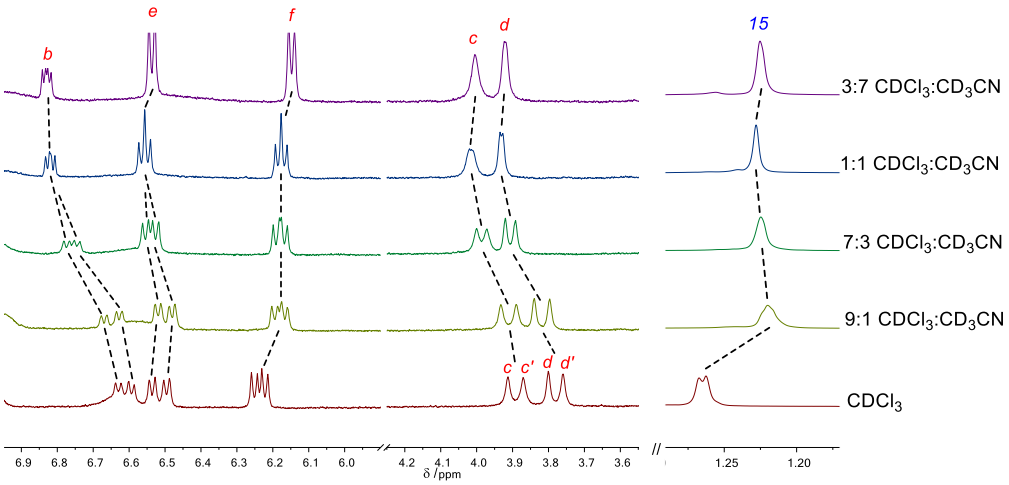

Figure 2.15. ^{1}H NMR (500 MHz, 298 K) spectra of *m*-**2.6a·Zn** measured in varying solvent systems. All ratios expressed as *v/v* ratios.

2.3.2 Effect of a Competing Ligand

Given the proven effect of a coordinating solvent on the co-conformational dynamism of the [2]rotaxane interlocked systems, the effect of addition of an exogeneous competitive ligand was investigated to further evidence interruptions to the pyridyl···Zn(II) interaction being the origin of the changes in the optical and ^{1}H NMR spectra of the interlocked molecules.

In chloroform, the Soret and Q bands of the [2]rotaxane *p*-**2.5a·Zn** displayed a small bathochromic shift compared with the non-interlocked axle *p*-**2.5c·Zn**, with the Soret band shifting from 408 to 410 nm (Figure 2.16). As the optical activity of the metalloporphyrin originates from the macrocycle π system of the porphyrin, and the macrocycle hydroquinone groups are largely in an orthogonal plane and thus would not be expected to strongly influence the optical activity of the porphyrin,[32] this shift can be attributed to the weak coordination of the macrocycle pyridyl nitrogen to the Zn(II) centre.

Pleasingly, upon addition of excess pyridine (py), a neutral ligand which is known to coordinate strongly to Zn(II) porphyrins to give five-coordinate complexes (K_a > 10^4 M^{-1}),[33] to chloroform solutions of the rotaxane ***p*-2.5a·Zn** and axle ***p*-2.5c·Zn**, both the axle and [2]rotaxane underwent a further bathochromic shift to 418 nm. The observed shifts to a common wavelength value are strongly indicative of the saturation of both Zn(II) metalloporphyrin centres with pyridine.

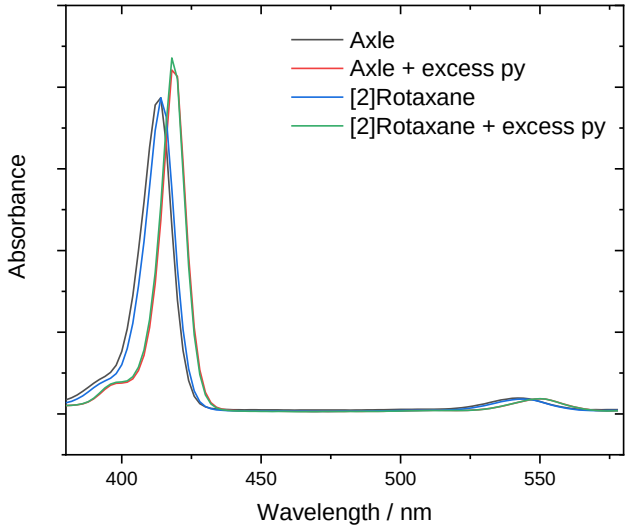

Figure 2.16. UV-visible spectra (2 μM, $CHCl_3$) of the Soret and Q band absorption regions of solutions of [2]rotaxane ***p*-2.5a·Zn** and non-interlocked axle ***p*-2.5c·Zn** in the presence and absence of excess pyridine.

It was expected that under such a pyridine-saturated regime, the macrocycle would reside over the axle triazole motif of the [2]rotaxane, the pyridine acting as a 'molecular brake' with coordination to the Zn(II) metalloporphyrin attenuating the co-conformational dynamics of the system.[34] In order to probe this, a ^{1}H NMR titration of a $CDCl_3$ solution of ***p*-2.5a·Zn** upon successive addition of 1 mM pyridine-d_5 was performed (Figure 2.17). Upon addition of excess pyridine, the axle resonances became highly asymmetric, indicative of the macrocycle now being 'trapped' on one side of the central porphyrin as the axial pyridine ligand prevented translocation of the macrocycle. In particular, the large downfield shift of one of the axle triazole signals, relative to the other (*7*, *7'*: $\Delta\delta \approx$

0.75 ppm), concomitant with the splitting of methylene signals adjacent to the triazole (*6*, *6'* and *8*, *8'* $\Delta\delta \approx 0.5$ ppm), are strongly indicative of the macrocycle residing close to one of the rotaxane's two triazole axle moieties. The lack of macrocycle translocation in the [3]rotaxanes, inferred earlier by the higher resolution of the ^{1}H spectra of the [3]rotaxane *p*-**2.5b·Zn** and attributed to translocation being inhibited by the mutual repulsion of the two macrocycles, was confirmed by the lack of observed desymmetrisation in the NMR spectrum of *p*-**2.5b·Zn** upon addition of excess pyridine-d_5.

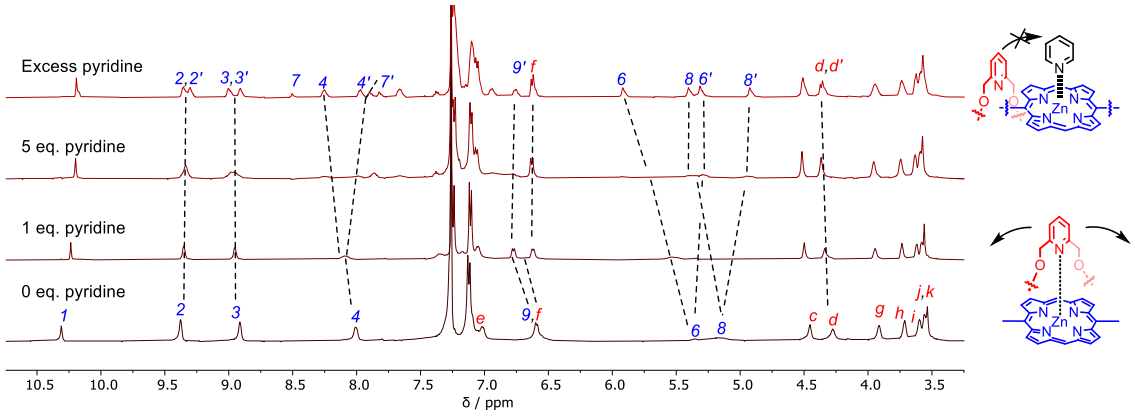

Figure 2.17. Truncated ^{1}H NMR spectra (500 MHz, $CDCl_3$, 298 K) of *p*-**2.5a·Zn** upon successive addition of py-d_5. RHS: Representative illustration of 'molecular brake' behaviour of axial py-d_5 ligand.

2.3.3 Synthesis of Demetallated [2]Rotaxanes

In order to confirm that the origin of the rotaxane inter-component macrocycle pyridyl···zinc(II) metalloporphyrin axle interaction was a Lewis acid-base association, rather than π-π interactions, the dynamic properties of the demetallated porphyrin-containing [2]rotaxane congener *p*-**2.5a·H$_2$** were investigated. Addition of TFA to a solution of *p*-**2.5a·Zn** in DCM afforded, after 2 h, the free-base porphyrin-containing [2]rotaxane *p*-**2.5a·H$_2$** in 91% yield (Scheme 2.4). Demetalation was confirmed by the presence of the characteristic free base porphyrin N*H* proton resonance at *c.* −3 ppm in the ^{1}H NMR spectrum of *p*-**2.5a·H$_2$** (Figure 2.18) and by HR-ESI-MS. The increased rate

of macrocycle translocation upon removal of Zn(II), as evidenced by the resolution of axle proton resonances *7* and *5*, suggests the Zn(II) metalloporphyrin···pyridyl interactions substantially retard the dynamic motion of the system. This phenomenon may be regarded as a neutral analogue of the 'molecular speed bump' behaviour reported by Stoddart and co-workers, who have previously employed electrostatic repulsions between a positively-charged cyclobis(paraquat-*p*-phenylene)macrocycle and axle positively-charged bipyridinium motifs to retard shuttling between two macrocycle binding sites.[35]

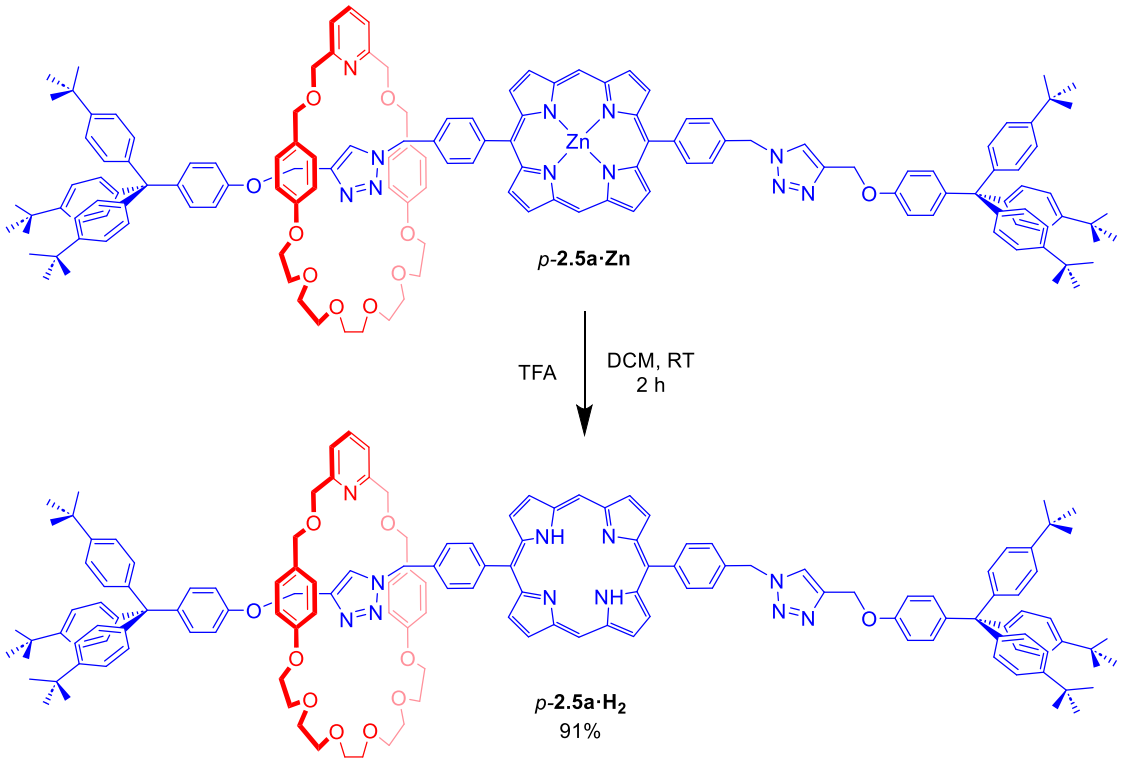

Scheme 2.4. Synthesis of free base porphyrin-containing [2]rotaxane ***p*-2.5a·H$_2$**.

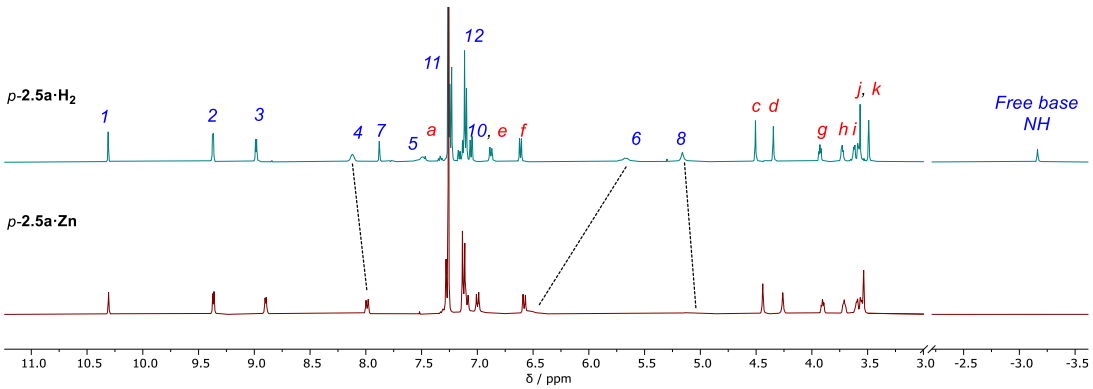

Figure 2.18. Stacked ^{1}H NMR spectra (400 MHz, $CDCl_3$, 298 K) [2]rotaxanes *p*-**2.5a·Zn** and *p*-**2.5a·H$_2$**.

To further confirm the increased freedom of the macrocycle to translocate over the demetallated porphyrin, variable-temperature ^{1}H NMR spectroscopic studies were undertaken, with fast exchange being observed down to 241 K at 1 mM in $CDCl_3$, evidencing a much lower barrier to shuttling than in *p*-**2.5a·Zn**, where the dynamic motion of the rotaxane displayed a coalescence temperature of 262 K (*vide infra*).

The clear hypsochromic shift of the Soret band *p*-**2.5a·H$_2$** compared to the metalloporphyrin was discernible to the naked eye and was confirmed by UV-visible spectroscopy in $CHCl_3$ (Figure 2.19). This shift can be attributed to a greater HOMO-LUMO gap in the free base porphyrin which lacks the HOMO destabilisation in the dianionic metalloporphyrin ligand.[36, 37] The optical spectra show an increase in the splitting of the Q band from two peaks to four. This change is attributed to the local symmetry of the porphyrin being broken by the presence of two NH protons (D_{4h} to D_{2h}) such that the *x*- and *y*- plane vibrations of the porphyrin are no longer degenerate.[30]

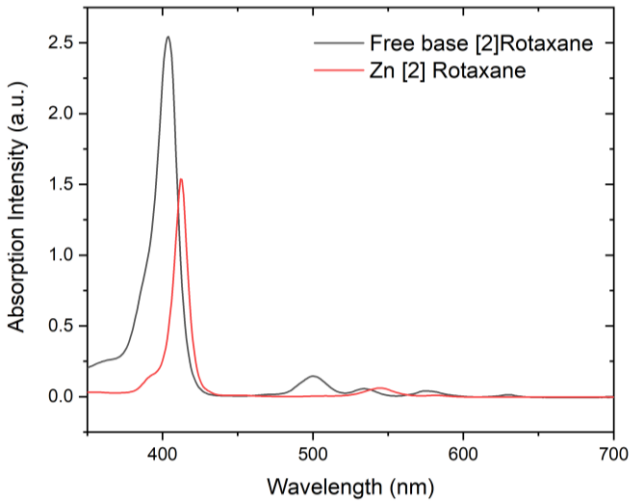

Figure 2.19. UV-visible spectra (2 μM, $CHCl_3$) of the Soret and Q band absorption of solutions of *p*-**2.5a·Zn** and *p*-**2.5a·H₂**.

2.3.4 Variation of Metalloporphyrin Metal Centre

The spectroscopic properties of the free-base rotaxane *p*-**2.5a·H₂** clearly demonstrated the influence of the presence or absence of the metal-pyridyl interaction on [2]rotaxane co-conformation. To further explore this effect, the substitution of Zn(II) with Ni(II) and Cd(II) was explored. Ni(II) exhibits a preference for square planar geometry and as such *p*-**2.5a·Ni** would be expected to behave similarly to the free base rotaxane *p*-**2.5a·H₂**,[38] lacking the readily available axial coordination site of Zn(II) metalloporphyrins, while the increased Lewis acidity of Cd(II) would be expected to retard macrocycle translocation to a greater extent than Zn(II).[39]

The free-base rotaxane *p*-**2.5a·H₂** was metallated by refluxing a DMF solution of *p*-**2.5a·H₂** with the corresponding metal acetate, $Ni(OAc)_2{\cdot}4(H_2O)$ or $Cd(OAc)_2{\cdot}2(H_2O)$, for 4 hours, and the crude product purified by preparative TLC affording *p*-**2.5a·Ni** with a yield of 87% (Scheme 2.5). Metalation was confirmed by HR-ESI-MS and the absence of the free-base proton resonance in the ^{1}H NMR spectrum. Unfortunately, the Cd(II) metalloporphyrin product *p*-**2.5a·Cd** was unable to be isolated by preparative TLC or by size-exclusion chromatography, likely due to the kinetic lability of Cd(II)

metalloporphyrins, wherein the Cd(II) is too large to fit in the porphyrin binding cavity and so resides out of the ligand plane, resulting in weaker complexation.[40, 41] The non-interlocked axle *p*-**2.5c·Ni** was obtained in high (92%) overall yield by analogous TFA-induced demetalation of *p*-**2.5c·Zn** followed by metalation.

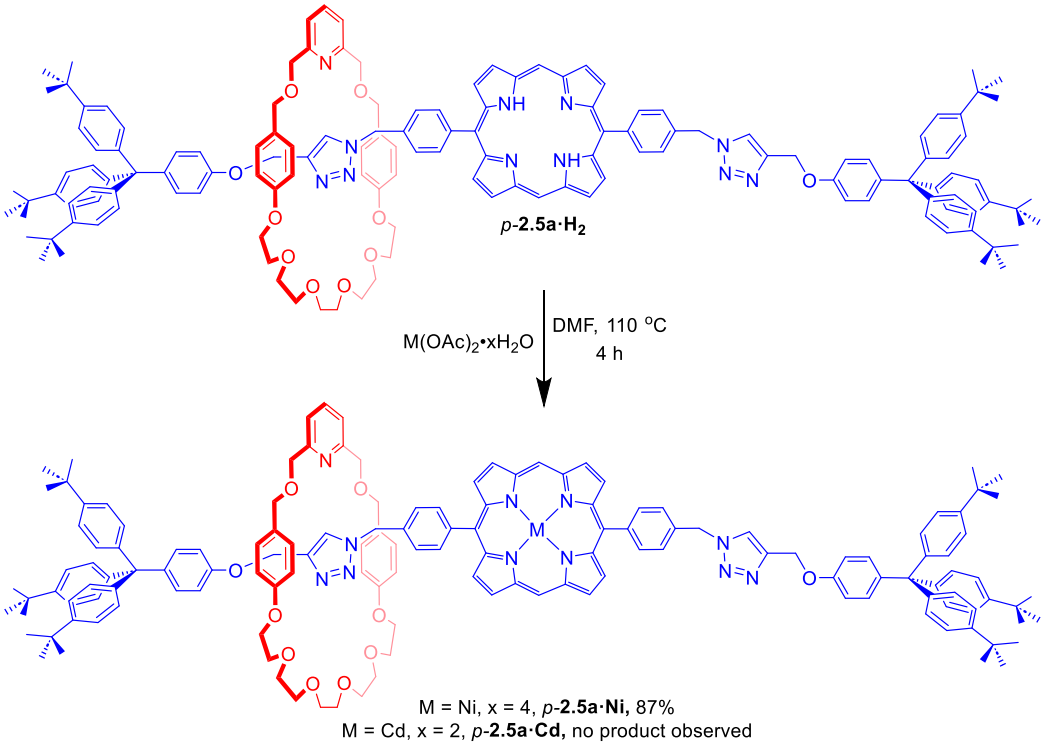

Scheme 2.5. Synthesis of *p*-**2.5a·Ni** and attempted synthesis of *p*-**2.5a·Cd**.

The ^{1}H NMR spectrum of *p*-**2.5a·Ni** was similar to *p*-**2.5a·H$_2$**, consistent with the rapid translocation of the macrocycle across the Ni(II) metalloporphyrin core, indicating only very weak pyridyl-Ni(II) interactions (Figure 2.20 a) The UV-visible spectra of *p*-**2.5a·Ni** and *p*-**2.5c·Ni** showed no significant bathochromic shift in their Soret-band (λ_{max} = 398 nm in $CHCl_3$ for both compounds), further evidencing the lack of significant inter-component interaction (Figure 2.20 b), consistent with previous reports of the instability of 5-coordinate Ni(II) porphyrin species.[42, 43]

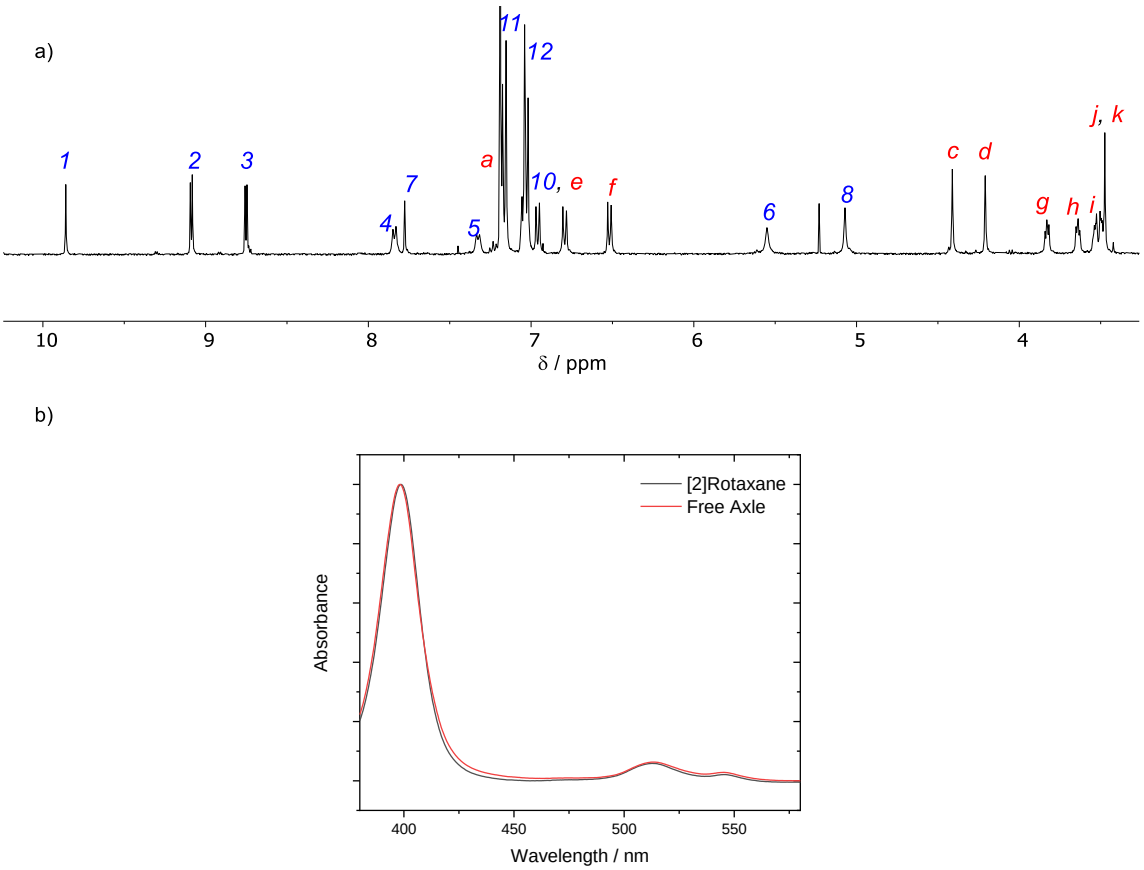

Figure 2.20. a) ^{1}H NMR (400 MHz, $CDCl_3$, 298 K) of *p*-**2.5a·Ni**. b) UV-visible spectra (2 μM, $CHCl_3$) of the Soret and Q band absorption of solutions of *p*-**2.5a·Ni** and *p*-**2.5c·Ni**.

2.3.5 Quantification of Macrocycle Shuttling Activation Parameters

In order to quantify the strength of Zn(II) metalloporphyrin···pyridyl interaction in each of the MIM systems, variable temperature ^{1}H NMR spectroscopic studies were performed to determine the thermodynamic activation parameters of the dynamic translocation of the macrocycle in the metallated and demetallated [2]rotaxanes. At higher temperatures, when translocation of the macrocycle over the porphyrin core is rapid on the NMR timescale, the spectra were highly symmetric, whereas desymmetrisation of the axle and macrocycle resonances is observed at lower temperatures where the rate of shuttling becomes slow on the NMR timescale (Figure 2.21).

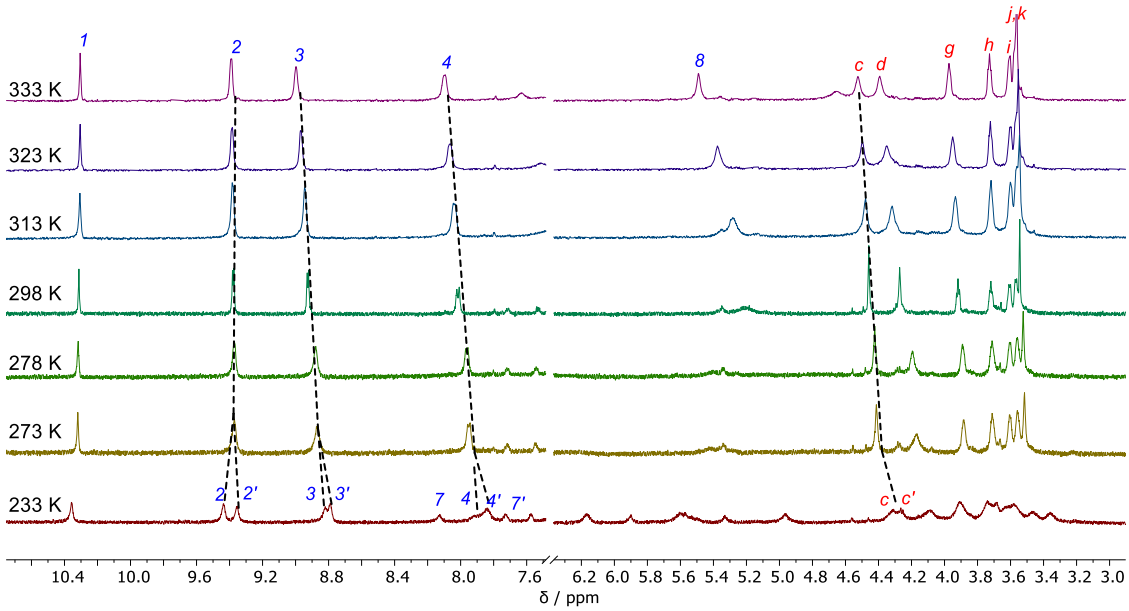

Figure 2.21. ^{1}H NMR spectra (500 MHz, $CDCl_3$) of *p*-**2.5a·Zn** at varied temperature.

Rotaxane *p*-**2.5a·Zn** displayed coalescence of the porphyrin resonances at 262 K, whereas in the absence of the macrocycle pyridyl···Zn(II) interaction, *p*-**2.5a·H$_2$** required cooling to 241 K in order to observe coalescence. The rate constants *k* for the shuttling motion were calculated by analysis of the frequency gap between resonances of exchanging nuclei (in the slow-exchange regime) and line width (in the fast exchange regime) at the various temperatures.[44] This enabled calculation of the thermodynamic activation parameters for the process according to the Eyring equation (Equation 2.1).[45]

$$k = \frac{\kappa k_B T}{h} e^{\frac{\Delta S^{\ddagger}}{R}} e^{-\frac{\Delta H^{\ddagger}}{RT}}, \qquad (2.1)$$

where: R = gas constant, k_B = Boltzmann constant, h = Planck constant. Transmission coefficient, κ, assumed to be unity.

From Equation 2.1:

$$\ln\frac{k}{T} = \frac{-\Delta H^{\ddagger}}{RT} + \ln\frac{\kappa k_B}{h} + \frac{\Delta S^{\ddagger}}{R}, \qquad (2.2)$$

Thus, a graph of ln(k/T) against 1/T (Figure 2.22) enables the calculation of the enthalpy and entropy of activation ($\Delta H^{\ddagger}$ and $\Delta S^{\ddagger}$, respectively) for each rotaxane (Table 2.1).

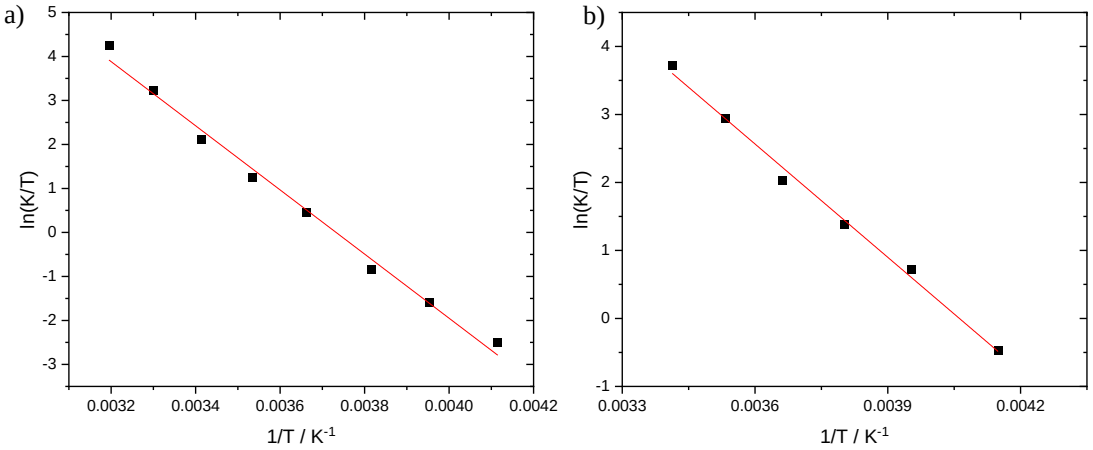

Figure 2.22. Eyring plots for the rate of macrocycle translocation in a) *p*-**2.5a·Zn** b) *p*-**2.5a·H₂** at 1 mM in $CDCl_3$.

	T_c (K)	$\Delta H^{\ddagger}$ (kJ mol^{-1})	$\Delta S^{\ddagger}$ (J K^{-1} mol^{-1})
p-**2.5a·Zn**	262	61	29
p-**2.5a·H₂**	241	46[a]	-10
p-**2.5a·Ni**	238	42	-21
m-**2.6a·Zn**	255	49	-20

Table 2.1. Thermodynamic parameters for macrocycle shutting in [2]rotaxanes, calculated from variable temperature ^{1}H NMR spectroscopic studies at 1 mM in $CDCl_3$. T_c denotes coalescence temperature. Transmission coefficient, κ, assumed to be unity. Errors < 5% unless stated otherwise. [a]Error <10%

As expected, the enthalpy of activation for macrocycle translocation in *p*-**2.5a·Zn** indicates an endothermic process, as the pyridyl···Zn(II) interaction is lost upon macrocycle shuttling. The relatively low magnitude of $\Delta H^{\ddagger}$ highlights the non-covalent nature of the interaction, which is facilitated by the mechanical bond. As expected, $\Delta H^{\ddagger}$ is of significantly smaller magnitude for the free-base rotaxane *p*-**2.5a·H₂** as the energy barrier posed by overcoming the Zn(II)···pyridyl interaction no longer has to be overcome on shuttling, and for the Ni(II) rotaxane is consistent with the preference of Ni(II) to remain square planar, and thus not interact significantly with the macrocycle pyridyl. Interestingly, a markedly lower $\Delta H^{\ddagger}$ for the *meta* geometry rotaxane, *m*-**2.6a·Zn**, over the

para congener *p*-**2.5a·Zn** was observed, likely due to subtle steric effects disfavouring the macrocycle···porphyrin interaction.

Discussion of the entropies of activation is more complex. The positive entropy of activation for *p*-**2.5a·Zn** likely arises from macrocycle translocation causing deviation from the dominant co-conformation in which axial coordination of the Zn(II) by the macrocycle pyridyl limits the co-conformational freedom of the macrocycle. For the other calculated systems, wherein a weaker Zn(II) metalloporphyrin···pyridyl interaction occurs, as evidenced by the lower calculated $\Delta H^{\ddagger}$ values, and hence lower co-conformational bias, the negative entropy of activation likely arises from the loss of macrocycle conformational freedom upon passing over the widest part of the axle – the metalloporphyrin core. Such an observation is in keeping with the report by Silvi and co-workers of negative entropy of activation for the shuttling of a DB24C8 macrocycle over an axle amide group,[46] which necessitated rigidification of the crown ether core. These negative entropies of activation vary within a narrow range, with the variation likely due to complex factors, such as solvation of the rotaxanes in solution.

2.3.6 Calculation of Co-conformational Bias

It was of interest to quantify the bias for the 'resting state' co-conformation, in which the macrocycle pyridyl is coordinated to the vacant Zn(II) axial coordination site. Quantitative UV-visible absorption titrations of the rotaxanes and corresponding free axles with pyridine enabled the binding constants of pyridine to both the rotaxanes and non-interlocked axles (K_{rot} and K_{ax} respectively). Assuming the same binding mode of pyridine and the macrocycle pyridyl to the Zn(II) centre, the equilibrium constant for formation of the 'resting state', K_{rs}, can be calculated by equation 2.3 (Figure 2.23):[47]

$$K_{rs} = \frac{K_{ax}}{K_{rot}} - 1 \qquad (2.3)$$

where K_{ax} is the binding constant for pyridine to the axle, and K_{rot} for pyridine to the [2]rotaxane (Figure 2.23).

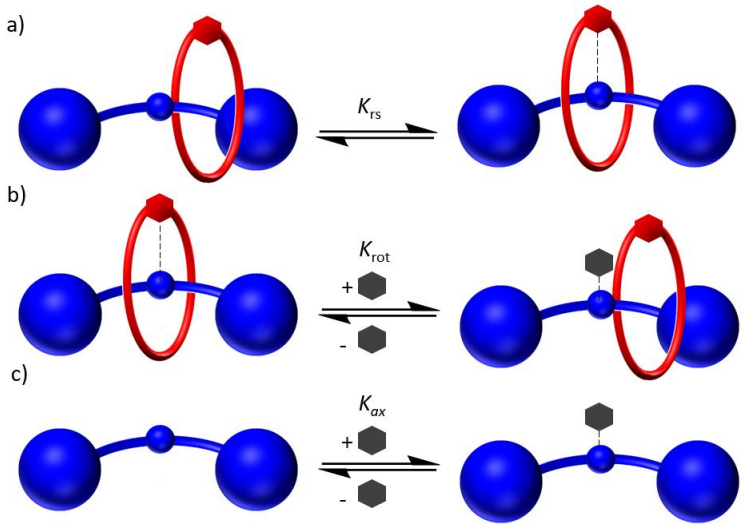

Figure 2.23. Cartoon depiction of the equilibria in equation 2.3.

	K_{ax} (M^{-1})	K_{rot} (M^{-1})	K_{rs} (M^{-1})	% 'resting state co-conformation'
***p*-2.5a·Zn**	7630	2850	1.7	63
***m*-2.6a·Zn**	5560	4810	0.15	15

Table 2.2. Binding constants and %self-inclusion calculated from titration of 25 mM pyridine solution with 7.5 μM ***p*-2.5a·Zn** and ***m*-2.6a·Zn** in $CHCl_3$. Errors in experimental binding constants < 10%. T = 298 K.

As expected from the VT-NMR studies, there is a significant inter-component interaction, resulting in co-conformational bias for the 'resting state' co-conformation in ***p*-2.5a·Zn**, with a 63% co-conformational occupancy calculated from the K_{rs} value, compared with only 15% occupancy in the *meta* isomer (Table 2.2). This is consistent with the greater enthalpic penalty for shuttling in ***p*-2.5a·Zn**, compared with ***m*-2.6a·Zn**. It is particularly noteworthy that the shuttling activation enthalpy of ***m*-2.6a·Zn** approaches that of ***p*-2.5a·H$_2$**, in which no inter-component coordination, and hence no co-conformational bias, is observed. The presence of a strong inter-component interaction in ***p*-2.5a·Zn** may

be used to tentatively rationalise the appreciable 24% yield of the higher order [3]rotaxane *p*-**2.5b·Zn**, and the overall 100% MIM product yield in the synthesis of *p*-**2.5a·Zn** and *p*-**2.5b·Zn**. It is postulated that this rotaxination proceeds through a pseudo[2]rotaxane intermediate, in which one of the two CuAAC stoppering reactions has proceeded, catalysed through Cu^{I} bound in the macrocycle interior. The inter-component pyridyl···Zn(II) interaction retards macrocycle translocation, such that the second stoppering reaction is completed by a separate Cu(I)-complexed macrocycle, resulting in the formation of the higher order [3]rotaxane *p*-**2.5b·Zn** in significant yield (Figure 2.24).

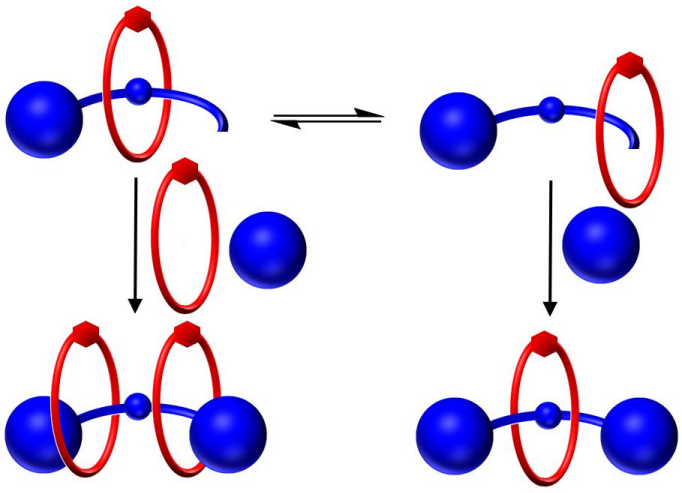

Figure 2.24. Cartoon depiction of pathways to [2] and [3]rotaxane formation during AMT reactions.

2.4 Anion Binding Studies

Given the proven Lewis acidity of the metalloporphyrin-containing interlocked structures, and their ability to bind neutral pyridine, the binding of the Lewis acidic centre to halides was investigated through the UV-visible host-guest spectroscopic titration of the [2]rotaxane *p*-**2.5a·Zn** and guest halide salts with the non-coordinating tetrabutylammonium (TBA) counterion. Initial studies were performed in 1:1 *v/v* chloroform:acetonitrile, as the variable solvent composition ^{1}H NMR studies indicated

the dynamic motion of the [2]rotaxane was in the intermediate regime in this solvent system. Unfortunately, upon serial addition of a 100 mM TBACl or TBABr solution into 2 μM *p*-**2.5a·Zn** solution no significant perturbations were observed in either the Soret band absorption or emission spectra, likely due to competitive binding of the MeCN solvent to the Zn(II) centre.

To confirm the observed lack of binding arose from solvent-competition, and not due to the macrocycle binding to the porphyrin and inhibiting halide coordination, the titrations were repeated with the non-interlocked axle *p*-**2.5c·Zn** and again no significant perturbations in the optical spectra were observed. The lack of binding in this solvent medium is attributed to the competing effect of acetonitrile in the interaction of the macrocycle pyridyl N donor atom with the metalloporphyrin centre, as seen in the earlier variable solvent ^{1}H NMR studies.

In marked contrast, upon addition of TBAX (X = Cl, Br) solutions to *p*-**2.5a·Zn** dissolved in the less competitive solvent acetone, significant perturbations in the Soret band absorption spectra were observed, with a bathochromic shift arising from the axial coordination of the halide to the zinc metal centre (Figure 2.25). The presence of a clear isosbestic point evidences a 1:1 host:guest binding stoichiometry, consistent with the formation of a 5-coordinate Zn(II) metal centre. For iodide minimal change was observed, suggesting that I^- is too poor a Lewis base to bind appreciably to the Zn(II) centre.[48] Analysis of the UV-visible titration isotherms, using *Bindfit,*[49] revealed a trend in halide binding affinity, $Cl^- >> Br^- > I^-$, consistent with a Lewis acid-base interaction, in which the decreasing charge density of the halide ions down the group results in reduced binding affinities to a hard cation (Table 2.3). The observed trend is consistent with previously reported halide binding observed with tetraphenylporphyrin-Zn(II).[21]

Analogous titration experiments with the axle *p*-**2.5c·Zn** demonstrated the higher binding affinity of the non-interlocked axle for halides. Such a result is consistent with the rotaxane macrocycle acting as a competing ligand, inhibiting halide association. Indeed, the [3]rotaxane *p*-**2.5b·Zn** afforded yet lower binding constants than the [2]rotaxane, attributed to the presence of a second macrocycle increasing the effective concentration of the competing ligand at the metalloporphyrin centre.

Repeating the host-guest titrations with the *meta*-rotaxane analogue *m*-**2.6a·Zn** (Figure 2.26) revealed stronger halide binding (Table 2.4), despite the comparatively similar binding constants observed with the *para* and *meta* non-interlocked axles. Such an increase is likely consistent with the reduced Zn(II)···pyridyl interactions in the *meta*-rotaxane isomer, as quantified by the earlier VT-NMR studies, reducing the competition of the macrocycle for the Zn(II) axial coordination site.

UV-visible host-guest spectroscopic titrations with 2 μM *p*-**2.5a·Ni** and *p*-**2.5a·H$_2$** with 300 mM TBAX (X = Cl, Br, I) in acetone, showed no evidence of binding, even upon addition of *c.* 40,000 equivalents of halide. This is consistent with the lack of a facile 5th coordination site in these species.[42, 43]

	K_a (M^{-1})		
	***p*-2.5a·Zn**	***p*-2.5b·Zn**	***p*-2.5c·Zn**
Cl^-	660	550	910
Br^-	40	35	40
I^-	*a*	*a*	*a*

Table 2.3. Host–guest binding constants calculated by UV-visible titration of 2μM indicated host with 100 mM TBAX, X = Cl, Br, I solutions in acetone. Deviations in Soret band absorption upon binding fitted to a 1:1 host:guest stoichiometry. Errors <10%. *a* No binding observed. T = 298 K.

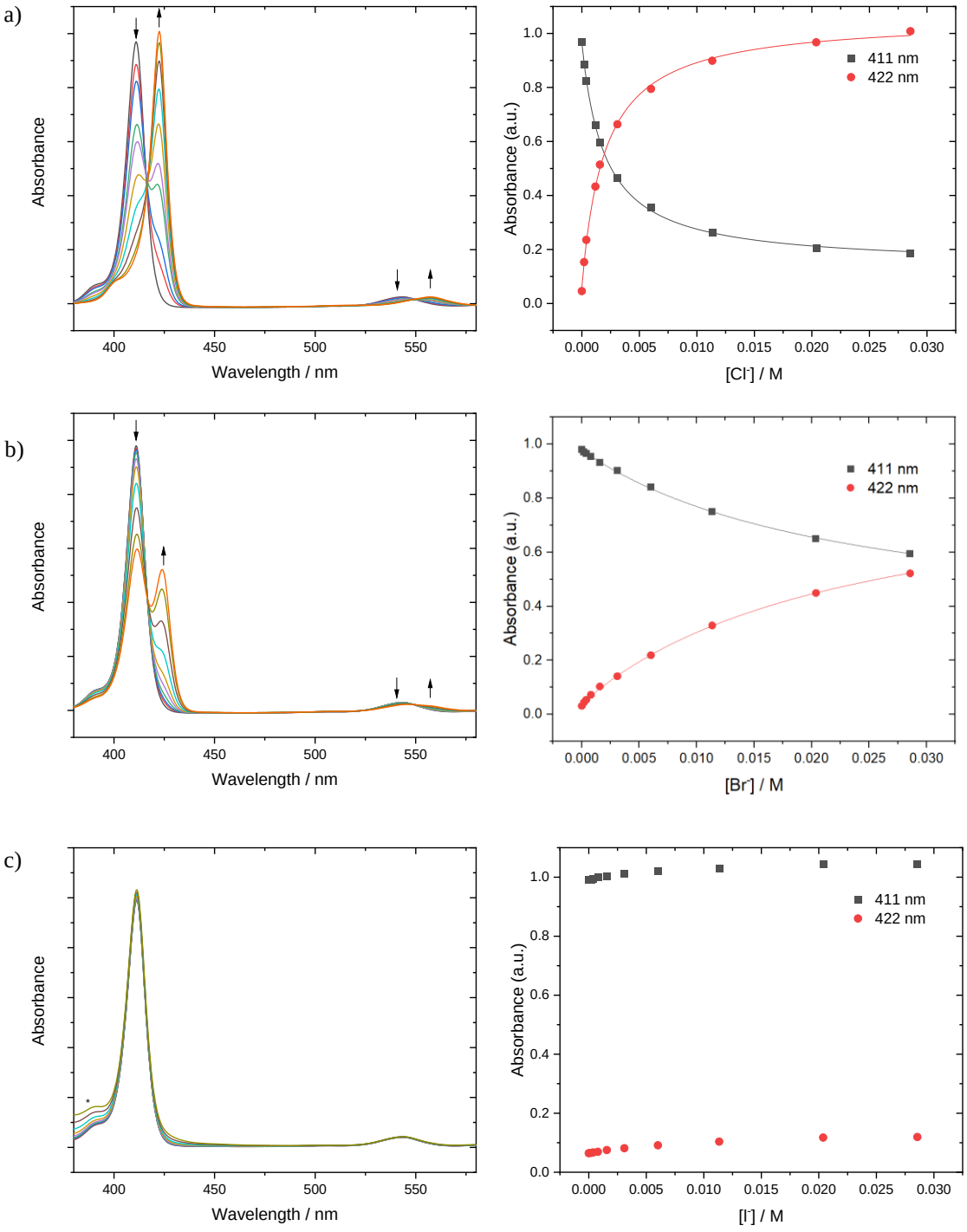

Figure 2.25. UV-visible spectra (2 μM, acetone) of the Soret and Q band absorptions of ***p*-2.5a·Zn**, upon successive additions of 100 mM TBAX a) X = Cl, b) X = Br, c) X = I, and corresponding binding isotherms. *Rise in low wavelength intensity in c) upon addition of TBAI solution attributed to formation of trace amounts of triiodide (I_3^-) species in TBAI solution.

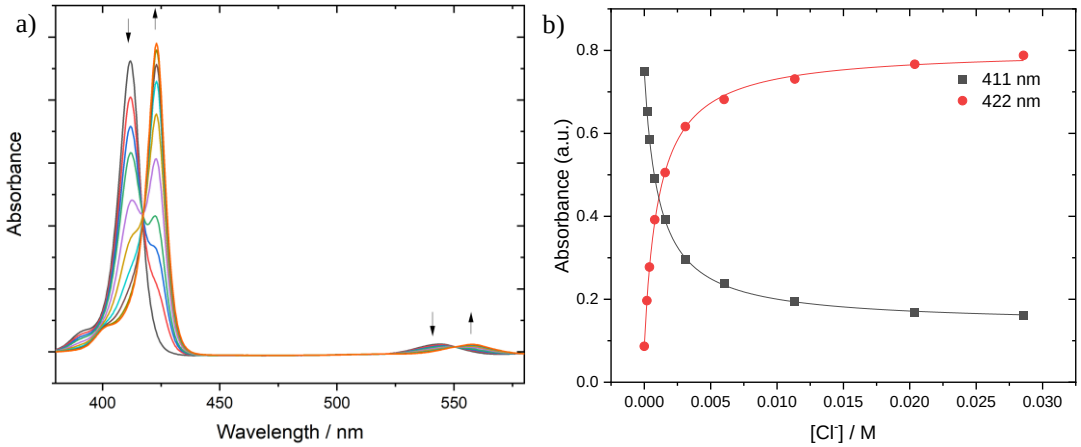

Figure 2.26. UV-visible spectra (2 μM, acetone) of the Soret and Q band absorptions of ***m*-2.6a·Zn**, upon successive additions of 100 mM TBACl and corresponding binding isotherm.

	K_a (M^{-1})		
	***m*-2.6a·Zn**	***m*-2.6b·Zn**	***m*-2.6c·Zn**
Cl^-	840	750	970
Br^-	40	30	40
I^-	*a*	*a*	*a*

Table 2.4. Host–guest binding constants calculated by UV-visible titration of 2μM indicated host with 100 mM TBAX, X = Cl, Br, I solutions in acetone. Deviations in Soret band absorption upon binding fitted to a 1:1 host:guest stoichiometry. Errors <10%. [a] No binding observed. T = 298 K.

The relatively weak halide binding necessitated the addition of large excesses of TBA halide for accurate binding constant determination (*c.* 15000 equivalents by the end of the titration). To discount changes in the ionic strength of the solution, arising from excess salt addition, as contributing to the perturbation of the observed spectra, an analogous titration experiment using the TBA salt of the non-coordinating hexafluorophosphate anion was performed.[50, 51] Reassuringly, only minimal changes to the spectra were observed (Figure 2.27 a).

Furthermore, to confirm the binding interaction as reversible Lewis acid-base association, silver(I) triflate, AgOTf, was added to the end solution of the TBACl/*p*-**2.5a·Zn** titration, Pleasingly, this resulted in AgCl precipitation, concomitant with a hypsochromic shift in the Soret band to the wavelength maximum to that of free *p*-**2.5a·Zn** (Figure 2.27 b), demonstrating halide binding to be a reversible process.

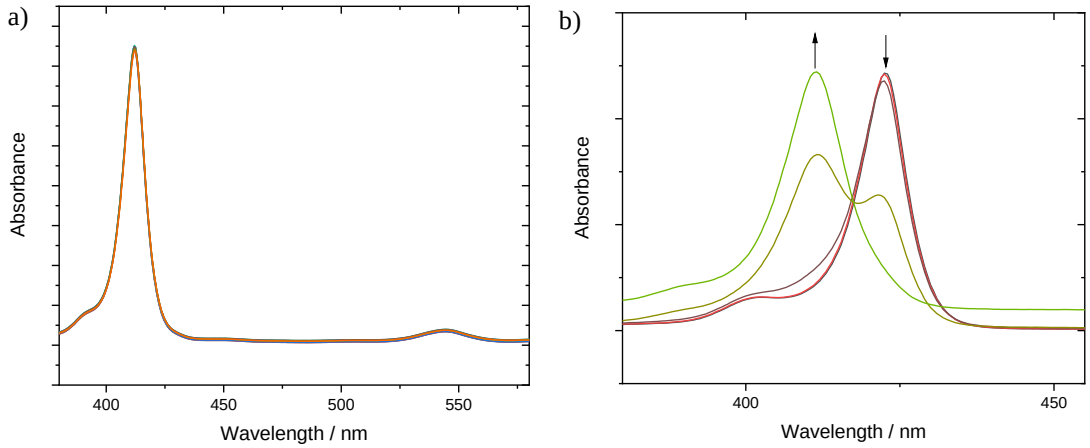

Figure 2.27. a) UV-visible spectra (2 μM, acetone) of a) the Soret and Q band absorption of *p*-**2.5a·Zn**, upon successive additions of 100 mM $TBAPF_6$, b) the Soret band of 2 μM *p*-**2.5a·Zn** solution with TBACl in acetone, upon successive addition of 100 μM AgOTf salt. Arrows indicate direction of change.

2.5 Preliminary Ion-Pair Binding Studies

The pyridyl group of the rotaxane macrocycle was expected to be capable of strong binding of exogeneous Zn^{2+} cations, competing with the inter-component pyridyl···Zn(II) metalloporphyrin interaction, thus reducing the occupancy of the Zn(II) metalloporphyrin by the macrocycle. Thus, significantly enhanced anion binding at the metalloporphyrin site was expected for binding in such an 'ion-pair' bound system, due to both favourable electrostatic interactions with the bound cation, and a positive allosteric effect in which coordination of exogeneous Zn^{2+}, between an axle triazole moiety and the macrocycle pyridyl, could induce a bias in the positioning of the macrocycle to reside at the triazole station, thus reducing the competition for halide binding at the metalloporphyrin centre (Figure 2.6 c). [52, 53]

Preliminary ^{1}H NMR titration studies with $Zn(ClO_4)_2$ were performed on *p*-**2.5a·Zn** in 1:1 *v/v* $CDCl_3$:CD_3CN. Sequential addition of Zn^{2+} to *p*-**2.5a·Zn** showed desymmetrisation of the axle, which was most pronounced in the axle *tert*-butyl groups (Figure 2.28). The perturbation gradually increased until 1.0 equivalent had been added, after which the spectra remained largely unchanged, indicating a near-quantitative binding of Zn^{2+} with a 1:1 host:guest binding stoichiometry. Furthermore, splitting and significant downfield shifts ($\Delta\delta > 0.15$ ppm) were observed for the macrocycle methylene proton *c*, and the axle methylene protons *6* and *8* and triazole proton *7*, strongly indicating participation of both the macrocycle pyridyl and axle triazole in the Zn^{2+} binding, and the translocation of the macrocycle to reside at the triazole binding station.

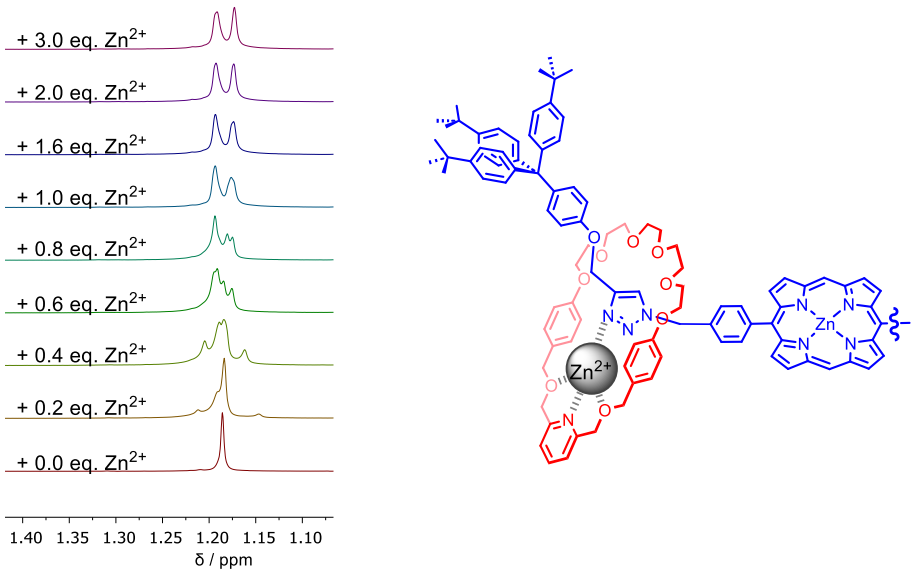

Figure 2.28. Truncated ^{1}H NMR spectra (500 MHz, 1:1 *v/v* $CDCl_3$:CD_3CN, 298 K) of *p*-**2.5a·Zn** showing stopper *tert*-butyl proton signal upon sequential additions of $Zn(ClO_4)_2$.

Encouraged by the observation of mechanical bond-enabled binding of Zn^{2+} in the cavity between the macrocycle pyridyl and axle triazole, it was of interest to investigate the subsequent recognition of anions at the exposed Zn(II) metalloporphyrin axle site. Qualitative sequential complexation experiments with both Zn^{2+} and TBABr were conducted on *p*-**2.5a·Zn** under analogous NMR conditions (Figure 2.29). Upon addition

of one equivalent of Zn^{2+} the spectra of both [2]rotaxanes became asymmetric, with particularly clear splitting of the porphyrin resonance *2*. Such splitting is consistent with the binding of Zn^{2+} between the pyridine bis-methanol macrocycle moiety and the triazole of the axle, inducing macrocycle shuttling to the triazole station and leading to an asymmetric spectrum by attenuation of the dynamic motion of the molecule. Subsequent addition of one equivalent of TBABr resulted in increased resolution of the porphyrin axle signals, providing strong evidence for the co-operative binding of both species.

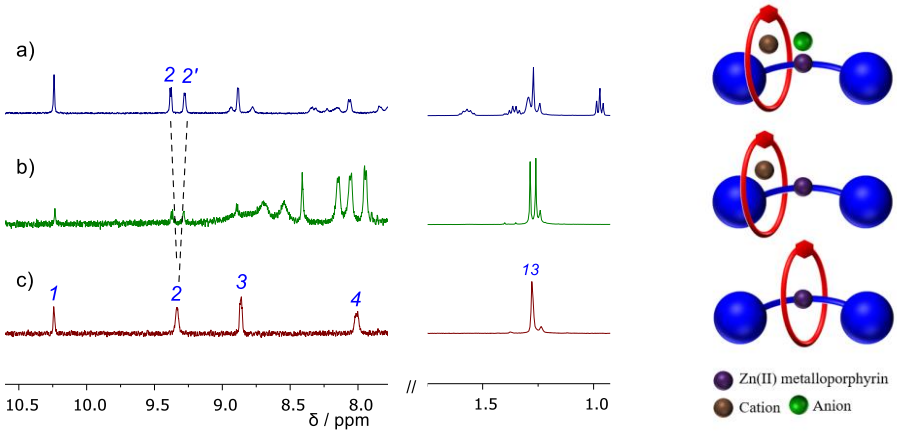

Figure 2.29. Truncated ^{1}H NMR spectra (500 MHz, 1:1 *v/v* $CDCl_3$:CD_3CN, 298 K) of [2]rotaxane *p*-**2.5a·Zn** with a) 1 equivalent of $Zn(ClO_4)_2$ and 1 equivalent of TBABr b) 1 equivalent of $Zn(ClO_4)_2$ c) free rotaxane *p*-**2.5a·Zn**.

To further elucidate the ion-pair binding ability of the rotaxanes, quantitative binding studies of TBAX (X = Cl, Br, I) to an equimolar solution of *p*-**2.5a·Zn** and $Zn(ClO_4)_2$ were conducted. As expected, significant perturbations in the ^{1}H NMR spectra of (*p*-**2.5a·Zn**)·Zn^{2+} were observed with increasing Br^- concentration up to one equivalent, however subsequent additions from 1.0–2.0 equivalents afforded no significant further perturbation. This provides strong evidence for a 1:1 binding stoichiometry of (*p*-**2.5a·Zn**)·Zn^{2+} host to Br^-, consistent with the ion-pair binding mode proposed. At higher concentrations of bromide, precipitation of $ZnBr_2$ became visibly noticeable in the sample and the spectra began to shift back to the free rotaxane spectrum (Figure 2.30).

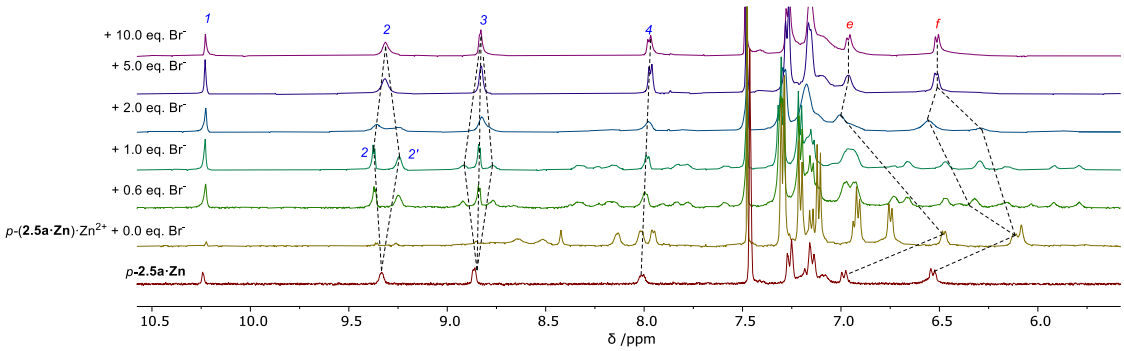

Figure 2.30. Truncated ^{1}H NMR spectra (500 MHz, 1:1 *v/v* $CDCl_3$:CD_3CN, 298 K) of Zn(II)-complexed [2]rotaxane (*p*-**2.5a·Zn**)·Zn^{2+} upon successive addition of TBABr.

2.6 Synthesis of a Heteroditopic Ion-Pair Binding Rotaxane

Armed with the promising preliminary evidence of the ability of *p*-**2.5a·Zn** to bind ion-pairs, a heteroditopic macrocycle-containing [2]rotaxane was targeted. It was hoped that such a macrocycle would better stabilise the bound ion-pair as an axle-separated ion-pair, overcoming the lattice enthalpies of metal halide salts which led to salt recombination with the first generation [2]rotaxane *p*-**2.5a·Zn**.

Such an approach was first reported by Knighton and Beer who utilised a heteroditopic macrocycle containing a 3-5-bis-amide pyridine anion binding motif and a calix[4]diquinone cation binding moiety together with an axle pyridine *N*-oxide component for the binding of alkali metal salts (Figure 2.31).[54]

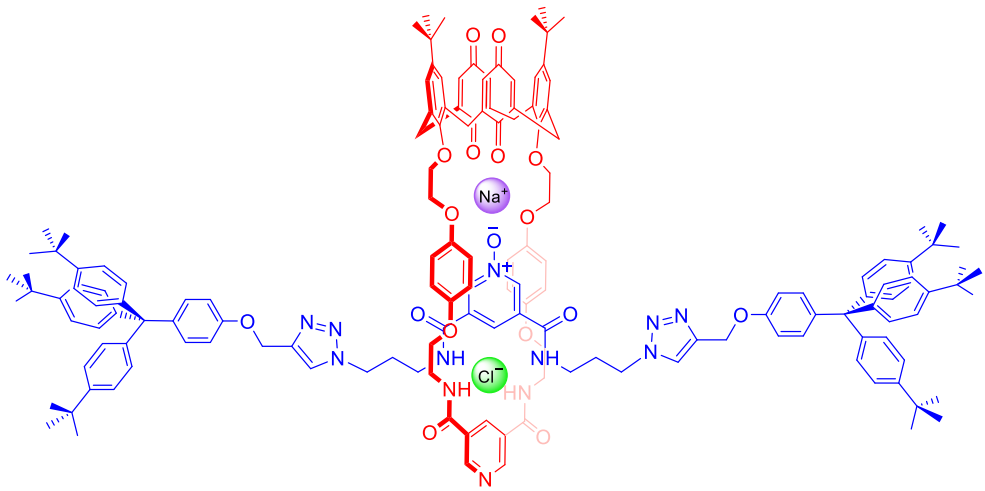

Figure 2.31. Heteroditopic [2]rotaxane reported by Knighton and Beer for alkali metal / halide ion-pair binding.

It was hoped that the incorporation of an XB bis-iodotriazole anion binding motif into a macrocycle containing the same pyridine bis-methanol cation binding motif as macrocycle **2.3** would enable enhanced ion-pair binding, in which a cation would be bound between the macrocycle pyridyl and axle triazole, and the anion bound by the macrocycle XB site.

2.6.1 Synthesis of a Halogen Bonding Heteroditopic Macrocycle

The synthesis of the target XB heteroditopic macrocycle **2.9** began with the initial preparation of bis-azide **2.7** from the commercially available hydroquinone bis(2-hydroxylethyl)ether (Scheme 2.6 a). Monotosylation of the hydroxyl groups with tosyl chloride (TsCl) under statistical conditions afforded the monotosylate in 36% yield which upon reaction with sodium azide in DMF gave the corresponding azide precursor.[55] Deprotonation of the remaining hydroxyl group using NaH in dry THF followed by reaction with 2,6-bis(bromomethyl)pyridine afforded the bis-azide, **2.7**, in 82% yield.[56]

The bis-iodo alkyne derivative **2.8** was prepared according to a literature procedure.[57] The Sonogashira reaction of 1,5-(bis-bromo)-3-*tert*-butylbenzene with trimethylsilylacetylene afforded the corresponding bis-TMS protected alkyne which could be readily iodinated with *N*-iodosuccinimide in the presence of silver nitrate to afford the target 1,5-bis(iodoethynyl)-3-*tert*-butylbenzene **2.8** in 89% yield (Scheme 2.6 b).

A Cu(I)-catalysed CuAAC click cyclisation reaction of **2.7** and **2.8** under high dilution conditions afforded macrocycle **2.9** in 32% yield after repeated preparative TLC purification (Scheme 2.6 c). The XB macrocycle was characterised by ^{1}H, ^{13}C{^{1}H} and ^{1}H-^{1}H NMR spectroscopy (Figure 2.32) and by HR-ESI-MS.

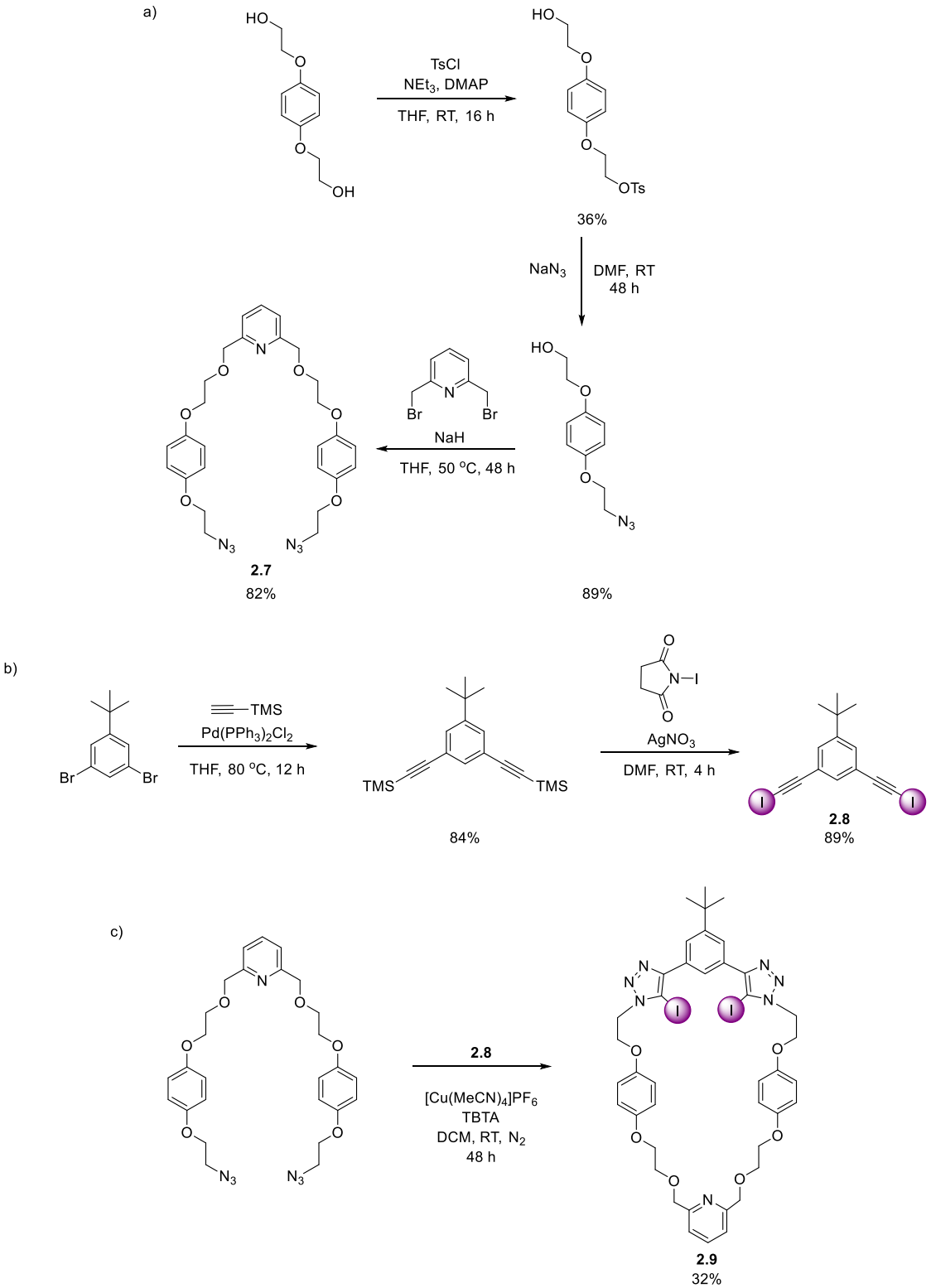

Scheme 2.6. Synthesis of a) bis-azide **2.7**, b) bis-iodoalkyne **2.8** and c) macrocycle **2.9**.

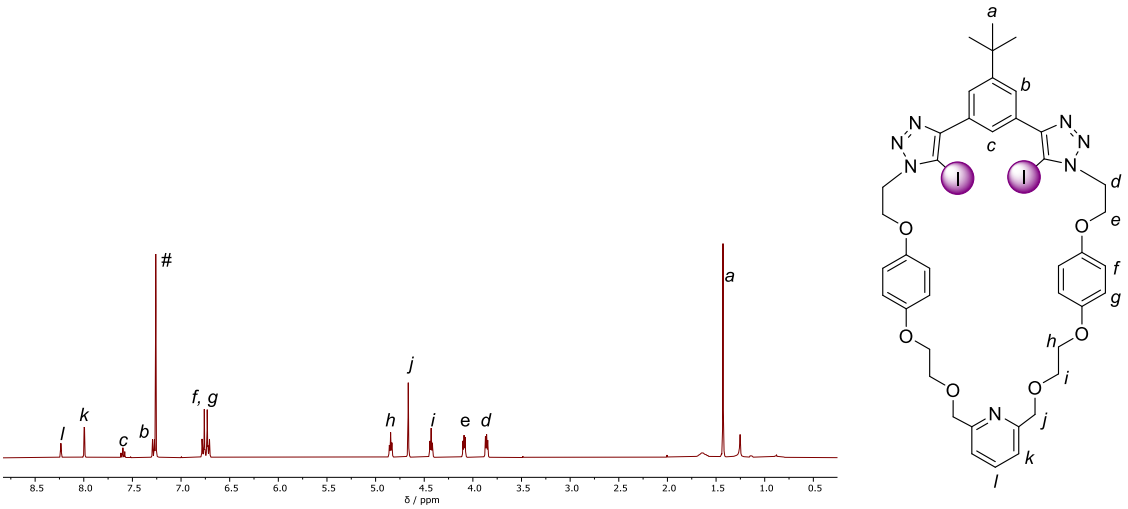

Figure 2.32. ^{1}H NMR (400 MHz, $CDCl_3$, 298 K) spectrum of macrocycle **2.9**. # denotes residual protiosolvent.

2.6.2 Synthesis of an Ion-Pair Receptor [2]Rotaxane with a Heteroditopic Macrocycle

The same rotaxination AMT reaction conditions as for the formation of *p*-**2.5a·Zn** (Scheme 2.3) were employed using macrocycle **2.9**. Unfortunately, after 5 days stirring at 60 °C, no interlocked product formation was observed, only the non-interlocked axle product *p*-**2.5c·Zn** and the free heteroditopic macrocycle **2.9** were isolated from the reaction mixture. It was postulated this may be due to mechanical dethreading of the macrocycle, due to its larger cavity size, which would be expected to be less prevalent at lower reaction temperatures. Therefore, the reaction was repeated in DCM at room temperature with frequent monitoring by TLC. Unfortunately, as in DCE, no interlocked product was observed, with only the non-interlocked axle product *p*-**2.5c·Zn** and the free macrocycle **2.9** isolated.

It was therefore decided to attempt rotaxination with the closely related isophthalamide-containing macrocycle **2.10**,[58] which could be readily synthesised by reduction of the bis-azide **2.7** to an amine, followed by an amide condensation reaction with bis-acid chloride 1,5-bis(chlorocarbonyl)-3-*tert*-butylbenzene (Scheme 2.7). This macrocycle has

previously been successfully used in rotaxination reactions to afford [2]rotaxanes with proven anion binding ability.[56]

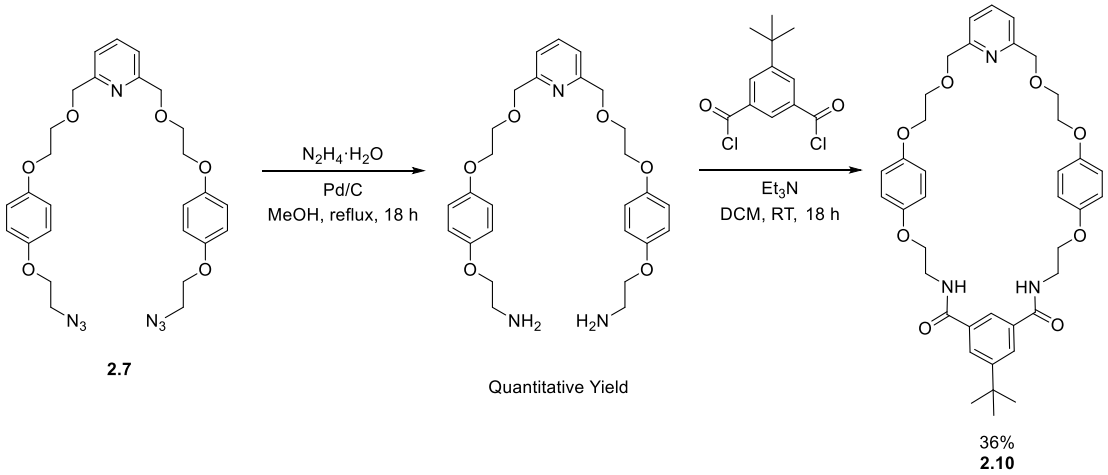

Scheme 2.7. Synthesis of macrocycle **2.10** (kindly supplied by Dr Andrew Docker).

Pleasingly, this macrocycle readily underwent a Cu(I)-catalysed AMT reaction under analogous conditions to the rotaxanes already reported in this chapter, forming the [2]rotaxane *p*-**2.11** in 73% yield upon reaction with the *para*-bis-azide *p*-**2.1·Zn** (Scheme 2.8). The rotaxane was fully characterised by ^{1}H, ^{13}C{^{1}H}, ^{1}H-^{1}H NMR spectroscopy and HR-ESI-MS, and the interlocked nature of the compound was confirmed by comparison of its ^{1}H NMR spectrum to the spectra of the non-interlocked components (Figure 2.33).

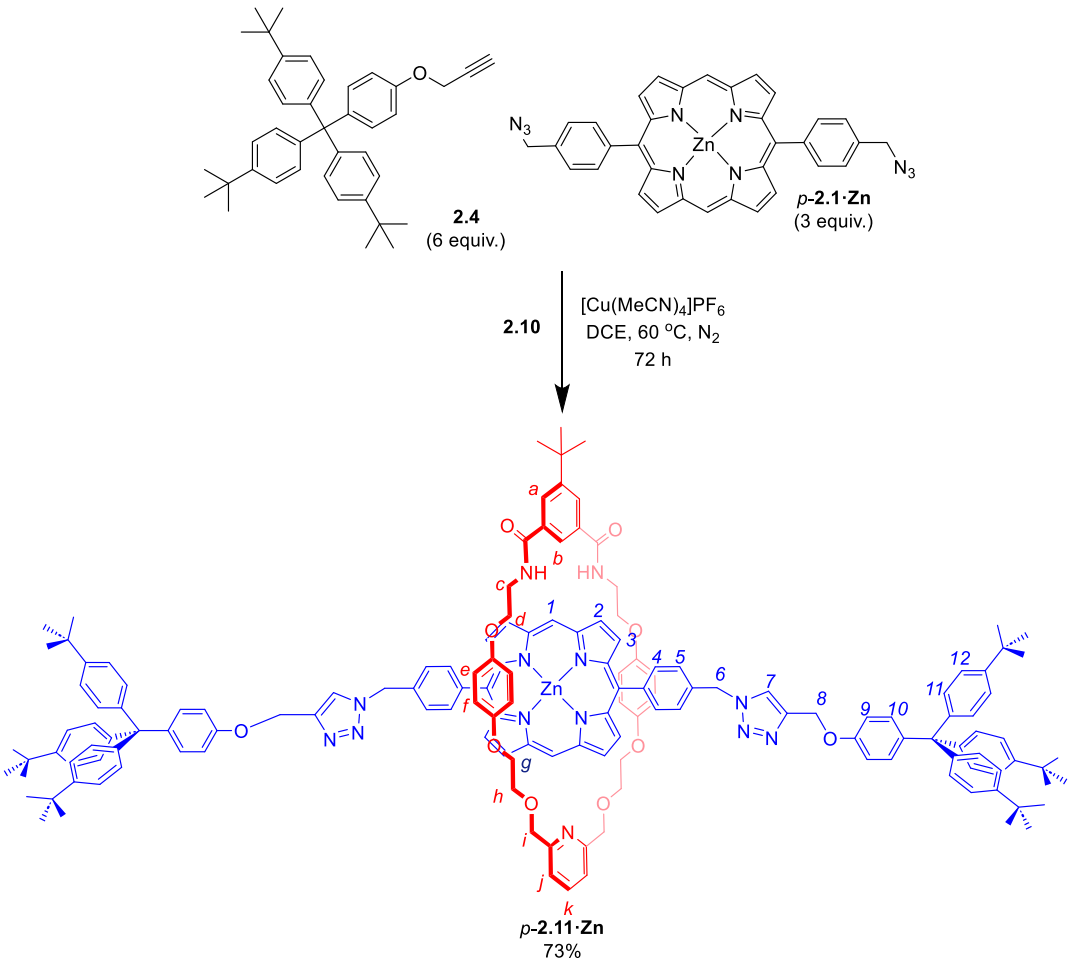

Scheme 2.8. Synthesis of [2]rotaxane *p*-**2.11·Zn**.

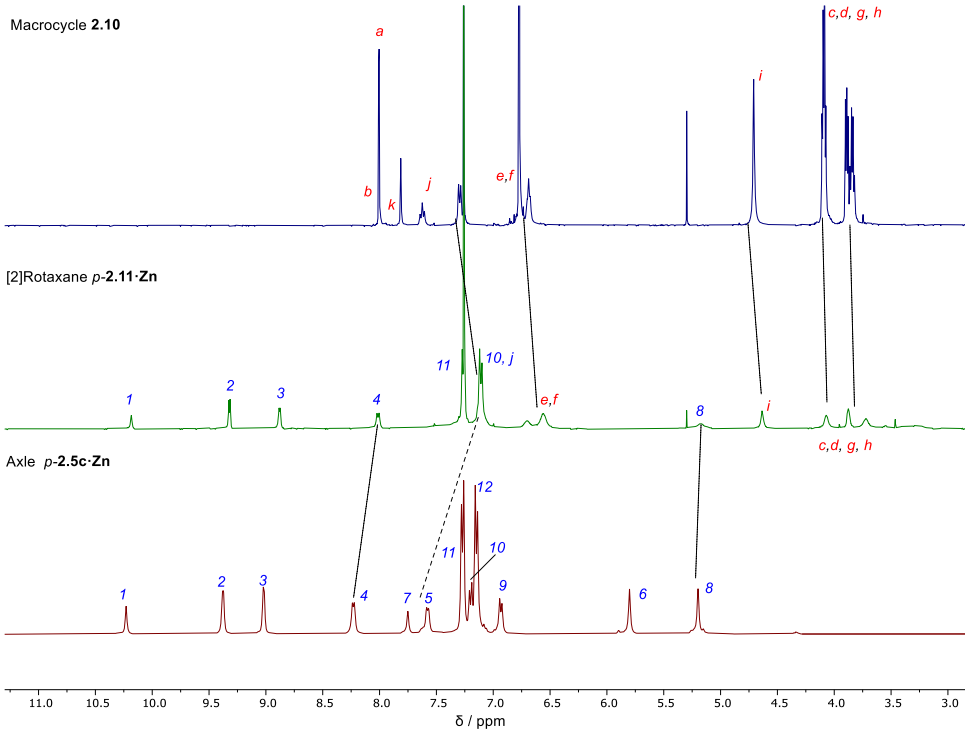

Figure 2.33. Stacked ^{1}H NMR spectra (400 MHz, $CDCl_3$, 298 K) of a) macrocycle **2.10**, b) [2]rotaxane *p*-**2.11·Zn** and non-interlocked axle *p*-**2.5c·Zn**.

The ^{1}H NMR spectrum of [2]rotaxane *p*-**2.11·Zn** showed similar diagnostic shifts to the NMR spectrum of *p*-**2.5a·Zn** including considerable broadening, suggesting that the interaction of the macrocycle pyridyl with the Zn(II) porphyrin was substantial. Therefore, to aid NMR assignment, a variable temperature ^{1}H NMR study was completed (Figure 2.34). Pleasingly, upon heating, the ^{1}H NMR spectrum of *p*-**2.11·Zn** became more clearly resolved, due to an increase in the relative rate of macrocycle translocation. Calculation of the activation parameters for the shuttling process, by Eyring analysis, revealed $\Delta H^{\ddagger} = 65$ kJ mol^{-1} and $\Delta S^{\ddagger} = 45$ J K^{-1} mol^{-1}, confirming the increased barrier to shuttling in *p*-**2.11·Zn** compared to *p*-**2.5a·Zn**.

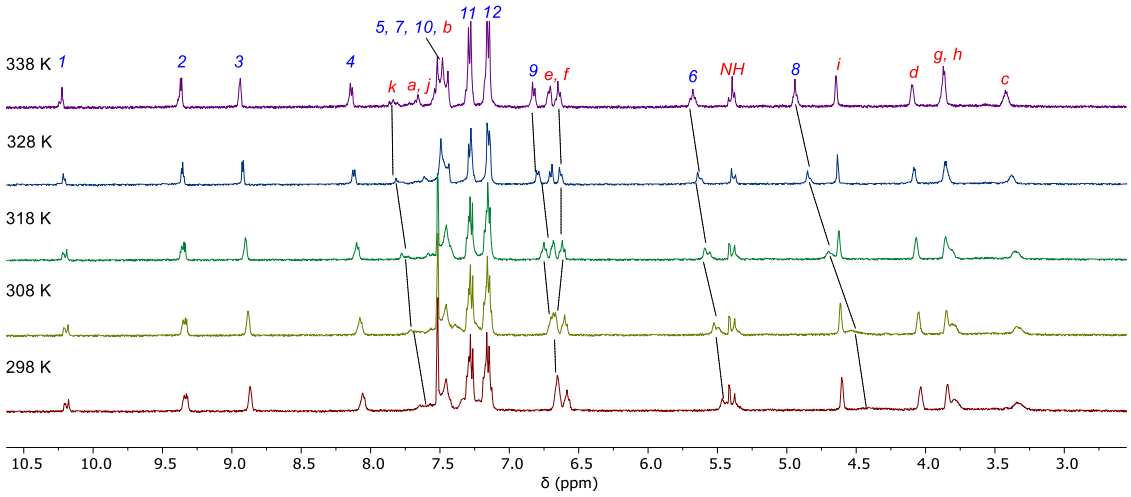

Figure 2.34. ^{1}H VT-NMR spectra (500 MHz, $CDCl_3$) of *p*-**2.11·Zn**.

Given the apparent broadening of the ^{1}H NMR spectrum of *p*-**2.11·Zn** due to pyridyl···Zn(II) interactions, *p*-**2.11·H$_2$** should have a sharply resolved ^{1}H NMR spectrum. Stirring a DCM solution of *p*-**2.11·Zn** with TFA afforded, after purification by preparative TLC, *p*-**2.11·H$_2$** in 92% yield. The room temperature ^{1}H NMR spectrum of *p*-**2.11·H$_2$** in chloroform is well-resolved and symmetric, consistent with free translocation of the macrocycle along the axle in the absence of pyridyl···Zn(II) interactions (Figure 2.35).

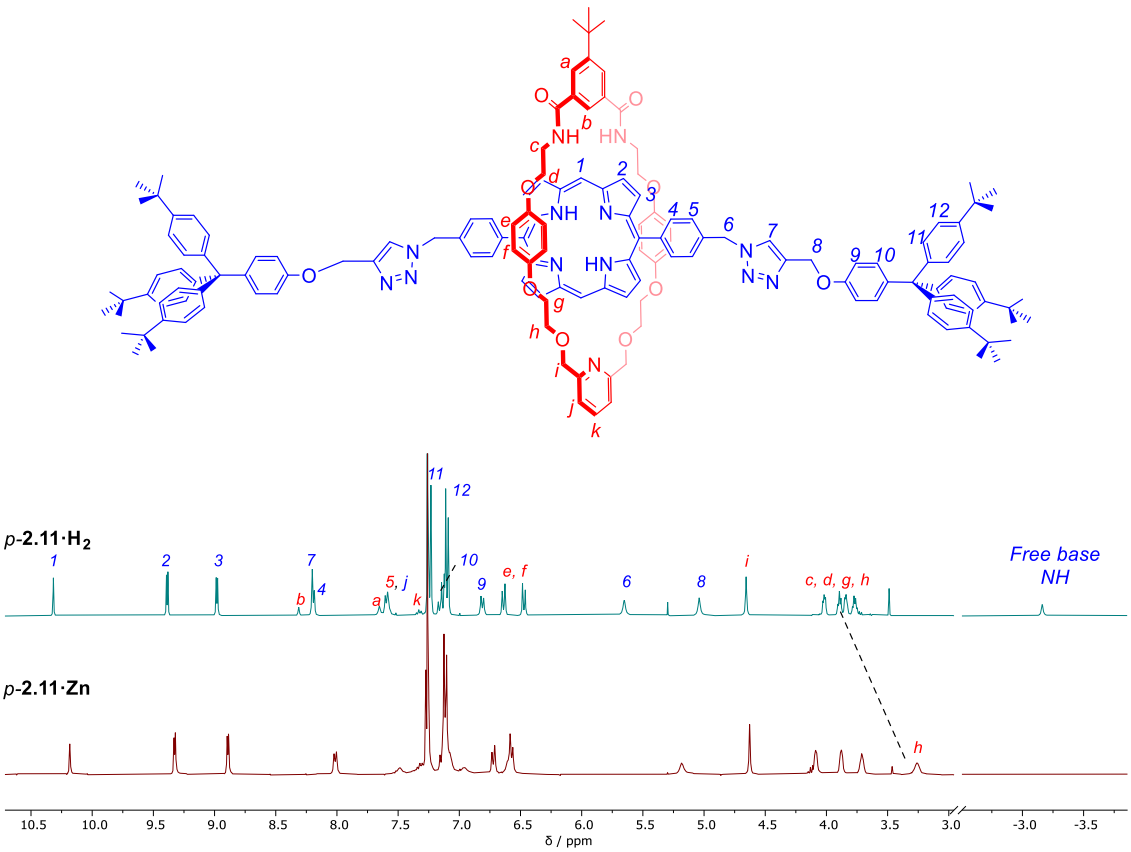

Figure 2.35. Stacked ^{1}H NMR (400 MHz, $CDCl_3$, 298 K) spectra of *p*-**2.11·Zn** and *p*-**2.11·H$_2$**.

2.6.3 Preliminary Anion Binding Studies

To provide a further insight into the strength of the pyridyl N···Zn(II) interaction in [2]rotaxane *p*-**2.11·Zn**, optical UV-visible titrations were performed in acetone with TBAX (X = Cl, Br, I), where the halide binding can be viewed as a ligand competition experiment against the macrocycle for the metalloporphyrin axial binding site, and compared with the binding constants determined by the analogous experiments with the first generation rotaxanes (Section 2.4).

As for the first generation rotaxanes, the Soret and Q bands underwent a bathochromic shift upon binding of a halide ligand, with the significant perturbation displaying definite isosbestic behaviour consistent with the predicted 1:1 host:guest binding geometry with a halide guest axially bound to the Lewis acidic Zn(II) centre (Figure 2.36).

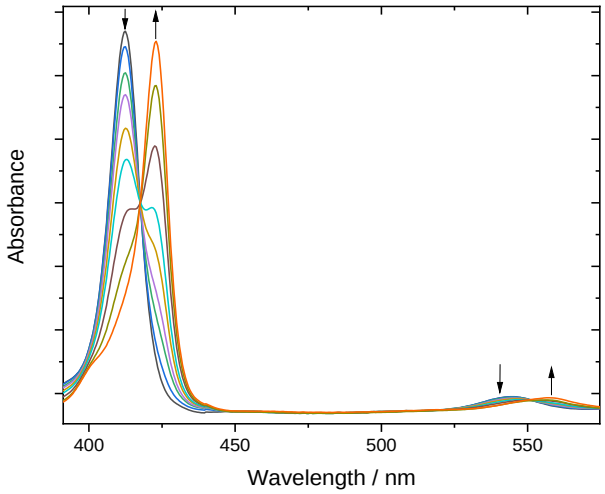

Figure 2.36. UV-visible spectra (2 μM, acetone) of the Soret and Q band absorption of *p*-**2.11·Zn**, upon successive additions of 100 mM TBACl.

The binding constants obtained follow the same trend as for the first generation rotaxanes (Table 2.5), Cl^- >> Br^-, with no binding observed for iodide, again following the trend in halide Lewis basicity. Interestingly, the chloride binding constant is significantly lower for rotaxane *p*-**2.11·Zn** than for the first generation rotaxane *p*-**2.5·Zn**, consistent with the greater activation parameters for macrocycle shuttling from the central porphyrin motif, as calculated in the earlier VT ^{1}H NMR studies.

	K_a (M^{-1})
Cl^-	190
Br^-	60
I^-	[a]

Table 2.5. Binding constants for halide anions determined by UV-visible spectroscopy in acetone. Errors <10%. [a] No binding observed. T = 298 K.

2.7 Ion-Pair Binding Studies

2.7.1 Lithium Cation Binding Studies

Advances in battery technology have resulted in a marked increase in global lithium salt demand,[59] however pollution from lithium mining is of public health concern, with excess

lithium salts being implicated in a number of neurological degenerative conditions, including Parkinson's disease and dementia.[60, 61] The selective sensing of lithium halide salts is challenging, due to the need to overcome their high lattice enthalpies, on account of the small cationic radius of the Li^+ cation, with only one previous report of a heteroditopic [2]rotaxane capable of selective recognition of lithium halide ion-pairs.[62] It was hoped the pyridyl macrocycle would be capable of binding Li^+ cooperatively with the axle triazole, inducing macrocycle shuttling and enabling the challenging, mechanical bond-facilitated, binding of lithium halide ion-pairs.

Prior to ion-pair binding studies, the ability of rotaxane *p*-**2.11·Zn** to bind Li^+ was investigated. ^{1}H NMR titrations were conducted in 7:3 *v/v* $CDCl_3$:CD_3CN. This ratio was selected to balance the poor solubility of the rotaxane *p*-**2.11·Zn** in CD_3CN and the poor solubility of $LiClO_4$ in $CDCl_3$. The ^{1}H NMR spectrum of *p*-**2.11·Zn** was well-resolved at room temperature in this solvent mixture, consistent with the variable solvent studies on *p*-**2.5·Zn** which demonstrated the ability of MeCN to act as a competing solvent for binding at the Zn(II) metalloporphyrin axial binding site, which would be expected to weaken the Zn(II)···pyridyl interaction, potentially enhancing Li^+ recognition.

Upon successive addition of a 25 mM $LiClO_4$ solution to 1 mM *p*-**2.11·Zn**, the macrocycle methylene resonance *i* shifted sharply downfield, consistent with cation binding in the pyridyl binding pocket. The adjacent ethylene protons *g*, *h* showed marked shifts (Figure 2.37). Furthermore, a significant downfield shift was observed for triazole proton *7*, strongly suggesting cooperative inter-component Li^+ binding at the axle triazole site. Monitoring proton *i*, *Bindfit* analysis of the resulting binding isotherm,[49] fitting to a 1:1 host-guest binding model, determined a binding constant of 285 M^{-1}. This is of lower magnitude than previously reported lithium binding constants in similar isophthalamide

macrocycle/axle triazole MIM binding cavitites,[62] but can be attributed to the competition between the Zn(II) Lewis acidic centre and the Li^+ cation for the pyridyl binding site of the macrocycle.

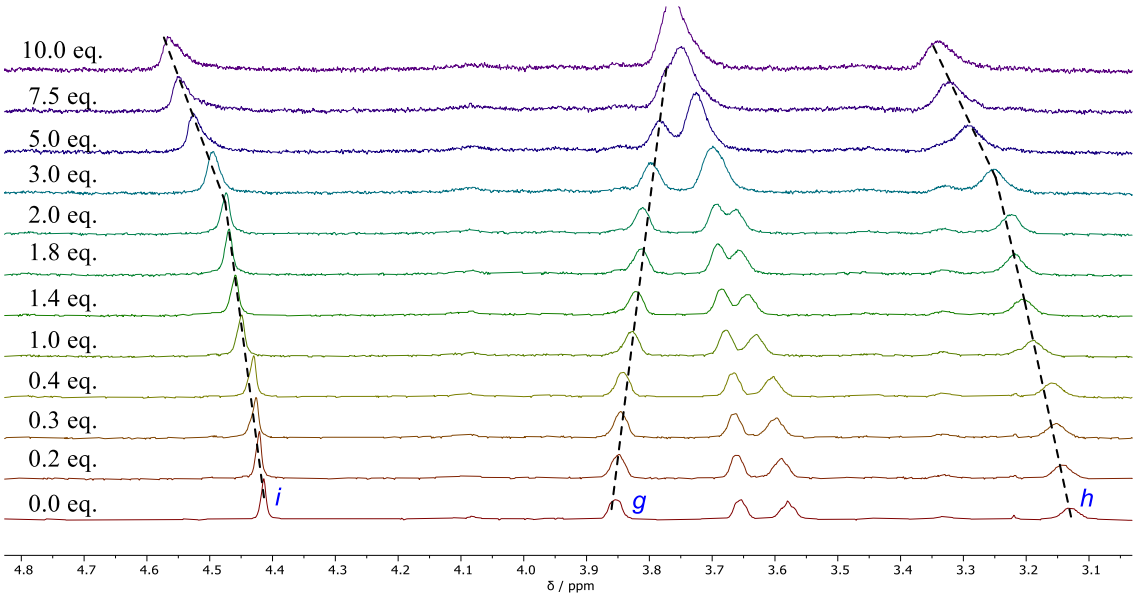

Figure 2.37. Truncated ^{1}H NMR (500 MHz, 7:3 *v/v* $CDCl_3$:CD_3CN, 298 K) spectra of [2]rotaxane *p*-**2.11·Zn** upon successive addition of $LiClO_4$.

Further evidence of the competition between the Zn(II) centre and Li^+ was obtained by measuring the UV-visible absorption spectrum of *p*-**2.11·Zn**, in 7:3 *v/v* $CHCl_3$:MeCN, in the presence and absence of excess Li^+ (Figure 2.38 a). Upon addition of a $LiClO_4$ solution, the Soret band of the rotaxane underwent a hypsochromic shift from 413 nm to 411 nm, closer to the value observed in the non-interlocked axle where macrocycle···Zn(II) interactions are absent, strongly indicating the ability of Li^+ binding to compete for the macrocycle pyridyl over the Zn(II) metalloporphyrin (Figure 2.38 b).

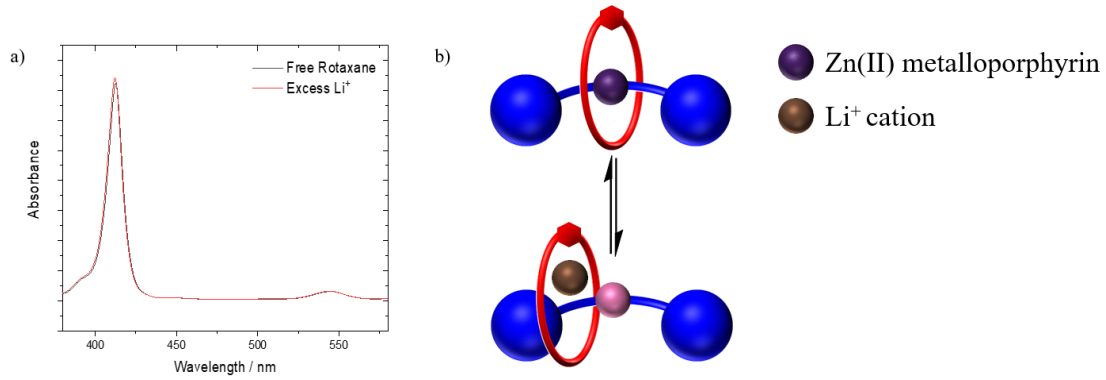

Figure 2.38. a) UV-visible absorption spectrum (2 μM, 7:3 *v/v* $CHCl_3$:MeCN) of ***p*-2.11·Zn** in the Soret and Q-band regions in the presence and absence of excess Li^+. b) Schematic depiction of stimuli induced co-conformational dynamism of ***p*-2.11·Zn** upon Li^+ binding.

2.7.2 Lithium Halide Ion-Pair Binding Studies

With the ability of the rotaxane to bind lithium cations confirmed, ^{1}H NMR titrations were conducted by successive addition of TBAX (X = Cl, Br, I) to equimolar solutions of [2]rotaxane ***p*-2.11·Zn** and $LiClO_4$. Based on the result of the titration in Section 2.7.1, approximately 20% of the ***p*-2.11·Zn** would be expected to be associated with Li^+ at the titration start point.

In the absence of Li^+ only very weak halide association upon addition of TBA halide salts to ***p*-2.11·Zn** (Cl^- K_a = 340 M^{-1}) was observed in 7:3 *v/v* $CDCl_3$:CD_3CN (Table 2.5), corresponding to halide binding at the axial 5th coordination side of the Zn(II) metalloporphyrin, requiring competition with the inter-component pyridyl···Zn(II) interaction (Figure 2.39 a). In the presence of co-bound Li^+ the possibility of two distinct anion binding modes arises: either the binding of an anion at the isophthalamide anion binding moiety of the macrocycle, or by Lewis acid-base association with the Zn(II) metalloporphyrin site, which is now more available for anion binding due to Li^+ binding sequestering the macrocycle pyridyl group, meaning the macrocycle no longer acts as a competing ligand for the 5th coordination site of the metalloporphyrin. Thus, halide binding affinity was expected to be significantly enhanced upon Li^+ binding, both due to

electrostatic attractions between the oppositely charged co-bound guests and potentially through the binding of a second halide anion at the Zn(II) metalloporphyrin, giving an overall 1:2 host:guest stoichiometry for the binding of halide ions to *p*-**2.11·Zn**·Li^+ (Figure 2.39 b).

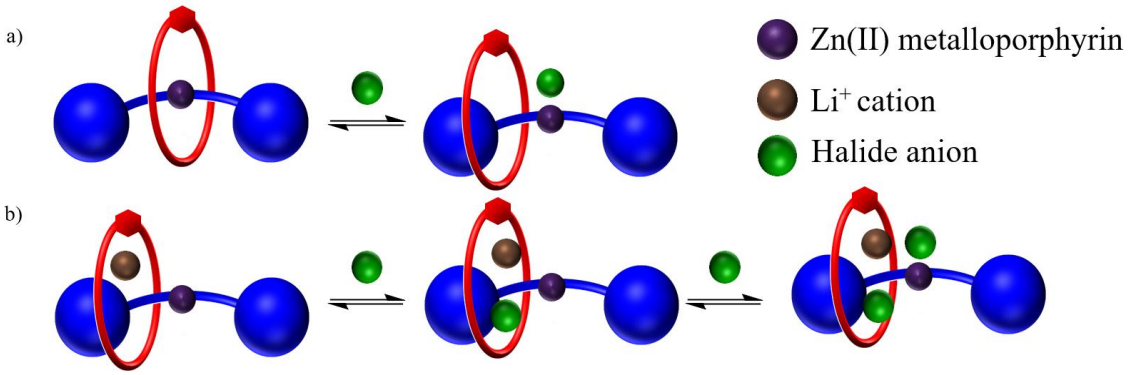

Figure 2.39. Schematic depiction of proposed binding modes of halides to *p*-**2.11·Zn** in the a) absence, and b) presence, of co-bound Li^+.

	0 e.q. Li^+	1 e.q. Li^+	
	K_a (M^{-1})	K_{11} (M^{-1})	K_{12} (M^{-1})
Cl^-	340	$> 10^5$	*a*
Br^-	200	$>10^4$	220
I^-	*NB*	1750	*b*

Table 2.6. Apparent binding constants for halide anions upon ^{1}H NMR titration, 298 K, 7:3 *v/v* $CDCl_3$:CD_3CN. Errors <5%. [a] Salt recombination observed. [b] Fitting consistent with 1:1 host:guest binding stoichiometry. [NB] No binding observed.

Upon addition of TBACl to an equimolar mixture of *p*-**2.11·Zn** and $LiClO_4$ in 7:3 *v/v* $CDCl_3$:CD_3CN the internal macrocycle phenyl proton *b* and isophthalamide N*H* proton underwent marked downfield shifts, confirming anion binding in the macrocycle isophthalamide cavity. Such perturbations were observed upon successive Cl^- addition until one equivalent had been added, consistent with quantitative binding of Cl^- ($K_a > 10^5$

M^{-1}) in the macrocycle, representing a significant enhancement over binding in the absence of Li^+ (K_a = 340 M^{-1}). The quantitative binding of Cl^-, when only 20% of Li^+ is bound under analogous conditions in the absence of a halide salt, evidences the co-operativity in binding facilitated by the heteroditopic macrocycle, where binding of the anion also enhances cation binding such that near stoichiometric binding of the ion-pair occurs. Further evidence that Cl^- also enhances Li^+ binding can be seen in the downfield shifts of the external pyridyl proton *k* and ethylene proton *h* upon Cl^- addition (Figure 2.40). Unfortunately, at higher concentrations of Cl^-, the precipitation of LiCl was observed, indicating that the rotaxane is not able to overcome the high lattice enthalpy of LiCl at higher concentrations of chloride, and thus forms only a 1:1 host-guest complex with *p*-**2.11·Zn**·Li^+.[63]

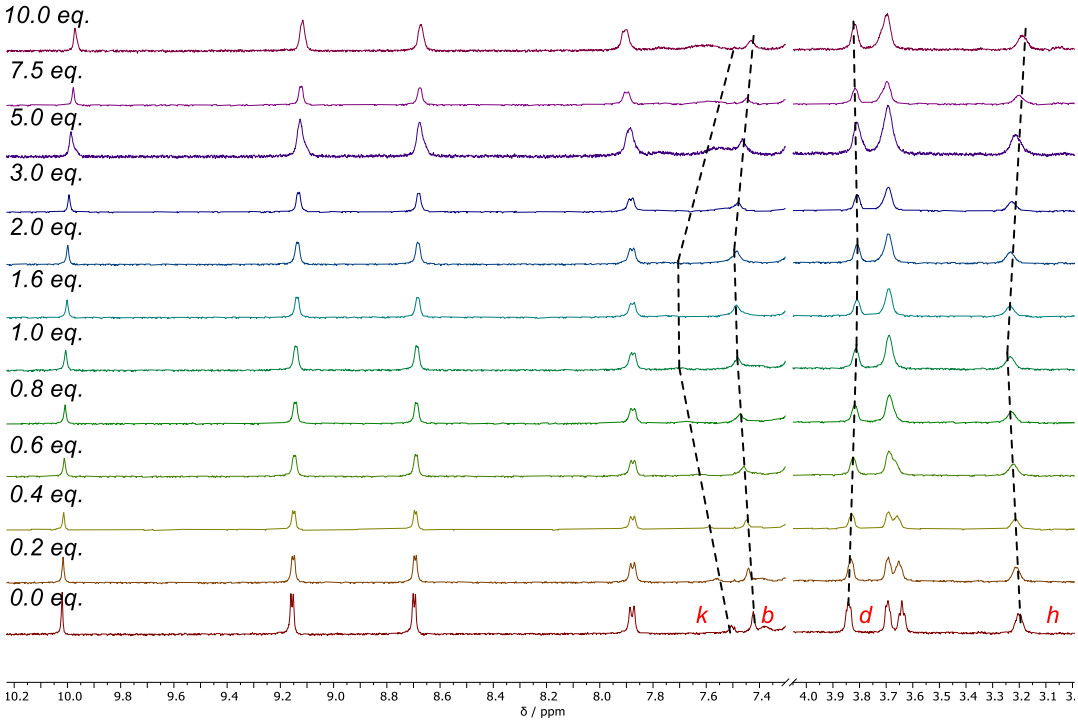

Figure 2.40. Stacked truncated ^{1}H NMR (500 MHz, 7:3 *v/v* $CDCl_3$:CD_3CN, 298 K) spectra of an equimolar solution of *p*-**2.11·Zn** and $LiClO_4$ upon successive additions of TBACl.

The analogous titration with TBABr also demonstrated strong halide binding, albeit not fully quantitative (K_{11} > 10^4 M^{-1}). More interestingly, the binding isotherm appeared

consistent with a 1:2 host:guest binding model, that is to say, a second binding mode was present with a binding constant much smaller than the first. Analysis of the quality of the fit of both a 1:1 and 1:2 binding model, in particular analysis of the randomness of the residuals arising from fitting to each binding stoichiometry, statistically justify the decision to infer a 1:2 binding mode from these titration data.[64] Interestingly K_{12} is comparable to the binding constant of the free rotaxane in the absence of Li^+, suggesting the second binding mode is indeed the proposed simple Lewis acid-base binding of a second bromide at the metalloporphyrin (Figure 2.39 b). The minor enhancement of the binding constant over that for the free metalloporphyrin is likely a combination of Li^+ biasing the macrocycle to reside away from the porphyrin and favourable electrostatic interactions from introducing a second anion close to the Li^+ cation.

The final titration with TBAI, demonstrated relatively weak binding, consistent with the lower charge density of I^-. The ^{1}H NMR shifts observed were analogous to the earlier titrations, the binding constant (K_{11} = 1750 M^{-1}) obtained was still significant compared to the absence of any binding activity for the free rotaxane. Fitting the data confirmed a 1:1 host:guest binding stoichiometry consistent with the low Lewis basicity of I^- rendering it unable to bind appreciably to the metalloporphyrin.

In summary, the binding isotherms for the three halides demonstrates the ability of the heteroditopic macrocycle **2.10** to facilitate axle-separated ion-pair binding in *p*-**2.11·Zn** (Figure 2.41), with trends consistent with the charge density, and hence Lewis basicity, of the anions. In all cases, binding constants were significantly higher than for binding by the rotaxane in the absence of Li^+. Unusually, this system enhances anion binding through two mechanisms, firstly through the electrostatic attraction between the lithium cation and halide anion ion-pair, and secondly, in the case of bromide binding, by removal

of the competing ligand at the metalloporphyrin to enable 1:2 host:guest binding (Figure 2.39 b). The unique binding behaviour of bromide is serendipitous, arising from its intermediate status in the series of halides: having a lower lattice enthalpy compared to LiCl, and thus not favouring salt recombination, but still acting as a sufficiently potent Lewis base to appreciably interact with the Zn(II) metalloporphyrin centre.

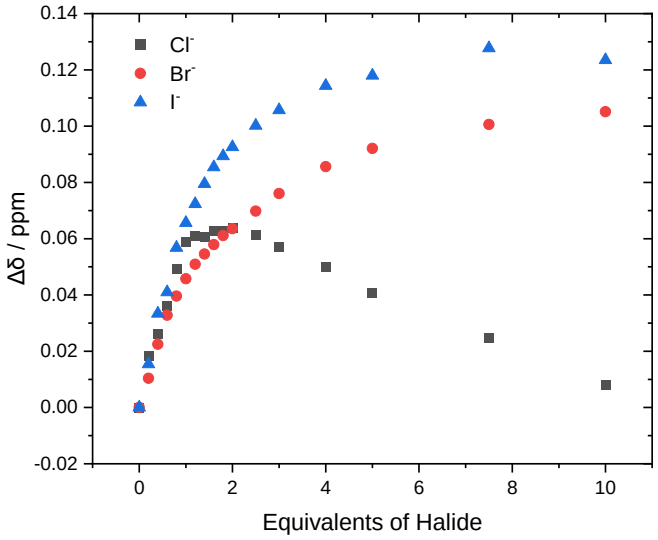

Figure 2.41. ^{1}H NMR binding isotherms, mapping phenyl proton *b* in an equimolar 7:3 *v/v* $CDCl_3$:CD_3CN solution of *p*-**2.11**·**Zn** and $LiClO_4$ upon successive additions of TBAX (X = Cl, Br, I).

2.8 Conclusions and Future Work

A series of Zn(II) metalloporphyrin-containing [2]- and [3]-rotaxanes has been prepared. The interaction between the axle Lewis acidic metal centre and macrocycle pyridyl moiety was shown to retard the translocation of the macrocycle along the axis of the [2]rotaxane. On the contrary, no translocation is observed in the [3]rotaxane due to mutual repulsion of the macrocycles.

The inter-component interaction between the macrocycle and Zn(II) metalloporphyrin can be monitored through its effects on the optical spectra of the porphyrin, most notably through the bathochromic shift induced in the Soret band of the UV-visible spectra of the

metalloporphyrins. The competing interaction between the macrocycle and the metalloporphyrin provides a unique mechanism for modulation of the dynamic motion of the [2]rotaxane interlocked system. Addition of a competing neutral Lewis base, pyridine, arrests the shuttling process, while the binding of anions at the metalloporphyrin provides a handle to investigate the competing interactions between an anion guest and the rotaxane macrocycle component in host-guest binding at the Lewis acidic centre.

The demetalation of the Zn(II) metalloporphyrin enabled the formation of free-base porphyrin and Ni(II) metalloporphyrin congeners, which do not possess a facile vacant coordination site, exploring the impact of Lewis acidity on the macrocycle-porphyrin interaction. Variable-temperature ^{1}H NMR studies demonstrated that greater affinity for axial coordination of the macrocycle pyridyl to give a 5-coordinate complex leads to a greater activation barrier for macrocycle shuttling.

The binding of anions by the first generation of metalloporphyrin [2]rotaxanes was investigated by optical and NMR titration studies. ^{1}H NMR studies attempting to quantify the binding of ion-pairs by rotaxane *p*-**2.5a·Zn** were unsuccessful due to salt recombination, as the binding affinities of the cation by the pyridyl macrocycle motif, and of the anion, were insufficient to overcome the lattice enthalpy of the corresponding salts. This result encouraged the synthesis of second generation rotaxanes with a heteroditopic macrocycle containing the same pyridyl moiety, but also incorporating an isophthalamide anion binding site. These rotaxanes showed similar retardation of shuttling by a pyridyl···Zn(II) interaction, but were able to stabilise a well-defined bound axle-separated LiCl ion pair. The Li^{+} complexed rotaxanes were able to form a 1:2 host-guest complex upon addition of excess TBABr, evidencing the initial ion-pair binding inducing macrocycle shuttling to the triazole station, such that a second bromide anion

can bind as a guest to the Zn(II) metalloporphyrin centre to form a 5-coordinate Lewis acid-base adduct, enabled by the reduced driving force for LiBr salt recombination on account of the lower lattice enthalpy of LiBr compared to LiCl. In contrast, the Lewis basicity of iodide is too low to bind at the Zn(II) metalloporphyrin, only binding with a 1:1 host:guest binding stoichiometry in which the iodide is bound in the macrocycle isophthalamide cavity. Thus, the intermediate position of bromide in the halide series enables a unique 1:2 host-guest binding mode for lithium halide ion-pair binding.

Future work will seek to explore the exploitation of the strong lithium halide binding by the axle triazole and isophthalamide macrocycle **2.10** to form pseudo[2]rotaxanes. Such a pseudorotaxane would be expected to undergo subsequent high-yielding AMT rotaxane formation reactions with pyridyl macrocycle **2.3**, as a route to achieve the challenging synthesis of a hetero[3]rotaxane and providing an unprecedented platform for studying the dynamic behaviour of [3]rotaxanes containing two competing significant pyridyl···Zn(II) inter-component interactions (Figure 2.42).

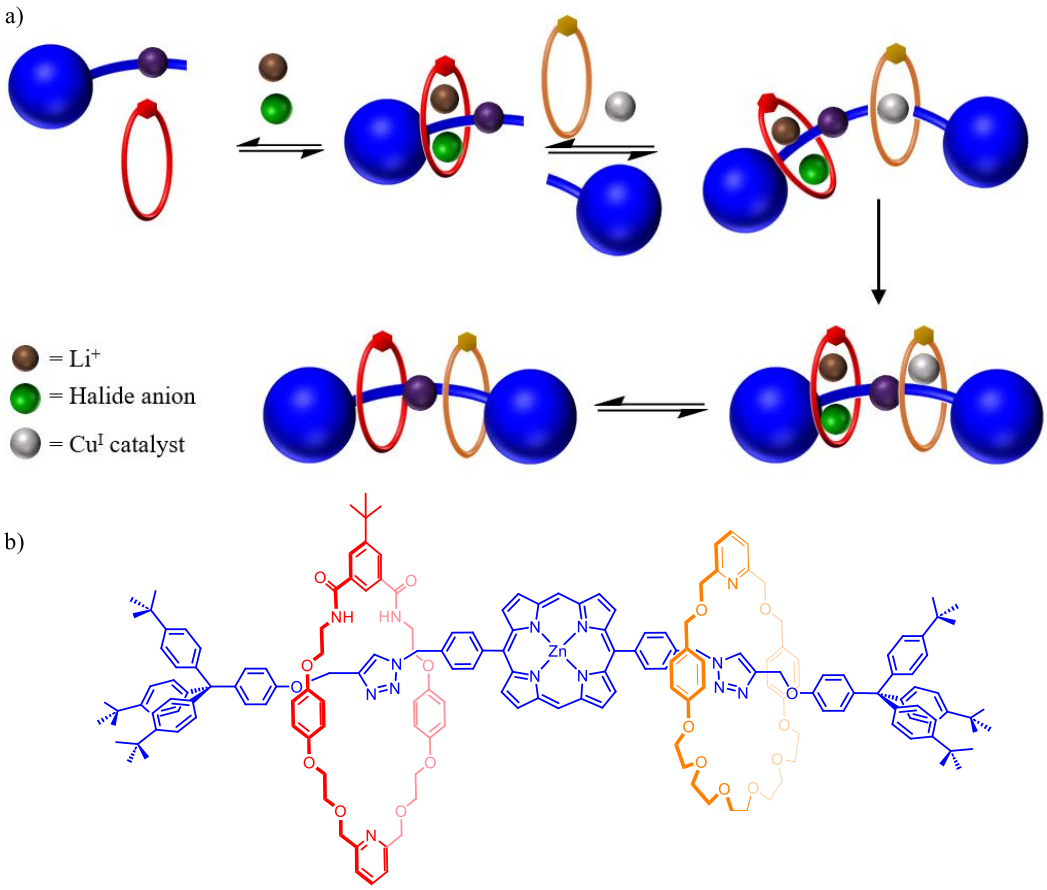

Figure 2.42. a) Schematic depiction of tandem ion-pair and AMT CuAAC synthesis of a hetero[3]rotaxane. b) Target hetero[3]rotaxane.

2.9 References

1. H. Scheer, in *Chlorophylls and Bacteriochlorophylls: Biochemistry, Biophysics, Functions and Applications*, eds. B. Grimm, R. J. Porra, W. Rüdiger and H. Scheer, Springer Netherlands, Dordrecht, 2006, DOI: 10.1007/1-4020-4516-6_1, pp. 1-26.
2. K. E. Anderson, J. R. Bloomer, H. L. Bonkovsky, J. P. Kushner, C. A. Pierach, N. R. Pimstone and R. J. Desnick, *Ann. Intern. Med.*, 2005, **142**, 439-450.
3. F. O'Leary and S. Samman, *Nutrients*, 2010, **2**, 299-316.
4. E. Margoliash, *Proc. Natl. Acad. Sci. U.S.A.*, 1963, **50**, 672-679.
5. V. Endeward, G. Gros and K. D. Jürgens, *Cardiovasc. Res.*, 2010, **87**, 22-29.
6. T. Li, H. L. Bonkovsky and J.-t. Guo, *BMC Struct. Biol.*, 2011, **11**, 13.
7. A. M. Humphrey, *Food Chem.*, 1980, **5**, 57-67.
8. F. Sondheimer, R. Wolovsky and Y. Amiel, *J. Am. Chem. Soc.*, 1962, **84**, 274-284.
9. K. M. Kadish and L. R. Shiue, *Inorg. Chem.*, 1982, **21**, 1112-1115.
10. H. G. Liddell, R. Scott, H. S. Jones and R. McKenzie, *A Greek-English Lexicon*, Clarendon Press, Oxford, 9th edn., 1940.
11. M. Gouterman, G. H. Wagnière and L. C. Snyder, *J. Mol. Spectrosc.*, 1963, **11**, 108-127.

12. L. R. Milgrom, *The colours of life : an introduction to the chemistry of porphyrins and related compounds*, Oxford University Press, Oxford, 1997.
13. J. B. Allison and R. S. Becker, *J. Chem. Phys.*, 1960, **32**, 1410-1417.
14. R. S. Becker and J. B. Allison, *J. Phys. Chem.*, 1963, **67**, 2662-2669.
15. A. S. Hinman and B. J. Pavelich, *J. Electroanal. Chem.*, 1989, **269**, 53-61.
16. C. Lee, D. H. Lee and J.-I. Hong, *Tetrahedron Lett.*, 2001, **42**, 8665-8668.
17. S. D. Starnes, S. Arungundram and C. H. Saunders, *Tetrahedron Lett.*, 2002, **43**, 7785-7788.
18. L. C. Gilday, N. G. White and P. D. Beer, *Dalton Trans.*, 2013, **42**, 15766-15773.
19. X. Ma, J. Zhang, J. Cao, X. Yao, T. Cao, Y. Gong, C. Zhao and H. Tian, *Chem. Sci.*, 2016, **7**, 4582-4588.
20. M. Wolf, A. Ogawa, M. Bechtold, M. Vonesch, J. A. Wytko, K. Oohora, S. Campidelli, T. Hayashi, D. M. Guldi and J. Weiss, *Chem. Sci.*, 2019, **10**, 3846-3853.
21. Y. Cheong Tse, R. Hein, E. J. Mitchell, Z. Zhang and P. D. Beer, *Chem. Eur. J.*, 2021, **27**, 14550-14559.
22. X.-Z. Wang and T. R. Burke Jr, *Synlett*, 2004, **2004**, 469-472.
23. R. W. Wagner, T. E. Johnson and J. S. Lindsey, *Tetrahedron*, 1997, **53**, 6755-6790.
24. D. A. Roberts, T. W. Schmidt, M. J. Crossley and S. Perrier, *Chem. Eur. J.*, 2013, **19**, 12759-12770.
25. R. J. Abraham, K. M. Smith, D. A. Goff and J. J. Lai, *J. Am. Chem. Soc.*, 1982, **104**, 4332-4337.
26. V. Aucagne, K. D. Hänni, D. A. Leigh, P. J. Lusby and D. B. Walker, *J. Am. Chem. Soc.*, 2006, **128**, 2186-2187.
27. J. D. Crowley, S. M. Goldup, A.-L. Lee, D. A. Leigh and R. T. McBurney, *Chem. Soc. Rev.*, 2009, **38**, 1530-1541.
28. M. Denis and S. M. Goldup, *Nat. Rev. Chem.*, 2017, **1**, 0061.
29. V. Aucagne, J. Berná, J. D. Crowley, S. M. Goldup, K. D. Hänni, D. A. Leigh, P. J. Lusby, V. E. Ronaldson, A. M. Z. Slawin, A. Viterisi and D. B. Walker, *J. Am. Chem. Soc.*, 2007, **129**, 11950-11963.
30. B. F. Kim and J. Bohandy, *Johns Hopkins APL Technical Digest*, 1981, **2**, 153-163.
31. R. Díaz-Torres and S. Alvarez, *Dalton Trans.*, 2011, **40**, 10742-10750.
32. T. L. C. Figueiredo, R. A. W. Johnstone, A. M. P. S. Sørensen, D. Burget and P. Jacques, *Photochem. Photobiol.*, 1999, **69**, 517-528.
33. L. Favereau, A. Cnossen, J. B. Kelber, J. Q. Gong, R. M. Oetterli, J. Cremers, L. M. Herz and H. L. Anderson, *J. Am. Chem. Soc.*, 2015, **137**, 14256-14259.
34. M. Dommaschk, J. Echavarren, D. A. Leigh, V. Marcos and T. A. Singleton, *Angew. Chem. Int. Ed.*, 2019, **58**, 14955-14958.
35. H. Li, Y.-L. Zhao, A. C. Fahrenbach, S.-Y. Kim, W. F. Paxton and J. F. Stoddart, *Org. Biomol. Chem.*, 2011, **9**, 2240-2250.
36. C. He, Q. He, C. Deng, L. Shi, D. Zhu, Y. Fu, H. Cao and J. Cheng, *Chem. Commun.*, 2010, **46**, 7536-7538.
37. A. Antipas, D. Dolphin, M. Gouterman and E. C. Johnson, *J. Am. Chem. Soc.*, 1978, **100**, 7705-7709.
38. S. G. Kruglik, V. V. Ermolenkov, V. A. Orlovich and P.-Y. Turpin, *Chem. Phys.*, 2003, **286**, 97-108.
39. D. P. Cormode, M. G. B. Drew, R. Jagessar and P. D. Beer, *Dalton Trans.*, 2008, 6732-6741.

40. N. Zheng, J. Zhang, X. Bu and P. Feng, *Cryst. Growth Des.*, 2007, **7**, 2576-2581.
41. C. McHiri, S. Dhifaoui, K. Ezzayani, M. Guergueb, T. Roisnel, F. Loiseau and H. Nasri, *Polyhedron*, 2019, **171**, 10-19.
42. W. S. Caughey, R. M. Deal, B. D. McLees and J. O. Alben, *J. Am. Chem. Soc.*, 1962, **84**, 1735-1736.
43. F. Gutzeit, M. Dommaschk, N. Levin, A. Buchholz, E. Schaub, W. Plass, C. Näther and R. Herges, *Inorg. Chem.*, 2019, **58**, 12542-12546.
44. J. F. Stoddart and C. J. Bruns, in *The Nature of the Mechanical Bond*, 2016, DOI: https://doi.org/10.1002/9781119044123.ch5, pp. 471-554.
45. H. Eyring, *J. Chem. Phys.*, 1935, **3**, 107-115.
46. S. Corra, C. de Vet, M. Baroncini, A. Credi and S. Silvi, *Chem*, 2021, **7**, 2137-2150.
47. S. W. Hewson and K. M. Mullen, *Org. Biomol. Chem.*, 2018, **16**, 8569-8578.
48. M. Nappa and J. S. Valentine, *J. Am. Chem. Soc.*, 1978, **100**, 5075-5080.
49. D. Brynn Hibbert and P. Thordarson, *Chem. Commun.*, 2016, **52**, 12792-12805.
50. Y. Gao, M. Yan and G. V. Korshin, *Environ. Sci. Technol.*, 2015, **49**, 5905-5912.
51. T. E. Sladewski, A. M. Shafer and C. M. Hoag, *Spectrochim. Acta A*, 2006, **65**, 985-987.
52. A. V. Leontiev, C. A. Jemmett and P. D. Beer, *Chem. Eur. J.*, 2011, **17**, 816-825.
53. J.-X. Yang, X. Zhang, Y.-Y. Qin and Y.-G. Yao, *Cryst. Growth Des.*, 2020, **20**, 6366-6381.
54. R. C. Knighton and P. D. Beer, *Chem. Commun.*, 2014, **50**, 1540-1542.
55. M. D. Lankshear, N. H. Evans, S. R. Bayly and P. D. Beer, *Chem. Eur. J.*, 2007, **13**, 3861-3870.
56. A. Brown, T. Lang, K. M. Mullen and P. D. Beer, *Org. Biomol. Chem.*, 2017, **15**, 4587-4594.
57. Y. C. Tse, A. Docker, Z. Zhang and P. D. Beer, *Chem. Commun.*, 2021, **57**, 4950-4953.
58. Kindly supplied by Dr Andrew Docker.
59. G. Martin, L. Rentsch, M. Höck and M. Bertau, *Energy Storage Mater.*, 2017, **6**, 171-179.
60. M. Niethammer and B. Ford, *Mov. Disord.*, 2007, **22**, 570-573.
61. P. Newman and M. Saunders, *Postgrad. Med. J.*, 1979, **55**, 701-703.
62. V. K. Munasinghe, J. Pancholi, D. Manawadu, Z. Zhang and P. D. Beer, *Chem. Eur. J.*, 2022, **28**, e202201209.
63. J. R. Rumble, ed., *CRC Handbook of Chemistry and Physics*, CRC Press, 2021.
64. F. Ulatowski, K. Dąbrowa, T. Bałakier and J. Jurczak, *J. Org. Chem.*, 2016, **81**, 1746-1756.

Chapter Three

Exploiting Pillar[5]Arene Host-Guest Chemistry for Rotaxane Assembly and Enhanced Optical Sensing of Biologically Relevant Substrates

3 Exploiting Pillar[5]arene Host-Guest Chemistry for Rotaxane Assembly and Enhanced Optical Sensing of Biologically Relevant Substrates

3.1 Pillar[5]arenes: Neutral Supramolecular Hosts

3.1.1 The Pillar[5]arene Moiety

In the years following the pioneering crown ether, cryptand and spherand alkali metal cation recognition works of Pedersen, Cram and Lehn,[1] a number of classes of supramolecular macrocyclic hosts capable of binding charged and neutral guests emerged, including cyclodextrins, calixarenes, cucurbiturils and, recently, pillar[*n*]arenes (P[*n*]As).[2-4] First reported in 2008 by Ogoshi and co-workers,[5] P[*n*]As are a series of macrocyclic hosts formed by condensation of benzene-1,4-diethers with paraformaldehyde (PFA) in the presence of a Lewis acidic catalyst such as BF_3. The resulting P[*n*]As possess highly-symmetric pillar-like structures, comprised of *n* benzene-1,4-diether subunits joined at the 2,5 positions by methylene linkers, with cyclisation arising due to solvent-templation effects. Synthesis in 1,2-dichloroethane (DCE) results in the formation of pillar[5]arenes (P5As),[6] whereas the same reaction in chlorocyclohexane affords the pillar[6]arene as the major product (Scheme 3.1).[7]

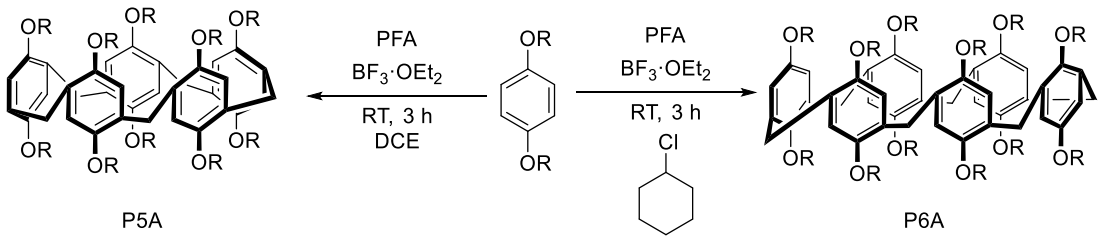

Scheme 3.1. Solvent-templated synthesis of generic P5As and P6As.

Since Ogoshi's initial report, P[*n*]As have been rapidly adopted by the supramolecular community, largely due to their facile one-step synthesis and ease of functionalisation of the benzene-1,4-diether precursors.[8] While initial research focused on the formation of

highly symmetrical P[*n*]As formed by homo-cyclo-oligomerisation, subsequent reports demonstrated the incorporation of functionality into hetero-P[*n*]As through two main methods: either the statistical incorporation of one or more functionalised subunits into a P[*n*]A scaffold, affording functionalised P5As (Scheme 3.2 a),[9] or the protection of the initial monomer, followed by post-synthetic deprotection and functionalisation of the subsequent P[*n*]A.[10] In a particularly marked example, in 2018, Zuilhof, Sue and co-workers reported the synthesis of a rim-differentiated P5A, in which each rim of the P5A was functionalised by an orthogonal protecting group, enabling facile post-macrocyclisation functionalisation of each rim in turn (Scheme 3.2 b).[11]

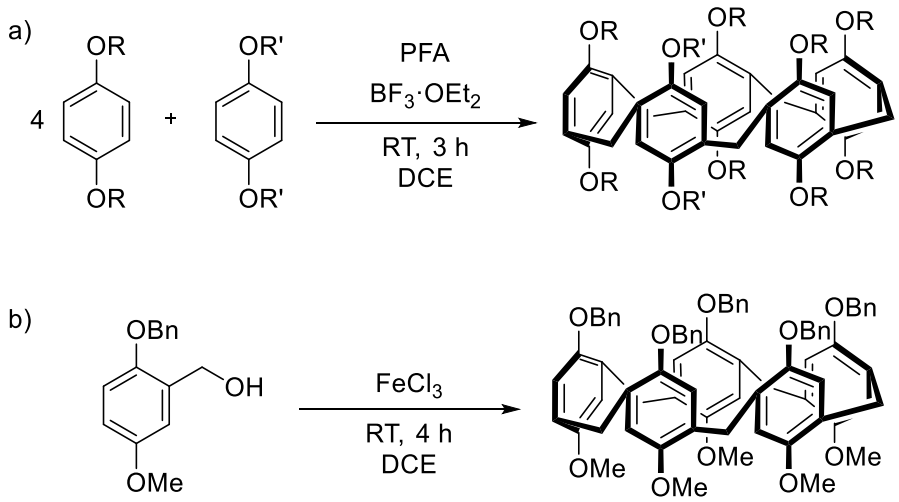

Scheme 3.2. Synthesis of functionalised P5As a) by statistical incorporation of a functionalised subunit, b) by a pre-orientated synthesis of a C_5 symmetric P5A with rim-differentiated orthogonal protecting groups.

3.1.2 P5As as Supramolecular Hosts

Ogoshi's first report of P5As demonstrated the ability of *per*-methoxy P5A to thread onto the alkyl chain of a viologen(4,4'-bipyridinium)-containing polymer,[5] with the threading of a dioctyl functionalised viologen guest observed through diagnostic marked upfield shifts in the guest ^{1}H NMR spectrum in acetone-d_6. In this case, the host-guest interaction arose through charge-transfer interactions between the electron-rich P5A cavity and the electron-deficient cationic viologen moiety. Such interactions were subsequently shown

to be more generic, with a *per*-hydroxy P5A able to associate with guests containing a range of paraquat and bis-pyridinium cationic motifs.[12]

The ability to functionalise P5As to target binding of a specific guest makes the P5A platform particularly attractive for supramolecular host-guest recognition. In 2012, Wang and co-workers reported the statistical incorporation of a single bis-urea functionalised benzene-1,4-diether motif into a P5A cyclic framework, which enabled pseudo[2]rotaxane binding of dicarboxylate salts in DMSO-d_6 through a combination of C—H···π interactions, arising between the P5A aryl rings and the alkyl backbone of the threaded guest, concomitant with HB interactions between the urea HB donor protons and the dicarboxylate anionic end groups (Figure 3.1 a).[13]

The inclusion of neutral guests within P5A hosts has also been reported. Stoddart and co-workers demonstrated the interpenetration of alkanediamines into a P5A with high binding affinities ($K_a > 10^4$ M^{-1}) in 1:1 *v/v* MeCN:H_2O (Figure 3.1 b), likely arising through a combination of C—H···π interactions and hydrophobic interactions.[14] Notably, the incorporation of a pyrene optical reporter group by a statistical synthesis of the P5A enabled the detection of host-guest threading by photoinduced electron transfer (PET) quenching of the pyrene emission.

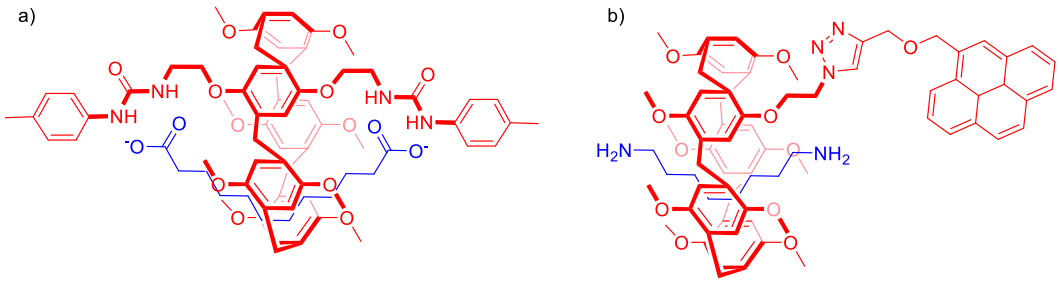

Figure 3.1. Previously reported P5A receptors. a) Dicarboxylate receptor reported by Wang and co-workers, b) alkanediamine optical sensor reported by Stoddart and co-workers.

The importance of dispersion interactions in the threading of neutral guests by P5As was powerfully demonstrated by Jia, Li and co-workers.[15] Considering the relative binding

strengths of 1,4-dihaloalkanes with *per*-ethoxy P5A in $CDCl_3$ solution, 1,4-difluorobutane might be expected to thread most strongly on account of fluorine possessing the highest electronegativity, leading to the most polarised alkyl backbone, resulting in strong C—H···π interactions. On the contrary, host-guest binding affinity was shown to increase with increased halogen polarisability, such that 1,4-di-iodobutane displayed the highest binding affinity in $CDCl_3$, highlighting the role of dispersion interactions in P5A host-guest interactions.

3.1.3 Mechanically Interlocked P5A Assemblies

As the host-guest threaded assemblies formed by P5As are pseudo[2]rotaxanes, perhaps unsurprisingly there has been interest in appending stopper groups to form rotaxanes with P5A macrocycles.[16-18] The first such report, by Stoddart and co-workers, was achieved by capping the pseudo[2]rotaxane assembly formed by the threading of 1,8-diamino-octane with *per*-methoxy P5A.[14] Reaction with 3,5-di-*tert*-butylbenzaldehyde, followed by reduction of the resulting imine formed the P5A-containing [2]rotaxane in a low yield of 7% (Figure 3.2 a).

Improving upon on the low MIM yield, Ogoshi and co-workers demonstrated the use of a CuAAC capping reaction on a pseudo[2]rotaxane formed by the threading of a P5A onto an axle-precursor containing a cationic pyridinium moiety.[18] The introduction of the charged group led to enhanced pseudo[2]rotaxane formation, leading to a 75% yield of [2]rotaxane after stoppering (Figure 3.2 b).

Following a report in which Li and co-workers demonstrated the strong threading of P5As onto electron deficient C_4 alkyl chains located between two triazoles,[19] Ogoshi and co-workers exploited the strong host-guest association between these motifs to form a

neutral pseudo[2]rotaxane which was capped by a double-stoppering CuAAC reaction to form [2]rotaxanes in 54% yield (Figure 3.2 c).[20]

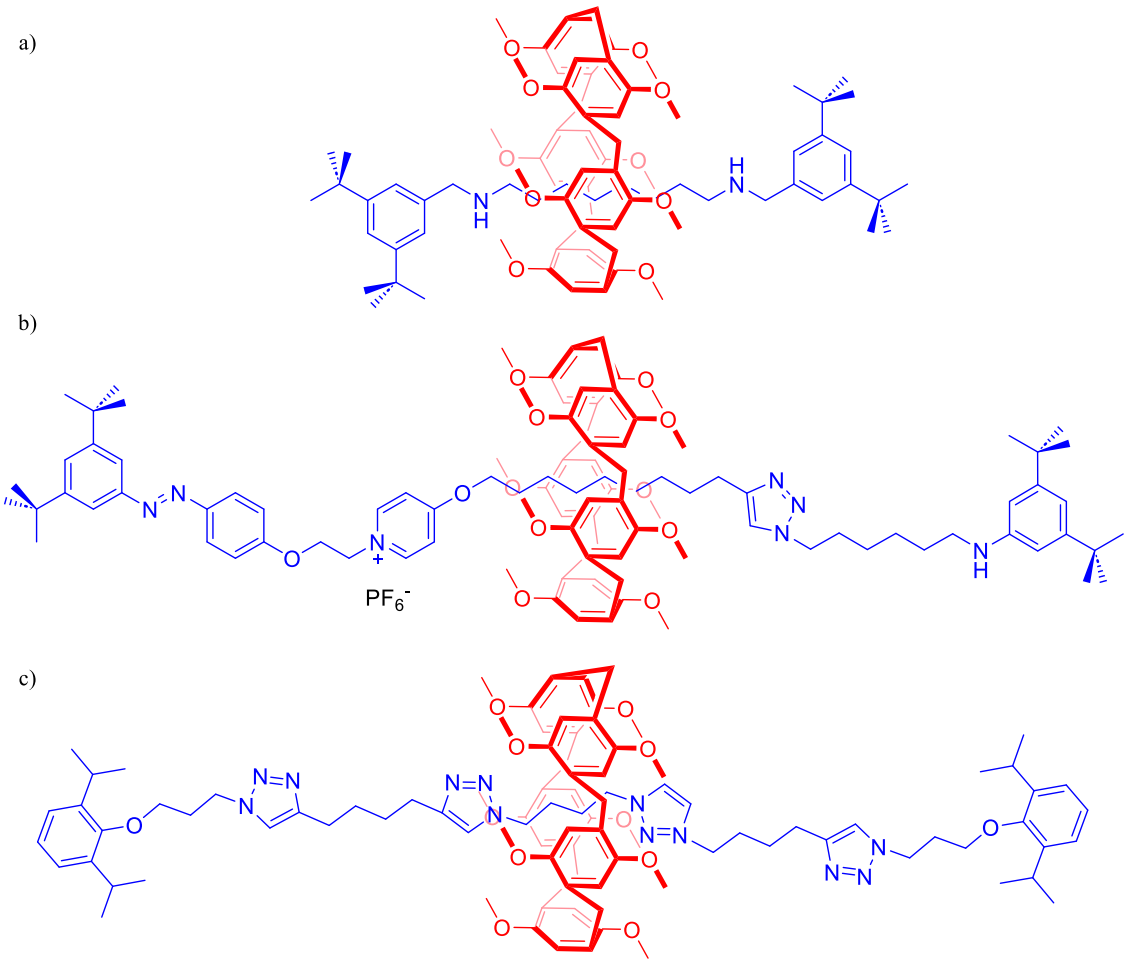

Figure 3.2. Previously reported [2]rotaxanes formed by stoppering of a P5A host-guest pseudo[2]rotaxane.

3.1.4 Project Aims

The serendipitous synthesis of interlocked [3]rotaxanes described in Chapter 2 demonstrated that AMT MIM-forming reactions performed on pseudo[2]rotaxanes assembled via strong inter-component interactions can afford higher order interlocked products in appreciable yields. The synthetic route used by Ogoshi to prepare the P5A [2]rotaxane shown in Figure 3.2 c,[20] where a pseudo[2]rotaxane assembly is stabilised by a mixture of axle C—H···P5A π and triazole C—H···O P5A side chain HB interactions, has clear parallels to the synthetic methods employed in Chapter 2, in which strongly

associated pseudo[2]rotaxane assemblies were stabilised by macrocycle pyridyl···Zn(II) metalloporphyrin axle interactions. More recent reports of P5A [3]rotaxanes have typically involved either post-synthetic modification to join two [2]rotaxanes together by a stopper exchange reaction,[21] or by stoppering higher order polypseudorotaxanes,[22, 23] both of which are synthetically more demanding than direct [3]rotaxane synthesis.

Thus, it was of interest to adapt Ogoshi's CuAAC 'click' rotaxination reaction by employing conventional AMT rotaxane synthetic methodologies to a P5A-containing pseudo[2]rotaxane as a potential route to higher order [4]rotaxanes, containing a P5A macrocycle and two AMT-compatible pyridyl macrocycles (Scheme 3.3).

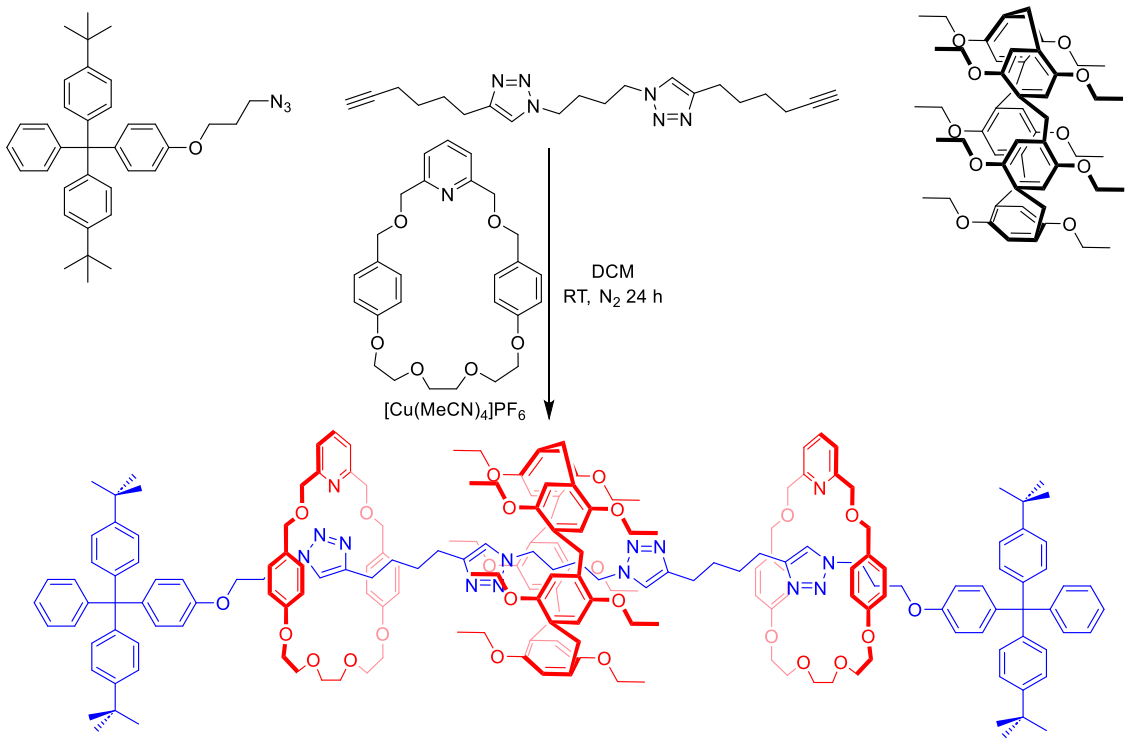

Scheme 3.3. Targeted higher order rotaxane synthesis employing AMT methodology.

3.2 Towards Active Metal Synthesis of Higher Order [*n*]Rotaxanes

The AMT MIM methodology used for the synthesis of the target higher order rotaxanes required the initial preparation of a bis-triazole axle precursor as described by Ogoshi and co-workers,[20] along with a novel pyridyl macrocycle capable of AMT reactions.

3.2.1 Synthesis of a P5A [2]Rotaxane

The bis-triazole containing bis-alkyne **3.1** was synthesised according to a literature procedure.[20] 1,4-Dibromobutane was stirred in DMSO with NaN_3 to afford 1,4-diazidobutane in quantitative yield, which was bench-stable despite the low carbon:nitrogen ratio.[24] The obtained 1,4-diazidobutane underwent a bis-CuAAC click reaction with 20 equivalents of octa-1,7-diyne to form the target diyne axle precursor **3.1** in 72% yield (Scheme 3.4).

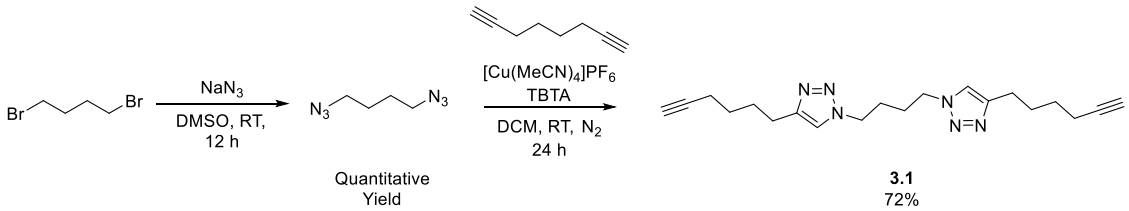

Scheme 3.4. Synthesis of axle precursor bisalkyne **3.1**.

Per-ethoxypillar[5]arene, **3.2**, was prepared by a literature procedure,[5] in which 1,4-diethoxybenzene and PFA were condensed in the presence of $BF_3{\cdot}OEt_2$, with DCE as a templating solvent, affording the target P5A **3.2** in 21% isolated yield (Scheme 3.5).

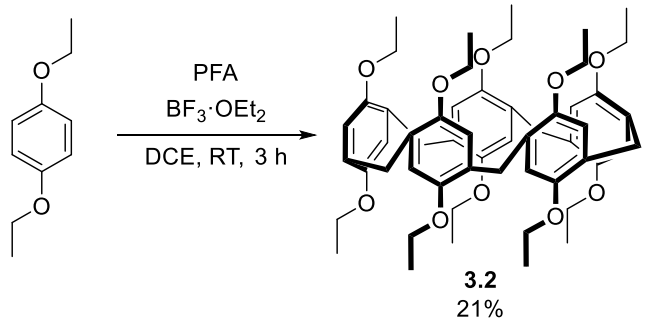

Scheme 3.5. Synthesis of perethoxypillar[5]arene **3.2**.

With axle precursor **3.1** and P5A **3.2** in hand, preliminary ^{1}H NMR pseudorotaxane assembly studies were performed in $CDCl_3$. Pleasingly, the ^{1}H NMR spectrum of an equimolar $CDCl_3$ solution of **3.1** and **3.2** showed significant evidence of interpenetration, with the threading/dethreading process being slow on the NMR timescale, allowing the ^{1}H resonances associated with the pseudorotaxane and the free axle to be simultaneously observed (Figure 3.3). In particular, the central axle precursor methylene proton resonances *7* and *8* are shifted markedly upfield, with *8* displaying a negative chemical shift, by the ring-currents of the P5A aromatic rings, strongly evidencing threading through the cavity. Quantitative ^{1}H NMR studies revealed 80% threading of **3.1** by **3.2** in a 1 mM equimolar $CDCl_3$ solution at 298 K.

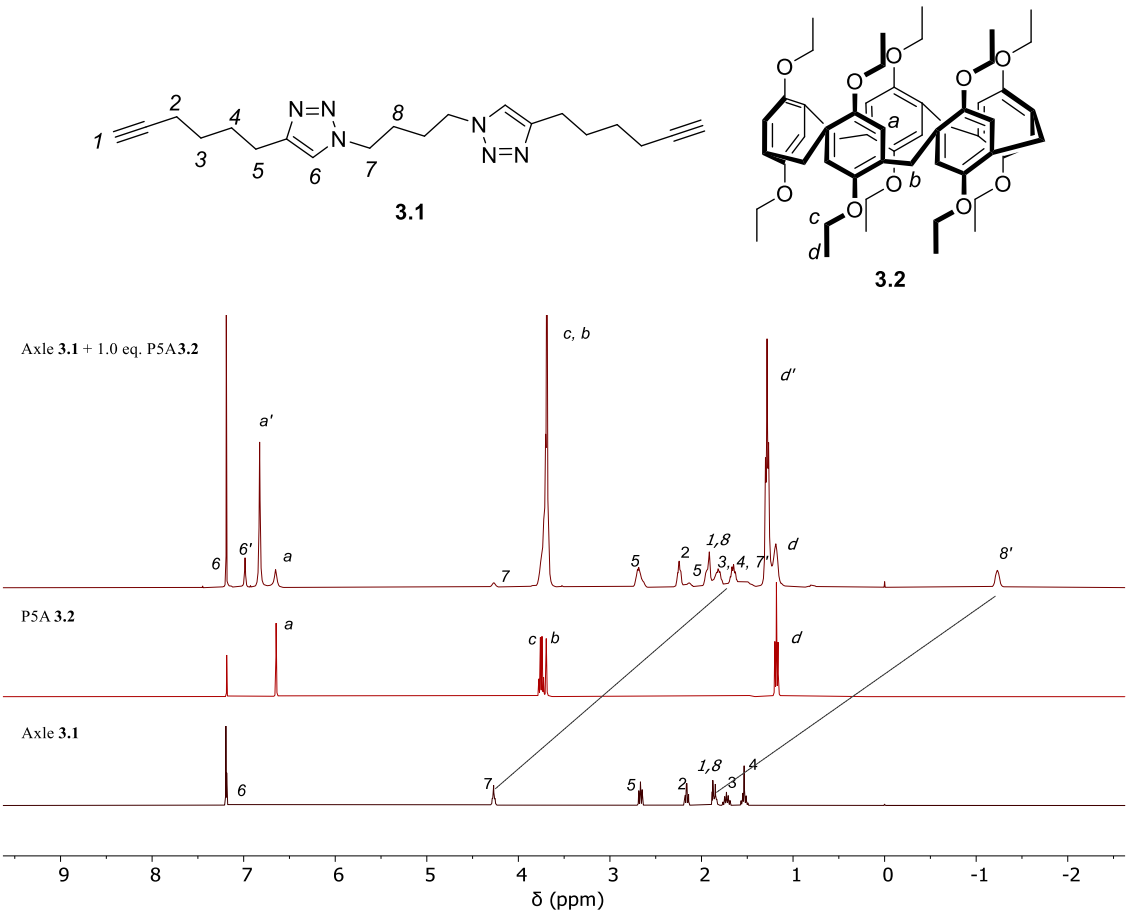

Figure 3.3. Stacked ^{1}H NMR spectra (500 MHz, $CDCl_3$, 298 K) of P5A **3.2**, axle synthon **3.1** and an equimolar solution of **3.1** and **3.2**. ' Denotes corresponding resonance in pseudorotaxane.

Having established evidence of strong pseudorotaxane assembly formation in equimolar solutions of **3.1** and **3.2**, a CuAAC stoppering reaction to form a [2]rotaxane was targeted. The novel terphenyl stopper azide **3.3** was synthesised, as bulky stoppers of comparable size are known to stopper rotaxanes containing macrocycles of a similar size (Scheme 3.6).[25] The stopper alcohol precursor was prepared in accordance with a literature procedure.[25] 4-*Tert*-butylbromobenzene underwent a Grignard reaction with methyl benzoate to form bis(p-*tert*-butylphenyl)phenylmethanol, followed by an addition reaction with phenol under acidic melt conditions. Reaction of commercial 3-bromo-1-propanol with NaN_3 at room temperature gave 3-azido-1-propanol in quantitative yield.[26] Tosylation of the azido-alcohol formed 3-azidopropyl 4-methylbenzenesulfonate, which readily underwent an S_N2 reaction with the stopper precursor alcohol to afforded the stopper azide **3.3** in 67% yield.

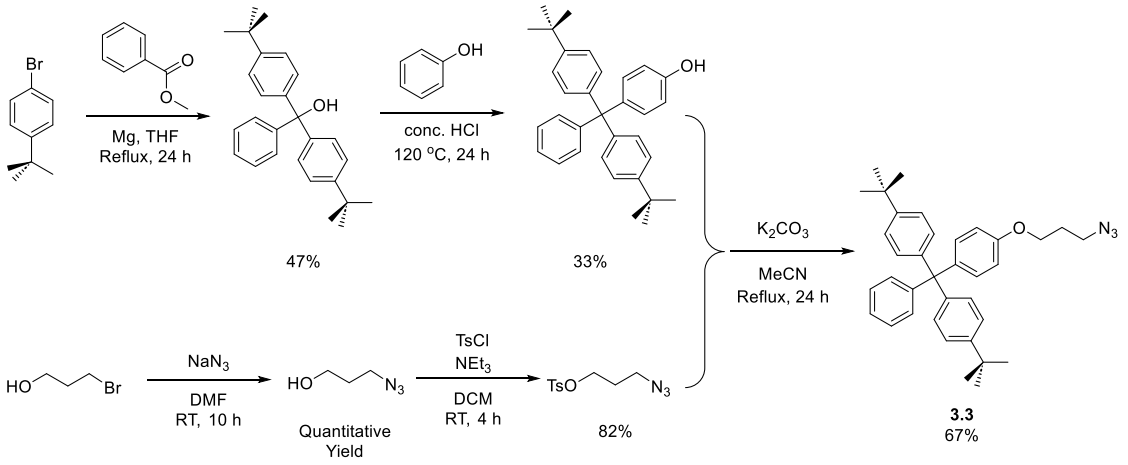

Scheme 3.6. Synthesis of stopper azide **3.3**.

A CuAAC rotaxane stoppering click reaction, between the pseudo[2]rotaxane formed between **3.1** and **3.2**, and stopper azide **3.3** was undertaken, in which 5 equivalents of P5A were employed to maximise pseudorotaxane threading (Scheme 3.7). Pleasingly, after 24 hours, TLC analysis revealed formation of [2]rotaxane **3.4**, along with the non-interlocked axle. Preparative TLC purification afforded **3.4** in 27% yield.

Characterisation of **3.4** by ^{1}H NMR confirmed the P5A wheel predominately resides over the central bis-triazole butyl linker, with similar marked upfield perturbations to those observed upon the pseudo[2]rotaxane assembly studies (Figure 3.4).

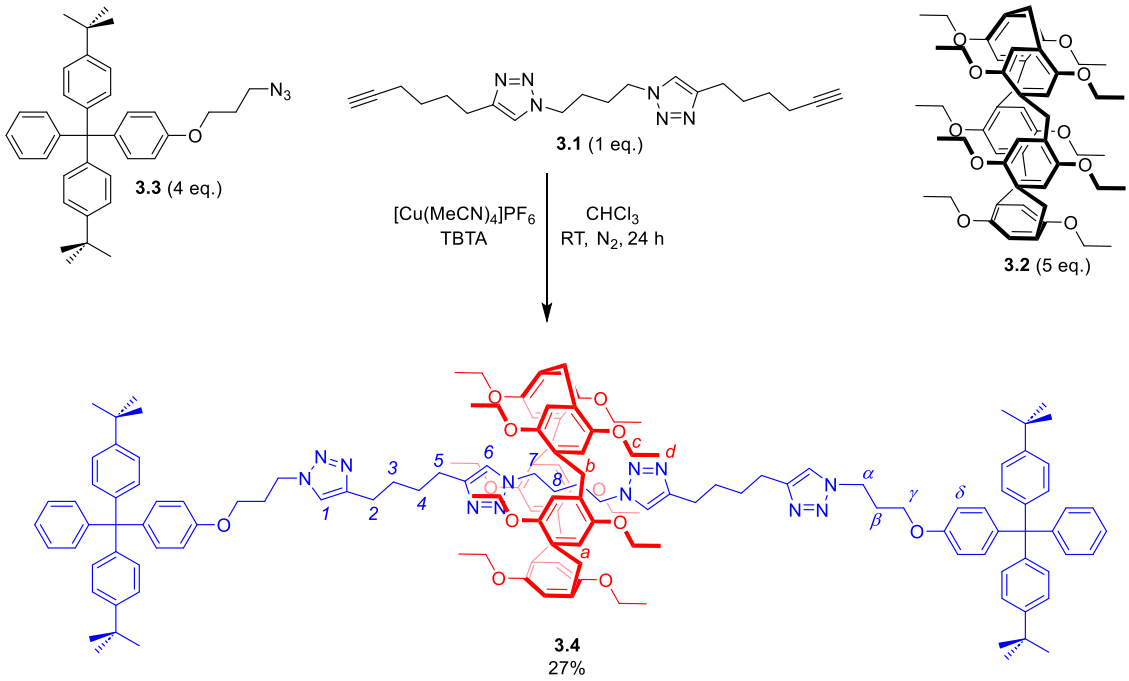

Scheme 3.7. Synthesis of [2]rotaxane **3.4**.

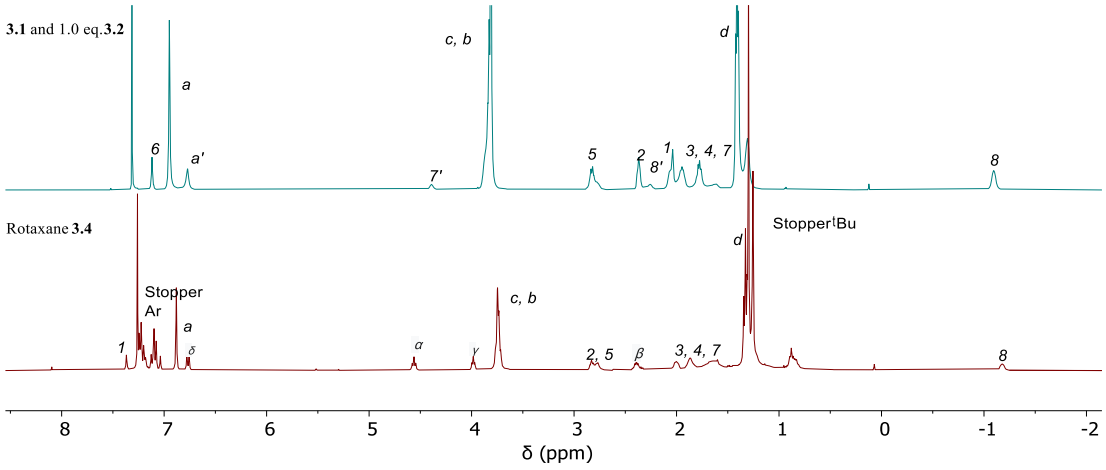

Figure 3.4. Stacked ^{1}H NMR spectra (500 MHz, $CDCl_3$, 298 K) of [2]rotaxane **3.4** and an equimolar solution of **3.1** and **3.2**. ' Denotes corresponding resonances in free (non-threaded) pseudorotaxane components.

3.2.2 Attempted Synthesis of Higher Order Rotaxanes

Encouraged by the formation of [2]rotaxane **3.4** by a CuAAC reaction, without the need to employ an exogenous templating method, it was anticipated that higher order [3] or [4]rotaxanes may be accessible using an AMT rotaxination methodology. In order to

investigate this possibility, the pyridyl macrocycle **3.5** was prepared in a similar fashion to the synthesis of macrocycle **2.3**, replacing the starting tosylate with triethylene glycol ditosylate (Scheme 3.8 a).

Initial AMT rotaxination studies were performed using the same reagent stoichiometries as for the synthesis of **3.4**, using one equivalent of Cu(I) catalyst pre-complexed with macrocycle **3.5** (Scheme 3.8 b). After 72 h, TLC analysis revealed the formation of two potential MIM products, which were isolated by preparative TLC. The two products were subsequently identified by ^{1}H NMR as macrocycle **3.5**-containing [2]rotaxane, **3.6** (18% yield), and the P5A [2]rotaxane **3.4** (24% yield), with no higher order interlocked structures detected.

This suggests the P5A-threaded bis-alkyne pseudo[2]rotaxane assembly is too sterically hindered to undergo AMT with the Cu(I) complexed pyridyl macrocycle. Thus, AMT rotaxane synthesis only occurs on the dethreaded bis-alkyne, resulting in only [2]rotaxane products **3.4** and **3.6** being isolated.

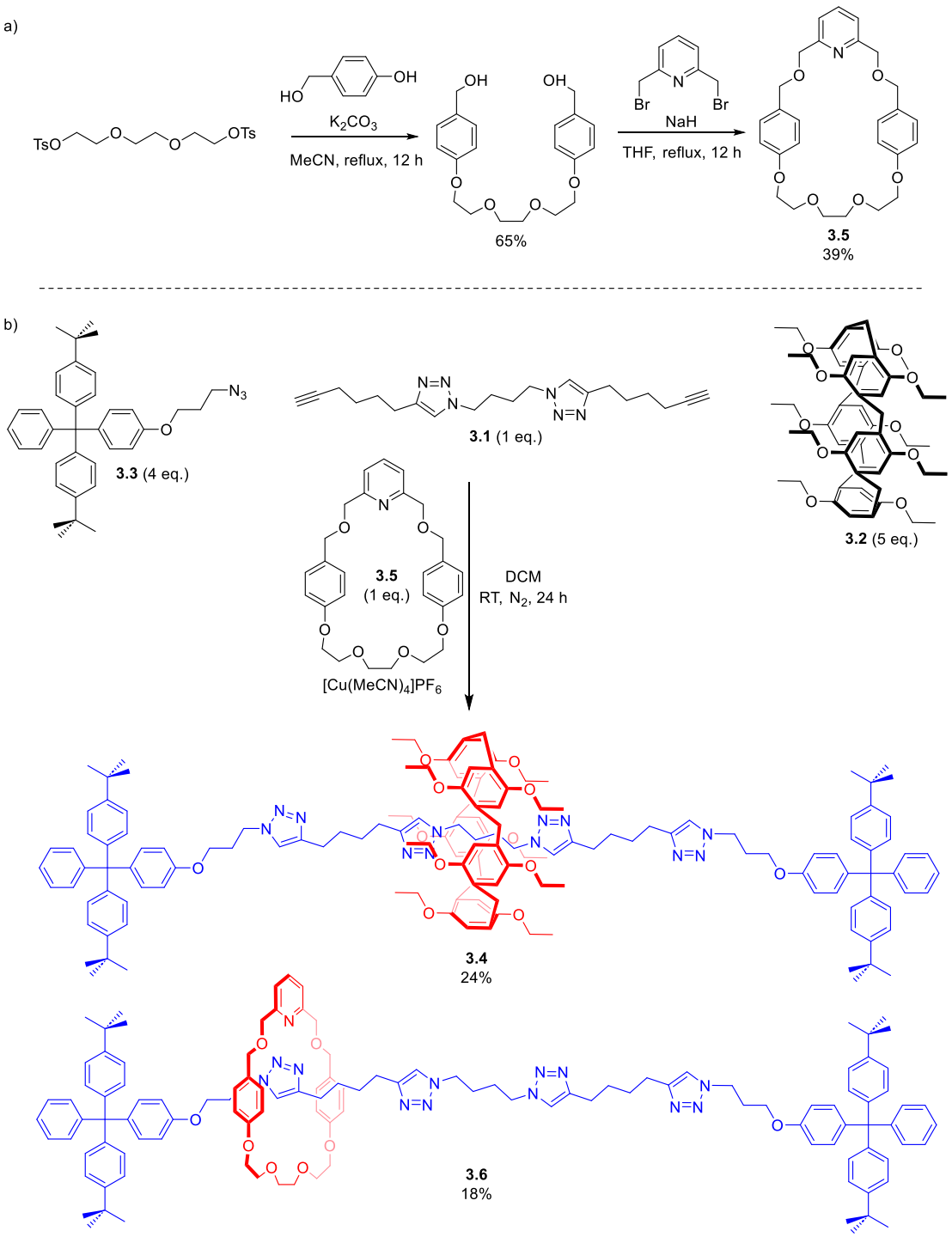

Scheme 3.8. a) Synthesis of macrocycle **3.5**, b) attempted synthesis of higher order [3]- and [4]-rotaxane affording only [2]rotaxanes **3.4** and **3.6**.

The rate of AMT rotaxane formation is known to be highly sensitive to steric effects.[27] Therefore the *per*-ethoxy P5A side-chains were replaced by methoxy groups, by repeating the P5A synthesis using 1,4-dimethoxybenzene in place of 1,4-diethoxybenzene to form *per*-methoxy P5A **3.7** (Scheme 3.9 a), and an elongated axle,

3.8, was targeted by CuAAC bis-click reaction of 1,4-diazidobutane with longer deca-1,9-diyne (Scheme 3.9 b). ^{1}H NMR pseudorotaxane studies confirmed the ability of **3.7** to thread axle **3.8** in an analogous manner to, and with similar binding affinities to, **3.1** and **3.2**.

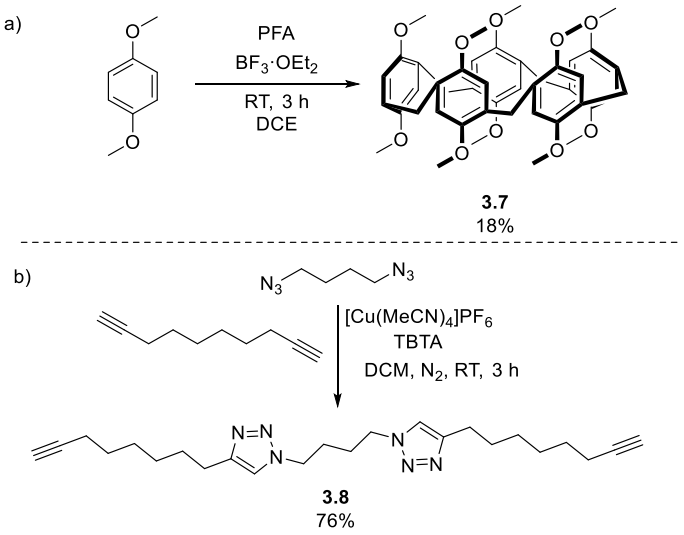

Scheme 3.9. a) Synthesis of P5A **3.7**, b) synthesis of elongated axle precursor **3.8**.

Repeating the AMT rotaxane synthesis with **3.7** as the P5A component, and **3.8** as the axle component, unfortunately did not lead to the observation of any higher order [3] or [4]rotaxane structures by ESI-MS, *in situ* ^{1}H NMR or TLC analysis. The size of the pyridyl macrocycle was also increased, using **2.3** in place of **3.5**, as the longer polyether linker would be expected to lead to further conformational flexibility for the macrocycle in the AMT reaction,[28] however no higher order rotaxanes were observed when **2.3** was used in place of **3.5** in the AMT reaction.

3.2.3 Conclusions and Future Work

A bis-azide containing two triazoles separated by a C_4 alkyl chain, **3.1**, previously reported by Ogoshi, was shown to form a pseudo[2]rotaxane assembly with P5A **3.2**, with 80% interpenetrated assembly observed for an equimolar 1 mM solution in $CDCl_3$. Stoppering of this assembly by the bulky stopper azide **3.3** afforded [2]rotaxane **3.4**¸ in which the P5A macrocycle component preferentially resides over the central C_4 alkyl

chain. Thus, in the pseudo[2]rotaxane, the peripheral alkynes protrude from the P5A host, and were expected to be available for subsequent AMT rotaxination reactions. However, the steric bulk of the pseudorotaxane assembly prevented the isolation of higher order [3]- or [4]-rotaxanes. Increasing the length of the axle, or size of the macrocycle did not enable the synthesis of higher order rotaxanes.

The cation binding studies in Chapter 2 demonstrated the ability of Li^+ to be bound between a macrocycle component pyridyl moiety and an axle component triazole. Future work will seek to synthesise hetero[3]rotaxanes by combining Li^+ templated threading of a pyridyl macrocycle with P5A threading onto an electron deficient axle precursor, to form hetero-pseudo[3]rotaxanes, which could be subsequently stoppered by a CuAAC 'click' rotaxination reaction providing a potential route to the challenging synthesis of P5A-containing hetero[3]rotaxanes (Scheme 3.10).

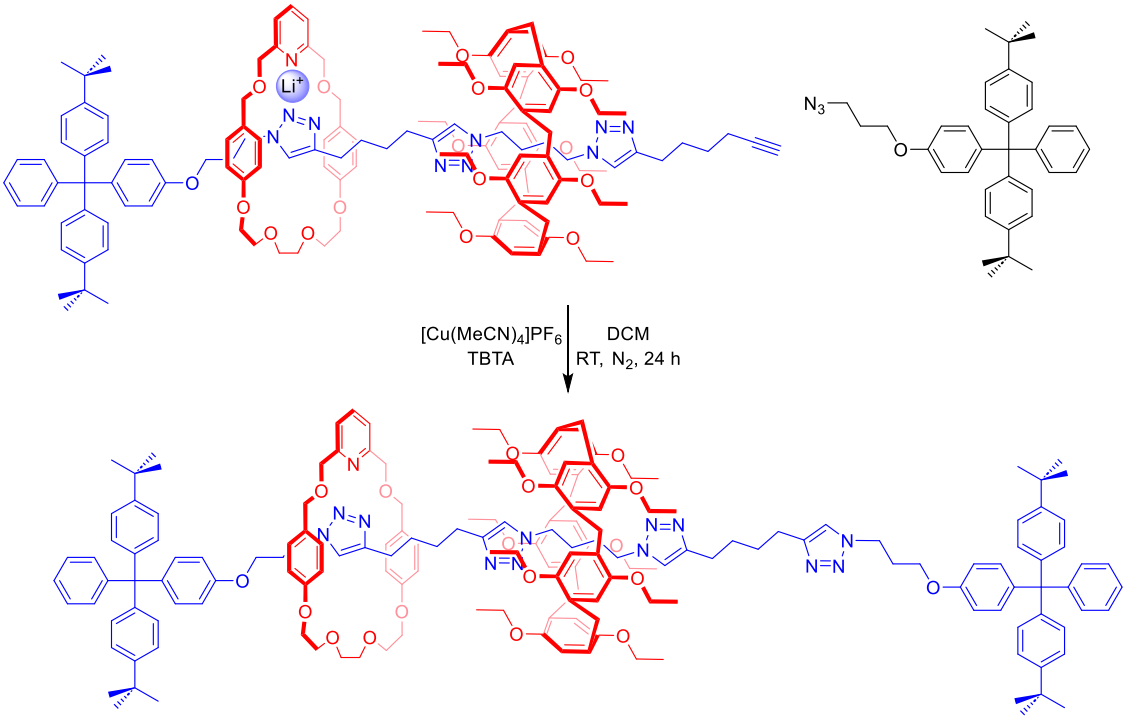

Scheme 3.10. Potential dual lithium cation templation methodology for forming hetero[3]rotaxanes by stoppering of a pseudo[3]rotaxane.

3.3 Synthesis of Interlocked Molecules by an Inorganic Click Reaction[a]

3.3.1 Introduction

Given the propensity of organometallic species to be stabilised by their incorporation into sterically shielded environments,[29-33] the incorporation of inorganic motifs into MIM topologies can serve as a route to stabilise air- and moisture-sensitive components by exploitation of the mechanical bond effect.[34, 35] Despite this, the incorporation of inorganic groups into MIMs remains underexplored due to the lack of readily accessible synthetic methodologies to incorporate such groups into interlocked architectures, with initial reports by Ogino and co-workers employing dative covalent bond formation to stopper cyclodextrin/diaminoalkane pseudorotaxanes with Co(III) complexes in low (*c.* 7%) yields.[36, 37] More recently, Gladysz and co-workers demonstrated the AMT synthesis of [2]rotaxanes with pre-functionalised Pt(II)-stopper containing axle components,[38, 39] while, in 2023, John, Szysko and co-workers demonstrated the AMT synthesis of inorganic-organic rotaxanes stoppered by silsesquioxane cage-like stoppers.[40]

Phosphaalkynes (R−C≡P), which are valence isoelectronic with alkynes, undergo 1,3-dipolar cycloaddition reactions with azides to afford 3H-1,2,3,4-triazaphospholes, bearing clear similarities to alkyne-azide CuAAC click chemistry.[41, 42] However, the click chemistry of phosphaalkynes remains challenging to access owing to their highly pyrophoric nature.[43] In 2021, Jones, Müller and co-workers described the stabilisation of the cyaphide ($C{\equiv}P^-$) ion by platinum complexation, and demonstrated that the complex undergoes click reactions with azides analogous to those of phosphaalkynes.[44] The same year, Goicoechea and co-workers reported a 'cyaphide transfer reagent' which undergoes

[a] *The work described in this section was conducted in collaboration with graduate student Alex Mapp, in the Goicoechea group, who performed the organometallic synthesis.*

salt metathesis reactions to form a range of metal cyaphide complexes, including a Au cyaphide complex (Figure 3.5).[45] The same group subsequently showed this Au cyaphide complex underwent cycloaddition reactions with a range of aliphatic and aromatic azides,[46] however the resulting complexes exhibited only limited air- and moisture-stability. It was therefore hoped the utilisation of the previously reported Au cyaphide complex **3.9** as a stoppering group for a P5A containing [2]rotaxane would lead to a mechanical bond effect stabilisation of the resulting organometallic axle groups.

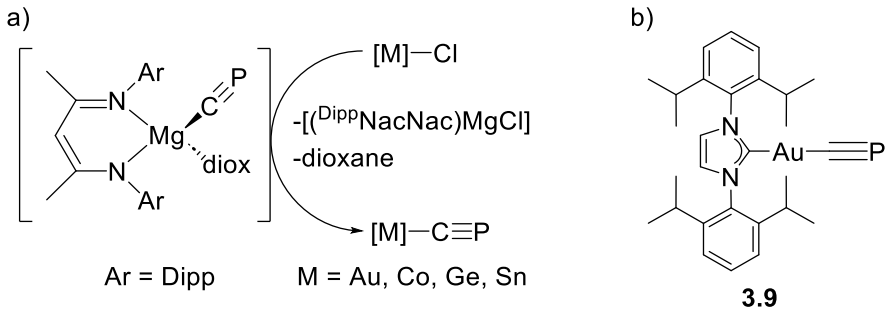

Figure 3.5. Goicoechea and co-workers' 'cyaphide transfer reagent', b) stopper precursor Au cyaphide complex **3.9**.

3.3.2 Synthesis of First Generation [2]Rotaxane

The gold cyaphide stopper precursor, **3.9**, was synthesised by Alex Mapp, in accordance with a literature procedure.[46] It was anticipated that **3.9** would undergo a copper-free, mechanical bond forming, cycloaddition stoppering reaction with a pseudo[2]rotaxane formed by the threading of a bis-alkyl azide and P5A, to form the target inorganic [2]rotaxane **3.10** (Figure 3.6).

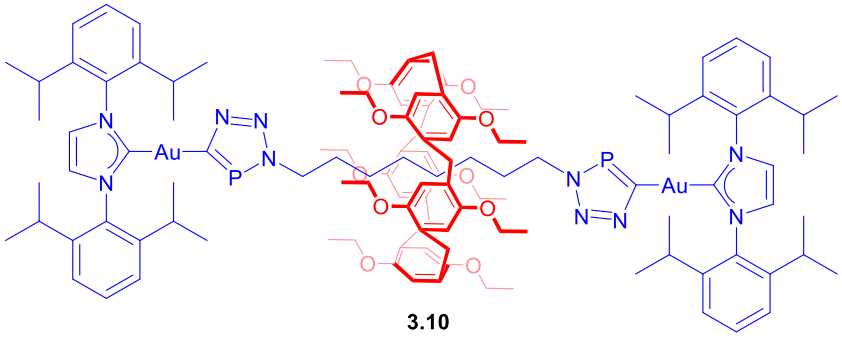

Figure 3.6.Target organometallic [2]rotaxane **3.10**.

The ability of *per*-ethylated P5A, **3.2**, to thread 1,8-diazido-octane in benzene was confirmed by ^{1}H NMR binding titrations. Successive additions of 1,8-diazido-octane to a benzene-d_6 solution of **3.2** led to the observation of marked downfield shifts in all P5A proton resonances, consistent with threading in a fast exchange regime (Figure 3.7). Fitting of the P5A aromatic resonance, *a*, shift with *Bindfit* enabled quantification of the binding affinity (K_a = 122 M^{-1}).[47]

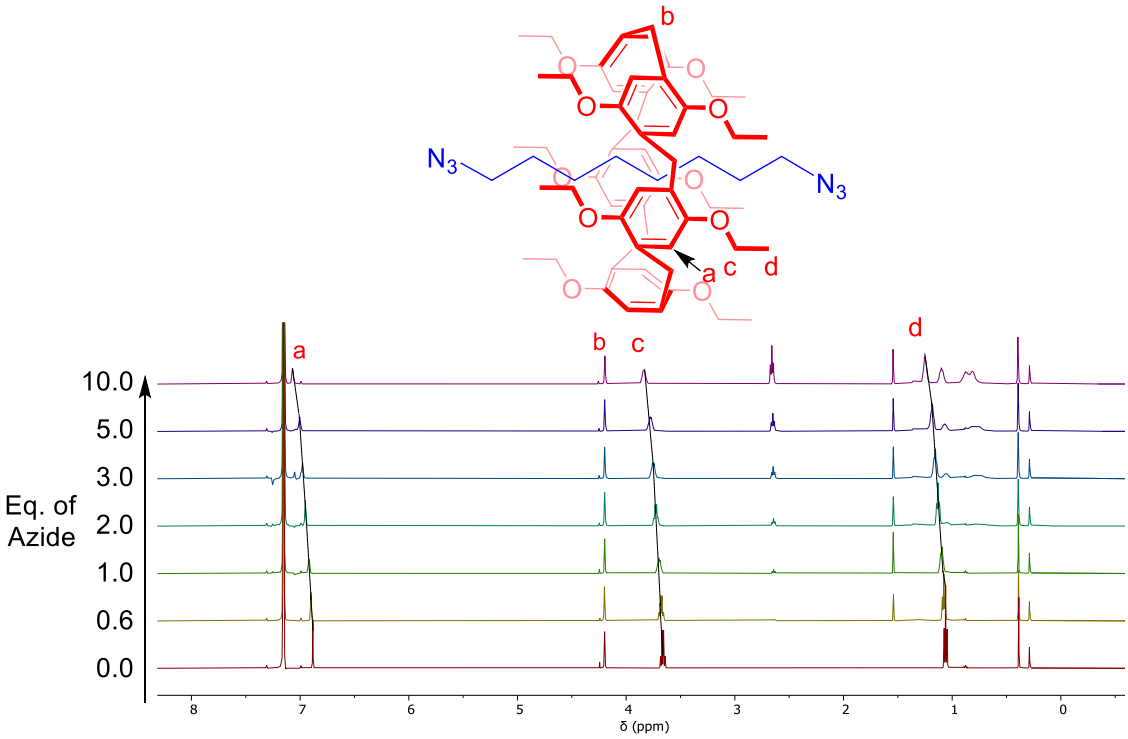

Figure 3.7. ^{1}H NMR (500 MHz, C_6D_6, 298 K) spectra of **3.2** upon successive additions of 1,8-diazido-octane.

With the threading of the axle precursor bis-azide by **3.2** confirmed, the synthesis of [2]rotaxane **3.10** was targeted (Scheme 3.11). P5A macrocycle **3.2** was pre-complexed with 1,8-diazido-octane upon dissolution in the minimum amount of benzene under an inert atmosphere at room temperature. Five equivalents of P5A were used to maximise the degree of pseudorotaxane formation and minimise the amount of free 1,8-diazido-octane in the reaction mixture. Two equivalents of the stopper **3.9** was then added and the mixture stirred overnight at room temperature, after which the rotaxane **3.10** and non-

interlocked axle **3.11** were observed *in situ* by the formation of two new $^{31}P\{^{1}H\}$ NMR environments at δ = 198.6 ppm and 199.9 ppm respectively, consistent with the formation of triazaphospholes.[45] Impressively, repeated $^{31}P\{^{1}H\}$ NMR spectroscopy of an aliquot of the crude reaction mixture, not stored under inert conditions, demonstrated a dramatic increase in the air- and moisture-stability of **3.10** and **3.11** over the precursor **3.9** Au complex (Figure 3.8).

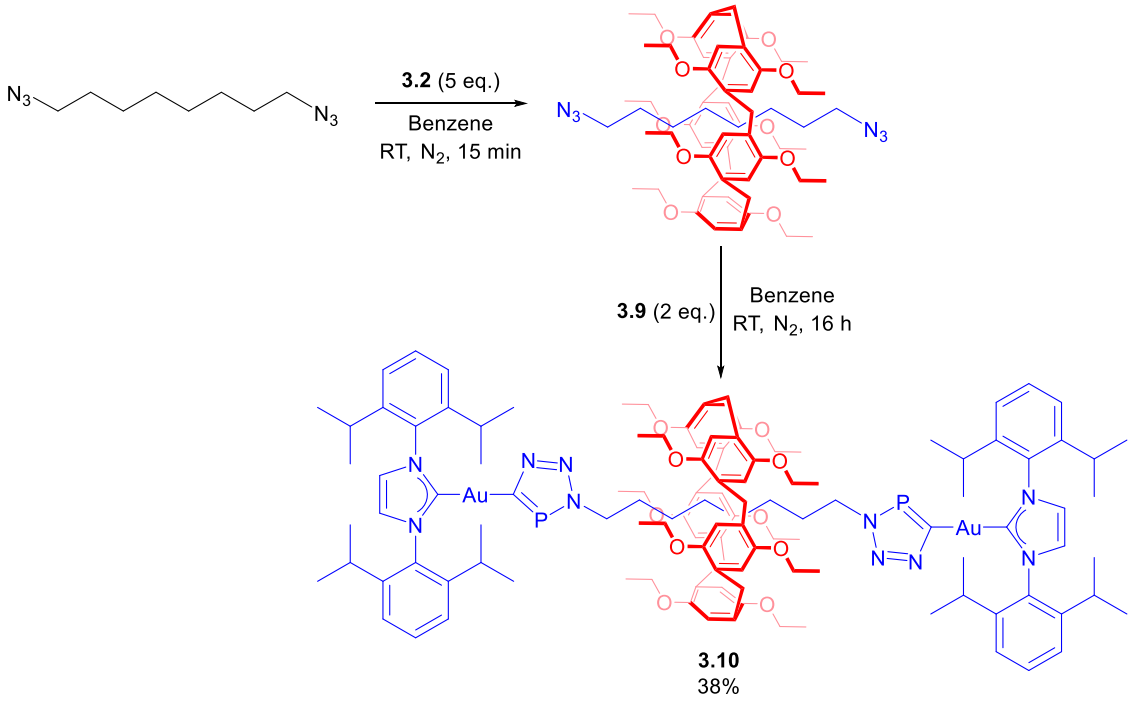

Scheme 3.11. Synthesis of [2]rotaxane **3.10**.

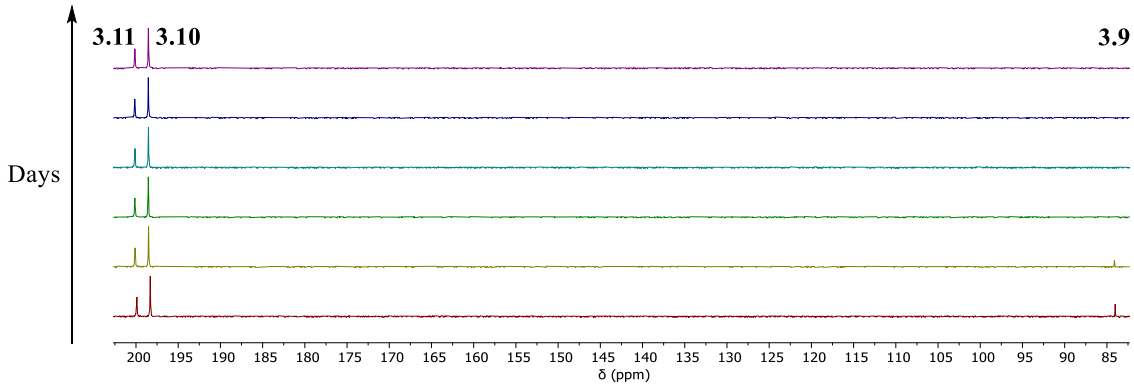

Figure 3.8. $^{31}P\{^{1}H\}$ NMR (162 MHz, C_6D_6, 298 K) of crude reaction mixture from reaction shown in Scheme 3.11, demonstrating the increased air- and moisture-stability of **3.10** and **3.11** over **3.9**.

The crude product was isolated by filtration and, impressively, was stable to purification by column chromatography to afford the target [2]rotaxane **3.10** in 38% yield. In marked contrast, the non-interlocked axle, a side-product of the rotaxane synthesis, was not stable to column chromatography, highlighting the remarkable stability afforded by the mechanical bond. The non-interlocked axle **3.11**, was therefore synthesised separately by stirring stoichiometric amounts of **3.9** and 1,8-diazido-octane in benzene overnight, and purified by washing with dry hexane. The mechanical bond enhancement to the rotaxane stability was further demonstrated by the bench stability of the pure rotaxane product**,** **3.10**, which demonstrated air- and moisture-stability even after 30 days, whereas substantial degradation of the axle, **3.11**, was observed by ^{31}P NMR spectroscopy over the same time span.

Comparison of the ^{1}H NMR spectra of **3.10** with the non-interlocked components, **3.2** and **3.11**, reveals marked upfield shifts in the ^{1}H resonances of the axle in the [2]rotaxane, confirming the formation of the interlocked structure (Figure 3.9). Interestingly, compared to the pseudorotaxane, the proton resonance for the methylene resonance closest to the triazaphospholes, *4*, was shifted downfield, likely due to the steric repulsion from the stopper preventing the P5A from translocating the full length of the axle. Furthermore, the oxygen-through-annulus rotation of the P5A is inhibited in the rotaxane, preventing interconversion of the planar chiral conformers of the P5A, resulting in the observed diastereotopic splitting of the P5A methylene protons.[17] The formation of the [2]rotaxane was further confirmed by single crystal XRD studies on crystals of **3.10** grown upon standing of the benzene reaction mixture (Figure 3.10). Examination of the solid state structure of **3.10** reveals C–H···π distances between the threaded alkyl chain hydrogen atoms and the π-planes of the P5A macrocycle in the range of 2.81−2.87 Å, a shorter distance than the sum of the van der Waals' radii (3.05 Å),[48] implying the presence

of significant C–H···π interactions. Such interactions are known to be stronger than dispersion interactions,[49] and as such are the likely driving force for formation of the pseudo[2]rotaxane between P5A **3.2** and 1,8-diazidooctane.[9]

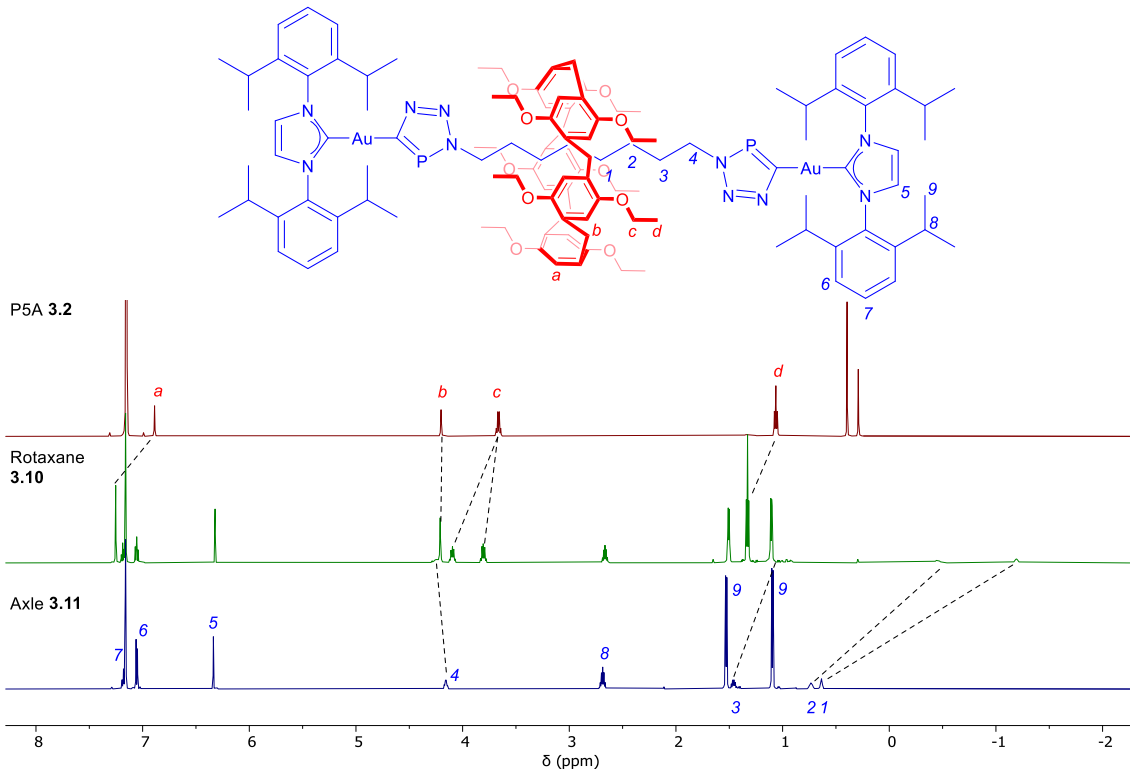

Figure 3.9. Stacked ^{1}H NMR (400 MHz, C_6D_6, 298 K) spectra of [2]rotaxane **3.10** and the non-interlocked components, P5A **3.2** and axle **3.11**.

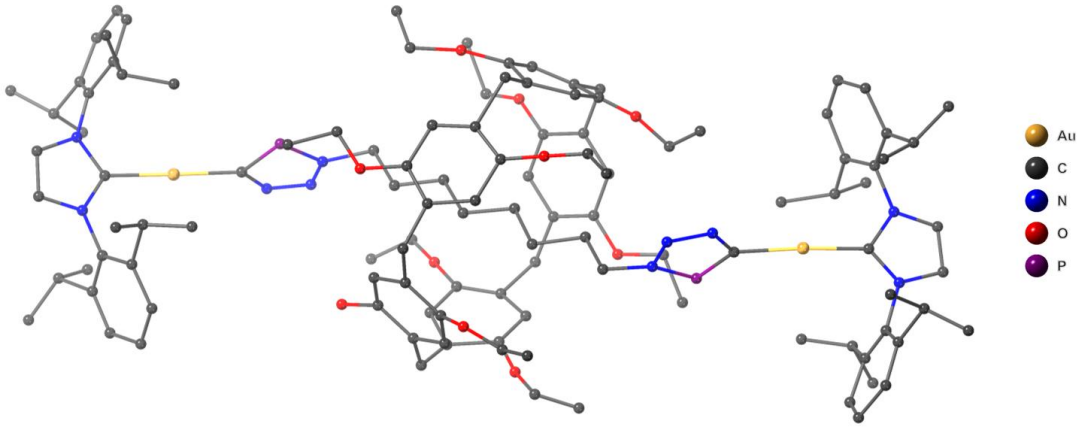

Figure 3.10. Single crystal XRD structure of **3.10**, solved by Prof. Jose M. Goicoechea. Hydrogen atoms omitted for clarity.

3.3.3 Synthesis of a [2]Rotaxane by a Stoichiometric Inorganic Click Reaction

The relatively weak association of **3.2** with 1,8-diazido-octane necessitated the use of five equivalents of P5A to assemble a sufficient amount of pseudo[2]rotaxane for subsequent rotaxane synthesis. To improve the degree of pseudorotaxane formation, and enable the synthesis of [2]rotaxanes in a stoichiometric inorganic click reaction, a bis-azide axle precursor containing two triazoles, expected to thread more strongly given the strong threading of **3.1** established earlier, was targeted.

1,4-Diazidobutane underwent a CuAAC click reaction with 1-bromo-but-3-yne to afford the bis-bromide **3.12** in 62% yield. **3.12** underwent an S_N2 reaction with NaN_3 to afford the target bis-azide thread **3.13**, in 56% yield, after purification by column chromatography (Scheme 3.12).

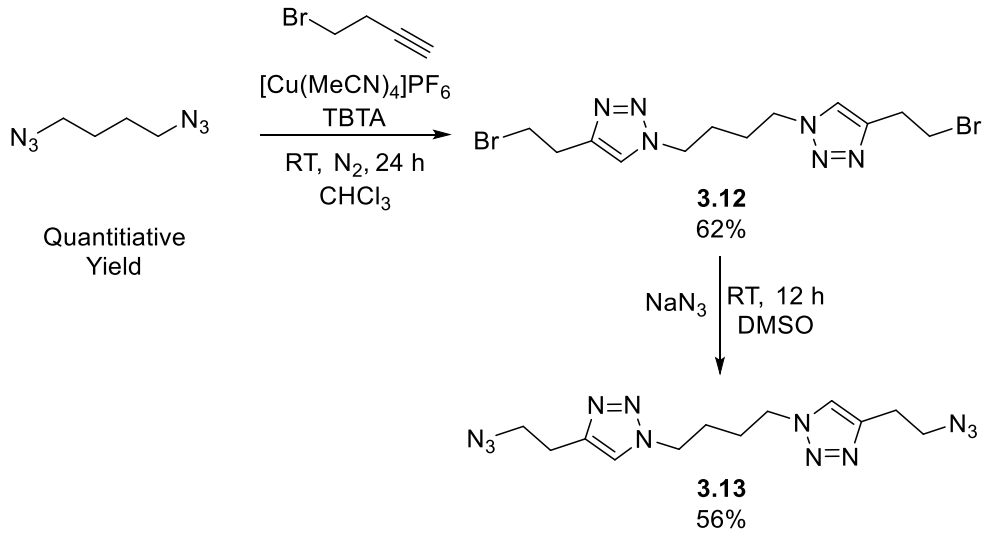

Scheme 3.12. Synthesis of axle precursor bis-azide **3.13**.

Pleasingly, ^{1}H NMR titration binding studies of **3.2** and **3.13** in benzene-d_6 displayed significant downfield perturbations in the ^{1}H NMR resonances of the P5A proton environments (Figure 3.11), which, upon *Bindfit* analysis revealed a significantly augmented host-guest binding constant for **3.13** compared to 1,8-diazido-octane (K_a =

12500 M^{-1}). Such an increased binding affinity likely arises from strong C−H···O HB interactions between the triazole motifs and the P5A side chains.[50]

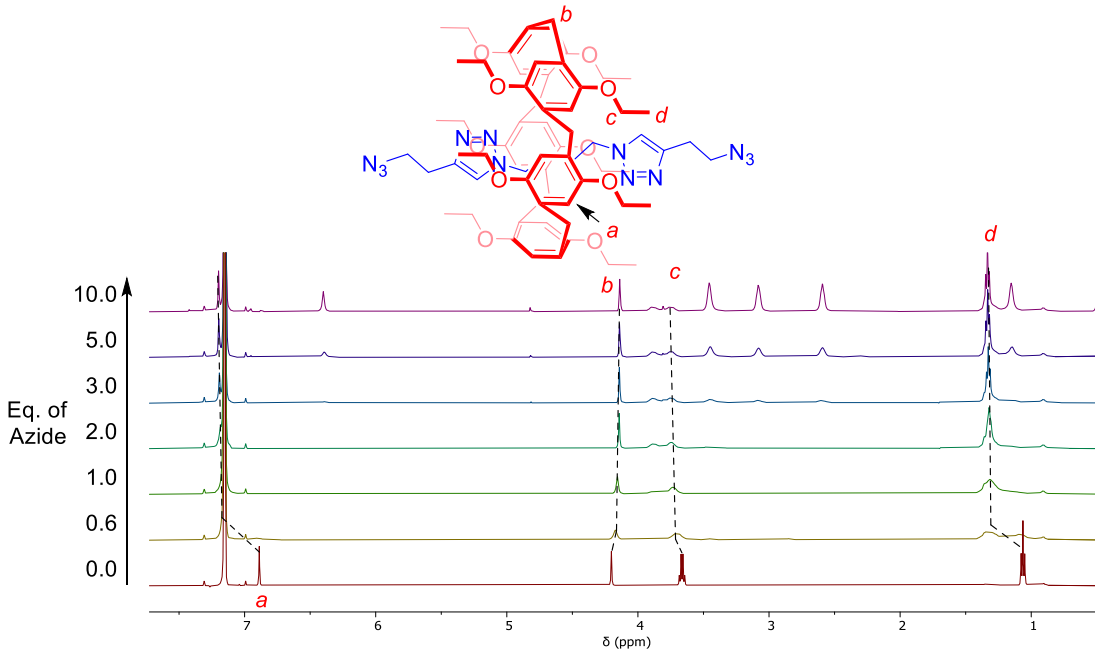

Figure 3.11. ^{1}H NMR (500 MHz, C_6D_6, 298 K) spectra of **3.2** upon successive additions of **3.13**.

With the axle precursor **3.13** being demonstrated to effectively form a pseudo[2]rotaxane with the P5A macrocycle, the synthesis of a [2]rotaxane using stoichiometric quantities of reagents was attempted. An equimolar mixture of axle precursor bis-azide **3.13** and P5A **3.2** were dissolved in the minimum amount of benzene and the mixture left to precomplex. Two equivalents of stopper **3.9** were added and the mixture stirred overnight under an inert atmosphere. After stirring overnight, the rotaxane product was visible by ESI-MS and TLC (Scheme 3.13). Rotaxane **3.14** was obtained after column chromatography in 65%, a significantly higher yield than that obtained in the synthesis of **3.10**, attributed to the enhanced stability of the pseudo[2]rotaxane assembly with the triazole-containing axle precursor. The increase in yield is particularly notable considering the use of stoichiometric quantities of all rotaxane components.

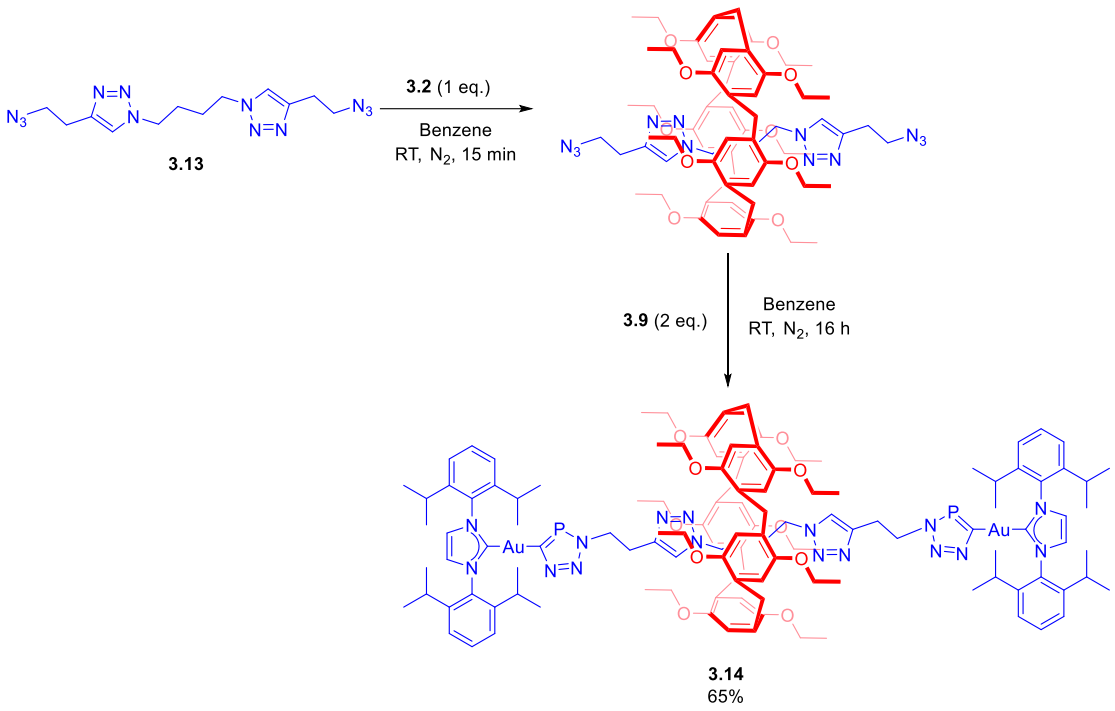

Scheme 3.13. Synthesis of [2]rotaxane **3.14**.

The corresponding non-interlocked axle, **3.15**, was synthesised by direct reaction of two equivalents of stopper **3.9** and axle precursor **3.13**. As for the [2]rotaxane **3.10**, analysis of the ^{1}H NMR spectra of **3.2**, **3.14** and **3.15** revealed marked downfield shifts in the P5A proton resonances of **3.14**, consistent with those seen for **3.10**, strongly indicating the formation of an interlocked structure (Figure 3.12). Marked upfield shifts were observed in resonances *1* and *2* compared to the non-interlocked axle, confirming the P5A macrocycle preferentially resides over the central portion of the axle, between the two triazoles, consistent with the threading studies for C_4 separated bis-triazole axles in Section 3.2. Interestingly, a significant downfield shift was observed for the axle triazole resonance *3* in the [2]rotaxane, attributed to C—H···O HB interactions between the triazole protons and the O atoms of the ethoxy P5A side chains of the macrocycle. Weakly diffracting crystals of **3.14** were grown by slow diffusion of toluene into hexane solutions of the [2]rotaxane. While the quality of the diffraction data was limited, which prevented the accurate measurement of C–H···π and C–H···O distances required to confirm the

presence of HB interactions, the data were of sufficient quality to confirm connectivity and the interlocked nature of the [2]rotaxane (Figure 3.13). As for **3.10**, the [2]rotaxane **3.14** demonstrated no significant change in its $^{31}P\{^{1}H\}$ NMR spectrum after 30 days, whereas degradation of the non-interlocked axle **3.15** was observed, highlighting the stability of the interlocked system over the non-interlocked axle.

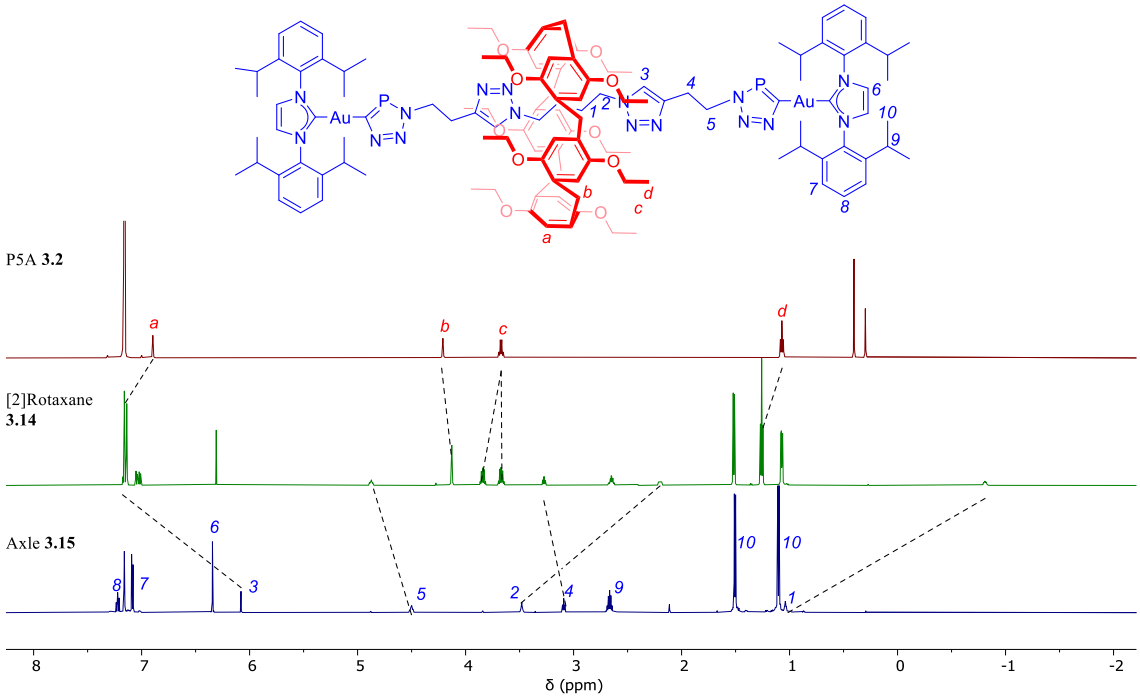

Figure 3.12. Stacked ^{1}H NMR (400 MHz, C_6D_6, 298 K) spectra of [2]rotaxane **3.14** and the non-interlocked components, P5A **3.2** and axle **3.15**.

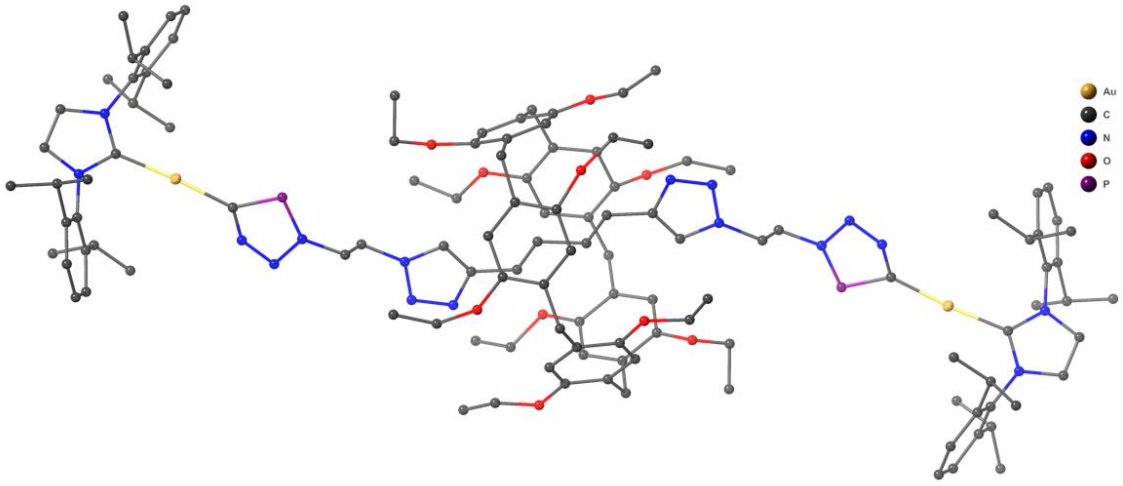

Figure 3.13. Single crystal XRD structure of **3.14**, solved by Prof. Jose Goicoechea. Hydrogen atoms omitted for clarity.

3.3.4 Conclusions and Future Work

The copper-free inorganic cyaphide-azide 'click' reaction was successfully employed on a pseudo[2]rotaxane assembly formed between 1,8-diazido-octane and P5A **3.2**, to synthesise the inorganic stopper-containing rotaxane **3.10** in appreciable yield (38%). Repeating the synthesis with a more electron deficient bis-azide axle precursor guest, **3.13**, not only enabled the synthesis of [2]rotaxane **3.14** with stoichiometric reagent quantities, but obtained a significantly augmented 65% yield, higher than similar reports of P5A-containing [2]rotaxinations with no exogeneous template.[20, 21] The mechanical bond was demonstrated to impart remarkable air and moisture stability on the organometallic-containing [2]rotaxanes, demonstrating a facile methodology for the stabilisation of organometallic species.

Future work will further explore the potential of this approach for the mechanical bond stabilisation of challenging reactive species. *N*-Heterocyclic carbenes (NHCs), carbenes stabilised by favourable electronic interactions with at least one adjacent nitrogen atom, are a species of growing interest due to their unusual reactivity, including their ability to activate gases such as CO and CO_2.[29, 51, 52] Their high reactivity usually necessitates their steric stabilisation with bulky side groups, in order to prevent dimerisation, with the deprotonation of sterically bulky imidazolium salts a common route to NHC synthesis.[53] Thus, it is of interest to investigate the potential ability of the mechanical bond to serve as a platform for the challenging stabilisation of NHCs. Champness and co-workers have previously reported the synthesis of P5A [2]rotaxanes by stoppering pseudo[2]rotaxane assemblies formed by the threading of P5As onto bis-imidazolium-containing axle precursors.[54] Future work will target such imidazolium [2]rotaxanes as a potential platform for the stabilisation of NHCs, in which the mechanically-bound proximal P5A macrocycle component serves to sterically shield an axle based NHC (Figure 3.14).

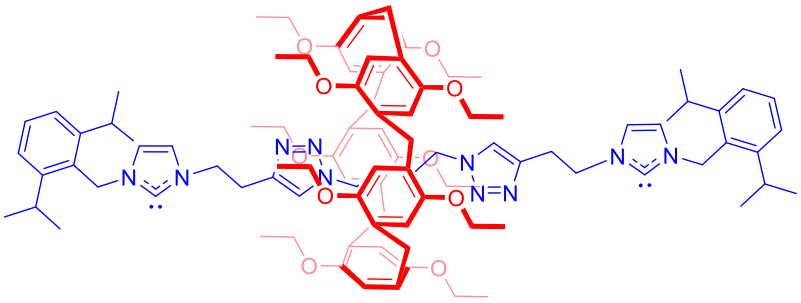

Figure 3.14. Future work target [2]rotaxane for the mechanical bond effect stabilisation of NHCs.

3.4 Halogen-Bonding BODIPY-Appended P5As for Optical Sensing of Dicarboxylates and a Chemical Warfare Agent Simulant[b]

3.4.1 Introduction

Some of the earliest reports of P5As, discussed in Section 3.1, focused on exploiting their cavities for the recognition of neutral and charged target analytes, in both organic and aqueous media. Indeed, the hydrophobic cavity of P5As has been demonstrated to be a promising molecular scaffold for the construction of hosts for guest recognition in aqueous media.[55, 56] However, to facilitate aqueous solubility such hosts are commonly highly charged, with previous examples including a decaquaternary amine-functionalised P5A and a decacarboxylate-appended P5A (Figure 3.15 a).[55, 57] Despite the increases in water solubility achieved by introducing such highly charged decoration onto the P5A host, the non-specific and non-directional nature of electrostatic attractions typically reduces the selectivity of the receptor.[58-61]

Neutral P5A receptors capable of relaying guest binding by an optical response, especially in aqueous mixtures, remain comparatively rare.[62] Building on the previously discussed report of Stoddart and co-workers for the fluorescence sensing of alkyl

[b] *This work was carried out in collaboration with graduate student Andrew J. Taylor.*

diamines in 1:1 *v/v* MeCN:H_2O (Section 3.1.2),[14] in 2019 Yang and co-workers reported a *per*-amino functionalised P5A which incorporated ten amine groups to impart water solubility on a neutral P5A.[63] The P5A host was able to selectively demonstrate a turn-off fluorescence response selectively for Au^{3+} over other tested alkali, alkaline earth and transition metal cations. Notably the binding affinity of this system was highly pH dependent due to the use of amine binding groups, and importantly arose not due to guest inclusion in the P5A cavity, but by exotopic coordination in a 2:1 host:guest binding mode between the amine groups of two P5As. Given the underexplored potential of utilising the P5A hydrophobic cavity to strongly thread a target analyte, it was of interest to construct a neutral fluorophore (BODIPY) functionalised P5A host system for sensing applications in aqueous-containing media.

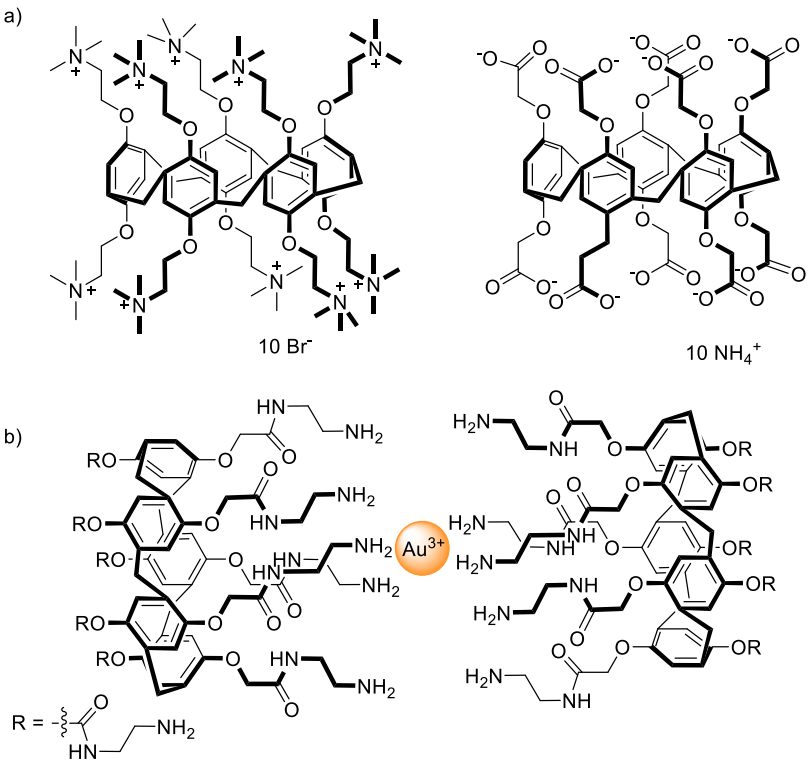

Figure 3.15. Previously reported a) highly charged P5As for host-threaded guest recognition in pure water, b) sensing of Au^{3+} with 2:1 host:guest binding stoichiometry by a water-soluble neutral P5A.

The lipophilic iodine donor atoms typically employed in XB interactions present a powerful supramolecular counterpart to the hydrophobic cavities of P5As for guest recognition and sensing in aqueous media.[64] Furthermore, XB interactions have previously been incorporated into optical sensing systems with the bright BODIPY fluorophore,[65, 66] enabling the sensing of a range of environmentally relevant substrates, including toxic hydrogen sulfide,[67] heavy metal cations,[68] and carcinogenic by-products of polymer production.[69]

Dicarboxylic acids (DCAs) and dicarboxylates (DCBs) (Figure 3.16 a) are vital intermediates in metabolic pathways, such as the Krebs' cycle, and their misregulation is implicated in a range of chronic illnesses such as kidney and liver disease.[70] The increasing employment of DCBs as linkers in metal-organic frameworks and polymer materials, has led to the emergence of DCBs as environmental pollutants of human health concern.[71]

DCBs are ideal candidates for sensing by an XB-appended P5A, as they contain a hydrophobic central carbon backbone, capable of threading through the P5A cavity, while their anionic end groups would be bound by the XB anion binding sites. Indeed, the threading of DCBs by a bis-urea appended P5A host system was demonstrated by ^{1}H NMR titration experiments in DMSO-d_6 (Figure 3.1 a).[13] This project targets the unprecedented incorporation of XB interactions into a bis-BODIPY functionalised P5A molecular host for the optical sensing of DCBs (Figure 3.16 b).

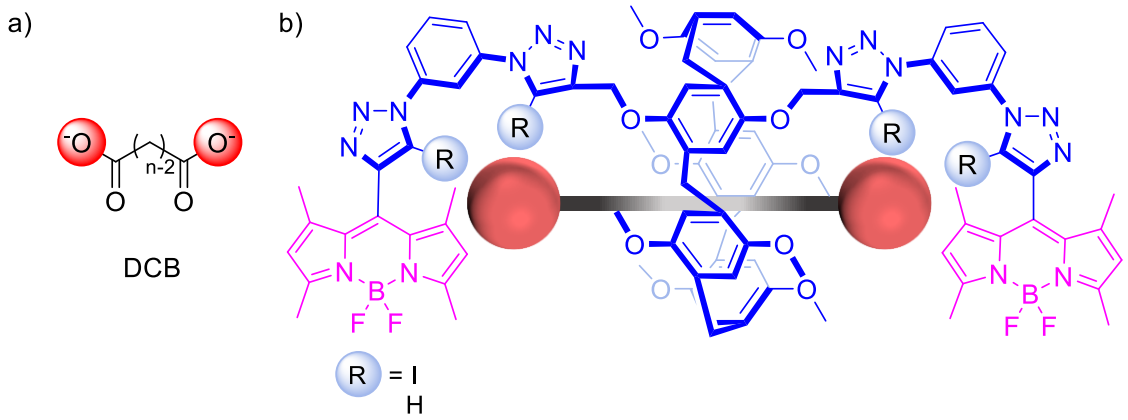

Figure 3.16. a) General structure of a DCB. b) Structure of target HB- and XB-BODIPY P5A receptor with schematic depiction of DCB guest binding mode.

3.4.2 Synthesis of an XB BODIPY-appended P5A

The synthesis of the target system exploited the CuAAC reaction of a previously reported BODIPY-XB receptor precursor azide,[66] with a bis-iodoalkyne functionalised P5A. The P5A bis-alkyne **3.16·HB** was prepared in accordance with a literature procedure.[72] The statistical incorporation of one equivalent of 1,4-bis(prop-2-yn-1-yloxy)benzene, prepared by the reaction of hydroquinone with propargyl bromide, into a DCE-templated P5A synthesis with 1,4-methoxybenzene in the presence of Lewis acidic BF_3 was attempted (Scheme 3.14). After 3 h, a mixture of *per*-methoxy P5A **3.7**, the target bis-alkyne P5A **3.16·HB**, and a number of regioisomeric *tetra*-alkyne substituted P5As was formed. These side products were removed by gradient elution chromatography, to afford the target P5A **3.16·HB**. Iodination of **3.16·HB** with *N*-iodomorpholine hydroiodide, in the presence of catalytic CuI, afforded the target bis-iodoalkyne P5A **3.16·XB** in quantitative yield.

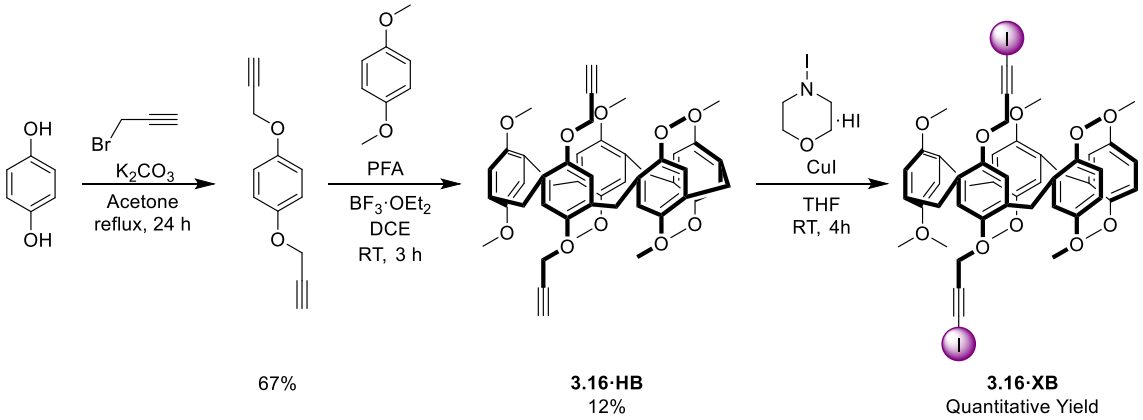

Scheme 3.14. Synthesis of bis-iodoalkyne P5A **3.16·XB**.

The BODIPY proto- and iodo-alkyne precursors **3.17·HB** and **3.17·XB** were prepared by Andrew Taylor in accordance with literature procedures (Scheme 3.15).[66, 73]

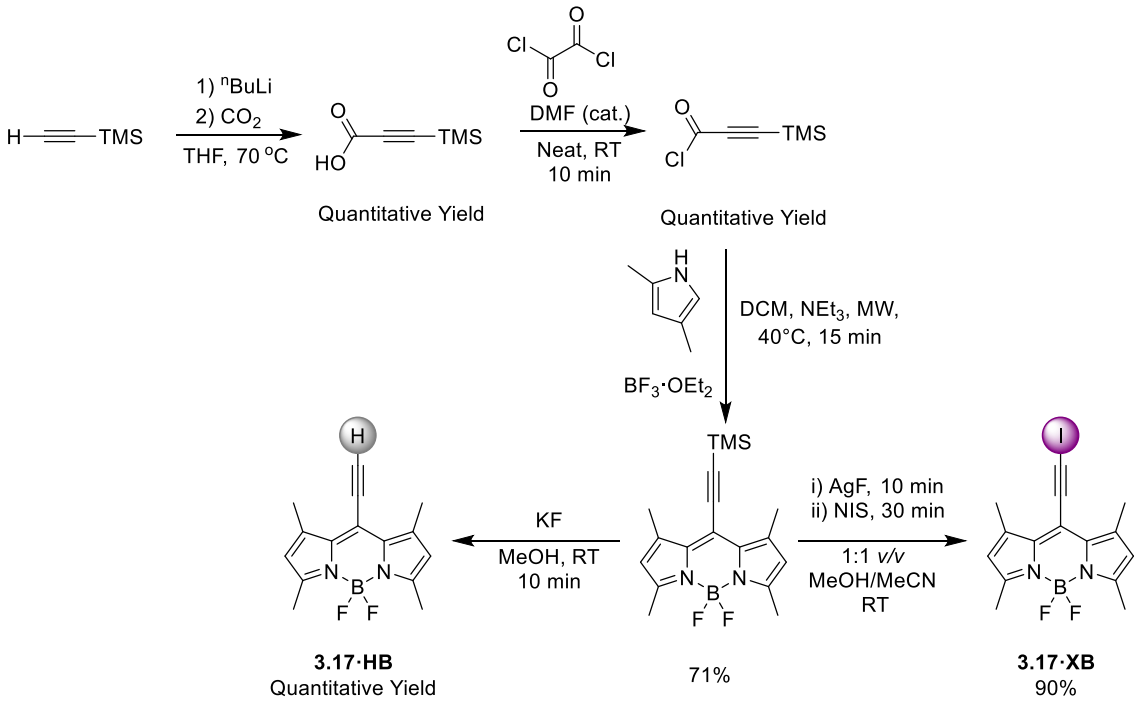

Scheme 3.15. Synthesis of BODIPY protoalkyne **3.17·HB** and iodoalkyne **3.17·XB**.

The HB and XB BODIPY alkynes **3.17·HB** and **3.17·XB** underwent CuAAC reactions with 1,3-diazidobenzene to afford the mono-click precursors **3.18·HB** and **3.18·XB** in 72% and 90% yield respectively. Reaction of two equivalents of **3.18·HB** and **3.18·XB** with the corresponding P5A bis-alkyne **3.16·HB** or **3.16·XB**, afforded the target HB and XB functionalised BODIPY appended P5A hosts **3.19·HB** and **3.19·XB** in 46% and 72% yield respectively (Scheme 3.16). Both compounds were characterised by ^{1}H and ^{13}C

NMR spectroscopy and mass spectrometry. As for compounds **3.10** and **3.14**, the ^{1}H NMR spectra displayed diastereotopic splitting, as the functionalised side-arms prevented oxygen-through-annulus rotation, and hence fast interconversion of the P5A planar chiral conformers (Figure 3.17).

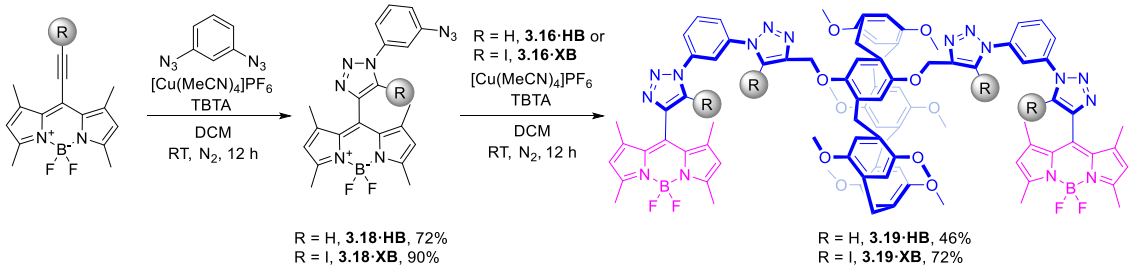

Scheme 3.16. Synthesis of target P5A receptors **3.19·HB** and **3.19·XB**.

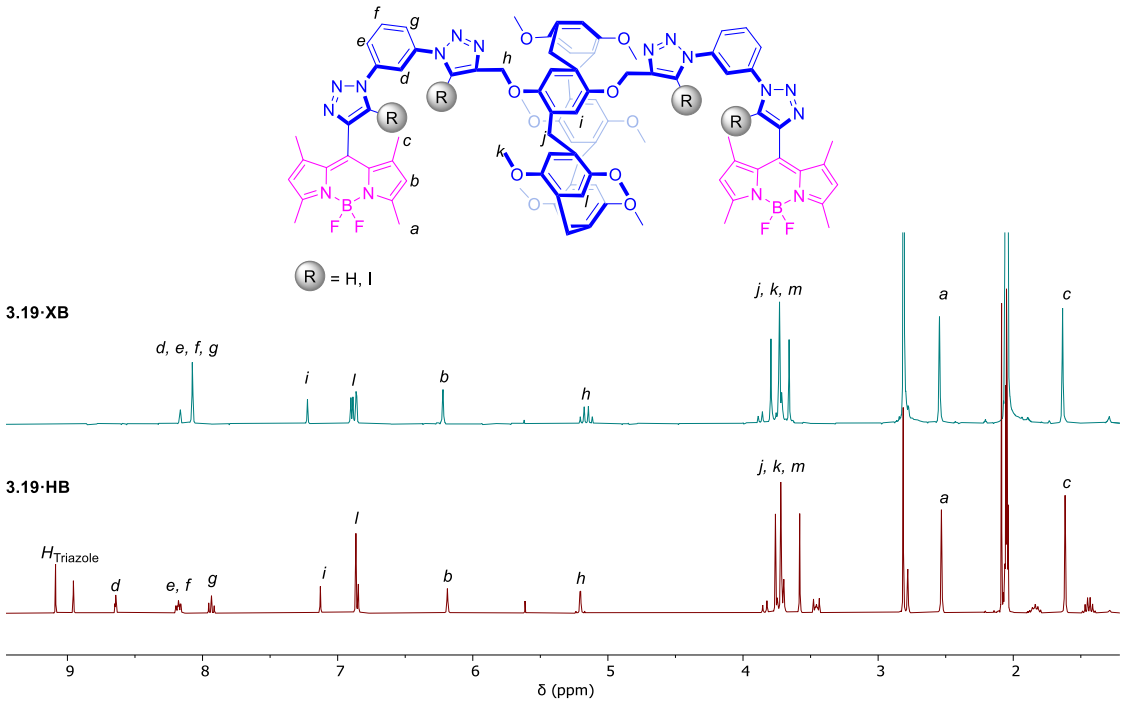

Figure 3.17. ^{1}H NMR (400 MHz, $CDCl_3$, 298 K) spectra of **3.19·HB** and **3.19·XB**.

Both receptors were further characterised by optical absorbance and emission spectroscopy (Figure 3.18). Both displayed optical spectral features consistent with the BODIPY chromophore, with **3.19·HB** and **3.19·XB** displaying absorbance maxima of 518 nm and 516 nm, respectively, and emission maxima of 531 nm and 532 nm in $CHCl_3$, corresponding to Stokes' shifts of 13 nm and 16 nm, respectively, consistent with previous literature reports of BODIPY-containing compounds.[75]

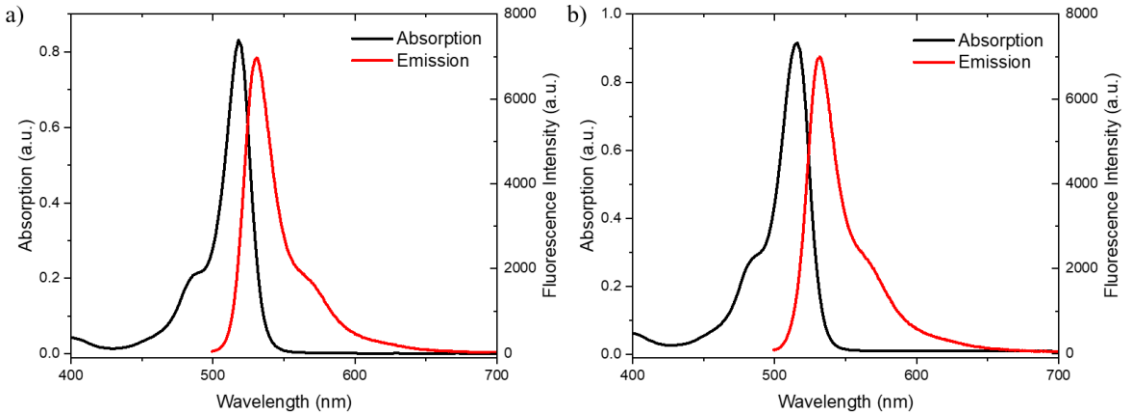

Figure 3.18. Absorption and emission spectra (1 μM, $CHCl_3$, 298 K) of a) **3.19·HB** and b) **3.19·XB**.

3.4.3 Optical Sensing of Dicarboxylates

With the target receptor P5As in hand, a series of alkyl chain DCB salts with the non-coordinating TBA counterion were prepared with the number of carbon backbone atoms, *n*, in the range *n* = 8 – 16. The corresponding DCA was suspended in H_2O and a 40 wt. % solution of TBAOH (aq.) was added dropwise until pH = 8.0.[76] The solution was filtered and the water removed *in vacuo* under high vacuum until ^{1}H NMR confirmed dryness of the DCB salt (Scheme 3.17).

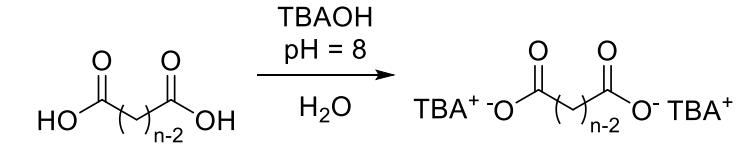

Scheme 3.17. Synthesis of $(TBA)_2$DCB guests.

The ability of both **3.19·HB** and **3.19·XB** to thread the DCB salts was confirmed by qualitative ^{1}H NMR binding studies in $CDCl_3$. Pleasingly, upon successive addition of TBA_2 dodecanedioate solution to the free hosts, significant upfield shifts in both the P5A aromatic proton peak and the methylene DCB environments were observed, consistent with threading of the DCB salt by the host (Figure 3.19). Furthermore, in the case of **3.19·HB**, a significant downfield shift in the triazole proton peaks ($\Delta\delta \approx 0.1$ ppm) was

observed, strongly suggesting HB interactions between the DCB and the triazole HB donor groups.

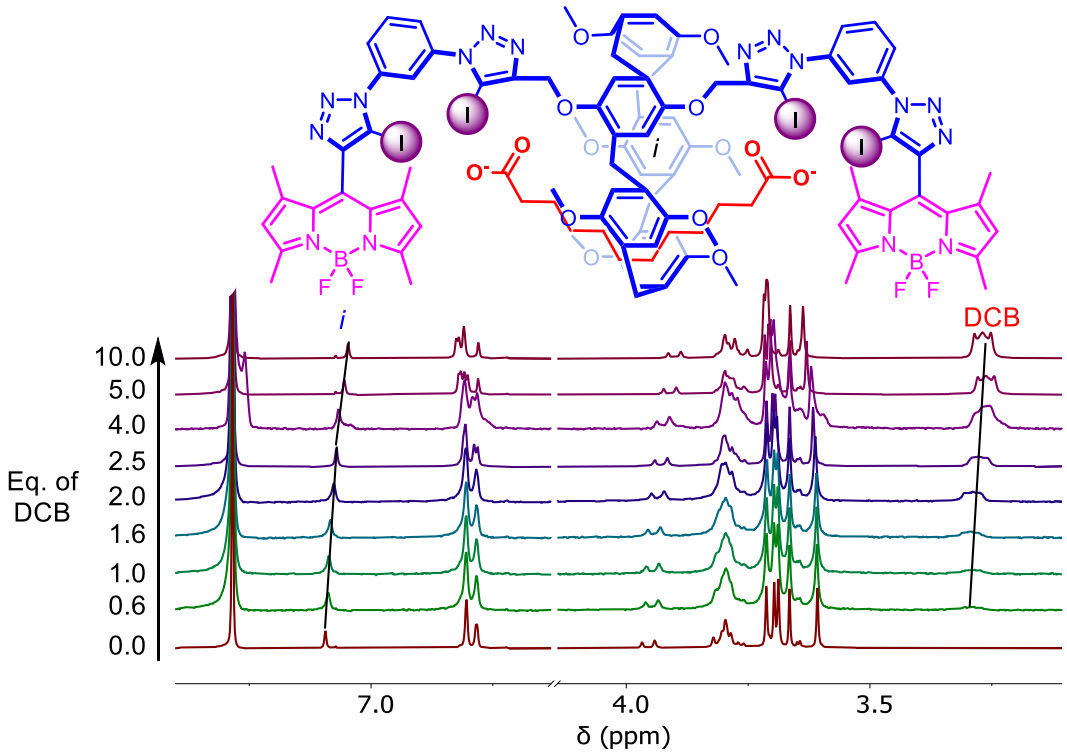

Figure 3.19. ^{1}H NMR spectra (500 MHz, $CDCl_3$, 298K) of **3.19·XB** upon successive additions of $(TBA^{+})_2\ ^{-}OOC(CH_2)_{10}COO^{-}$.

With ^{1}H NMR evidence of both HB and XB P5A host systems forming interpenetrative complexes with DCB salts, the ability of the receptors to relay such a threading event through an optical response was investigated by fluorescence host-guest binding titrations, in which the emission spectrum of the host, upon excitation at $\lambda = 490$ nm, was measured upon successive addition of solutions of the DCB salt in $CHCl_3$. Notably, a marked 'turn-on' fluorescence optical response was observed upon binding of the DCB guest by **3.19·XB** (Figure 3.20 a). In contrast, a negligible response was observed upon DCB addition to **3.19·HB**, despite the ^{1}H NMR binding studies indicating P5A-DCB threading (Figure 3.20 b). This lack of optical response upon DCB addition to **3.19·HB**, despite ^{1}H NMR studies indicating threading, is consistent with the previously reported

superior performance of XB systems for fluorescent signal transduction of anion binding events.[77]

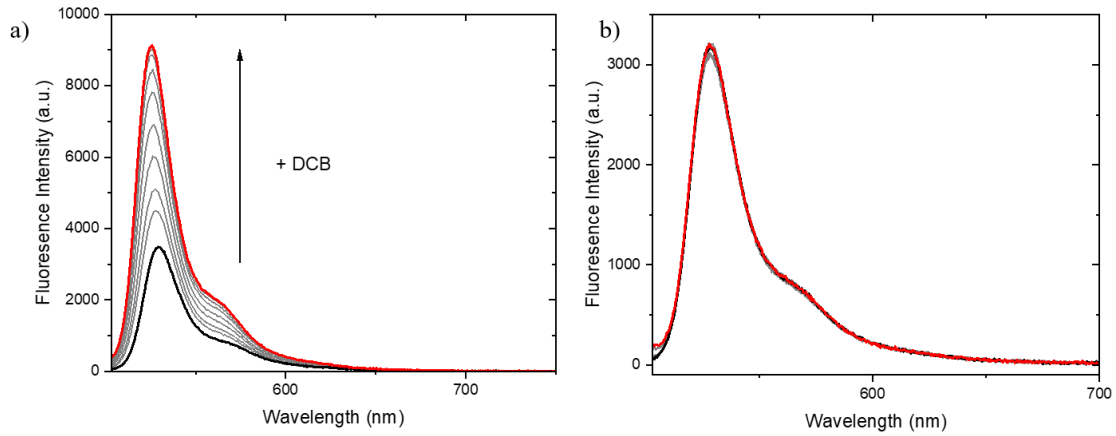

Figure 3.20. Stacked emission spectra (1 μM, $CHCl_3$, 298 K) of a) **3.19·XB**, and b) **3.19·HB**, upon successive addition of $(TBA^+)_2{}^-OOC(CH_2)_{10}COO^-$. λ_{ex} = 490 nm.

Analysis of the fluorescence **3.19·XB**-DCB titration binding isotherms determined 1:1 stoichiometric host-guest binding constants, K_a, revealing the strength of binding is strongly dependent upon the length of the carbon backbone (Table 3.1). Indeed, the strongest binding was observed for the intermediate length DCB, n = 12, which is postulated to be on account of the complementarity of the separation of the carboxylate chain ends with the separation of the XB donor iodotriazole sites. Importantly, only comparatively minimal binding was observed for OAc^-, which does not have a backbone capable of threading through the pillar[5]arene, demonstrating the necessity of threading through the P5A cavity for strong binding. Furthermore, other anions including Cl^-, Br^- and NO_3^- demonstrated significantly reduced binding constants over those for the DCB salts, further highlighting the selectivity of the system.

	K_a (M^{-1})
$^{-}OOC(CH_2)_6COO^{-}$	6800
$^{-}OOC(CH_2)_8COO^{-}$	8400
$^{-}OOC(CH_2)_{10}COO^{-}$	9900
$^{-}OOC(CH_2)_{12}COO^{-}$ [a]	8600
$^{-}OOC(CH_2)_{14}COO^{-}$	6700
OAc^{-} [b]	240 (60)
Cl^{-} [b]	1300 (320)
Br^{-} [b]	4700 (1200)
NO_3^{-} [b]	55 (20)

Table 3.1. Association constants K_a (M^{-1}) of receptor **3.19·XB** in $CHCl_3$. Determined at 298 K by global fitting of fluorescence isotherms. Unless stated otherwise, data fitted to a 1:1 host-guest stoichiometric binding model and errors < 5%. [a] Error <7%. [b] Fitted to 1:2 host-guest stoichiometric binding model, reported as K_{11} (K_{12}).

3.4.4 Optical Dicarboxylate Sensing in Aqueous-organic Media

Given the hydrophobic nature of the P5A central cavity,[78] and the proven importance of the role of threading in the sensing of DCBs, exploitation of the hydrophobic effect would be expected to give rise to significantly enhanced binding affinities in aqueous-containing media.

The potential important role of hydrophobic effects on DCB salt binding was investigated employing the TBA dodecanedioate salt, as this demonstrated the strongest binding in $CHCl_3$. In contrast to the organic media studies, addition of the DCB guest in 1:1 *v/v* H_2O:MeCN (buffered to pH = 8.0 with 50 mM HEPES) resulted in a decrease in fluorescence intensity for both **3.19·XB** and **3.19·HB**, consistent with DCB guest binding (Figure 3.21). Despite the relatively small (*c.*10%) optical response, fitting of the binding isotherms demonstrated a 10-fold enhancement in host-guest binding constant for **3.19·XB** compared with pure-organic media. While an optical response was now also observed for binding by **3.19·HB**, notably the binding constant was four-times lower than

the XB congener (Table 3.2). This is likely due to a lower degree of solvation of the XB donor groups compared with prototriazoles, on account of the presence of lipophilic iodine atoms, reducing the enthalpic penalty of binding site desolvation upon guest binding.[79]

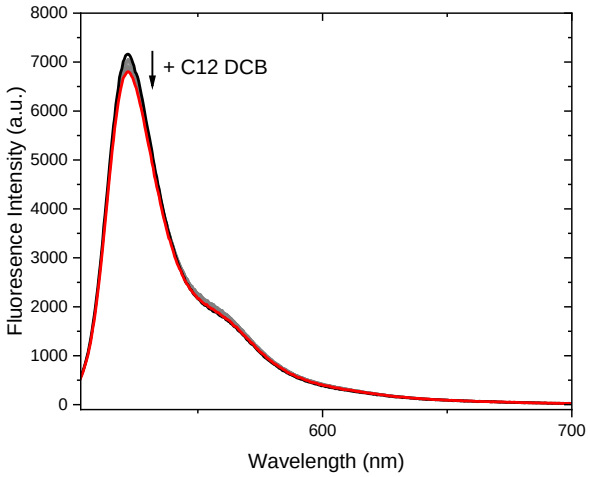

Figure 3.21. Stacked emission spectra (1 μM, 1:1 *v/v* MeCN:H_2O, pH = 8.0 (50 mM HEPES buffer)) of **3.19·XB**, upon successive addition of $(TBA^+)_2\ ^-OOC(CH_2)_{10}COO^-$. λ_{ex} = 490 nm.

K_a (M^{-1})	**3.19·XB**	**3.19·HB**
$^-OOC(CH_2)_{10}COO^-$	104,000	28,500

Table 3.2. Association constants K_a (M^{-1}) of receptors **3.19·XB** and **3.19·HB** with $^-OOC(CH_2)_{10}COO^-$ aqueous-organic mixtures. Determined at 298 K by global fitting of fluorescence isotherms to 1:1 host-guest stoichiometric binding model. Measured in 1:1 *v/v* MeCN:H_2O pH = 8.0 (50 mM HEPES buffer), errors < 15%.

3.4.5 Sensing of a Chemical Warfare Agent Simulant

Given the strong binding of the DCB salts, it was of interest to investigate the potential binding of neutral small molecules of anthropogenic concern. Sulfur mustard, bis(2-chloroethyl) sulfide (Figure 3.22 a), is a blistering agent which has been deployed in a number of conflicts since its first use during World War I, resulting in over 100,000 deaths.[80] In addition to blistering effects, exposure to sulfur mustard can result in potentially-fatal respiratory effects, as well as demonstrating mutagenic and carcinogenic behaviour.[81] Given the structure of sulfur mustard, consisting of a hydrophobic core and

terminal electron-withdrawing halides which can potentially be bound by HB or XB groups, it was anticipated that strong host-guest association would be observed between sulfur mustard and **3.19·XB**. As sulfur mustard is restricted under international law, 2-chloroethyl ethyl sulfide (CEES) was employed as a commercially available simulant of mustard gas (Figure 3.22 a).[82]

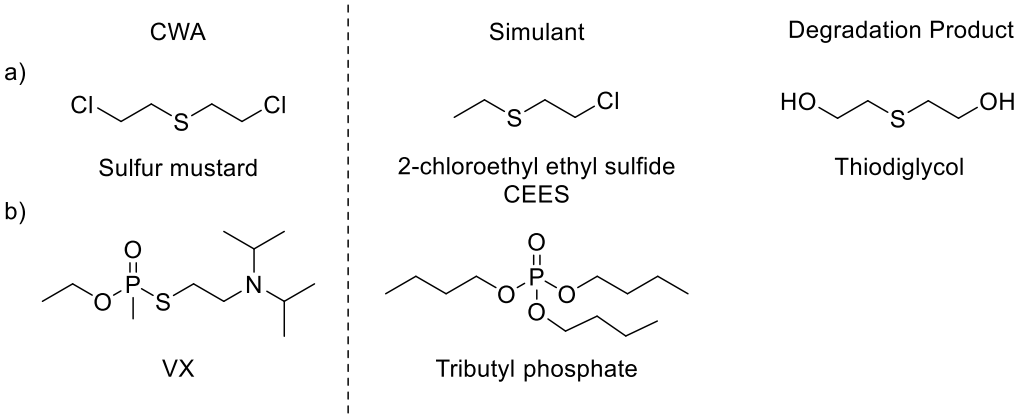

Figure 3.22. Structure of a) sulfur mustard and its tested simulant and degradation product, b) VX and its tested simulant.

Upon successive addition of CEES to 1:1 *v/v* H_2O:MeCN solutions of **3.19·XB** and **3.19·HB**, a modest, but distinct, (*c.* 10%) decrease in fluorescence intensity was observed (Figure 3.23 a). Global fitting of the titration data using *OriginPro* demonstrated markedly increased K_a values for CEES (528,000 M^{-1} and 145,000 M^{-1} for of **3.19·XB** and **3.19·HB** respectively) compared to the DCB binding constants.[83] Such an increase can be attributed to the increased hydrophobicity of the neutral CEES guest compared to the dianionic DCB salts. The role of hydrophobicity was further confirmed by attempted optical binding studies in $CHCl_3$. In the pure organic media, the magnitude of the change in emission intensity of **3.19·XB** was very small (*c.* 5%) which precluded accurate determination of the binding constant. However, it is apparent that binding in the mixed organic-aqueous media is at least an order of magnitude greater than in pure $CHCl_3$.

Pleasingly, no response was observed upon addition of thiodiglycol, the hydrolysis product of sulfur mustard, to either receptor, nor for tributyl phosphate, a simulant for V-series nerve agents,[84] to **3.19·XB** demonstrating the potential of the receptors for the selective optical sensing of sulfur mustard (Table 3.3). Phase separation was observed upon addition of tributyl phosphate to aqueous-organic solutions of **3.19·HB** preventing the measurement of any optical response.

	K_a (M^{-1})	
	3.19·XB	**3.19·HB**
$CH_3CH_2SCH_2CH_2Cl$ (CEES)	528,000	145,000
$HOCH_2CH_2SCH_2CH_2OH$ (Thiodiglycol)	*NR*	*NR*
$P(=O)Bu_3$	*NR*	*

Table 3.3. Association constants K_a (M^{-1}) of receptors **3.19·XB** and **3.19·HB** with CWA simulants in 1:1 *v/v* MeCN:H_2O. Determined at 298 K by global fitting of fluorescence isotherms to a 1:1 host-guest stoichiometric binding model. Errors < 7%. *NR* No optical response observed. *Phase separation observed.

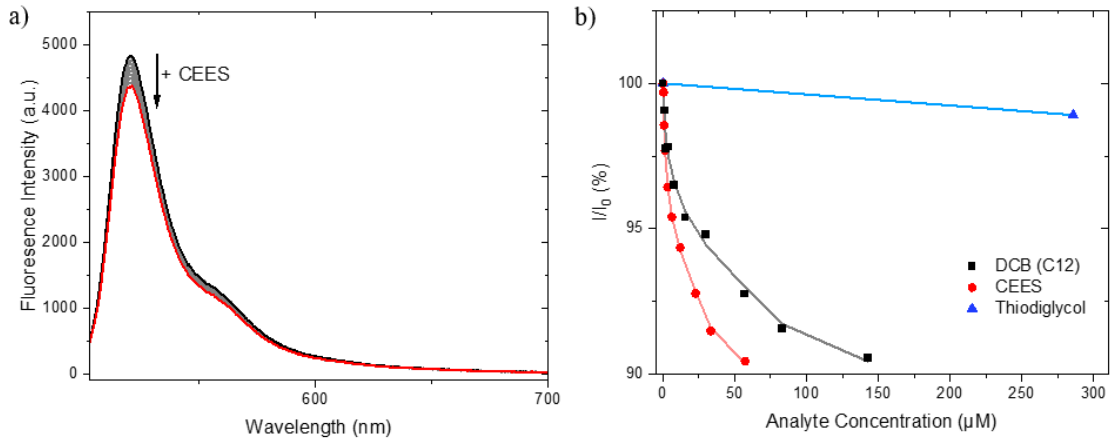

Figure 3.23. a) Stacked emission spectra (1 μM, 1:1 *v/v* MeCN:H_2O) of **3.19·XB**, upon successive addition of CEES. b) % Change in emission intensity (1 μM, 1:1 *v/v* MeCN:H_2O) of **3.19·XB**, upon addition of indicated analyte. λ_{ex} = 490 nm.

3.4.6 Limit of Detection of CWA Simulant

Given the relatively modest optical response of the receptors upon CEES binding, the limit of detection (LoD), that is the minimum concentration of CEES which could be

detected with statistical confidence, was calculated for both receptors, using Equation 3.1, in accordance with previous literature reports.[85, 86]

$$LoD = \frac{3\sigma}{S} \qquad (3.1)$$

σ = Standard deviation of each receptor's emission intensity at the emission maximum.

S = Initial slope of emission intensity curve on addition of analyte, taken from the first four measurements (M^{-1}).

The standard deviation of the free receptor's emission intensity was calculated by taking successive scans of the receptor solution (1 μM, 1:1 *v/v* H_2O:MeCN), prior to the addition of any CEES and the initial slope of the curve of the binding isotherms was measured by a linear fitting of the first four data points (Figure 3.24).[47] It is noteworthy that the limit of detection for CEES is very low for both receptors, 0.13 μM and 0.40 μM for **3.19·XB** and **3.19·HB** respectively, which, coupled with the selectivity for CEES over both the hydrolysis product of sulfur mustard and a simulant of a V-series CWA, demonstrated the power of combining the highly sensitive fluorescent optical spectroscopy technique with selective XB receptors for the construction of molecular sensors.

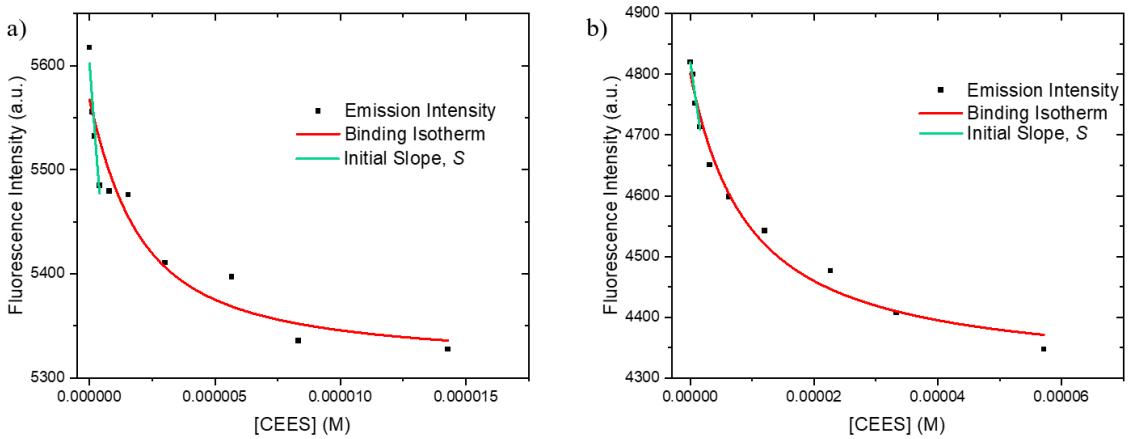

Figure 3.24. Intensity of fluorescence maximum (1 μM, 1:1 *v/v* MeCN:H_2O) upon successive addition of CEES to a) **3.19·XB** and b) **3.19·HB**, and the linear line used for LoD determination. λ_{ex} = 490 nm.

3.4.7 Conclusions and Future Work

BODIPY-appended XB and HB P5A receptors, **3.19·XB** and **3.19·HB** respectively, were synthesised by CuAAC click reactions of a BODIPY XB or HB azide with a P5A bis-alkyne. Qualitative ^{1}H NMR studies demonstrated both receptors form pseudo[2]rotaxane interpenetrated assemblies with DCBs in $CDCl_3$. Furthermore, **3.19·XB** demonstrated a marked turn-on optical fluorescence response upon DCB binding with high host-guest binding affinities. Both **3.19·XB** and **3.19·HB** displayed turn-off optical responses to DCB binding in HEPES buffered 1:1 *v/v* H_2O:MeCN at pH = 8, with **3.19·XB** demonstrating binding an order of magnitude greater in this 50% aqueous-containing mixture than in pure organic media, and approximately 4-times greater than **3.19·HB**, on account of the increased lipophilicity of the XB iodotriazole atoms over prototriazole analogues.

Impressively, the hydrophobicity of the BODIPY functionalised P5A systems facilitates the binding of CEES, a sulfur mustard CWA simulant, with remarkable binding affinity in the aqueous-organic mixture, with selectivity over the hydrolysis product of sulfur mustard, and a simulant of V-series nerve agents. The combination of BODIPY fluorophore functionalisation, integration of XB donor interactions and the hydrophobic P5A cavity results in a potent host system **3.19·XB** for sensing of both charged DCB and neutral CEES environmental pollutants.

Future work will seek to synthesise congeners of these systems containing zwitterionic pendants to facilitate the solubility of the receptors in 100% water (Figure 3.25). Sensing in pure water should not only lead to further augmentation in binding affinities by the hydrophobic receptors, but increase the utility of these systems in the fabrication of devices for the *in situ* detection of environmental pollutants in natural watercourses.

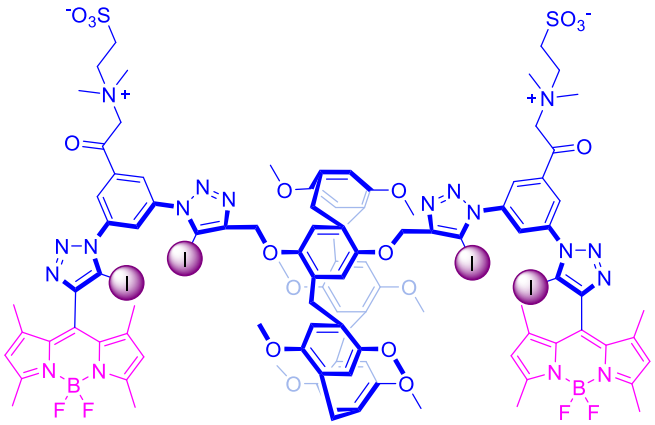

Figure 3.25. Zwitterionic pendant functionalised congener of **3.19·XB** targeting solubility in 100% aqueous media.

3.5 References

1. J.-M. Lehn, *Angew. Chem. Int. Ed. Engl.*, 1988, **27**, 89-112.
2. Q. D. Hu, G. P. Tang and P. K. Chu, *Acc. Chem. Res.*, 2014, **47**, 2017-2025.
3. S. J. Barrow, S. Kasera, M. J. Rowland, J. del Barrio and O. A. Scherman, *Chem. Rev.*, 2015, **115**, 12320-12406.
4. D.-S. Guo and Y. Liu, *Chem. Soc. Rev.*, 2012, **41**, 5907-5921.
5. T. Ogoshi, S. Kanai, S. Fujinami, T.-a. Yamagishi and Y. Nakamoto, *J. Am. Chem. Soc.*, 2008, **130**, 5022-5023.
6. T. Boinski and A. Szumna, *Tetrahedron*, 2012, **68**, 9419-9422.
7. T. Ogoshi, N. Ueshima, T. Akutsu, D. Yamafuji, T. Furuta, F. Sakakibara and T.-a. Yamagishi, *Chem. Commun.*, 2014, **50**, 5774-5777.
8. T. Ogoshi, T.-a. Yamagishi and Y. Nakamoto, *Chem. Rev.*, 2016, **116**, 7937-8002.
9. Z. Zhang, B. Xia, C. Han, Y. Yu and F. Huang, *Org. Lett.*, 2010, **12**, 3285-3287.
10. P. Demay-Drouhard, K. Du, K. Samanta, X. Wan, W. Yang, R. Srinivasan, A. C. H. Sue and H. Zuilhof, *Org. Lett.*, 2019, **21**, 3976-3980.
11. M. Guo, X. Wang, C. Zhan, P. Demay-Drouhard, W. Li, K. Du, M. A. Olson, H. Zuilhof and A. C. H. Sue, *J. Am. Chem. Soc.*, 2018, **140**, 74-77.
12. C. Li, Q. Xu, J. Li, Y. Feina and X. Jia, *Org. Biomol. Chem.*, 2010, **8**, 1568-1576.
13. Q. Duan, W. Xia, X. Hu, M. Ni, J. Jiang, C. Lin, Y. Pan and L. Wang, *Chem. Commun.*, 2012, **48**, 8532-8534.
14. N. L. Strutt, R. S. Forgan, J. M. Spruell, Y. Y. Botros and J. F. Stoddart, *J. Am. Chem. Soc.*, 2011, **133**, 5668-5671.
15. X. Shu, J. Fan, J. Li, X. Wang, W. Chen, X. Jia and C. Li, *Org. Biomol. Chem.*, 2012, **10**, 3393-3397.
16. C. Ke, N. L. Strutt, H. Li, X. Hou, K. J. Hartlieb, P. R. McGonigal, Z. Ma, J. Iehl, C. L. Stern, C. Cheng, Z. Zhu, N. A. Vermeulen, T. J. Meade, Y. Y. Botros and J. F. Stoddart, *J. Am. Chem. Soc.*, 2013, **135**, 17019-17030.
17. T. Ogoshi, D. Kotera, S. Nishida, T. Kakuta, T.-a. Yamagishi and A. M. Brouwer, *Chem. Eur. J.*, 2018, **24**, 6325-6329.
18. T. Ogoshi, D. Yamafuji, T. Aoki, K. Kitajima, T.-a. Yamagishi, Y. Hayashi and S. Kawauchi, *Chem. Eur. J.*, 2012, **18**, 7493-7500.
19. C. Li, K. Han, J. Li, Y. Zhang, W. Chen, Y. Yu and X. Jia, *Chem. Eur. J.*, 2013, **19**, 11892-11897.

20. T. Ogoshi, R. Iizuka, D. Kotera and T.-a. Yamagishi, *Org. Lett.*, 2015, **17**, 350-353.
21. N. Becharguia, I. Nierengarten, J.-M. Strub, S. Cianférani, M. Rémy, E. Wasielewski, R. Abidi and J.-F. Nierengarten, *Chem. Eur. J.*, 2024, **30**, e202304131.
22. T. Ogoshi, T. Aoki, S. Ueda, Y. Tamura and T.-a. Yamagishi, *Chem. Commun.*, 2014, **50**, 6607-6609.
23. K. Kato, K. Onishi, K. Maeda, M. Yagyu, S. Fa, T. Ichikawa, M. Mizuno, T. Kakuta, T.-a. Yamagishi and T. Ogoshi, *Chem. Eur. J.*, 2021, **27**, 6435-6439.
24. R. R. Farias, A. J. S. Mascarenhas, T. d. J. Santos and M. M. Victor, *Tetrahedron Lett.*, 2020, **61**, 152574.
25. A. V. Leontiev, C. A. Jemmett and P. D. Beer, *Chem. Eur. J.*, 2011, **17**, 816-825.
26. J. G. Badiang and J. Aubé, *J. Org. Chem.*, 1996, **61**, 2484-2487.
27. A. Noor, W. K. C. Lo, S. C. Moratti and J. D. Crowley, *Chem. Commun.*, 2014, **50**, 7044-7047.
28. H. Lahlali, K. Jobe, M. Watkinson and S. M. Goldup, *Angew. Chem. Int. Ed.*, 2011, **50**, 4151-4155.
29. J. M. Farrell, R. T. Posaratnanathan and D. W. Stephan, *Chem. Sci.*, 2015, **6**, 2010-2015.
30. D. W. Stephan and G. Erker, *Angew. Chem. Int. Ed.*, 2010, **49**, 46-76.
31. Z. R. Turner, J. T. Wilmore, N. H. Rees and J.-C. Buffet, *Dalton Trans.*, 2022, **51**, 3060-3074.
32. S. Planer, P. Małecki, B. Trzaskowski, A. Kajetanowicz and K. Grela, *ACS Catal.*, 2020, **10**, 11394-11404.
33. Y. Li and A. H. Flood, *J. Am. Chem. Soc.*, 2008, **130**, 12111-12122.
34. L. Shen, Y. Zhao, D. Dai, Y.-W. Yang, B. Wu and X.-J. Yang, *Chem. Commun.*, 2020, **56**, 1381-1384.
35. J. T. Wilmore and P. D. Beer, *Adv. Mater.*, 2024, DOI: https://doi.org/10.1002/adma.202309098, 2309098.
36. H. Ogino, *J. Am. Chem. Soc.*, 1981, **103**, 1303-1304.
37. H. Ogino and K. Ohata, *Inorg. Chem.*, 1984, **23**, 3312-3316.
38. N. Weisbach, Z. Baranová, S. Gauthier, J. H. Reibenspies and J. A. Gladysz, *Chem. Commun.*, 2012, **48**, 7562-7564.
39. H. Amini, Z. Baranová, N. Weisbach, S. Gauthier, N. Bhuvanesh, J. H. Reibenspies and J. A. Gladysz, *Chem. Eur. J.*, 2019, **25**, 15896-15914.
40. R. A. Grzelczak, A. Władyczyn, A. Białońska, Ł. John and B. Szyszko, *Chem. Commun.*, 2023, **59**, 7579-7582.
41. W. Rösch, T. Facklam and M. Regitz, *Tetrahedron*, 1987, **43**, 3247-3256.
42. Y. Y. C. Yeung Lam Ko, R. Carrié, A. Muench and G. Becker, *J. Chem. Soc., Chem. Commun.*, 1984, 1634-1635.
43. J.-C. Guillemin, T. Janati and J.-M. Denis, *J. Org. Chem.*, 2001, **66**, 7864-7868.
44. T. Görlich, D. S. Frost, N. Boback, N. T. Coles, B. Dittrich, P. Müller, W. D. Jones and C. Müller, *J. Am. Chem. Soc.*, 2021, **143**, 19365-19373.
45. D. W. N. Wilson, S. J. Urwin, E. S. Yang and J. M. Goicoechea, *J. Am. Chem. Soc.*, 2021, **143**, 10367-10373.
46. E. S. Yang, A. Mapp, A. Taylor, P. D. Beer and J. M. Goicoechea, *Chem. Eur. J.*, 2023, **29**, e202301648.
47. D. Brynn Hibbert and P. Thordarson, *Chem. Commun.*, 2016, **52**, 12792-12805.

48. H. Suezawa, T. Yoshida, M. Hirota, H. Takahashi, Y. Umezawa, K. Honda, S. Tsuboyama and M. Nishio, *J. Chem. Soc., Perkin Trans. 2*, 2001, DOI: 10.1039/B106052J, 2053-2058.
49. S. Tsuzuki, K. Honda, T. Uchimaru, M. Mikami and K. Tanabe, *J. Am. Chem. Soc.*, 2000, **122**, 3746-3753.
50. S. Wang, X. Shao and W. Cai, *J. Chem. Phys. C.*, 2017, **121**, 25547-25553.
51. M. N. Hopkinson, C. Richter, M. Schedler and F. Glorius, *Nature*, 2014, **510**, 485-496.
52. W. Liu, Y. Xie, Z. Tong, J. Sun, L. Chen and J. Xu, *J. CO2 Util.*, 2023, **75**, 102566.
53. B. G. Vittal, P. J. Bony and P. Sudeep, in *Carbene*, eds. S. Satyen and M. Arunava, IntechOpen, Rijeka, 2022, DOI: 10.5772/intechopen.102561, p. Ch. 7.
54. P. Langer, L. Yang, C. R. Pfeiffer, W. Lewis and N. R. Champness, *Dalton Trans.*, 2019, **48**, 58-64.
55. T. Ogoshi, M. Hashizume, T.-a. Yamagishi and Y. Nakamoto, *Chem. Commun.*, 2010, **46**, 3708-3710.
56. M. Bojtár, A. Paudics, D. Hessz, M. Kubinyi and I. Bitter, *RSC Adv.*, 2016, **6**, 86269-86275.
57. Y. Ma, X. Ji, F. Xiang, X. Chi, C. Han, J. He, Z. Abliz, W. Chen and F. Huang, *Chem. Commun.*, 2011, **47**, 12340-12342.
58. Y. Sun, F. Guo, T. Zuo, J. Hua and G. Diao, *Nat. Commun.*, 2016, **7**, 12042.
59. J.-D. Ding, J.-F. Chen, Q. Lin, H. Yao, Y.-M. Zhang and T.-B. Wei, *Polym. Chem.*, 2018, **9**, 5370-5376.
60. H. Li, D.-X. Chen, Y.-L. Sun, Y. B. Zheng, L.-L. Tan, P. S. Weiss and Y.-W. Yang, *J. Am. Chem. Soc.*, 2013, **135**, 1570-1576.
61. Q. Lin, F. Zheng, L. Liu, P.-P. Mao, Y.-M. Zhang, H. Yao and T.-B. Wei, *RSC Adv.*, 2016, **6**, 111928-111933.
62. Y. Mei, Q.-W. Zhang, Q. Gu, Z. Liu, X. He and Y. Tian, *J. Am. Chem. Soc.*, 2022, **144**, 2351-2359.
63. S.-M. Chan, F.-K. Tang, C.-S. Kwan, C.-Y. Lam, S. C. K. Hau and K. C.-F. Leung, *Mater. Chem. Front.*, 2019, **3**, 2388-2396.
64. A. Borissov, I. Marques, J. Y. C. Lim, V. Félix, M. D. Smith and P. D. Beer, *J. Am. Chem. Soc.*, 2019, **141**, 4119-4129.
65. Y. Cheong Tse, R. Hein, E. J. Mitchell, Z. Zhang and P. D. Beer, *Chem. Eur. J.*, 2021, **27**, 14550-14559.
66. A. J. Taylor, R. Hein, S. C. Patrick, J. J. Davis and P. D. Beer, *Angew. Chem. Int. Ed.*, 2024, **63**, e202315959.
67. J. Yue, Y. Tao, J. Zhang, H. Wang, N. Wang and W. Zhao, *Chem. Asian J.*, 2021, **16**, 850-855.
68. A. V. Raveendran, P. A. Sankeerthana, A. Jayaraj and P. Chinna Ayya Swamy, *Results Chem.*, 2022, **4**, 100297.
69. J.-Y. Lu, J.-X. Wang, Y. Li, Q.-Y. Chen, L.-L. Qu, S.-C. Meng and M.-Q. Wang, *Sens. Actuators B Chem.*, 2021, **331**, 129396.
70. I. Martínez-Reyes and N. S. Chandel, *Nat. Commun.*, 2020, **11**, 102.
71. P. A. Przybylińska and M. Wyszkowski, *Ecol. Chem. Eng. S*, 2016, **23**, 347-356.
72. J. Bi, X. Zeng, D. Tian and H. Li, *Org. Lett.*, 2016, **18**, 1092-1095.
73. M. Albrecht, A. Lippach, M. P. Exner, J. Jerbi, M. Springborg, N. Budisa and G. Wenz, *Org. Biomol. Chem.*, 2015, **13**, 6728-6736.
74. K. Hiratsuka, F. T. Salim, K. Takahashi, T. Nakamura and Y. Sagara, *Bull. Chem. Soc. Jpn.*, 2022, **95**, 1474-1480.

75. X.-Y. Zhu, H.-W. Yao, Y.-J. Fu, X.-F. Guo and H. Wang, *Anal. Chim. Acta*, 2019, **1048**, 194-203.
76. Q. Duan, W. Xia, X. Hu, M. Ni, J. Jiang, C. Lin, Y. Pan and L. Wang, *Chem. Commun.*, 2012, **48**, 8532.
77. F. Zapata, A. Caballero, N. G. White, T. D. W. Claridge, P. J. Costa, V. T. Félix and P. D. Beer, *J. Am. Chem. Soc.*, 2012, **134**, 11533-11541.
78. B. Gómez-González, L. García-Río, N. Basílio, J. C. Mejuto and J. Simal-Gandara, *Pharmaceutics*, 2022, **14**, 60.
79. M. J. Langton, S. W. Robinson, I. Marques, V. Félix and P. D. Beer, *Nat. Chem.*, 2014, **6**, 1039-1043.
80. A. P. Watson and G. D. Griffin, *Environ. Health Perspect.*, 1992, **98**, 259-280.
81. Institute of Medicine, *Veterans at Risk: The Health Effects of Mustard Gas and Lewisite*, The National Academies Press, Washington, DC, 1993.
82. B. Picard, I. Chataigner, J. Maddaluno and J. Legros, *Org. Biomol. Chem.*, 2019, **17**, 6528-6537.
83. OriginLab Corporation, *OriginPro*, 2023.
84. B. Li, J. Kong, L. Yang, L. Zhang, Z. Zhang and C. Li, *Int. J. Mass spectrom.*, 2020, **451**, 116320.
85. E. J. Mitchell, A. J. Beecroft, J. Martin, S. Thompson, I. Marques, V. Félix and P. D. Beer, *Angew. Chem. Int. Ed.*, 2021, **60**, 24048-24053.
86. W. Chen, C. Guo, Q. He, X. Chi, V. M. Lynch, Z. Zhang, J. Su, H. Tian and J. L. Sessler, *J. Am. Chem. Soc.*, 2019, **141**, 14798-14806.

Chapter Four

Towards Supramolecular Metal Salen Complexes for Ring Opening Polymerisation

4 Towards Supramolecular Metal Salen Complexes for Ring Opening Polymerisation

4.1 Introduction

4.1.1 The Salen Ligand

Salen ligands are a class of tetradentate N_2O_2-coordinating bis-Schiff base ligands (Figure 4.1), which have found favour in, *inter alia*, transition metal catalysis.[1] Salen is an attractive scaffold, as its facile modular synthesis from functionalised salicylaldehyde and ethylenediamine derivatives allows for easy modification of the electronic and steric properties of the ligand and for the introduction of chiral backbones through the use of chiral amines, previously exploited for enantioselective catalysis.[2] Chelate preorganisation of the tetradentate binding site gives rise to formation of stable transition metal complexes upon addition of the corresponding metal halide or acetate salts, which typically precipitate from solution as pure complexes,[3] making salen particularly useful when the final system may not be stable to other purification techniques, such as chromatography.

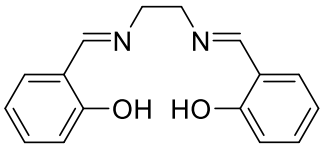

Figure 4.1. *N*,*N*′-Ethylenebis(salicylimine), the simplest salen ligand.

The first reported transition metal salen complex came in 1938, when Tsumaki reported the reversible binding of O_2 by Co(II) salen, providing potential for the straightforward synthesis of oxygen carriers (Figure 4.2 a).[4, 5] Substitution of the salen backbone with ancillary ligands to form an octahedral Co(III) centre enabled the synthesis of a range of biomimetic systems, such as a model complex of a vitamin B_{12} centre.[6] Subsequently, the catalytic potential of transition metal salen complexes has been demonstrated for a range

of applications, most notably Jacobsen's epoxidation catalyst, containing a C_2 symmetric Mn(III) salen complex with a cyclohexyl backbone, which can effect highly enantioselective epoxidation of alkyl- and aryl-substituted alkenes with *ee* > 90% (Figure 4.2 b).[2]

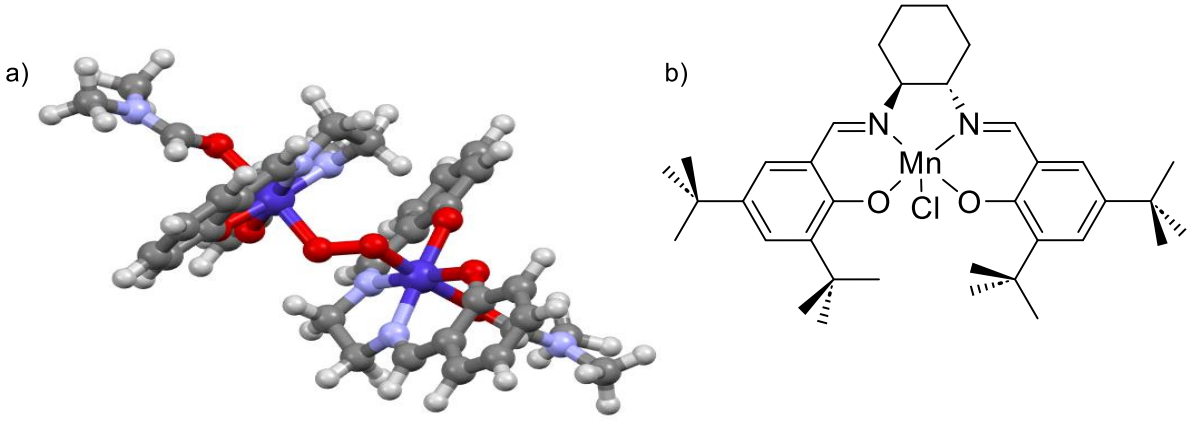

Figure 4.2. a) Single crystal XRD structure of O_2 binding by Co(II) salen, with co-bound DMF solvent,[7] b) Jacobsen's asymmetric epoxidation catalyst.

4.1.2 Ring-opening Polymerisation

Few areas of modern life are untouched by polymer chemistry, from the use of polylactic acid (PLA) for medical implants to polyethylene for plastic packaging.[8, 9] Over 400 million tonnes of plastic were produced worldwide in 2022.[10] Widespread polymer production poses two major challenges – the need to use renewable feedstocks, such as cyclic esters derived from biomass, and the need for sustainable end of life routes, to reduce the estimated 79% of plastics consumed in the UK which are sent to landfill.[11, 12]

Polyesters and polycarbonates have been presented as sustainable polymers, due to their derivation from biorenewable monomers, such as lactide and a range of epoxides, and naturally occurring degradation routes. Such polymers can be synthesised by ring-opening polymerisation (ROP) of cyclic esters. Furthermore, the ring-opening co-polymerisation (ROCOP) of epoxides with carbon dioxide to form polycarbonates

provides an effective route towards carbon capture and utilisation, in which sequestered carbon dioxide is converted to a useful commodity polymer.[13]

4.1.3 Ring-opening Polymerisation Catalysis

In the presence of a Lewis acid, such as a transition metal catalytic centre, cyclic esters typically undergo ROP via the coordination insertion mechanism, first proposed by Dittrich and Schulz (Figure 4.3).[14] ROP of polymers which possess stereocentres, such as lactide, using a stereoselective catalyst enables the optimisation of material properties, by modifying the degree of crystallinity of the polymer through control of the stereochemistry of the polymeric chain linkages.[15, 16]

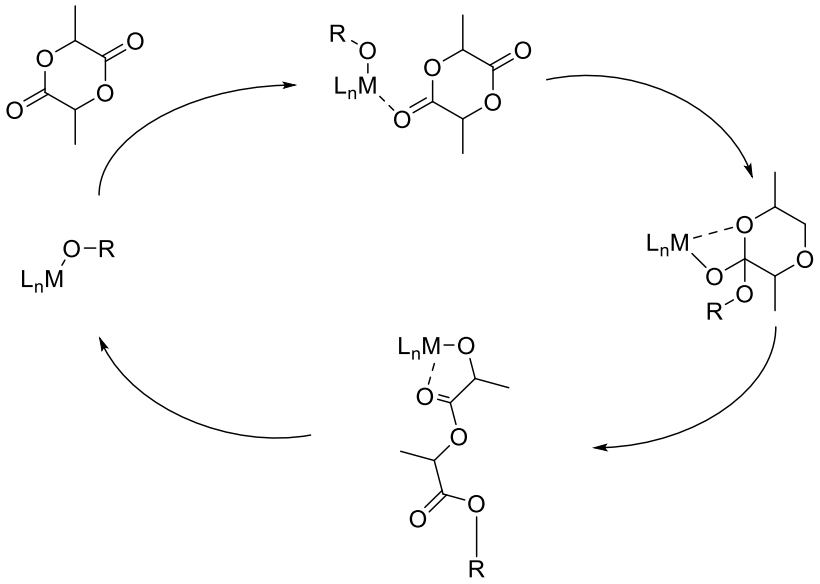

Figure 4.3. The coordination-insertion mechanism for lactide ROP. R = propagating polymeryl chain.

Salen metal complexes have wide precedence in ROP and ROCOP reactions. In the case of ROP, incorporation of a chiral backbone has been used to effect stereoselective PLA synthesis. One of the first such catalysts was an Al(III) salen catalyst developed by Spassky and co-workers.[17] The chirality of the salen backbone allowed for enantiomorphic site control (stereocontrol afforded by the chirality of the catalyst) to

yield majority-isotactic PLA, the stereochemistry of which could be fine-tuned by modifying the chirality of the salen backbone (Figure 4.4 a).

Compared to ROP, the ROCOP of anhydrides and epoxides is less explored. ROCOP utilising carbon dioxide is emerging as a field of particular industrial interest due to the potential to move from a carbon capture and storage model to carbon capture and use, adoption of which would provide an economic incentive for carbon capture.[18]

The use of Co(III) and Cr(III) salen complexes has been widely reported for epoxide/CO_2 ROCOP (Figure 4.4 b).[19, 20] More recently, Williams and co-workers demonstrated binding of an alkali metal cation in a crown ether pocket adjacent to a salen leads to increased activity and selectivity in epoxide/CO_2 ROCOP (Figure 4.4 c). [21] In 2021, Williams and co-workers produced a series of *ortho*-vanillin derived salen catalysts capable of both ROP of lactones and ROCOP of epoxides and carbon dioxide, with activities higher than many commercially employed lactone ROP catalysts (Figure 4.4 d).[22]

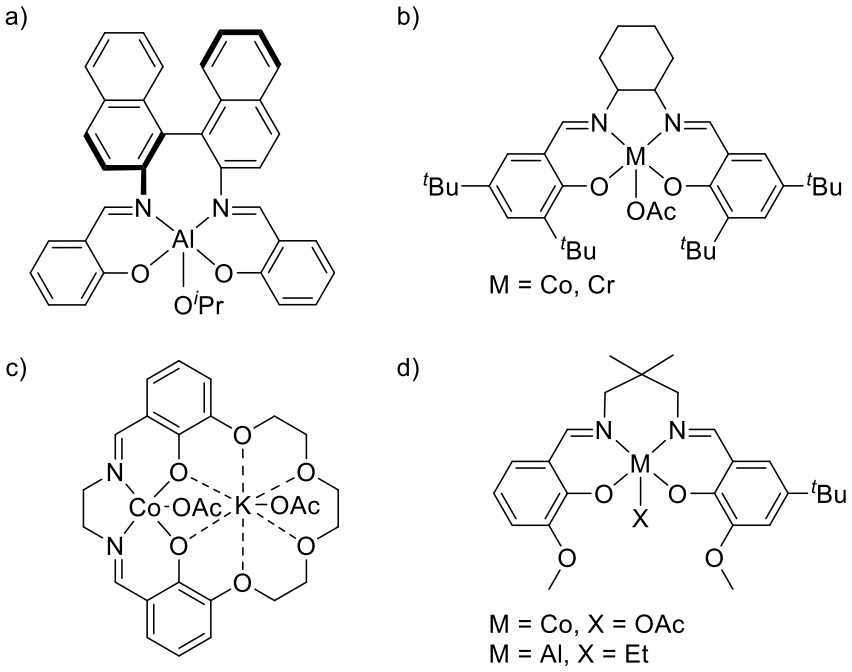

Figure 4.4. Selection of salen based catalysts for ROP and ROCOP.

4.1.4 Co-catalysts for ROCOP

ROCOP of epoxides and carbon dioxide or anhydrides with a monometallic catalyst typically uses an exogenous co-catalyst.[23] Commonly, this is a halide with a bulky, non-coordinating, ammonium cation, such as bis(triphenylphosphine)iminium chloride (PPNCl). Less commonly, organobases such as DMAP have been employed. Due to the possibility of the co-catalyst promoting side reactions, such as the formation of cyclic carbonate species, low loadings are typically used, however this reduces the efficacy of catalysis due to the low effective concentration of the catalyst/co-catalyst pair. To overcome this limitation, recent work has sought to incorporate an ammonium halide ion-pair on a pendant ammonium binding site to increase the effective concentration of the catalyst/co-catalyst pair (Figure 4.5).[24] Binding of the growing polymeryl chain by the ammonium salt also holds the chain in proximity to the catalytic metal centre, reducing back-biting, in which the anionic polymer chain end inserts back into the polymer chain, forming a cyclic species and terminating polymerisation, and other side reactions in the polymerisation process.[25]

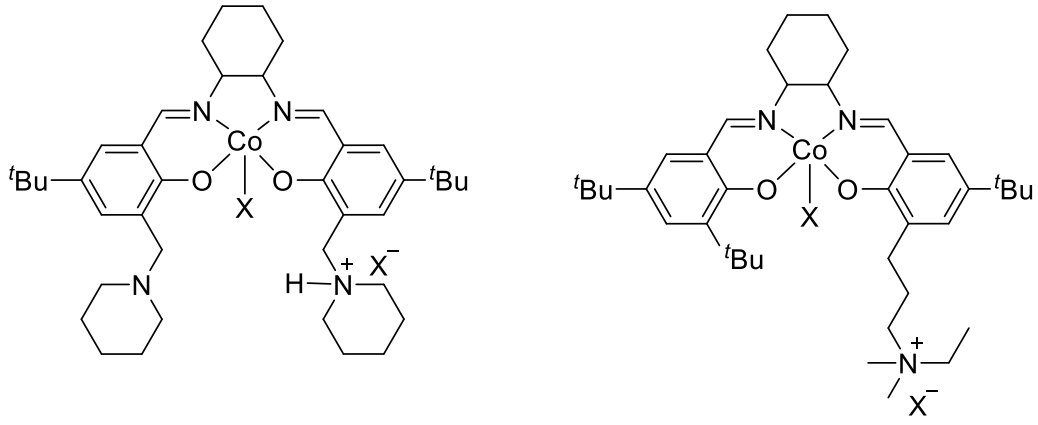

Figure 4.5. Co(III) salen complexes with tethered ammonium salts for intramolecular co-catalyst binding. X = Halide, OAc^-.

4.1.5 Rotaxanes for Ring-opening Polymerisation

The only report demonstrating a rotaxane catalyst for ROP was made in 2019 by Lim *et al*.[26] A [2]rotaxane comprising of an axle with an organocatalytic HB thiourea moiety and a secondary ammonium capable of binding a dibenzo-24-crown-8 macrocycle was, upon deprotonation, demonstrated to effect stereoselectivity in the ROP of *rac*-lactide (Figure 4.6). The authors postulated that the stereoselectivity arose through the slow rate of diffusion of the macrocycle between the axle amine and thiourea binding stations, affording chain-end control over polymer stereochemistry, as the slow shuttling results in the growing polymeryl chain adopting a preferential orientation prior to the next monomer insertion, leading to the formation of isotactic PLA. Increasing the amine basicity and the preference of the crown ether macrocycle to reside at the amine binding station, resulted in faster ROP and a decrease in stereoselectivity, demonstrating the ability of the mechanical bond to modulate reactivity through the dynamic motion of the macrocycle.

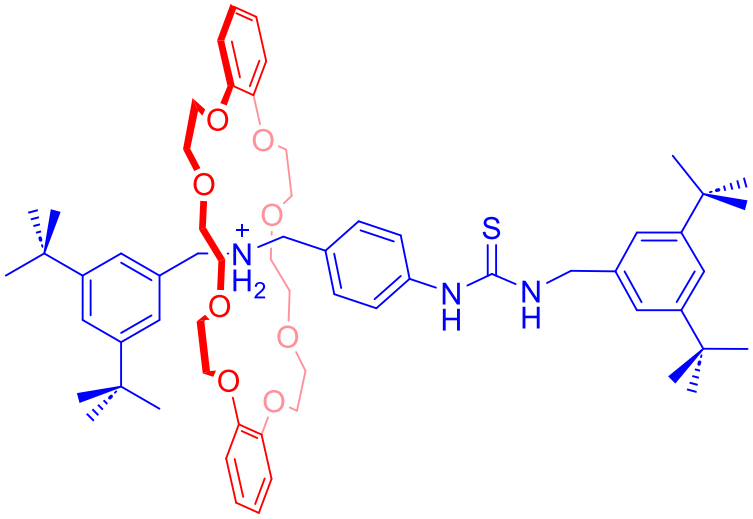

Figure 4.6. Rotaxane catalyst for the isoselective ROP of lactide, reported by Lim *et al*.

4.1.6 Project Aims

This project seeks to bring together the catalytic potency of metal salen complexes and the ability of the mechanical bond to modulate reactivity. It aims to demonstrate novel

MIM and acyclic structures incorporating supramolecular features inspired by the wide range of previously-reported ROP and ROCOP sustainable polymerisation catalysts, such as anion binding sites in close proximity to the transition metal site or stimuli-responsive conformational dynamism for on/off switchable catalysis. Such opportunities to exploit non-covalent interactions are underexplored in polymerisation catalysis. Initial studies will focus on the development of catalytically-active metal salen complexes housed within the axle of a [2]rotaxane, with the macrocycle component bearing an XB motif to target co-catalyst binding concomitant with polyether alkali metal cation complexation (Figure 4.7).

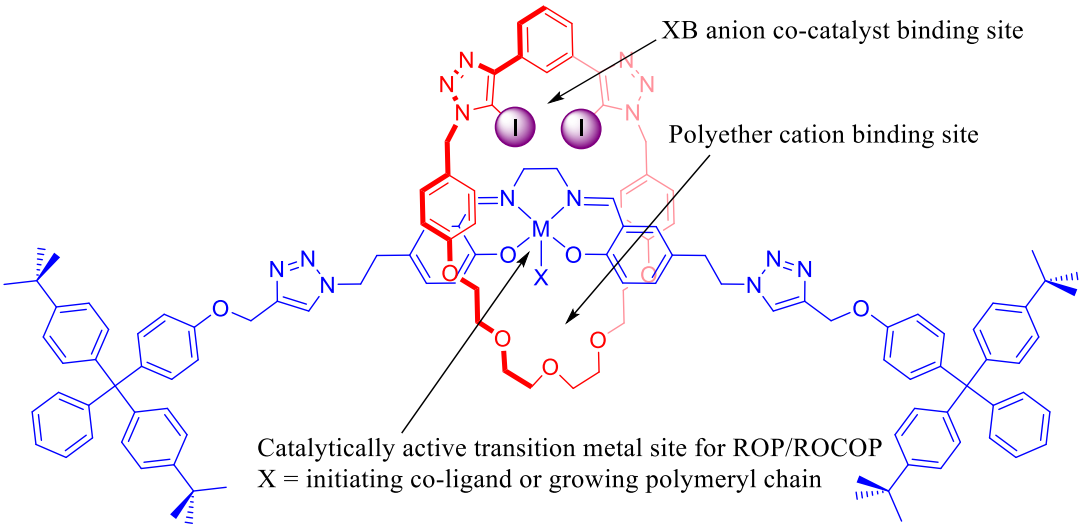

Figure 4.7. Initial target [2]rotaxane.

4.2 Salen-containing Rotaxanes for Polymerisation Catalysis

4.2.1 Synthesis of Axle Precursor Synthons

The design strategy for the interlocked systems targeted the synthesis of a novel salen bis-azide synthon. Such a synthon was expected to undergo CuAAC AMT rotaxination reactions with polyether chain-containing macrocycles, to append bulky stopper groups to the bis-azide, forming [2]rotaxanes.

To that end, the salen bis-azide was prepared. The reaction of commercially available 2-(4-hydroxyphenyl)ethanol with thionyl chloride in toluene formed 4-(2-chloroethyl)phenol in 62% yield, which readily underwent an S_N2 reaction with sodium azide to form 4-(2-azidoethyl)phenol in near-quantitative yield.[27] Selective formylation to 5-(2-azidoethyl)salicylaldehyde was achieved through a magnesium chelation-mediated *ortho*-formylation reaction, in which the chelation of Mg(II) by the phenolate and the oxygen of the inbound carbonyl produced the desired regioselectivity with 64% yield. Condensation of the aldehyde with ethylenediamine formed the desired salen bis-azide ligand **4.1·H₂** in 80% yield (Scheme 4.1).

Nickel(II) was selected for initial metal complexation studies, as it is diamagnetic, non-aggregating, air-stable, forms complexes with salen-type ligands which are stable to silica chromatography,[28] and has previously been reported for catalysis of ROP and ROCOP reactions.[29-32] The d^8 electron configuration of the Ni(II) metal centre was expected to favour a square planar geometry and therefore to produce Ni(II) salen complexes without an associated co-ligand. Metalation of the ligand **4.1·H₂** with Ni(II) acetate tetrahydrate in methanol afforded the Ni(II) complex **4.1·Ni** in quantitative yield, which readily precipitated from the methanolic reaction mixture and was used without further purification.

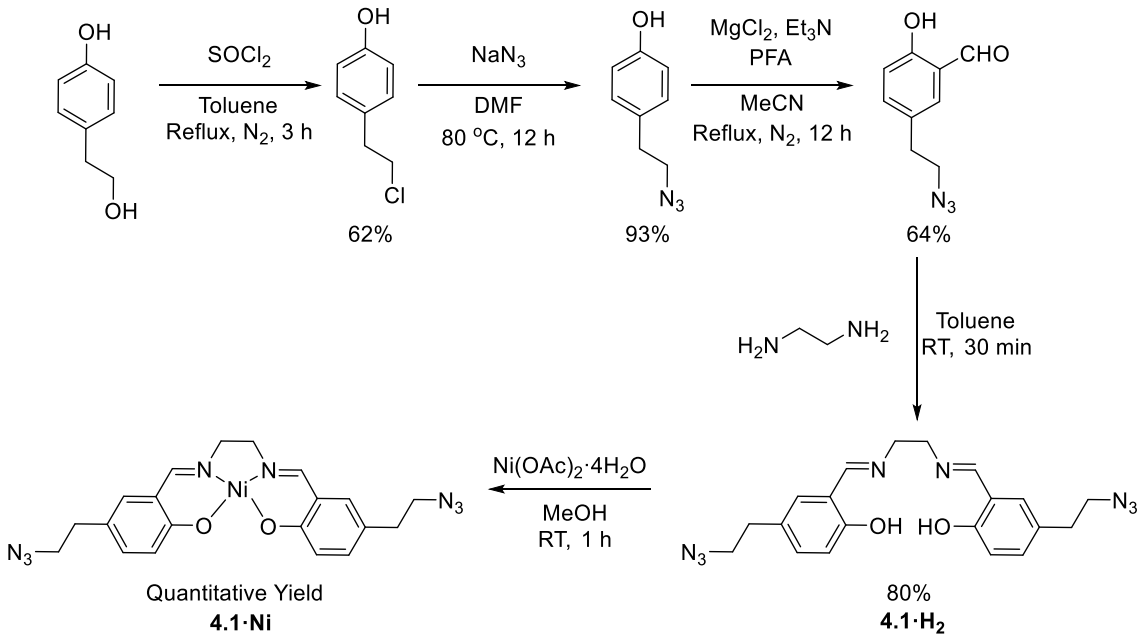

Scheme 4.1. Synthesis of a novel Ni(II) bis-4-(2-azidoethyl)salen complex.

The bulky stopper alkyne **4.2** was synthesised according to a literature procedure (Scheme 4.2).[33] Methyl benzoate reacted with 2 equivalents of 4-*tert*-butylbromobenzene, in a double Grignard reaction, and the resulting bis(*p*-*tert*-butylphenyl)phenylmethanol was reacted with molten phenol under acidic conditions. The resulting phenol reacted with propargyl bromide under mildly basic conditions to afford **4.2** in moderate (30%) yield.

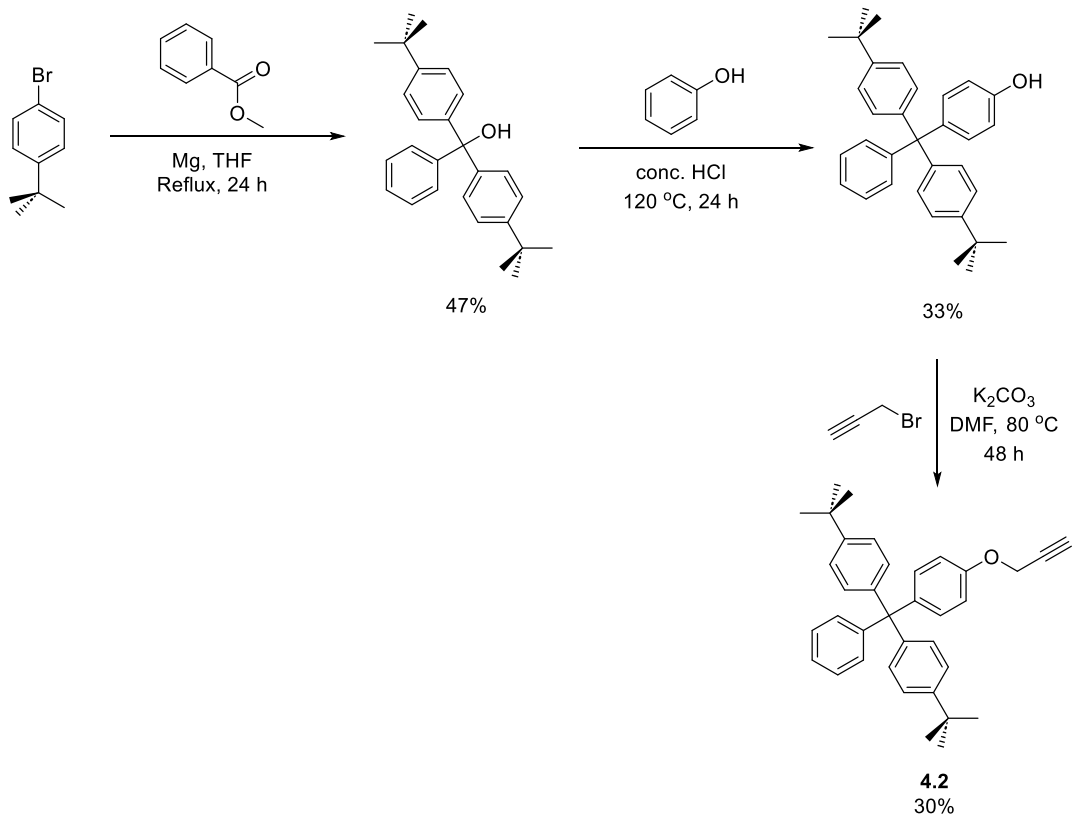

Scheme 4.2. Synthesis of stopper alkyne **4.2**.

4.2.2 Synthesis of a Novel XB Macrocycle

The targeted XB macrocycle was prepared from the CuAAC click reaction of a polyether bis-azide with 1,3-di(iodoethynyl)benzene under high-dilution conditions (Scheme 4.3). The bis-azide was prepared by the reaction of 4-(hydroxymethyl)phenol with tetraethylene glycol ditosylate forming a dialcohol, which, following tosylation, readily underwent an S_N2 reaction with sodium azide to form the bis-azide precursor in 89% yield.[34] A CuAAC cyclisation reaction was attempted under high dilution conditions between the bis-azide and 1,3-di(iodoethynyl)benzene. The resulting macrocycle was detected by mass spectrometry, however, it proved highly insoluble in organic and aqueous media, and separation from insoluble polymeric side products was not possible. To improve macrocycle solubility, a *tert*-butyl group was incorporated into the structure by repeating the CuAAC click cyclisation reaction with 1,3-di(iodoethynyl)-5-*tert*-

butylbenzene, which, after chromatographic purification, produced the target XB macrocycle **4.3** in 42% yield.

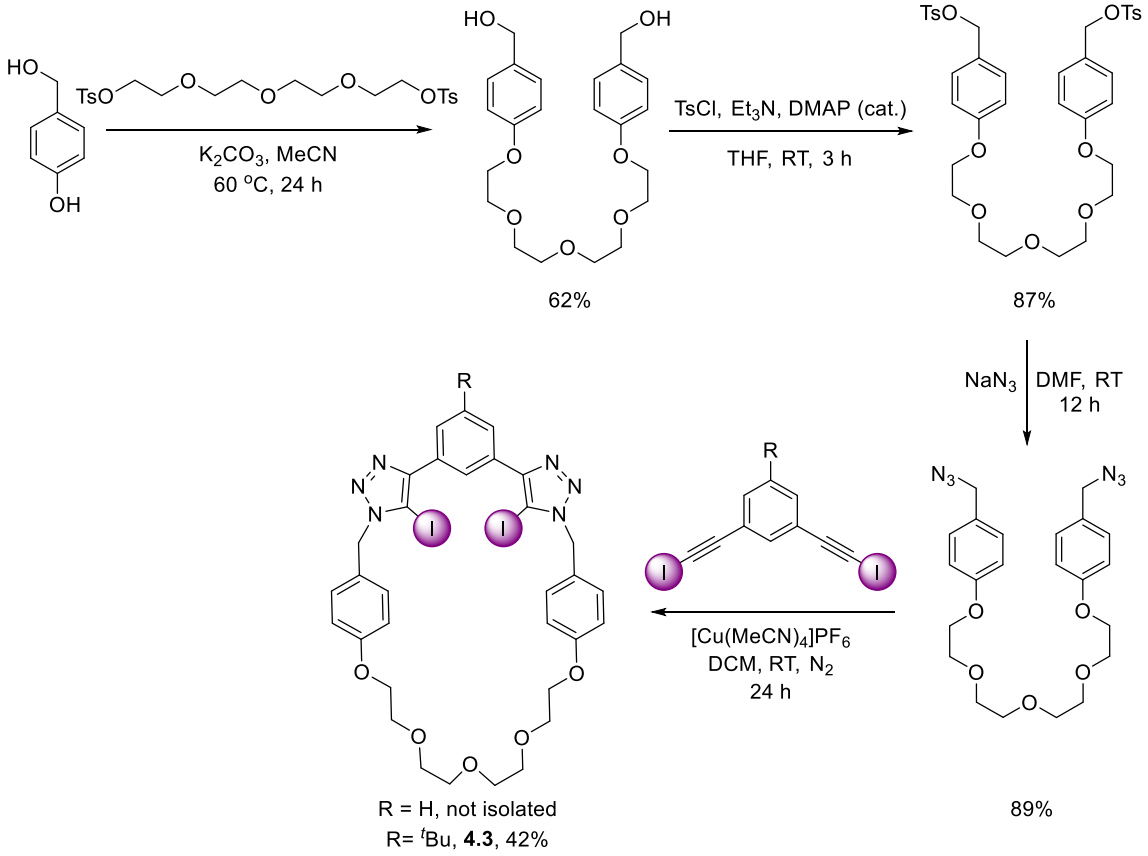

Scheme 4.3. Synthesis of XB macrocycle **4.3**.

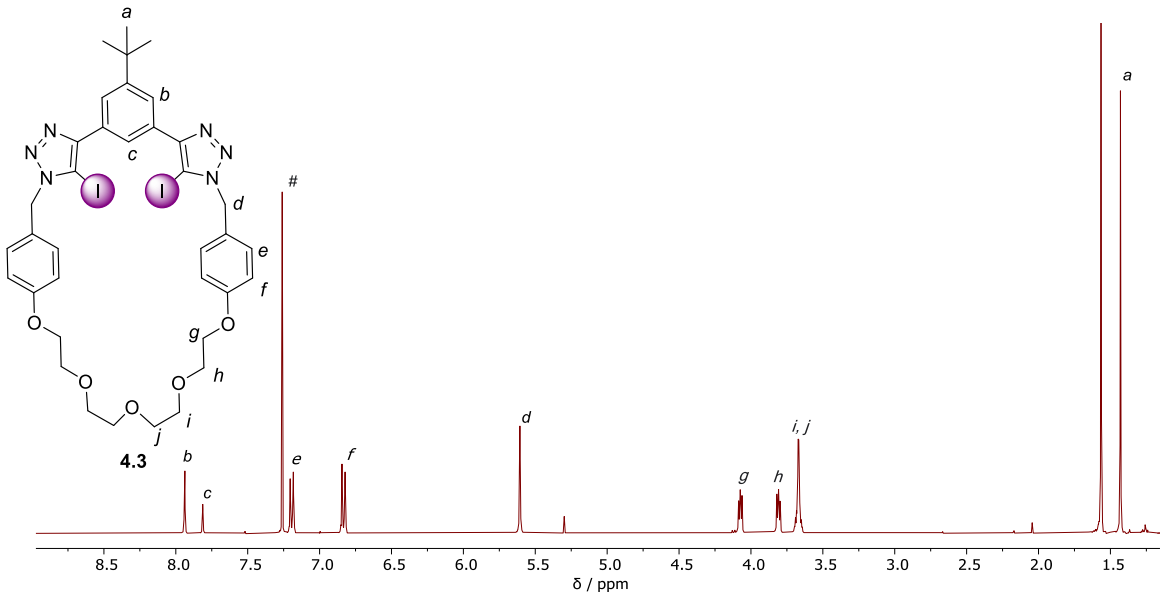

Figure 4.8. ^{1}H NMR ($CDCl_3$, 400 MHz, 298 K) spectrum of macrocycle **4.3**. # Denotes residual protio solvent.

4.2.3 Synthesis of Ni(II) Salen-containing [2]Rotaxanes

Initial attempts at the challenging synthesis of the target [2]rotaxane were made with the XB macrocycle **4.3** and the axle components **4.1·Ni** and **4.2** to form the interlocked structure, through an AMT approach. A DCM solution of macrocycle **4.3** was prepared with one equivalent of $[Cu(MeCN)_4]PF_6$ catalyst. Upon addition of six equivalents of stopper alkyne **4.2** and three equivalents of bis-azide **4.1·Ni**, the CuAAC AMT reaction was expected to form the target interlocked product. (Scheme 4.4).

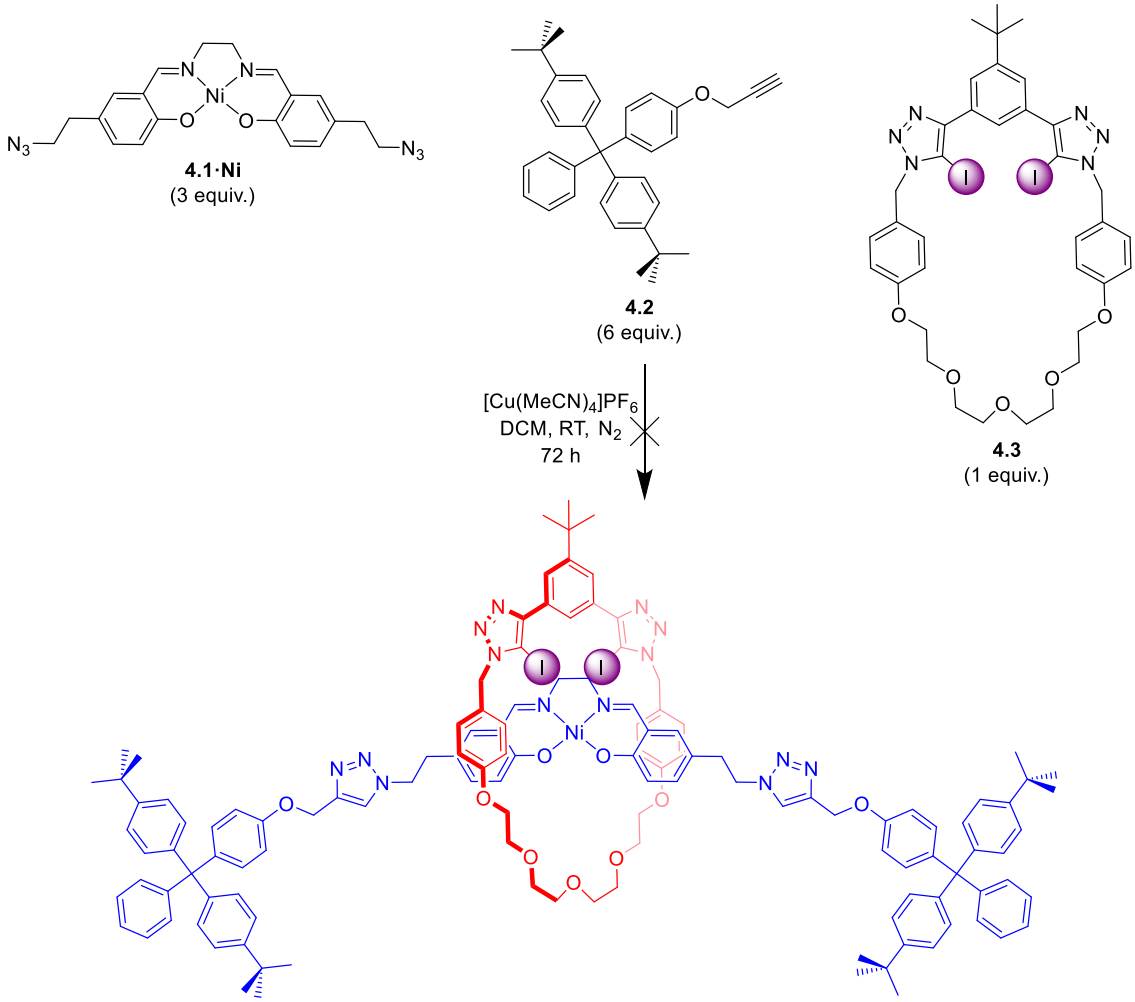

Scheme 4.4. Attempted synthesis of target Ni(II) salen-containing XB [2]rotaxane.

After 5 days however, no interlocked product was observed, only the non-interlocked axle product **4.4·Ni** and recovered macrocycle **4.3** were isolated from the crude reaction mixture by preparative TLC. This was attributed to the very low binding affinity of the

macrocycle to Cu(I). The reaction was repeated using analogous AMT conditions with pyridyl moiety-containing macrocycles, **2.3, 3.5** and a tetraethylene glycol congener, **4.5**, prepared in 51% yield by an analogous synthesis to its tri- and penta-ethylene glycol analogues (Scheme 4.5 a). Pleasingly, [2]rotaxanes **4.6·Ni** – **4.8·Ni** were isolated via preparative TLC purification in 14 − 18% yield (Scheme 4.5 b) and characterised by ^{1}H and ^{13}C{^{1}H} 1-D, and ^{1}H-^{1}H 2-D NMR spectroscopy and mass spectrometry. Reducing the size of the macrocycle resulted in a marginally decreased yield of the interlocked product, likely due to increased steric hindrance for the CuAAC MIM forming reaction occurring in the cavity of the macrocycle.[35]

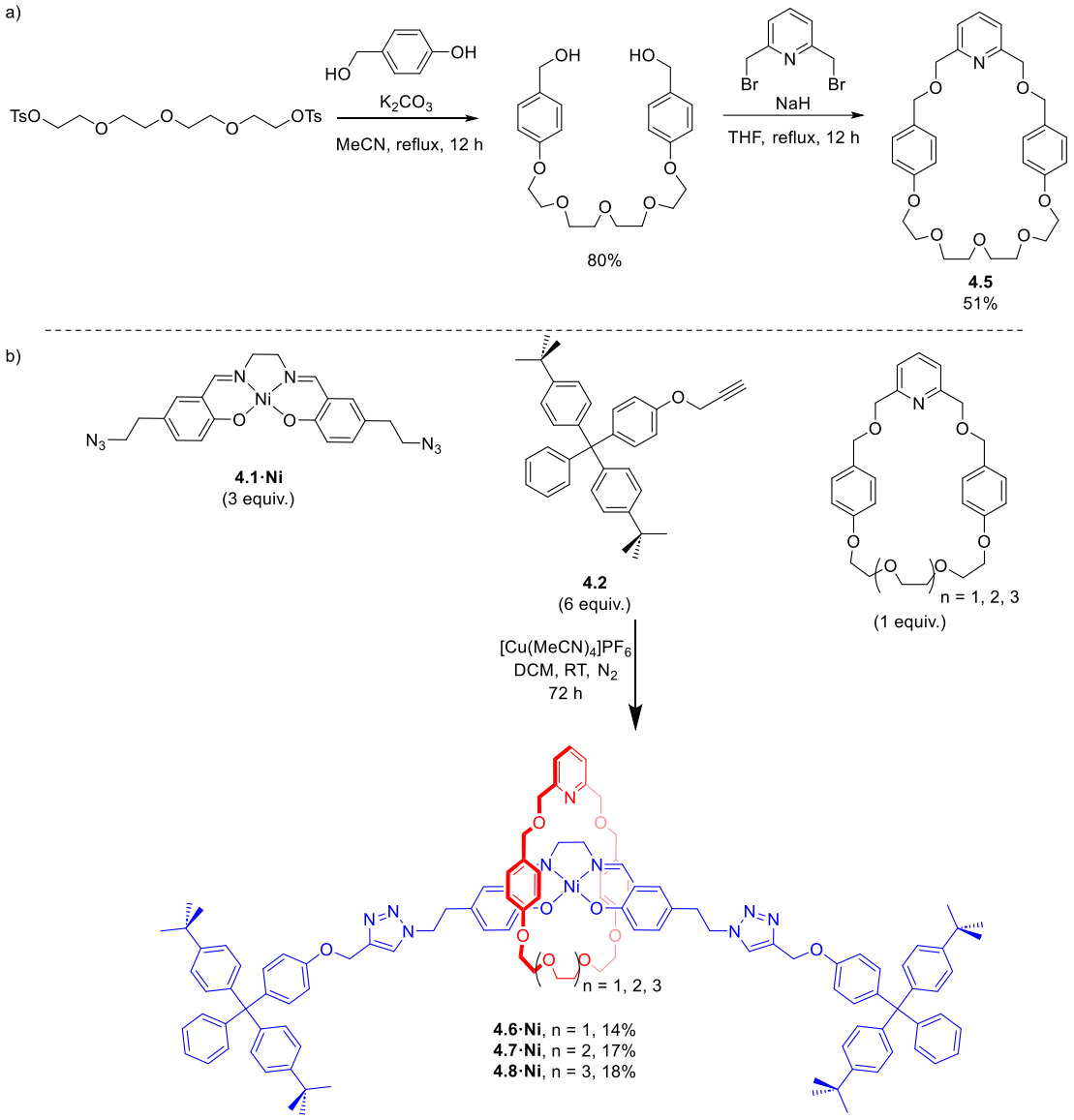

Scheme 4.5. a) Synthesis of macrocycle **4.5**, b) synthesis of [2]rotaxanes **4.6·Ni** – **4.8·Ni**.

A comparison of the ^{1}H NMR spectra of the respective [2]rotaxanes to the non-interlocked axle **4.4·Ni** and the corresponding free pyridyl macrocycle confirmed the formation of the interlocked product (Figure 4.9). The macrocycle and axle salen alkyl protons are shifted significantly upfield compared to the spectra of the individual non-interlocked axle and macrocycle components. This is consistent with the shielding experienced due to the mechanical bond positioning the aromatic rings of these

components in close proximity, leading to ring-current perturbations to the ^{1}H NMR environments.

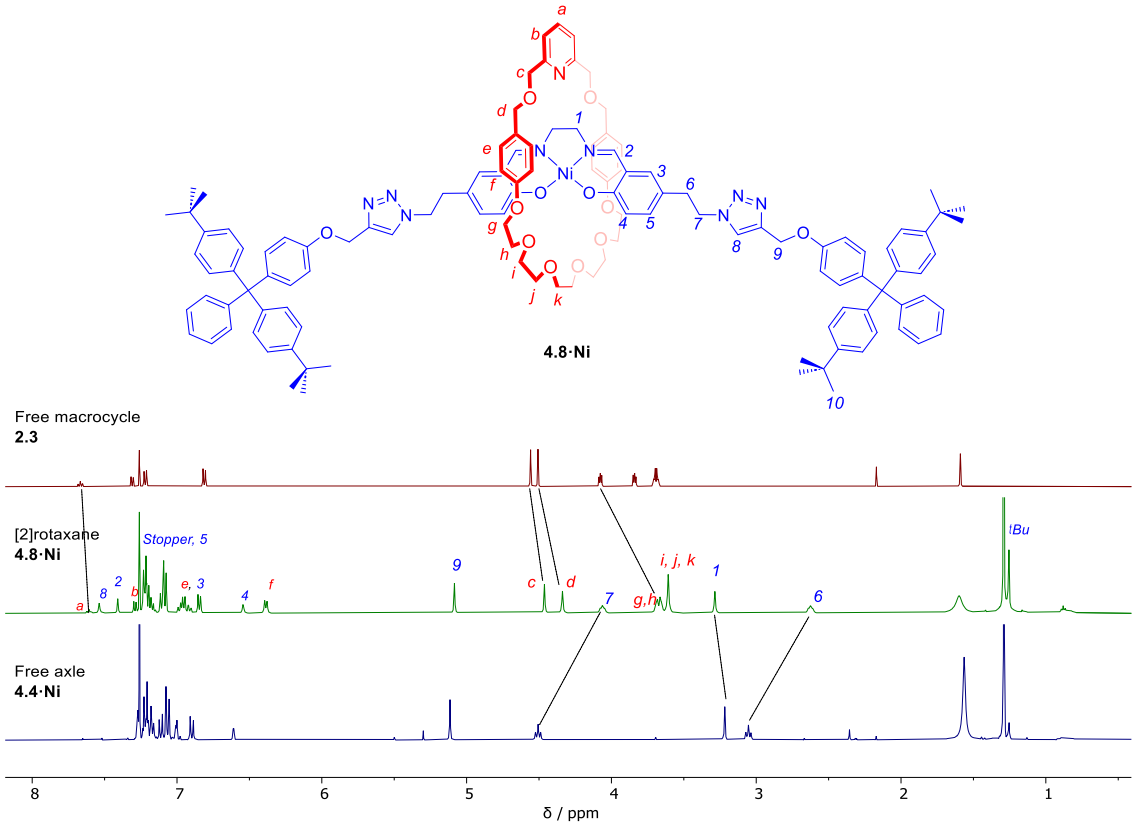

Figure 4.9. Stacked ^{1}H NMR (400 MHz, $CDCl_3$, 298 K) of [2]rotaxane **4.8·Ni**, and the corresponding non-interlocked macrocycle, **2.3**, and axle **4.4·Ni**.

Decreasing the size of the polyether chain, and hence the size of the macrocycle cavity, led to changes in the room temperature [2]rotaxane ^{1}H NMR spectra, consistent with changes in the dynamic movement of the macrocycle along the rotaxane axle (Figure 4.10). With the largest ring size, employing the pentaethylene glycol-containing macrocycle **2.3**, the [2]rotaxane ^{1}H NMR spectrum is clearly resolved, with resonances demonstrating the symmetry of the axle. This is consistent with the macrocycle readily diffusing along the axle on the NMR timescale. Decreasing the size of the macrocyclic cavity by using a tetraethylene glycol linker leads to substantial broadening of the axle resonances *6* and *7*, suggesting the dynamic process was approaching the coalescence point at room temperature. With the smallest macrocycle, containing a triethylene glycol

linker, the apparent symmetry of the ^{1}H NMR spectrum is lost, implying that the macrocycle, with its smaller cavity, is now moving along the axle slower than the NMR timescale, consistent with increased steric interactions between the axle and macrocycle. Unfortunately, the poor solubility of the [2]rotaxanes in common deuterated organic solvents precluded VT NMR studies to quantify the relative macrocycle shuttling rates.

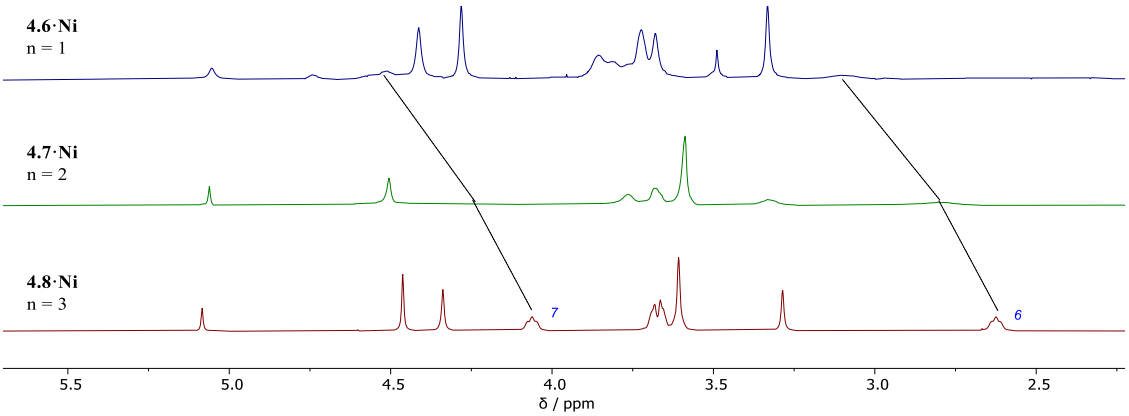

Figure 4.10. Stacked truncated ^{1}H NMR (400 MHz, $CDCl_3$, 298 K) spectra of [2]rotaxanes **4.6·Ni – 4.8·Ni** demonstrating broadening of the spectra upon decreasing macrocycle size.

4.2.4 Preliminary ROCOP Testing

Initial polymerisation attempts sought to mirror conditions previously reported for ROCOP of CO_2 and epoxides,[21] with the rotaxanes **4.6·Ni – 4.8·Ni**, and one equivalent of PPNCl co-catalyst, suspended in each of the target epoxides, propylene oxide (PO), cyclohexene oxide (CHO) and the bio-derived monomer limonene oxide (LO), [Catalyst]:[PPNCl]:[Epoxide] = 1:1:1000. As the Ni(II) centre in rotaxanes **4.6·Ni** – **4.8·Ni** does not contain an initiating co-ligand, 0.5 equivalents of benzyl alcohol were added to the polymerisation mixture to serve as an exogeneous ROCOP initiator.[36] The suspensions was transferred to a stainless steel reaction vessel, and placed under pressure in a 40 bar CO_2 atmosphere (Scheme 4.6). Unfortunately, after 72 hours, no monomer conversion was observed, attributed to the poor solubility of catalysts **4.6·Ni** – **4.8·Ni** in the epoxides.

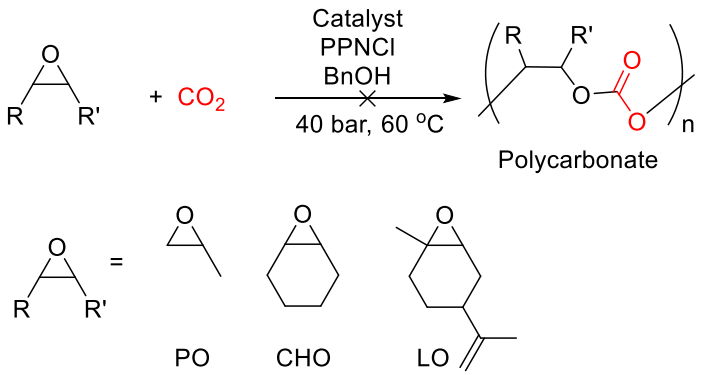

Scheme 4.6. Initial polymerisation reactions attempted. [Catalyst]:[PPNCl]:[BnOH]:[Epoxide] = 1:1:0.5:1000.

4.2.5 Attempted Synthesis of Co(III) [2]Rotaxane Congeners

Given the poor solubility of **4.6·Ni** – **4.8·Ni**, and the lack of observed polymerisation activity, the synthesis of their Co(III) congeners was targeted as Co(III) salens are known to display high polymerisation activities,[37] and therefore may demonstrate activity even at the low catalyst loadings necessitated by the poor solubility.

To that end, using Schlenk techniques, **4.1·H$_2$** was dissolved in an anhydrous methanolic solution of Co(OAc)$_2$. After stirring for 1 hour under an inert atmosphere, cannula filtration afforded **4.1·Co^{II}** as a red solid. The ^{1}H NMR spectrum of **4.1·Co^{II}** displayed significant paramagnetic broadening, consistent with successful metalation with paramagnetic Co(II) (Scheme 4.7). The solid was dissolved in DCM and glacial acetic acid (AcOH) added. The mixture was stirred under an O_2 atmosphere for 48 hours and the solvent and residual AcOH removed *in vacuo* (Scheme 4.7). Unfortunately, the ^{1}H NMR spectrum of the resulting solid still demonstrated significant paramagnetic broadening, demonstrating unsuccessful oxidation of the Co(II) centre in **4.1·Co^{II}** (Figure 4.11), likely due to the salen ligand **4.1** being insufficiently electron-rich to stabilise the Co(III) oxidation state.

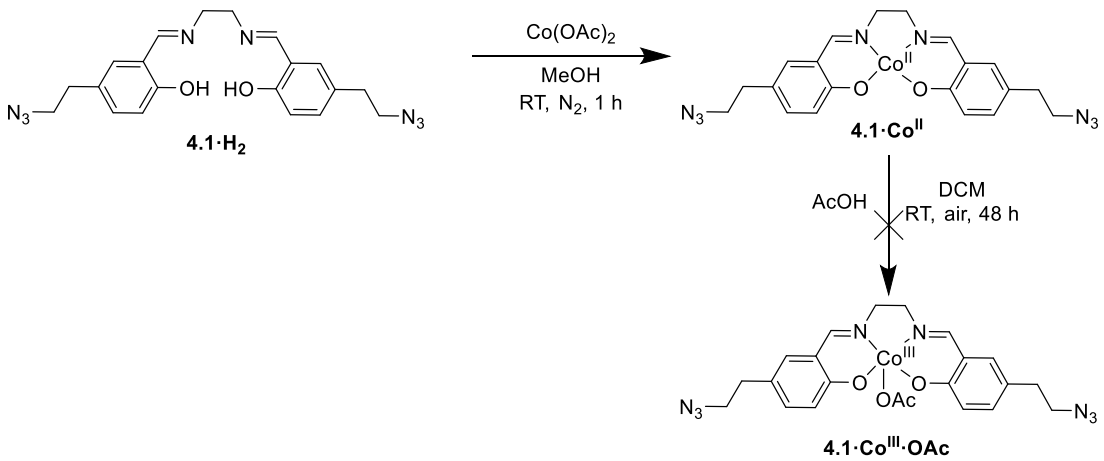

Scheme 4.7. Attempted synthesis of **4.1·Co^{III}·OAc**.

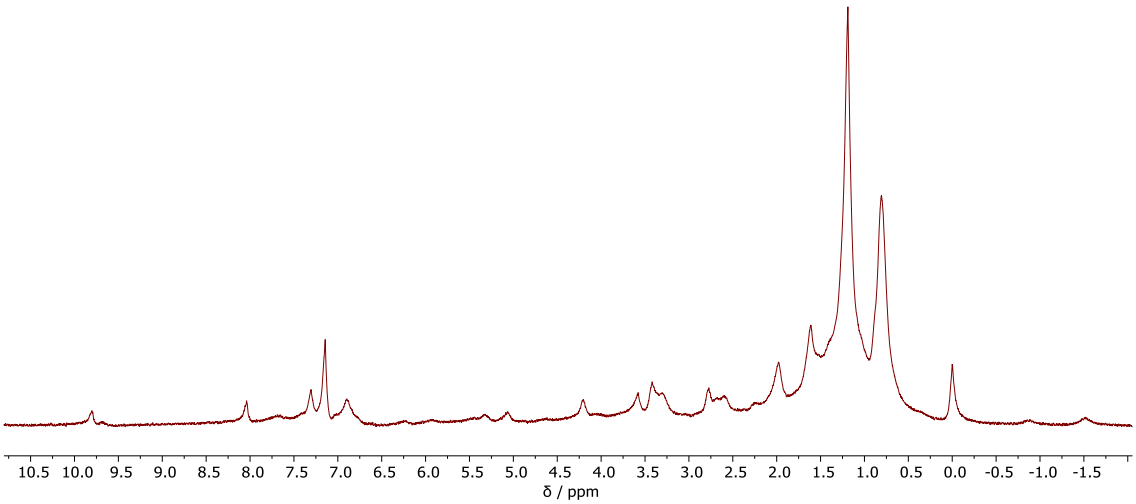

Figure 4.11. ^{1}H NMR (400 MHz, $CDCl_3$, 298 K) spectrum of the product of the attempted synthesis of **4.1·Co^{III}·OAc** showing significant paramagnetic broadening.

As it is known that subtle changes in the ethylene alkyl backbone linker of salen-type ligands can affect their electronic properties and transition metal complex stability,[38] the synthesis of the so-called salcy congener of **4.1·Co^{III}·OAc**, with a cyclohexyl backbone, was performed. Condensation of 5-(2-azidoethyl)salicylaldehyde with *trans*-1,2-diaminocyclohexane afforded the bis-azido salcy ligand **4.9·H$_2$**. The Co(III) complex **4.9·Co^{III}·OAc** was prepared by an analogous procedure to the attempted synthesis of **4.1·Co^{III}·OAc** (Scheme 4.8). Pleasingly, while paramagnetic broadening was observed in the ^{1}H NMR spectrum of **4.9·Co^{II}**, after exposure to air in the presence of AcOH, a well-resolved ^{1}H NMR spectrum of **4.9·Co^{III}·OAc** was observed, in addition to a diagnostic change in the colour of the compound from red to dark green,[39] confirming the

successful oxidation of the metal centre to the diamagnetic Co(III) oxidation state (Figure 4.12).

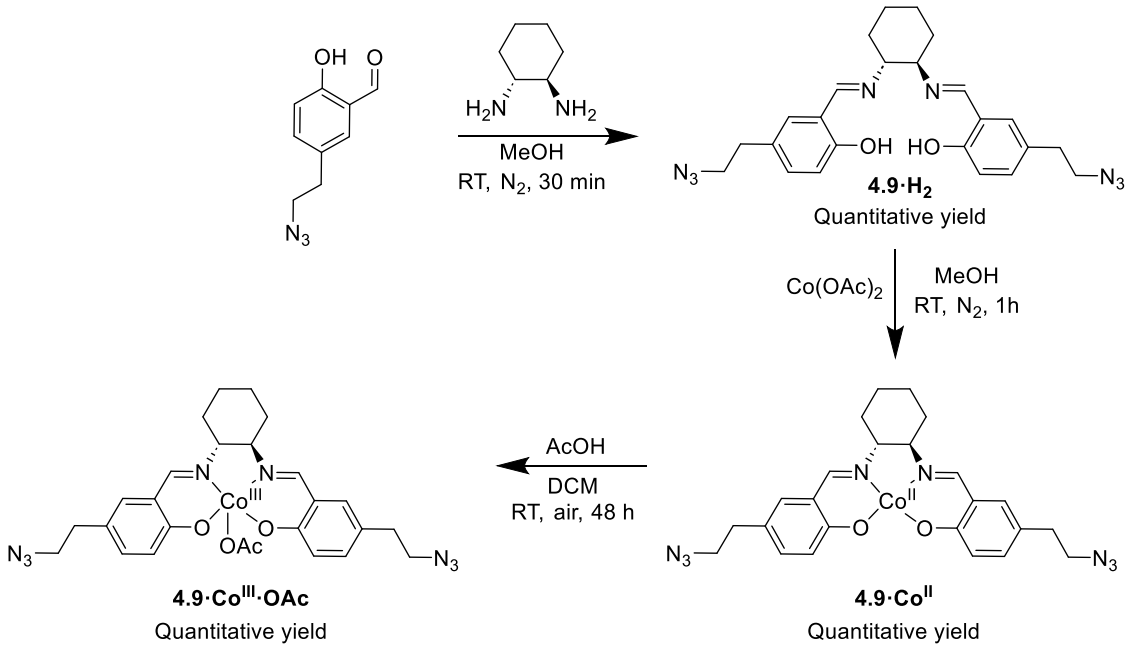

Scheme 4.8. Synthesis of **4.9·Co^{III}·OAc**.

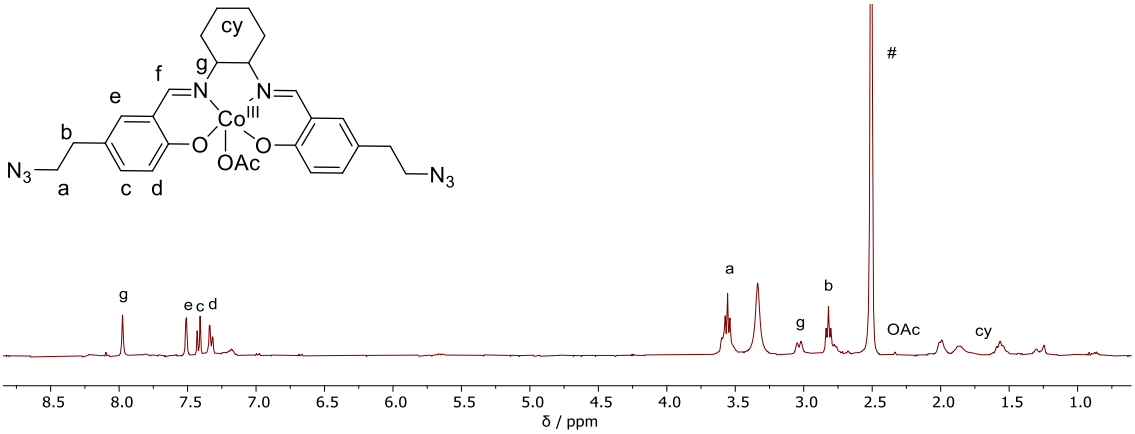

Figure 4.12. ^{1}H NMR (400 MHz, DMSO-d_6, 298 K) spectrum of **4.9·Co^{III}·OAc**. # Denotes residual protio solvent.

With **4.9·Co^{III}·OAc** in hand, the synthesis of the corresponding Co(III) [2]rotaxane was attempted, under analogous AMT conditions to the synthesis of **4.8·Ni**. Unfortunately, no conversion of **4.9·Co^{III}·OAc** was observed, likely due to redox processes forming a CuAAC inactive Cu(II) complex.

4.3 Crown Ether-appended Salen Complexes for Cation and Ion-Pair Recognition

4.3.1 Synthesis of Crown Ether Pendant Salen Complexes

Following the reports by Williams and co-workers of highly active bimetallic catalysts for CO_2/epoxide ROCOP containing a Co(III) salen complex with an alkali metal cation bound in a proximal crown ether-like pocket (Figure 4.4 c),[21] salen complexes containing benzo-15-crown-5 (B15C5) pendants were prepared. B15C5 is known to form 2:1 stoichiometric host:guest sandwich complexes selectively upon K^+ complexation, in which all 10 crown ether oxygen atoms participate in binding.[40, 41] Therefore, it was postulated that the highly active bimetallic arrangement reported by Williams could be selectively assembled by the introduction of a potassium salt, rather than the analogous sodium salt, potentially acting as a route to on/off switchable catalysis (Figure 4.13).[42]

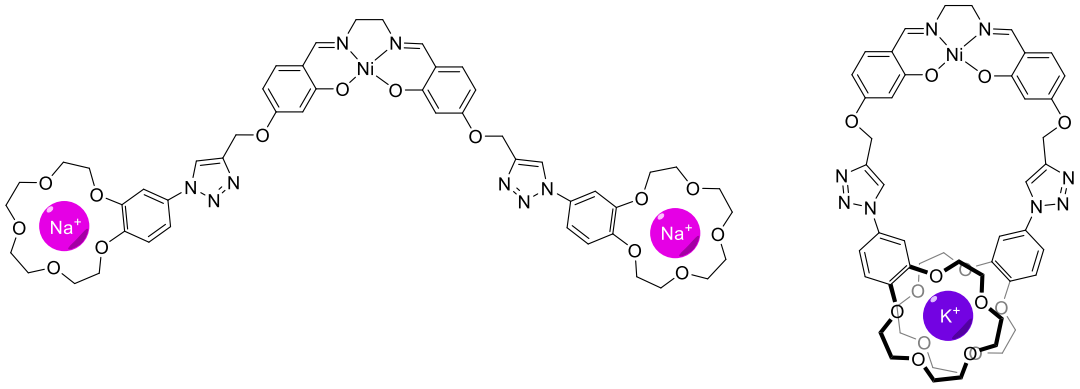

Figure 4.13. Selective cation binding-induced conformational changes in targeted B15C5-appended salen complexes.

B15C5 was synthesised according to a literature procedure.[43] Tetraethylene glycol was chlorinated with thionyl chloride, and the resulting polyether bis-chloride was refluxed with catechol under basic conditions and an inert atmosphere, to form B15C5 in 47% yield. Nitration of B15C5 with a mixture of concentrated nitric acid in 1:1 *v/v* chloroform and acetic acid gave B15C5-NO_2 which underwent reduction with hydrazine monohydrate in the presence of a palladium(II) on carbon catalyst to afford B15C5-NH_2.

Diazotisation of the amine and reaction with NaN_3 produced B15C5-N_3 in 76% yield (Scheme 4.9).

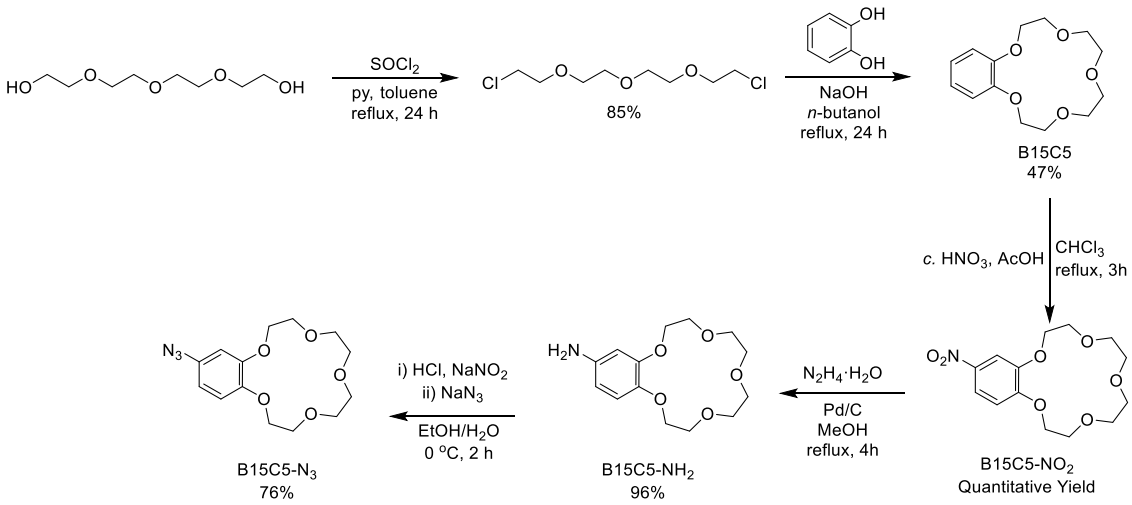

Scheme 4.9. Synthesis of B15C5-N_3.

The corresponding salicylaldehyde alkyne synthon **4.10** was produced by the reaction of 2,4-dihydroxybenzaldehyde with propargyl bromide in the presence of potassium carbonate. Thermodynamically controlled regioselective *para* substitution was achieved in 62% yield through the use of K_2CO_3 as a weak base to selectively deprotonate the *para* phenol hydroxyl group, maintaining intramolecular hydrogen bonding between the carbonyl oxygen and the *ortho* phenolic proton. The CuAAC reaction of alkyne **4.10** with B15C5-N_3 generated the salicylaldehyde pro-ligand **4.11** in 69% yield, which upon subsequent condensation with ethylenediamine followed by addition of Ni(II) acetate tetrahydrate formed the target salen complex **4.12·Ni**, isolated by filtration in 88% yield (Scheme 4.10).

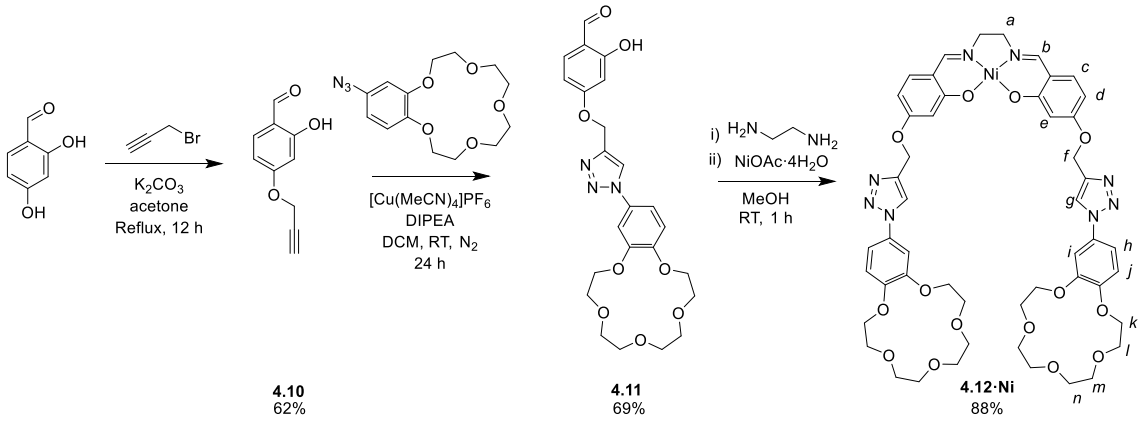

Scheme 4.10. Synthesis of **4.12·Ni**.

4.3.2 Alkali Metal Cation Binding Studies of a Salen Nickel Complex with B15C5 Pendants

In order to assess the binding stoichiometry of alkali metal cations with salen **4.12·Ni**, ^{1}H NMR binding studies were undertaken, monitoring the ^{1}H NMR signals of **4.12·Ni** during successive additions of a solution of the alkali metal cation with the non-coordinating tetrakis[3,5-bis(trifluoromethyl)phenyl]borate ($BAr^F{}_4^-$) counter-anion in 1:1 *v/v* $CDCl_3$:CD_3CN.

As expected, significant downfield perturbations in the aliphatic crown ether proton resonances, *k*, *l*, *m* and *n*, were observed upon addition of the alkali metal $BAr^F{}_4^-$ salts, consistent with deshielding of the crown ether protons by the bound cation. Addition of $KBAr^F{}_4$ showed near-quantitative ($K_a > 10^5$ M^{-1}) binding of one equivalent of K^+, after which the methylene resonance *f* stabilised, consistent with the formation of a 1:1 stoichiometric host-guest sandwich complex (Figure 4.14 a). The significant shift in *f* is attributed to the change in the spatial environment of the proton as the pendant arms fold inwards to form the bis-B15C5 sandwich complex. On binding of Na^+, no change in the methylene proton *f* was observed and the crown ether proton resonances continued to evolve until two equivalents of Na^+ had been added (Figure 4.14 b, c), consistent with

the formation of a 1:2 stoichiometric host-guest complex, with the smaller Na^+ cation preferentially binding inside each B15C5 cavity. Again, binding was near-quantitative.

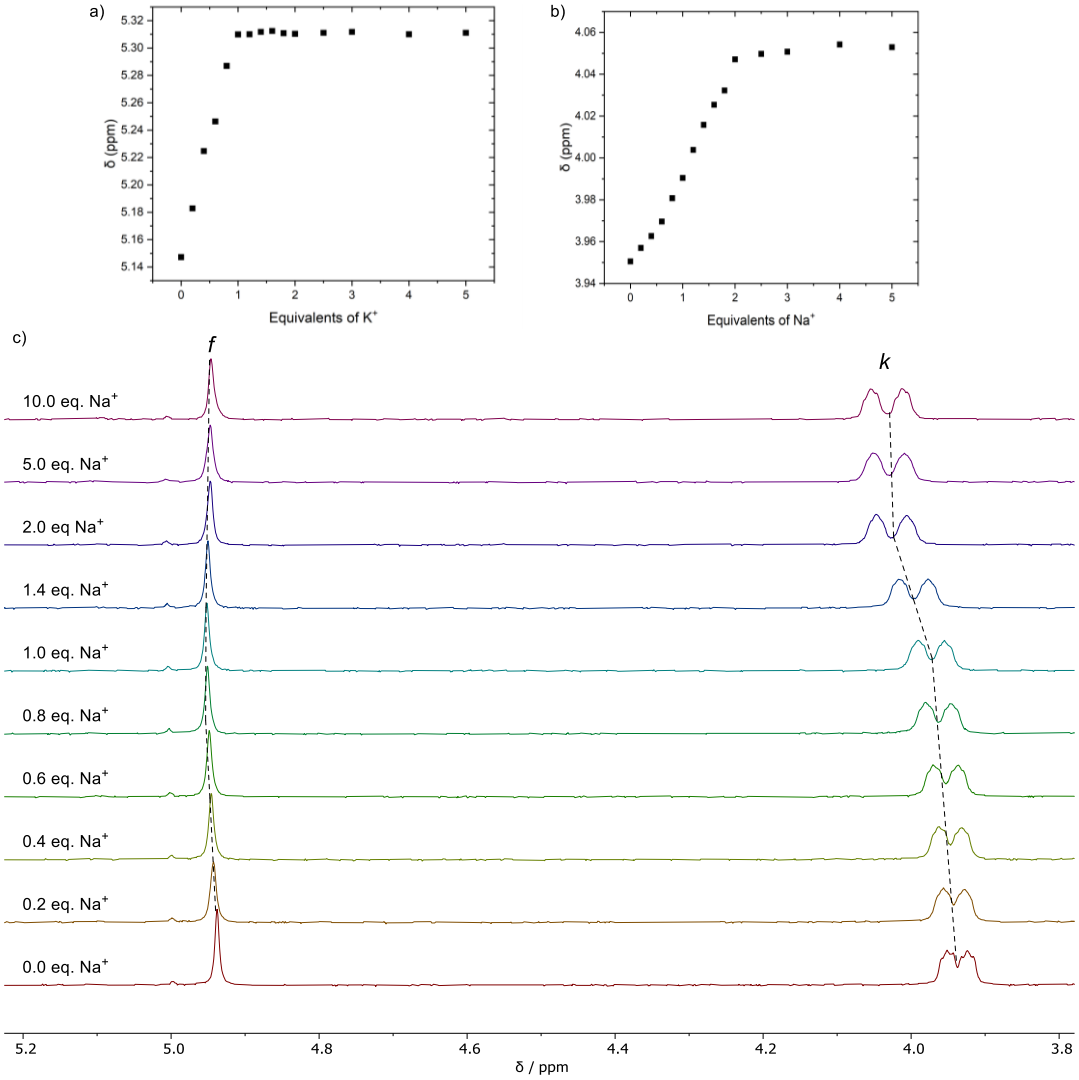

Figure 4.14. a) Binding isotherms showing ^{1}H NMR resonance of proton *f* of **4.12·Ni** upon sequential addition of a) $KBAr^F_4$ and b) $NaBAr^F_4$ solutions. c) Partial ^{1}H NMR spectra of **4.12·Ni** upon sequential addition of $NaBAr^F_4$. All NMR spectra recorded in 1:1 *v/v* $CDCl_3$:CD_3CN, 500 MHz, 298 K.

4.3.3 Preliminary Ion-Pair Recognition Studies

The preorganisation of salen complex **4.12·Ni** upon formation of a K^+ bis-B15C5 sandwich complex was predicted to create a binding cavity into which an anion could be subsequently bound exploiting favourable proximal ion-pair electrostatic effects concomitant with C—H···A^- HB interactions from the triazole motifs (Figure 4.15 a).

Moreover, such an ion-pair complex may be able to stabilise a growing anionic polymeryl chain during catalysis. Whereas no iodide binding was observed in the absence of an alkali metal cation, or in the presence of Na^+, ^1H NMR titration of a TBAI solution into a solution of **4.12·Ni** and one equivalent of $KBAr^F{}_4$ in 1:1 *v/v* CD_3CN:$CDCl_3$ resulted in perturbations of the triazole proton resonance *g* consistent with halide association in the cavity between the bound potassium and the Ni salen linker motif (Figure 4.15 b). The resulting binding isotherms were analysed using a 1:1 binding model with *Bindfit*,[44] revealing weak I^- association (K_a = 26 M^{-1}).

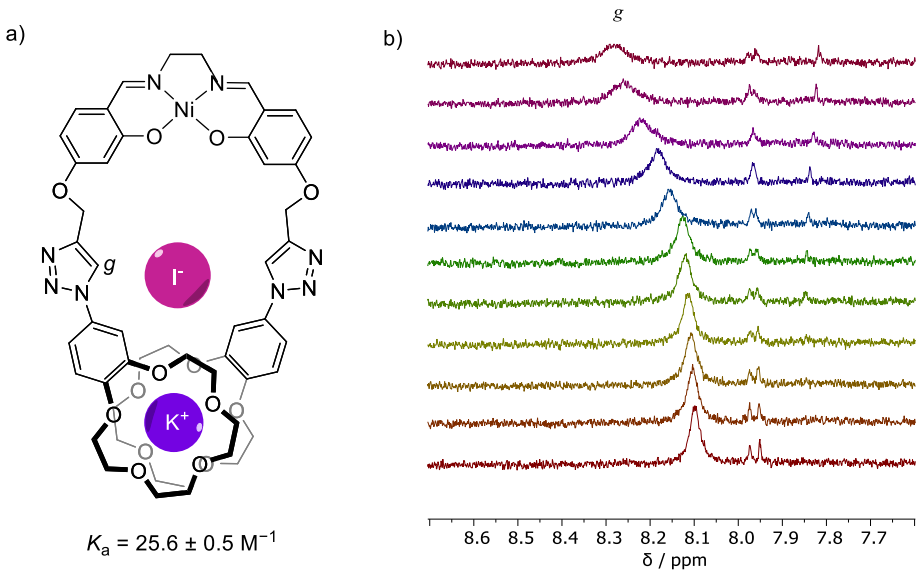

Figure 4.15. a) Depiction of proposed I^- binding mode by **4.12·Ni**·K^+ in 1:1 *v/v* $CDCl_3$:CD_3CN. b) Stacked truncated ^1H NMR (500 MHz, 1:1 *v/v* $CDCl_3$:CD_3CN, 298 K) spectra of **4.12·Ni**·K^+ showing triazole resonance region upon successive addition of I^-.

4.3.4 Attempted Synthesis of an XB-functionalised Ni Salen Complex for Enhanced Ion-Pair Recognition

In order to enhance the ion-pair binding ability of **4.12·Ni**, an XB congener was targeted, incorporating iodotriazole motifs for enhanced anion binding. To that end, the iodoalkyne analogue of **4.10** was prepared (Scheme 4.11). Propargyl alcohol was iodinated by stirring with KOH and I_2 overnight, forming the corresponding iodoalkyne alcohol which was chlorinated by reaction with thionyl chloride. The iodoalkyne was reacted with 2,4-

dihydroxybenzaldehyde under analogous basic reaction conditions to the synthesis of **4.10**. Unfortunately, only an inseparable mixture of the target iodoalkyne and protoalkyne **4.10** was obtained.

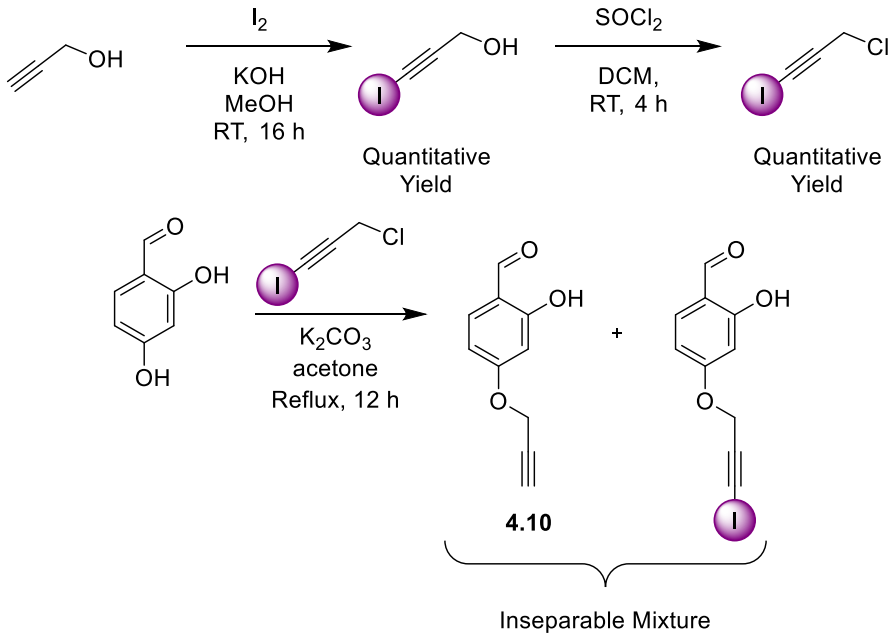

Scheme 4.11. Attempted synthesis of iodoalkyne congener of **4.10**.

As this result was attributed to the likely cleavage of the weak bond between the *sp* hybridised alkyne carbon and the iodine atom during the heating required for ether linkage formation, an alternative synthetic strategy was devised, wherein the iodotriazole would be synthesised prior to the high temperature Williamson ether synthesis step, with the stronger iodine–sp^2 hybridised carbon bond hopefully preventing cleavage of the C–I bond (Scheme 4.12). The earlier synthesised iodo-propargyl alcohol underwent a CuAAC reaction with B15C5-N_3 to form an alcohol terminated synthon, which was chlorinated with $SOCl_2$, and reacted with 2,4-dihydroxybenzaldehyde in an analogous reaction to the formation of **4.10**. Unfortunately, once again, an inseparable mixture of the desired product and the prototriazole analogue, **4.11**, was obtained.

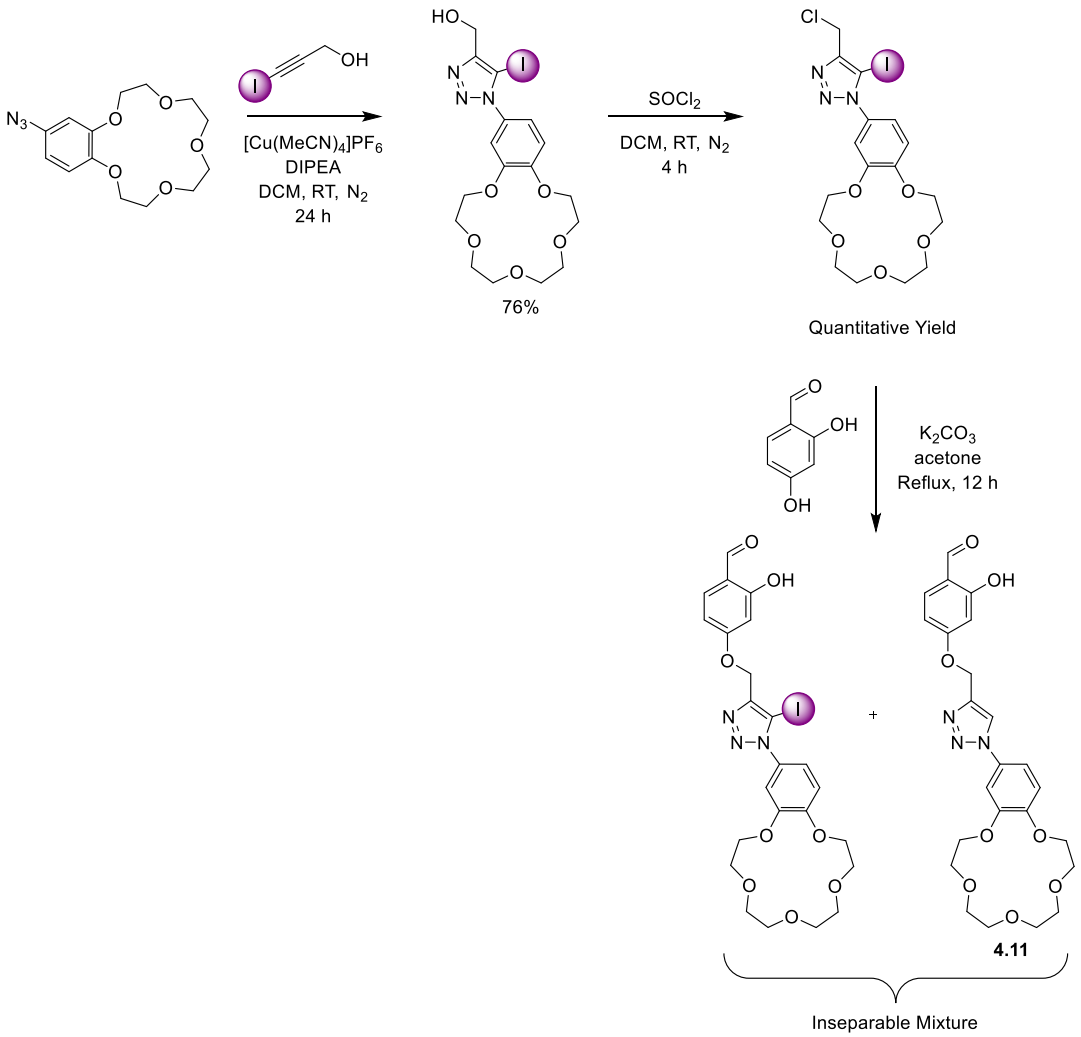

Scheme 4.12. Alternative route in the attempted synthesis of iodo-alkyne congener of **4.11**.

With the apparent synthetic inaccessibility of the XB congener of **4.12·Ni**, an alternative route to enhanced anion binding was targeted through the synthesis of a regioisomer of **4.12·Ni**, in which the crown ether pendent group was moved from the *meta* to the *ortho* position relative to the salen ligand oxygen atoms. It was anticipated that reducing the size of the anion binding cavity in the K^+ bis-B15C5 sandwich complex would enhance HB interactions between the triazole protons and the guest anion, leading to enhanced binding affinities.

To this end, the reaction of 2,3-dihydroxybenzaldehyde with propargyl bromide, under kinetic control with the strong base NaH, formed 3-(ethynyloxy)-2-hydroxybenzaldehyde in 42% yield. This alkyne underwent a high yielding CuAAC click

reaction with B15C5-N_3 to form pro-ligand **4.13** in 89% yield. Condensation of **4.13** with ethylenediamine, followed by *in situ* metalation with $Ni(OAc)_2 \cdot 4H_2O$, formed the target complex **4.14·Ni** in 38% overall yield.

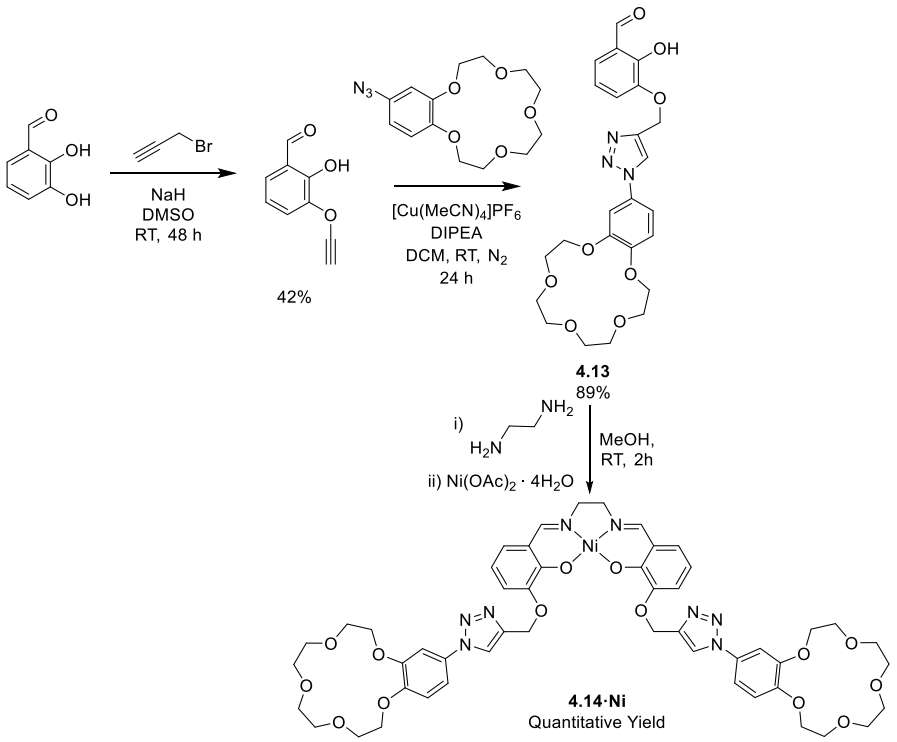

Scheme 4.13. Synthesis of ion-pair receptor **4.14·Ni**.

Pleasingly, upon performing ^{1}H NMR titration studies with successive additions of $KBAr^F{}_4$ or $NaBAr^F{}_4$ to **4.14·Ni** in 1:1 *v/v* CD_3CN:$CDCl_3$, similar perturbations were observed to those for **4.12·Ni**, indicating selective formation of the bis-B15C5 1:1 host:guest sandwich complex upon K^+ complexation to afford **4.14·Ni**·K^+. *Bindfit* analysis of the ^{1}H anion binding titration of TBAI with **4.14·Ni**·K^+ in 1:1 *v/v* CD_3CN:$CDCl_3$ demonstrated a ten-fold increase in binding constant (K_a = 270 M^{-1}) over **4.12·Ni**·K^+,[44] presumably due to enhanced triazole C—H···I^- HB interactions in the smaller cavity. Unfortunately, titrations with TBACl and TBABr resulted in salt recombination and visible precipitation of the KX (X = Cl, Br) salt in the NMR sample tube indicating the relatively weak halide anion binding was unable to overcome the high lattice enthalpy of the KX salt.

4.3.5 Synthesis of a Co(III) Congener for ROCOP Catalysis

In order to produce a potential catalyst for ROCOP, the Co(III) congener of **4.12·Ni**, with a cyclohexyl backbone to stabilise the Co(III) centre, was targeted. The pro-ligand **4.11** underwent Schiff base condensation with *trans*-1,2-diaminocyclohexane in anhydrous methanol under Schlenk conditions in the presence of $Co(OAc)_2$. After 30 minutes, the methanolic solution was removed by cannula filtration, and the resulting solid was dissolved in DCM and AcOH added. The reaction mixture was stirred under an O_2 atmosphere for 24 h and the volatiles removed *in vacuo* to afford **4.15·Co^{III}·OAc** as a dark green semi-crystalline solid in near quantitative yield (Scheme 4.14).

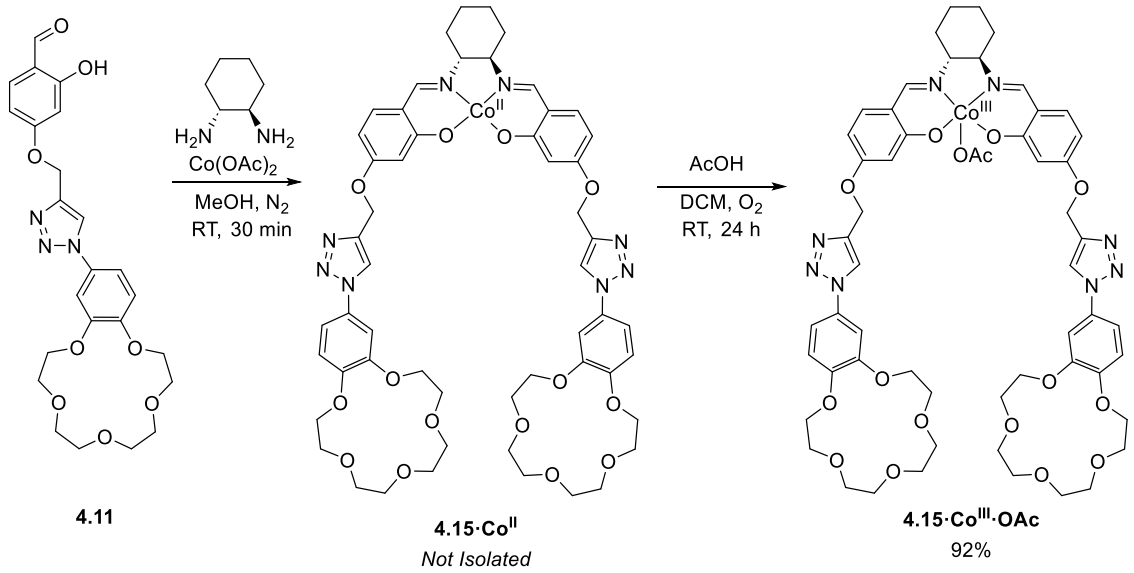

Scheme 4.14. Synthesis of Co(III) target catalyst **4.15·Co^{III}·OAc**.

Initial polymerisation attempts sought to mirror the conditions previously reported for ring opening co-polymerisation (ROCOP) of CO_2 and CHO with bimetallic catalysts.[21] [**4.15·Co^{III}·OAc**·K]$^+$[BAr$^F{}_4$]$^-$ was prepared by mixing one equivalent of KBAr$^F{}_4$ and **4.15·Co^{III}·OAc** in a 1:1 *v/v* $CDCl_3$:CD_3CN solution, and the solvent removed *in vacuo* to obtain the catalyst as a solid. The resulting bimetallic salt was dissolved in CHO [Catalyst]:[Epoxide] = 1:50, and the polymerisation mixture heated to 80 °C under 40 bar CO_2 pressure. Unfortunately, after 72 hours, no monomer conversion was observed.

Varying the pressure, temperature and the identity of the epoxide monomer to PO or LO did not afford any polymer formation. Subsequent work by Williams and co-workers has shown the distance between the co-bound alkali metal cation and the transition metal centre is critical to achieving catalytic activity in polymerisation. Catalysts with Co(III)—M(I) distances lower than those in **4.15·Co^{III}·OAc**·K^+ have been since shown to have too great a Co(III)-M(I) separation for polymerisation activity.[45]

4.4 Halogen Bonding Acyclic Salen Complexes for Co-catalyst Binding

4.4.1 Synthesis of XB Acyclic Salen Receptors

Inspired by reports of the incorporation of tethered co-catalyst binding groups to salen catalysts, the synthesis of a Ni(II) salen complex with bis-XB pendants was targeted. The stringently linear XB binding groups were expected to bind common anionic co-catalyst species, such as chloride, close to the catalytic metal centre, improving performance over the previous reports of non-directional electrostatic co-catalyst binding discussed in Section 4.1.4.

The Sonogashira coupling of 3,5-dibromopyridine with trimethylsilylacetylene and subsequent iodination produced 3,5-di(iodoethynyl)pyridine,[46] which readily underwent a CuAAC click reaction with one equivalent of benzyl azide to form the mono-iodotriazole product **4.16** in 87% yield (Scheme 4.15). Subsequent CuAAC reaction with 5-(2-azidoethyl)salicylaldehyde (Section 4.2.1) produced the desired aldehyde pro-ligand **4.17** in 70% yield. Condensation with ethylenediamine in the presence of nickel(II) acetate tetrahydrate formed XB metallo-receptor **4.18·Ni**, with 87% yield (Scheme 4.15).

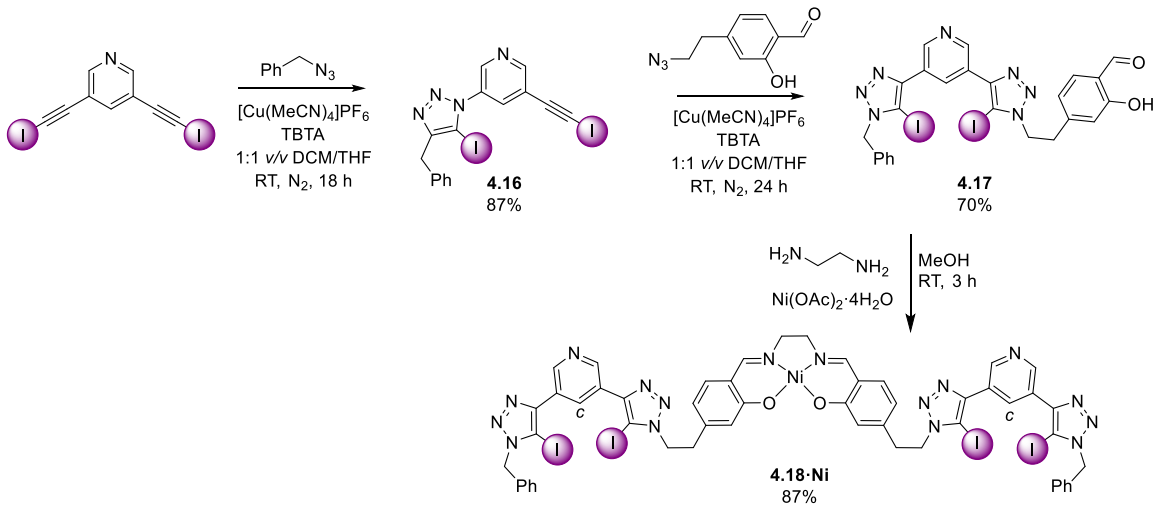

Scheme 4.15. Synthesis of the anion receptor **4.18·Ni**. *c* Denotes internal pyridyl proton monitored in subsequent anion binding studies.

4.4.2 Preliminary Anion Binding Studies

To assess the potential for the binding of a co-catalyst anion, ^{1}H NMR halide anion titration binding studies were undertaken with a range of TBAX salts (X = Cl, Br, I). The poor solubility of **4.18·Ni** in mixed $CDCl_3/CD_3CN$ solvent media necessitated the use of a competitive 20% *v/v* DMSO-d_6 in $CDCl_3$ solvent system. Successive additions of the halide salt led to perturbations in the internal pyridyl proton resonance, *c*, consistent with binding in the XB bis-triazole cleft. Monitoring the NMR resonance of the internal pyridyl proton upon successive additions of the TBA halide salt, followed by *Bindfit* analysis,[44] allowed for calculation of 1:2 stoichiometric host:anion association constants where a halide anion binds at each of the receptor's 3,5-bis-iodotriazole pyridyl recognition sites (Table 4.2) demonstrating selectivity for iodide binding (K_{11} = 1650 M^{-1}), with lower binding constant values observed for Cl^- and Br^- (K_{11} < 1000 M^{-1}).

To enhance the anion binding affinity of the complex, electron deficient *per*-fluorophenyl substituents were appended to the pyridyl motifs of the salen structure to further polarise the iodotriazoles and increase the magnitude of the σ-hole on the iodine XB donor atoms (Scheme 4.16).[47] Repeating the synthesis of **4.18·Ni** substituting benzyl azide for *per*-

fluorophenyl phenyl azide in the first step, obtained the *per*-fluorinated complex **4.21·Ni** in good overall yield.

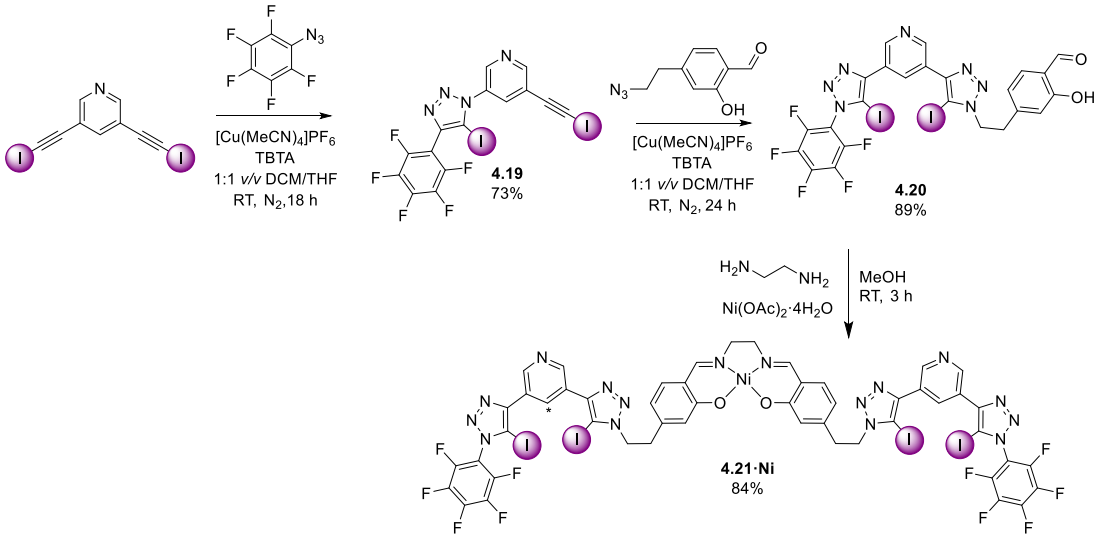

Scheme 4.16. Synthesis of fluorinated receptor **4.21·Ni** for enhanced anion binding.

Pleasingly, a significant enhancement in halide binding constant was observed with the more electron deficient iodotriazole motifs of **4.21·Ni** (Table 4.2), consistent with the increased polarisation of the iodotriazoles enhancing the XB I···anion interactions. Unfortunately, the poor solubility of **4.21·Ni** precluded any appreciable catalyst loading of **4.21·Ni** for ROCOP investigation.

	4.18·Ni		**4.21·Ni**	
	K_{11} / M^{-1}	K_{12} / M^{-1}	K_{11} / M^{-1}	K_{12} / M^{-1}
Cl^-	610	155	1060	270
Br^-	780	195	2780	690
I^-	1650	410	3120	780

Table 4.2. Binding constants of **4.18·Ni** and **4.21·Ni** with halide anions in 20% DMSO-d_6 *v/v* in $CDCl_3$. Binding constants calculated with *Bindfit*.[44] Errors less than 10%. Anions added as their TBA salts. Binding model assumes $K_{11} = 4\ K_{12}$. T = 298 K.

4.5 Conclusions and Future Work

This chapter has demonstrated the potential of a range of [2]rotaxane MIM and non-interlocked Ni(II) and Co(III) salen complexes to exhibit cation and anion binding behaviours reminiscent of previously reported ROP and ROCOP catalysts.

A novel salen bis-azide synthon was employed in the synthesis of a series of Ni(II) salen axle-containing [2]rotaxanes, **4.6·Ni – 4.8·Ni**, as potential MIM catalysts for the ROCOP of CO_2 and a range of epoxides. However, their poor solubility prevented their use as ROCOP catalysts, even at high CO_2 pressure. A Co(III) congener was targeted, due to the high ROCOP activity previously reported for Co(III) complexes, however CuAAC AMT rotaxination reactions on Co(III) salcy bis-azide **4.9·Co^{III}·OAc** were unsuccessful.

Inspired by the previously reported high ROCOP activity of heterobimetallic salen complexes containing a transition metal salen and an alkali metal cation bound in a proximal crown ether-like binding pocket,[21] Ni(II) salen complexes **4.12·Ni** and **4.14·Ni**, with appended B15C5 motifs were synthesised. These complexes selectively form a proximal bimetallic complex upon addition of K^+, which is bound as a 1:1 host:guest bis-B15C5 sandwich complex adjacent to the Ni(II) centre, while the addition of Na^+ leads to 1:2 host:guest binding, with the smaller alkali metal cation bound in each of the B15C5 sites. This system demonstrates the potential of supramolecular catalyst systems to effect on/off switchable bimetallic catalysis upon a binding event, with the proximal bimetallic arrangement required for catalysis only accessed upon K^+ binding. These complexes, when in a co-bound K^+ sandwich conformation, were shown to bind iodide within the salen-crown ether binding pocket, strongly suggesting this conformation may be capable of stabilising an anionic polymeryl chain end during ROCOP. The Co(III) complex **4.15.Co^{III}·OAc** was synthesised, however displayed no ROCOP activity. Subsequent

reports by Williams and co-workers indicate this is due to the intermetallic separation in the sandwich complex being too great for effective catalysis.[45]

Two XB appended Ni(II) salen complexes, **4.18·Ni** and **4.21·Ni**, were also synthesised and shown to bind halide anions, demonstrating neutral, pH-independent, salen complexes capable of binding a co-catalyst halide anion in close proximity to the transition metal catalytic centre. Future work will seek to demonstrate the utility of similar systems in ROP and ROCOP reactions. The production of Co(III) congeners of complexes **4.18·Ni** and **4.21·Ni** will be targeted as Co(III) salen complexes are known to be highly active and selective in epoxide/CO_2 ROCOP. The principal challenges will be preventing aggregation and ensuring the complete oxidation of the Co(II) precursors to Co(III). To achieve this, the ethylene salen backbone will be replaced with cyclohexyl, while introduction of *tert*-butyl groups to the salen phenyl rings should sterically impede aggregation (Figure 4.16).

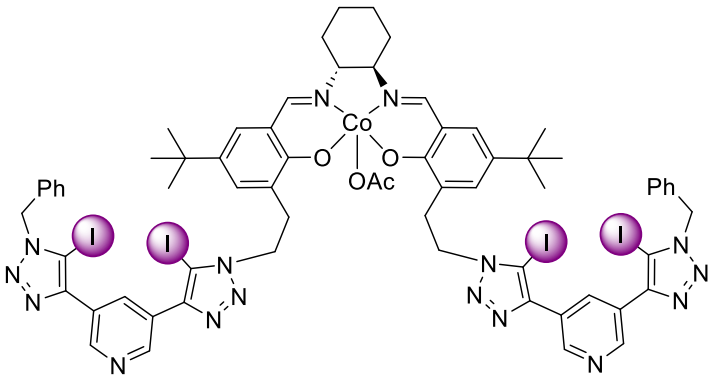

Figure 4.16. Co(III) salen complex with halogen bonding co-catalyst binding sites.

To bring together both the displayed anion and cation recognition behaviours, an ion-pair binding macrocycle will be targeted. Such a macrocycle will contain the metal salen, linked to a polyether cation binding pocket by iodotriazole moieties for anion binding and recognition (Figure 4.17 a). The compounds will be studied for potential ion-pair

binding and catalysis applications. Exploiting the [2]catenane synthetic methodology pioneered by Chiu and co-workers,[48, 49] and recently expanded to include MIM-forming CuAAC reactions by Beer and co-workers,[50, 51] alkali-metal cation templated [2]catenane synthesis will also be attempted to produce unprecedented salen-containing catenanes for potential polymerisation catalysis. (Figure 4.17 b).[52]

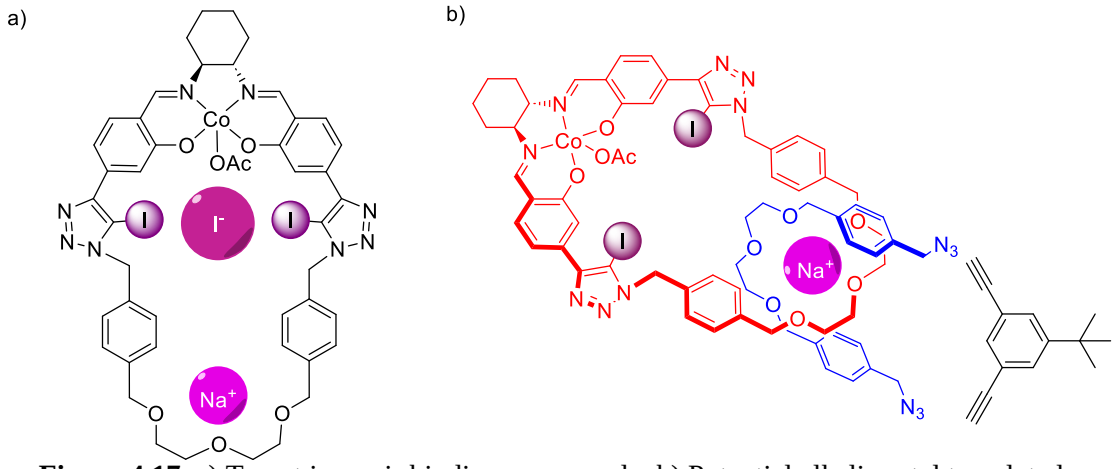

Figure 4.17. a) Target ion-pair binding macrocycle. b) Potential alkali-metal templated catenation reaction.

4.6 References

1. S. Shaw and J. D. White, *Chem. Rev.*, 2019, **119**, 9381-9426.
2. W. Zhang, J. L. Loebach, S. R. Wilson and E. N. Jacobsen, *J. Am. Chem. Soc.*, 1990, **112**, 2801-2803.
3. P. G. Cozzi, *Chem. Soc. Rev.*, 2004, **33**, 410-421.
4. T. Tokuichi, *Bull. Chem. Soc. Jpn.*, 1938, **13**, 252-260.
5. T. G. Appleton, *J. Chem. Educ.*, 1977, **54**, 443.
6. C. Huilan, H. Deyan, L. Tian, Y. Hong, T. Wenxia, Jian, Peiju and Chenggang, *Inorg. Chem.*, 1996, **35**, 1502-1508.
7. M. Calligaris, G. Nardin, L. Randaccio and A. Ripamonti, *J. Chem. Soc. A.*, 1970, 1069-1074.
8. S. E. M. Selke and J. D. Culter, *Plastics Packaging*, Hanser, 3rd edn., 2016.
9. R. E. Drumright, P. R. Gruber and D. E. Henton, *Adv. Mater.*, 2000, **12**, 1841-1846.
10. *Plastics – the fast Facts 2023*, Plastics Europe, https://plasticseurope.org/wp-content/uploads/2023/10/Plasticsthefastfacts2023-1.pdf, 2023.
11. R. Geyer, J. R. Jambeck and K. L. Law, *Science Advances*, 2017, **3**, e1700782.
12. Z. Zhong, P. J. Dijkstra and J. Feijen, *Angew. Chem. Int. Ed.*, 2002, **41**, 4510-4513.
13. Y. Zhu, C. Romain and C. K. Williams, *Nature*, 2016, **540**, 354-362.
14. V. W. Dittrich and R. C. Schulz, *Angew. Makromol. Chem.*, 1971, **15**, 109-126.
15. G. Perego, G. D. Cella and C. Bastioli, *J. Appl. Polym. Sci.*, 1996, **59**, 37-43.

16. Z. R. Turner, J. T. Wilmore, N. H. Rees and J.-C. Buffet, *Dalton Trans.*, 2022, **51**, 3060-3074.
17. N. Spassky, M. Wisniewski, C. Pluta and A. Le Borgne, *Macromol. Chem. Phys.*, 1996, **197**, 2627-2637.
18. D. J. Darensbourg, *Inorg. Chem.*, 2010, **49**, 10765-10780.
19. Z. Qin, C. M. Thomas, S. Lee and G. W. Coates, *Angew. Chem. Int. Ed.*, 2003, **42**, 5484-5487.
20. D. J. Darensbourg, R. M. Mackiewicz, J. L. Rodgers and A. L. Phelps, *Inorg. Chem.*, 2004, **43**, 1831-1833.
21. A. C. Deacy, E. Moreby, A. Phanopoulos and C. K. Williams, *J. Am. Chem. Soc.*, 2020, **142**, 19150-19160.
22. W. T. Diment, T. Stößer, R. W. F. Kerr, A. Phanopoulos, C. B. Durr and C. K. Williams, *Catal. Sci. Technol.*, 2021, **11**, 1737-1745.
23. G. Trott, P. K. Saini and C. K. Williams, *Philos. Trans. R. Soc. A*, 2016, **374**, 20150085.
24. J. Liu, W.-M. Ren, Y. Liu and X.-B. Lu, *Macromol.*, 2013, **46**, 1343-1349.
25. K. Nakano, T. Kamada and K. Nozaki, *Angew. Chem. Int. Ed.*, 2006, **45**, 7274-7277.
26. J. Y. C. Lim, N. Yuntawattana, P. D. Beer and C. K. Williams, *Angew. Chem. Int. Ed.*, 2019, **58**, 6007-6011.
27. A. Makarem, K. D. Klika, G. Litau, Y. Remde and K. Kopka, *J. Org. Chem.*, 2019, **84**, 7501-7508.
28. M. Tsunoda, M. Fleischmann, J. S. Jones, N. Bhuvanesh, M. Scheer and F. P. Gabbaï, *Dalton Trans.*, 2016, **45**, 5045-5051.
29. G.-L. Liu and B.-T. Ko, *Polymer*, 2022, **260**, 125371.
30. G. Xiao, B. Yan, R. Ma, W. J. Jin, X. Q. Lü, L. Q. Ding, C. Zeng, L. L. Chen and F. Bao, *Polym. Chem.*, 2011, **2**, 659-664.
31. N. V. Reis, A. C. Deacy, G. Rosetto, C. B. Durr and C. K. Williams, *Chem. Eur. J.*, 2022, **28**, e202104198.
32. A. Routaray, S. Mantri, N. Nath, A. K. Sutar and T. Maharana, *Polyhedron*, 2016, **119**, 335-341.
33. A. V. Leontiev, C. A. Jemmett and P. D. Beer, *Chem. Eur. J.*, 2011, **17**, 816-825.
34. Y. Vida, E. Perez-Inestrosa and R. Suau, *Tetrahedron Lett.*, 2005, **46**, 1575-1577.
35. A. Noor, W. K. C. Lo, S. C. Moratti and J. D. Crowley, *Chem. Commun.*, 2014, **50**, 7044-7047.
36. F. Della Monica and C. Capacchione, *Asian J. Org. Chem.*, 2022, **11**, e202200300.
37. W.-M. Ren, X. Zhang, Y. Liu, J.-F. Li, H. Wang and X.-B. Lu, *Macromol.*, 2010, **43**, 1396-1402.
38. C. T. Cohen, T. Chu and G. W. Coates, *J. Am. Chem. Soc.*, 2005, **127**, 10869-10878.
39. Y. Zhao, M. Yu, S. Zhang, Z. Wu, Y. Liu, C.-H. Peng and X. Fu, *Chem. Sci.*, 2015, **6**, 2979-2988.
40. W. Xu, K. Clinger, M. L. Hackert and N. S. Poonia, *J. Incl. Phenom. Macrocycl. Chem.*, 1985, **3**, 163-172.
41. A. J. Taylor, A. Docker and P. D. Beer, *Chem. Asian J.*, 2023, **18**, e202201170.
42. C. J. Pedersen and H. K. Frensdorff, *Angew. Chem. Int. Ed. Engl.*, 1972, **11**, 16-25.
43. C. J. Pedersen, *J. Am. Chem. Soc.*, 1967, **89**, 7017-7036.
44. D. Brynn Hibbert and P. Thordarson, *Chem. Commun.*, 2016, **52**, 12792-12805.

45. F. Fiorentni, A. C. Deacy and C. K. Williams, unpublished work.
46. S. W. Robinson and P. D. Beer, *Org. Biomol. Chem.*, 2017, **15**, 153-159.
47. A. Docker, C. H. Guthrie, H. Kuhn and P. D. Beer, *Angew. Chem. Int. Ed.*, 2021, **60**, 21973-21978.
48. S.-T. Tung, C.-C. Lai, Y.-H. Liu, S.-M. Peng and S.-H. Chiu, *Angew. Chem. Int. Ed.*, 2013, **52**, 13269-13272.
49. K.-D. Wu, Y.-H. Lin, C.-C. Lai and S.-H. Chiu, *Org. Lett.*, 2014, **16**, 1068-1071.
50. H. M. Tay, Y. C. Tse, A. Docker, C. Gateley, A. L. Thompson, H. Kuhn, Z. Zhang and P. D. Beer, *Angew. Chem. Int. Ed.*, 2023, **62**, e2022147.
51. H. M. Tay, A. Docker, Y. Cheong Tse and P. D. Beer, *Chem. Eur. J.*, 2023, **29**, e202301316.
52. A. Inthasot, S.-T. Tung and S.-H. Chiu, *Acc. Chem. Res.*, 2018, **51**, 1324-1337.

Chapter Five

Conclusions

5 Conclusions

The work described in this thesis sought to demonstrate the exploitation of non-covalent inter-component interactions in rotaxane and pseudorotaxane assemblies as a potent supramolecular tool for enhanced MIM synthesis, host-guest recognition and sensing, and for potential catalytic applications.

Chapter Two presented the high yielding synthesis of two regioisomeric pairs of Zn(II) metalloporphyrin-containing [2]- and [3]-rotaxanes, *p*-**2.5a·Zn** and *p*-**2.5b·Zn**, and *m*-**2.6a·Zn** and *m*-**2.6b·Zn**. The interlocked systems contained a macrocycle bearing a pyridyl-moiety capable of a strong rotaxane inter-component pyridyl macrocycle···Zn(II) metalloporphyrin axle interaction. Variable-temperature ^{1}H NMR investigations demonstrated this inter-component interaction retards the inherent dynamic shuttling motion of the [2]rotaxane, leading to marked co-conformational bias towards the macrocycle residing at the metalloporphyrin axle station site. The resultant co-conformational bias was removed by demetalation of the rotaxane, and by synthesis of rotaxane congener *p*-**2.5a·Ni** containing a coordinatively saturated Ni(II) metalloporphyrin. This interaction is also postulated to be responsible for the remarkable combined near quantitative yields of [2]- and higher order [3]-rotaxane in the AMT synthesis of *p*-**2.5a·Zn** and *p*-**2.5b·Zn**.

Displacement of the macrocycle from the axial coordination site of the Zn(II) metalloporphyrin by a competing pyridine Lewis base or halide anionic guest resulted in marked optical perturbations in the UV-visible optical spectra of the [2]rotaxanes, acting as a novel signal transduction mechanism for the binding of Lewis basic guests, in which halide anion binding strength was modulated by the inter-component interaction. In order to investigate the exploitation of these systems for ion-pair sensing of environmentally

relevant lithium halide salts, a congener of *p*-**2.5a·Zn** with a heteroditopic macrocycle component, *p*-**2.11·Zn**, was synthesised. This [2]rotaxane system underwent shuttling of the macrocycle upon Li^+ addition, to enable convergent binding of the alkali metal cation guest between the axle triazole and macrocycle pyridyl motifs. The inclusion of an isophthalamide anion binding motif in the macrocycle of *p*-**2.11·Zn** enabled binding of Li^+/X^- (X = Cl, Br, I) axle-separated ion-pairs. While iodide is not sufficiently Lewis basic to bind to the Zn(II) metalloporphyrin centre, and addition of excess Cl^- resulted in thermodynamically favourable salt recombination and precipitation of LiCl, for Li^+/Br^-, in addition to binding the axle-separated LiBr ion-pair, a second bromide anion could bind at the Zn(II) metalloporphyrin recognition site, highlighting the ability of judiciously designed MIMs to effect selective recognition of ion-pairs.

Chapter Three exploits the host-guest chemistry of the pillar[5]arene (P5A) motif for MIM synthesis and sensing. Inspired by the high AMT rotaxination yields of *p*-**2.5a·Zn** and *p*-**2.5b·Zn**, pseudo[2]rotaxane assemblies formed by threading of a P5A by an electron deficient bis-alkyne, **3.1**, were targeted as axle precursors in an AMT CuAAC MIM-forming reaction as a potential route towards higher order [3]- or [4]-rotaxanes. Unfortunately, the steric demands of AMT rotaxination precluded the formation of higher order P5A-containing rotaxanes. The facile formation of host-guest P5A macrocycle-containing pseudo[2]rotaxanes in the absence of any exogeneous template was subsequently targeted for the challenging synthesis of inorganic motif-stoppered rotaxanes by a copper(I)-free phosphaalkyne-azide click reaction of a gold(I) cyaphide stopper, **3.9**, with a P5A macrocycle-bis-azide axle precursor pseudo[2]rotaxane. Using bis-triazole axle precursor **3.13** enabled an unprecedented ‘inorganic click’ rotaxination reaction which, using only stoichiometric quantities of the MIM components, resulted in the formation of [2]rotaxane **3.14** in impressive 65% yield. Importantly, the [2]rotaxane

demonstrated remarkable air- and moisture-stability compared to the non-interlocked axle **3.15** and, unlike **3.15**, was stable to purification by column chromatography, demonstrating the mechanical bond to act as a facile route to stabilisation of air- and moisture-sensitive organometallic species.

The unprecedented combination of BODIPY fluorophore-appended XB and HB binding groups with P5A hosts was achieved through the synthesis of **3.19·XB** and **3.19·HB**. The host-guest threading of anionic dicarboxylates through the hydrophobic cavity of these P5As formed pseudo[2]rotaxane assembles with high binding constants, affording optical fluorescent responses to binding in both organic (**3.19·XB**) and impressively, 50% *v/v* aqueous-MeCN mixed solvent media (**3.19·XB** and **3.19·HB**). The systems also displayed the selective recognition and sensing of a neutral simulant of the chemical warfare agent sulfur mustard, CEES, over the hydrolysis product of sulfur mustard, and a simulant of a V-series nerve agent. The high binding constants obtained for recognition of the neutral small molecule CEES ($K_a > 10^5$ M^{-1}), and the low limit of detection (< 1 μM) demonstrates the unique potency of combining supramolecular XB binding and P5A hydrophobic threading interactions in sensor host design.

Chapter Four targets transition metal salen complex axle containing [2]rotaxanes as sustainable polymerisation catalysts for biorenewable polycarbonate production. A novel Ni(II) salen bis-azide, **4.1·Ni** was incorporated into a series of [2]rotaxanes with macrocycles containing polyether-linked pyridyl macrocycles, **4.6·Ni** – **4.8·Ni**. The use of these rotaxanes as catalysts for ring-opening co-polymerisation (ROCOP) of a range of epoxides and CO_2 was targeted, however the poor solubility of **4.6·Ni** – **4.8·Ni** precluded appreciable catalyst loading. Inspired by previous reports of transition metal-alkali metal bimetallic catalysts for ROCOP, a bis-B15C5-appended Ni(II) salen **4.12·Ni**

derivative was synthesised, and selectively formed a proximal bimetallic conformation on addition of K^+ due to formation of a bis-B15C5 sandwich complex. As stabilisation of a growing anionic polymeryl chain enhances control over polymerisation by reducing side reactions, the ability of the Ni(II) salen-bis-B15C5 K^+ sandwich complex to bind halide anions was investigated. The synthesis of regioisomer **4.14·Ni**, which reduced the size of the cavity between the K^+ and Ni(II) salen centre, demonstrated a 10-fold increase in binding constant for I^- binding in 1:1 *v/v* $CDCl_3$:CD_3CN. Encouraged by both the anion binding capability and the selective formation of a potentially catalytically active bimetallic configuration upon K^+ binding, a Co(III) congener was synthesised for catalysis testing. While no catalytic activity was observed for epoxide/CO_2 ROCOP, likely due to too great an inter-metallic separation between the salen transition metal and the bound K^+, this system provides a demonstration of the powerful potential future applications of supramolecular ion-pair host-guest interactions for 'on/off' switchable polymerisation catalysis. Finally, two Ni(II) salen complexes with appended XB groups for co-catalyst binding, **4.18·Ni** and **4.21·Ni**, were synthesised and demonstrated the ability of XB functionalisation to provide neutral and pH-independent sites for co-catalyst binding in proximity to the transition metal centre. Future work will seek to demonstrate the utility of Co(III) congeners of these systems for ROCOP reactions.

Overall, the work in this thesis demonstrates the exploitation of non-covalent inter-component interactions in MIM and pseudo-MIM supramolecular systems for enhanced synthesis of rotaxanes with up to 100% MIM yield, and for the mechanical bond to impart air- and moisture- stability on organometallic-containing systems. Modulating the macrocycle-axle inter-component attractive forces in [2]rotaxanes can result in anion and ion-pair optical sensing capabilities, while in aqueous media the interpenetration of

charged or neutral guests into a hydrophobic host acts a powerful method for selective sensing of environmental pollutants with low limits of detection. The judicious incorporation of a range of supramolecular interactions into transition metal complexes demonstrates potential for better-controlled polymerisation catalysis both through switchable ‘on/off’ catalysis through binding-induced conformational changes, and the binding of co-catalysts.

Chapter Six

Experimental

6 Experimental

6.1 General Experimental Procedures

6.1.1 Reagents and Instrumentation

Solvents and reagents were purchased from commercial suppliers and used as received. Dry solvents were obtained by purging with nitrogen and passing through a MBraun MPSP-800 column. Where indicated, solvents were further degassed by purging with N_2 for 15 minutes immediately prior to use. H_2O was deionised and micro-filtered using a Milli-Q® Millipore machine.

Triethylamine was distilled from, and stored over, potassium hydroxide. Tris[(1-benzyl-1H-1,2,3-triazol-4-yl)methyl]amine is abbreviated as TBTA.

50 mM HEPES buffer was prepared by dissolving HEPES (*N*-(2-hydroxyethyl)piperazine-*N'*-(2-ethanesulfonic acid)) in deionised water and then adjusting the pH to 8.0 by addition of small volumes of a 3 M NaOH solution.

Experiments were conducted at room temperature unless otherwise stated. Merck silica gel 60 was used for flash column chromatography. Neutral Brockman grade I activated alumina was purchased from Merck and used for purification as received. TBA salts were stored in vacuum desiccators prior to use. NMR spectra were either recorded on a Bruker Avance III HD Nanobay NMR spectrometer equipped with a 9.4 T magnet or a Bruker NEO 600 with broadband helium cryoprobe. Chemical shifts are quoted in parts per million relative to the residual solvent peak.

UV-visible and fluorescence measurements were carried out on a Horiba Duetta using quartz cuvettes with a path length of 10 mm. Unless otherwise noted, all fluorescence spectra were acquired with a wavelength of excitation of 490 nm, 5 nm excitation and

emission slits and were recorded in, at least, triplicate repeat measurements to ensure signal stability.

Single-crystal X-ray diffraction data were collected and solved by Prof. Jose Goicoechea. The data were collected using an Oxford Diffraction Supernova dual-source diffractometer equipped with a 135 mm Atlas CCD area detector. Crystals were selected under Paratone®-N oil, mounted on micromount loops and quench-cooled using an Oxford Cryosystems open flow N_2 cooling device. Data were collected at 150 K using mirror monochromated Cu K_α (λ = 1.54184 Å) radiation and processed using the *CrysAlisPro* package,[1] including unit cell parameter refinement and inter-frame scaling (carried out using SCALE3 ABSPACK). Structures were subsequently solved using direct methods.[2, 3]

6.1.2 General Method for ^{1}H NMR Binding Titrations

^{1}H NMR titrations were recorded on a Bruker Avance III NMR spectrometer equipped with a 11.75 T magnet at 298 K. Unless stated otherwise, titrations were carried out by successive addition of a 50 mM stock solution of the target guest to a 1 mM solution of host, such that 1.0 equivalent of guest corresponds to a 10.0 μL stock solution addition. The sample was thoroughly mixed by inversion of the NMR tube prior to each spectrum being collected. 17 data points were collected, upon addition of 0.0, 0.2, 0.4, 0.6, 0.8, 1.0, 1.2, 1.4, 1.6, 1.8, 2.0, 2.5, 3.0, 4.0, 5.0, 7.5 and 10.0 equivalents of guest. All systems for which binding constants are quoted displayed fast NMR exchange at 298 K. The changes in chemical shift upon binding were fitted using *Bindfit* to a 1:1 stoichiometric binding model unless specified otherwise.[4] For 1:2 host-guest binding stoichiometries, the binding model used was selected by comparison of the covariance of fit for each binding model, according to the methods laid out by Hibbert and Thordarson.[5]

6.1.3 General Method for Optical Binding Titrations

UV-visible and fluorescence titration studies were performed using a Horiba Duetta at 298 K using quartz cuvettes with a path length of 10 mm. The guest was dissolved in a stock solution of the host to ensure constant host concentration. In a typical experiment, successive aliquots of a guest solution of appropriate concentration were added to 1.0 mL of the host solution. The cuvette was inverted to thoroughly mix the sample prior to each data collection. Changes in the optical spectra were fitted by a global fitting using either *Bindfit* or *OriginPro*,[4, 6] with a 1:1 host:guest binding model used unless specified otherwise.

6.2 Synthesis and Characterisation of Novel Compounds in Chapter 2

Free base *meta*-Functionalised Porphyrin, ***m*-2.2·H$_2$**

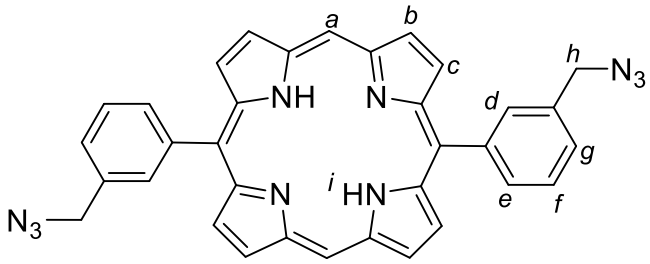

***m*-2.2·H$_2$**

3-(Azidomethyl)benzaldehyde (1.00 g, 6.21 mmol)[7] and dipyrrolemethane (0.91 g, 6.21 mmol)[8] were dissolved in dry DCM (1200 mL) and the solution degassed under exclusion of light for 30 min. Trifluoroacetic acid (0.36 mL, 4.72 mmol) was added dropwise and the reaction mixture stirred at room temperature under N_2 for 24 h. 2,3-Dichloro-5,6-dicyano-*p*-benzoquinone (2.11 g, 9.31 mmol) was added as a solid, and the mixture stirred for 2 h, before dropwise addition of triethylamine (0.87 mL, 6.21 mmol). The reaction mixture was concentrated *in vacuo* and loaded onto a silica pad. The crude product was eluted with DCM (500 mL) until the solution ran clear. The purple solution was concentrated to 50 mL *in vacuo* and the product precipitated with MeOH as a purple crystalline solid. Yield: 0.89 g (50%).

^{1}H NMR (500 MHz, $CDCl_3$, 298 K) δ: 10.35 (s, 2H, H_a), 9.42 (d, J = 4.6 Hz, 4H, H_b), 9.07 (d, J = 4.6 Hz, 4H, H_c), 8.33 – 8.20 (m, 4H, $H_{d,e}$), 7.89 – 7.77 (m, 4H, $H_{f,g}$), 4.70 (s, 4H, H_h), -3.13 (s, 2H, H_i) ppm.

^{13}C{^{1}H} NMR (126 MHz, $CDCl_3$, 298 K) δ: 147.1, 145.3, 142.0, 134.8, 134.6, 134.2, 131.9, 130.9, 127.7, 127.6, 118.4, 105.5, 54.9 ppm.

HR-ESI-MS *m/z* calculated for $[C_{34}H_{25}N_{10}]^+$, $[M+H]^+$: 573.2258, found: 573.2257.

Zn(II) *meta*-Functionalised Metalloporphyrin, ***m*-2.2·Zn**

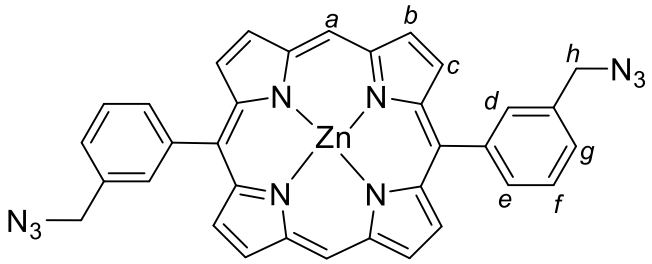

***m*-2.2·Zn**

The free-base porphyrin ***m*-2.2·H$_2$** (0.89 g, 1.55 mmol) was suspended in a 1:1 *v/v* mixture of DCM and MeOH (100 mL). $Zn(OAc)_2 \cdot 2H_2O$ (1.71 g, 7.95 mmol) was injected as a saturated methanolic solution. The resulting suspension was stirred under N_2 for 24 h, and the solvent removed *in vacuo* to afford a pink solid, which was taken up in DCM (200 mL) and washed with water (3 x 100 mL). The organic layer was dried over $MgSO_4$ and the volatiles removed *in vacuo* to afford ***m*-2.2·Zn** as a pink solid which was used for subsequent synthesis without further purification. Yield: 988 mg (Quantitative).

^{1}H NMR (500 MHz, $CDCl_3$) δ: 10.28 (s, 2H, H_a), 9.39 (d, J = 4.5 Hz, 4H, H_b), 9.04 (d, J = 4.5 Hz, 4H, H_c), 8.18 (d, J = 7.4 Hz, 2H, H_e), 8.11 (s, 2H, H_d), 7.74 (t, J = 7.4 Hz, 2H, H_f), 7.68 (d, J = 7.4 Hz, 2H, H_g), 4.52 (s, 4H, H_h) ppm.

^{13}C NMR (126 MHz, $CDCl_3$) δ: 150.0, 149.6, 144.1, 134.9, 134.7, 133.5, 132.1, 131.8, 127.2, 127.0, 118.8, 106.0, 55.1 ppm.

HR-ESI-MS *m/z* calculated for $[C_{34}H_{23}N_{10}Zn]^+$, $[M+H]^+$: 635.1393, found: 635.1385.

Macrocycle **2.3**

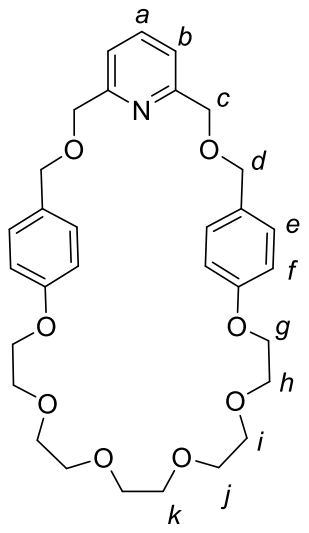

2.3

NaH (0.80 g, 19.92 mmol, 60% *w/w* dispersion) was suspended in anhydrous THF (100 mL) and stirred at 70 °C for 30 minutes. Separate solutions of 2,6-bis(bromomethyl)pyridine (1.19 g, 4.98 mmol) and the diol 1,14-bis-(4-(hydroxymethyl)phenoxy)-3,6,9,12-tetraoxadecane (2.03 g, 4.98 mmol),[9] each in THF (50 mL), were added dropwise to the refluxing solution over the course of 3 hours. Once the addition was complete, the mixture was left to stir overnight at 70 °C. After which, the mixture was left to cool to room temperature and was carefully quenched by the addition of MeOH (50 mL). The resultant mixture was concentrated to dryness *in vacuo* and the crude reaction mixture partitioned between DCM (250 mL) and H_2O (250 mL). The organic phase was collected and washed with H_2O (250 mL), dried over $MgSO_4$ and the solvent removed *in vacuo*. The crude reaction mixture was purified by column chromatography (3:2:0.3 *v/v* DCM:EtOAc:MeOH) to afford the product **2.3** as a white solid. Yield: 1.05 g (38%).

^{1}H NMR (500 MHz, $CDCl_3$, 298 K) δ: 7.67 (t, J = 7.7 Hz, 1H, H_a), 7.33 (d, J = 7.7 Hz, 2H, H_b), 7.23 (d, J = 8.6 Hz, 4H, H_e), 6.83 (d, J = 8.6 Hz, 4H, H_f), 4.57 (s, 4H, H_c), 4.50 (s, 4H, H_d), 4.09 (dd, J = 5.7, 4.0 Hz, 4H, H_g), 3.83 (dd, J = 5.7, 4.0 Hz, 4H, H_h), 3.73 – 3.63 (m, 12H, $H_{i,k,j}$) ppm.

$^{13}C\{^{1}H\}$ NMR (126 MHz, $CDCl_3$, 298 K) *δ:* 158.5, 157.8, 137.0, 130.0, 129.9, 120.5, 114.5, 72.0, 71.8, 71.0, 70.8, 70.7, 69.6, 67.6 ppm.

HR-ESI-MS *m/z* calculated for $[C_{31}H_{40}NO_8]^+$, $[M+H]^+$: 554.2748, found: 554.2747.

Para-substituted Zn(II) Metalloporphyrin [2]-and [3]-Rotaxanes ***p*-2.5a·Zn**, ***p*-2.5b·Zn**

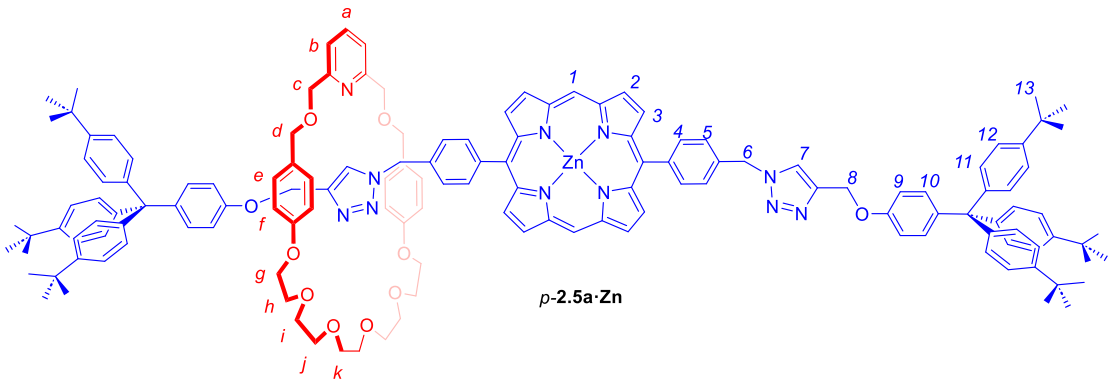

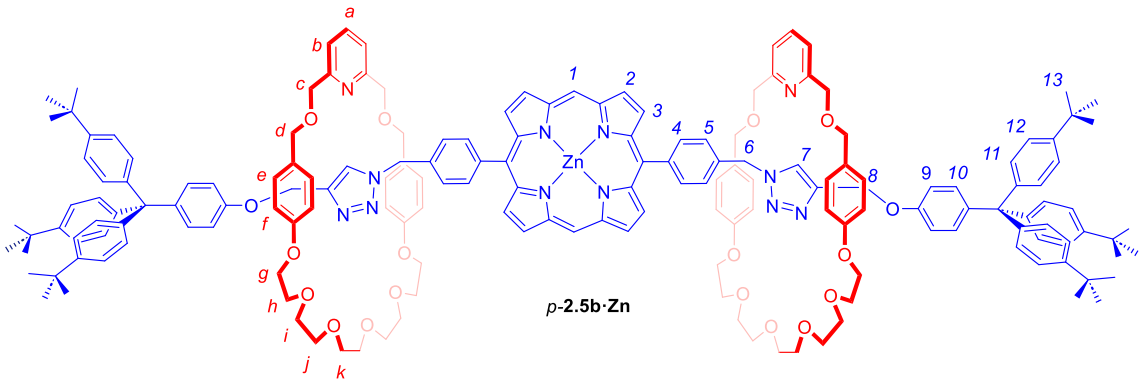

Macrocycle **2.3** (10.0 mg, 0.018 mmol) and $[Cu(MeCN)_4]PF_6$ (6.7 mg, 0.018 mmol) were added to dry, degassed DCE (1.6 mL) in a sealed flask. The mixture was purged with N_2 for 10 min, and stirred at room temperature for 30 min. Stopper alkyne **2.4** (59.0 mg, 0.108 mmol)[10] and the *para*-metalloporphyrin bis-azide ***p*-2.1·Zn** (34.0 mg, 0.054 mmol)[11] were dissolved in degassed DCE (3 mL) and the resulting solution purged with N_2 for 5 min. The porphyrin solution was added dropwise to the copper solution, and the reaction mixture heated to 60 °C for 3 days. The reaction was cooled to room temperature and the solvent removed *in vacuo*. The residue was taken up in DCM (30 mL) and washed with aqueous NH_4OH/EDTA (2 x 20 mL) and water (20 mL). The combined aqueous layers were re-extracted with further DCM (20 mL) and the combined organic layers

dried over $MgSO_4$ and the volatiles removed *in vacuo*. The products were obtained by preparative TLC (4% MeOH *v/v* in DCM, followed by 2:89:9 *v/v* MeOH:DCM:EtOAc) as red solids.

p-**2.5a·Zn** Yield: 31.2 mg (76%).
^{1}H NMR (500 MHz, $CDCl_3$, 298 K) *δ:* 10.31 (s, 2H, H_1), 9.36 (d, J = 4.4 Hz, 4H, H_2), 8.89 (d, J = 4.4 Hz, 4H, H_3), 7.98 (d, J = 7.5 Hz, 4H, H_4), 7.28 (m, 15H, $H_{11,a,b}$), 7.11 (m, 20H, $H_{5,9,12}$), 6.99 (m, 8H, $H_{10,e}$), 6.57 (d, J = 8.2 Hz, 4H, H_f), 6.49 (broad s, 4H, H_6), 5.05 (broad s, 4H, H_8), 4.43 (s, 4H, H_c), 4.25 (s, 4H, H_d), 3.89 (t, J = 5.0 Hz, 4H, H_g), 3.71 (t, J = 5.0 Hz, 4H, H_h), 3.59 (t, J = 5.0 Hz, 4H, H_i), 3.55 (t, J = 5.0 Hz, 4H, H_j), 3.53 (s, 4H, H_k), 1.33 (s, 54H, H_{13}) ppm.

^{13}C{^{1}H} NMR (126 MHz, $CDCl_3$, 298 K) *δ*: 158.3, 157.6, 149.7, 149.6, 148.4, 144.2, 141.6, 139.9, 139.3, 136.9, 134.9, 132.2, 131.7, 130.9, 130.8, 130.7, 129.8, 129.5, 128.8, 124.1, 124.1, 120.0, 115.3, 114.5, 114.4, 114.1, 113.2, 113.0, 106.2, 72.2, 71.3, 70.8, 70.7, 70.7, 69.5, 67.2, 63.1, 34.4, 31.4 ppm.

HR-ESI-MS *m/z* calculated for $[C_{145}H_{154}N_{11}O_{10}Zn]^+$, $[M+H]^+$: 2274.1200 found: 2274.1237.

p-**2.5b·Zn** Yield: 6.1 mg (24%).
^{1}H NMR (500 MHz, $CDCl_3$, 298 K) *δ*: 10.30 (s, 2H, H_1), 9.37 (d, J = 4.5 Hz, 4H, H_2), 8.95 (d, J = 4.5 Hz, 4H, H_3), 7.96 (d, J = 7.6 Hz, 4H, H_4), 7.82 (s, 2H, H_7), 7.29 (t, J = 7.8 Hz, 2H, H_a), 7.24 (d, J = 8.6 Hz, 12H, H_{11}), 7.22 (d, J = 7.6 Hz, 4H, H_5), 7.11 (d, J = 8.6 Hz, 12H, H_{12}), 7.07 (m, 8H, $H_{9,b}$), 7.03 (d, J = 8.3 Hz, 8H, H_e), 6.75 (d, J = 8.1 Hz, 4H, H_{10}), 6.61 (d, J = 8.3 Hz, 8H, H_f), 5.40 (s, 4H, H_6), 4.88 (s, 4H, H_8), 4.46 (s, 8H, H_c), 4.23 (m, 8H, H_d), 3.93 (m, 8H, H_g), 3.73 (m, 8H, H_h), 3.61 (m, 8H, H_i), 3.57 (m, 8H, H_j), 3.54 (app. s, 8H, H_k), 1.31 (s, 54H, H_{13}) ppm.

^{13}C{^{1}H} NMR (126 MHz, $CDCl_3$, 298 K) *δ*: 158.4, 157.6, 156.3, 149.9, 149.5, 148.3, 144.2, 144.1, 139.7, 142.3, 136.9, 134.8, 134.3, 132.8, 132.7, 132.2, 131.8, 130.9, 130.7, 129.8, 129.6, 126.3, 124.3, 124.1, 120.0, 119.4, 114.4, 113.3, 72.2, 71.3, 70.8, 70.8, 70.7, 69.6, 67.2, 63.1, 61.5, 34.3, 31.4 ppm.

HR-ESI-MS Mass calculated for $[C_{176}H_{192}N_{12}O_{18}Zn]^{2+}$, $[M+2H]^{2+}$: 1414.1974, found: 1414.1989.

Para-substituted Zn(II) Metalloporphyrin Axle ***p*-2.5c·Zn**

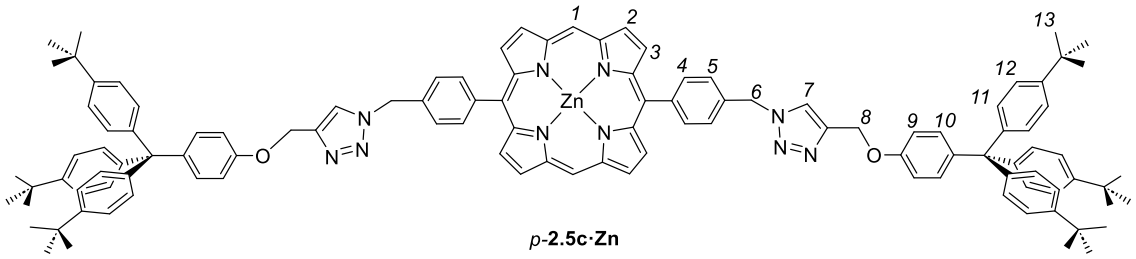

p-**2.5c·Zn**

Bis-azido zinc(II) metalloporphyrin *p*-**2.1·Zn** (200 mg, 0.314 mmol)[11] was dissolved in dry and degassed THF (8 mL) in a sealed flask and degassed for five minutes. TBTA (100 mg, 0.189 mmol) and $[Cu(MeCN)_4]PF_6$ (93.7 mg, 0.252 mmol) were added and the solution was degassed for a further five minutes. A solution of stopper alkyne **2.4** (358 mg, 0.660 mmol)[10] in degassed anhydrous THF (4 mL) was prepared and added into the microwave vial before degassing for five minutes. The solution was stirred under positive pressure of N_2 for two days at room temperature. The reaction mixture was diluted with DCM (40 mL), washed with aqueous NH_4OH/EDTA (30mL x 2), brine (30 mL) and H_2O (30 mL). The combined organic fractions were dried over $MgSO_4$ and the volatiles removed *in vacuo*. The product was purified by column chromatography (3:7 *v/v* hexane:DCM graded to 1:9 *v/v* EtOAc:DCM) to obtain the product as a purple solid. Yield 0.252 g (47%).

^{1}H NMR (400 MHz, $CDCl_3$, 298 K) δ: 10.23 (s, 2H, H_1), 9.38 (d, J = 4.4 Hz, 4H, H_2), 9.02 (d, J = 4.4 Hz, 4H, H_3), 8.23 (d, J = 6.5 Hz, 4H, H_4), 7.75 (s, 2H, H_7), 7.57 (d, J = 6.5 Hz, 4H, H_5), 7.27 (d, J = 7.9 Hz, 12H, H_{11}), 7.20 (d, J = 8.4 Hz, H_{10}), 7.16 (t, J = 7.9 Hz, 12H, H_{12}), 6.93 (d, J = 8.4 Hz, 4H, H_9), 5.80 (s, 4H, H_6), 5.20 (s, 4H, H_8), 1.32 (s, 54H, H_{13}) ppm.

^{13}C{^{1}H} NMR (101 MHz, $CDCl_3$, 298 K) δ: 156.3, 149.9, 149.6, 148.5, 145.0, 144.2, 144.0, 140.4, 135.5, 133.5, 132.5, 132.1, 131.8, 130.9, 126.2, 124.2, 123.0, 118.5, 113.4, 106.1, 63.2, 62.2, 54.3, 34.4, 31.5 ppm.

HR-ESI-MS: *m/z* calculated for **[**$C_{114}H_{114}N_{10}NaO_2Zn]^+$, $[M+Na]^+$: 1741.8315, found: 1741.8329.

Para-substituted Free Base [2]Rotaxane *p*-**2.5a·H$_2$**

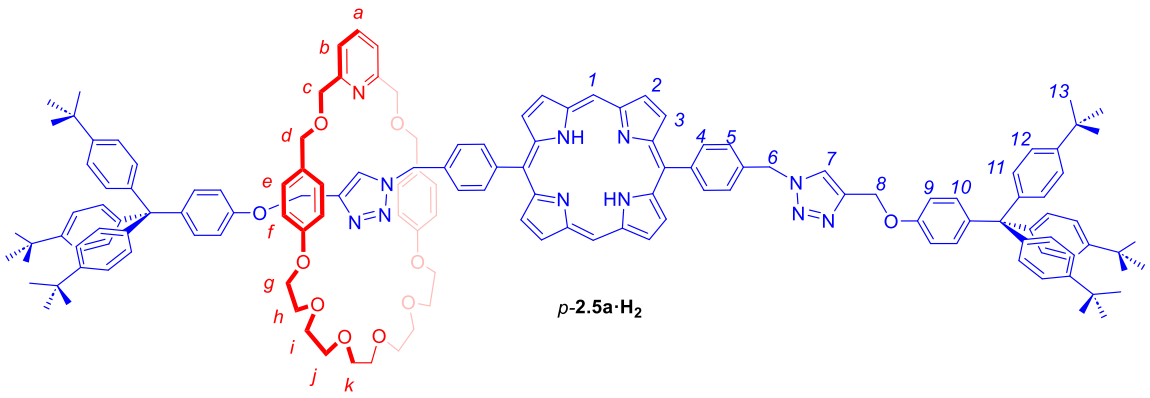

Trifluoroacetic acid (0.05 mL, 0.66 mmol) was added dropwise to a solution of *p*-**2.5a·Zn** (15 mg, 6.60 μmol) in dry DCM (5 mL) in a sealed flask before stirring for four hours at room temperature. Aqueous $NaHCO_3$ (1.0 M) was added to the reaction mixture until effervescence ceased, whereupon an additional 10 mL was added. The organic layer was collected and the aqueous layer further extracted with DCM (10 mL x 3). The combined organic layers were washed with 1.0 M $NaHCO_3$ (20 mL) and H_2O (30 mL x 4) and dried over $MgSO_4$. The solvent was removed *in vacuo* and the crude product purified by preparative thin layer chromatography (2:8:90 *v/v* MeOH:EtOAc:DCM), *p*-**2.5a·H$_2$** was afforded as a red solid. Yield: 13.3 mg (91%).

^{1}H NMR (400 MHz, $CDCl_3$, 298 K) δ: 10.31 (s, 2H, H_1), 9.37 (d, J = 4.6 Hz, 4H, H_2), 8.99 (d, J = 4.6 Hz, 4H, H_3), 8.12 (s, 4H, H_4), 7.88 (s, 2H, H_7), 7.49 (s, 4H, H_5), 7.33 (t, J = 7.7 Hz, 1H, H_a), 7.23 (d, J = 8.6 Hz, 12H, H_{11}), 7.19 – 7.07 (m, 18H, $H_{b,10,12}$), 7.06 (d, J = 8.3 Hz, 4H, H_9), 6.88 (d, J = 8.6 Hz, 4H, H_e), 6.65 – 6.58 (d, J = 8.6 Hz, 4H, H_f), 5.67 (s, 2H, H_6), 5.16 (s, 2H, H_8), 4.51 (s, 4H, H_c), 4.35 (s, 4H. H_d), 3.93 (t, J = 4.8 Hz, 4H, H_g), 3.73 (t, J = 4.8 Hz, 4H, H_h), 3.65 – 3.55 (m, 12H, $H_{i,\,j,\,k}$), 1.30 (s, 54H, H_{13}), −3.16 (s, 2H, N*H*) ppm.

^{13}C{^{1}H} NMR (101 MHz, $CDCl_3$, 298 K) δ: 158.4, 158.3 157.6, 156.3, 156.3 148.3, 147.0, 144.1, 140.0, 135.2, 134.4, 132.3, 132.3, 131.8, 131.2, 130.8, 130.0, 129.9, 129.6, 126.7, 124.1, 120.1, 114.4, 113.3, 113.3, 105.4, 72.3, 71.5, 70.8, 70.7, 69.6, 67.2, 63.1, 61.9, 53.8, 34.3, 31.4 ppm. Undetected aromatic signals believed to be coincident.

HR-ESI-MS *m/z* calculated for $[C_{145}H_{156}N_{10}O_{10}]^+$, $[M+H]^+$: 2211.2064, found 2211.2051.

Para-substituted Ni(II) Metalloporphyrin [2]Rotaxane ***p*-2.5a·Ni**

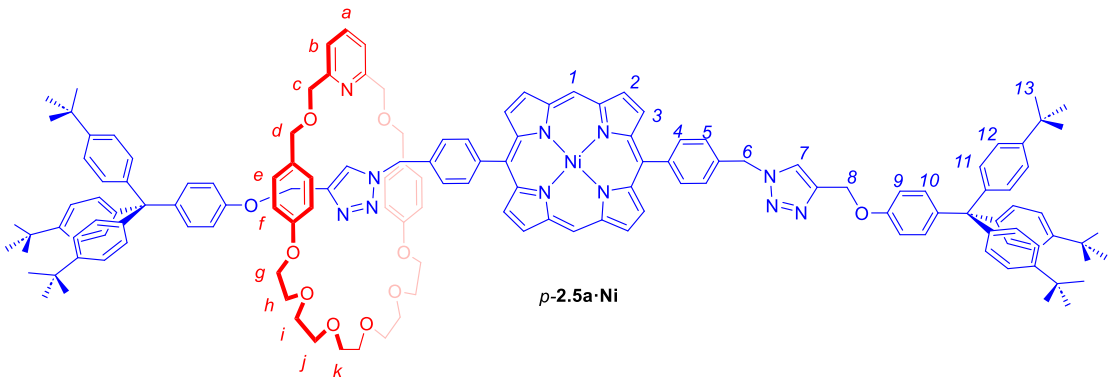

***p*-2.5a·H$_2$** (11.8 mg, 0.005 mmol) and Ni(OAc)$_2$·4H$_2$O (30.0 mg, 0.12 mmol) were dissolved in degassed dry DMF (1.5 mL) in a sealed flask before heating at reflux for four hours. The reaction mixture cooled to room temperature and the volatiles removed *in vacuo*. The red residual solid was taken up in DCM (20 mL) and washed with H$_2$O (50 mL). The aqueous layer was back extracted with DCM (20 mL x 3) to minimise loss of product. The combined organic layer was washed with H$_2$O (40 mL x 4) and dried over MgSO$_4$. The volatiles were removed *in vacuo* and ***p*-2.5a·Ni** obtained by purifying by preparative TLC (2:8:90 *v/v* MeOH:EtOAc:DCM). Yield: 10.5 mg (87%).

^{1}H NMR (600 MHz, CDCl$_3$, 298 K) δ: 9.93 (s, 2H, H_1), 9.16 (d, J = 4.7 Hz, 4H, H_2), 8.82 (d, J = 4.7 Hz, 4H, H_3), 7.91 (d, J = 7.3 Hz, 4H, H_4), 7.84 (s, 2H, H_7), 7.39 (d, J = 7.3 Hz, 4H, H_5), 7.29 (t, J = 7.8 Hz, 1H, H_a), 7.24-7.21 (m, 14H, $H_{11,\,b}$), 7.15-7.08 (d, 16H, $H_{10,12}$), 7.04 (d, J = 8.6 Hz, 4H, H_9), 6.86 (d, J = 8.8 Hz, 4H, H_e), 6.59 (d, J = 8.8 Hz, 4H, H_f), 5.61 (s, 4H, H_6), 5.14 (s, 4H, H_8), 4.49 (s, 4H, H_c), 4.30 (s, 4H, H_d), 3.91 (t, J = 4.8 Hz, 4H, H_g), 3.72 (t, J = 4.8 Hz, 4H, H_h), 3.67 – 3.53 (m, 12H, $H_{i,\,j,\,k}$), 1.30 (s, 54H, H_{13}) ppm.

^{13}C{^{1}H} NMR (151 MHz, CDCl$_3$, 298 K) δ: 158.4, 157.6, 156.3, 148.4, 144.6, 144.2, 142.7, 142.6, 141.2, 140.1, 137.0, 134.4, 134.2, 132.5, 132.3, 132.2, 130.7, 129.9, 129.6, 126.6, 124.1, 123.6, 120.1, 117.5, 114.4, 113.3, 105.2, 72.3, 71.5, 70.8, 70.7, 69.5, 67.2, 63.1, 61.9, 53.8, 50.9, 34.3, 31.4 ppm.

HR-ESI-MS *m/z* calculated for [C$_{145}$H$_{154}$N$_{11}$O$_{10}$Ni]$^+$, [M+H]$^+$: 2267.1228, found: 2267.1250.

Meta-substituted Zn(II) Metalloporphyrin [2]- and [3]-Rotaxanes *m*-**2.6a·Zn**, *m*-**2.6b·Zn**

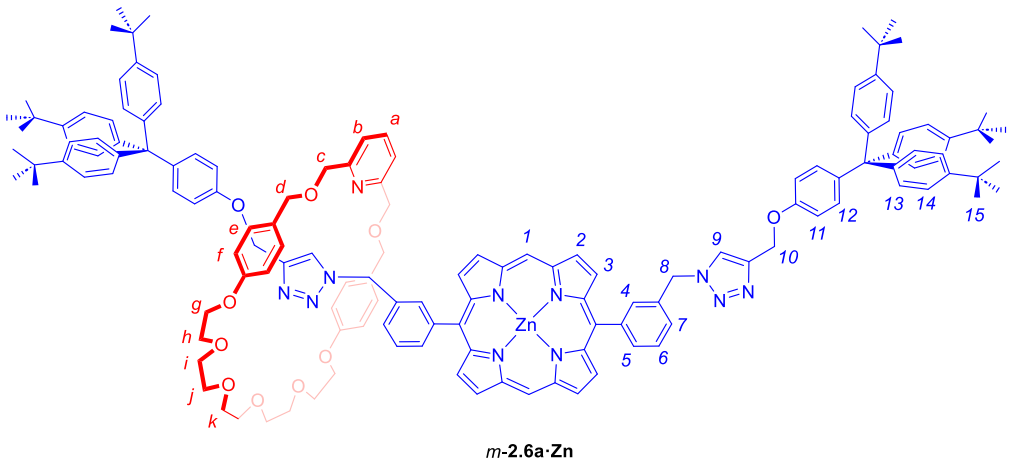

m-**2.6a·Zn**

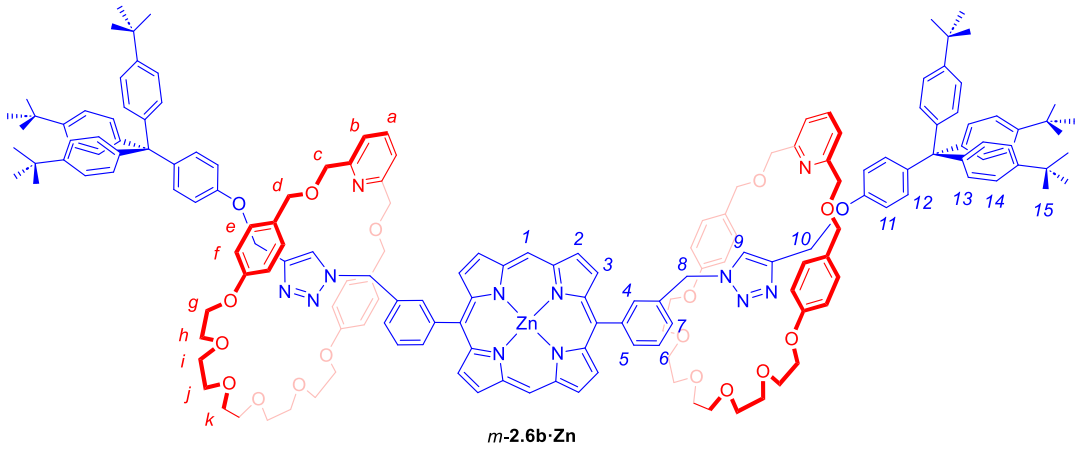

m-**2.6b·Zn**

Macrocycle **2.3** (20.0 mg, 0.036 mmol) and $[Cu(CH_3CN)_4]PF_6$ (6.4 mg, 0.017 mmol) were added to degassed dry DCE (1.6 mL) in a sealed flask. The mixture was then purged with N_2 for 5 minutes before stirring at room temperature under N_2 for 15 minutes. A solution of *m*-**2.2·Zn** (69.0 mg, 0.108 mmol) in dry, degassed DCE (1.0 mL) was added, followed by addition of a solution of stopper alkyne **2.4** (118.0 mg, 0.216 mmol)[10] in dry, degassed DCE (1.0 mL). The reaction mixture was purged with N_2 for 5 minutes and then heated at 60 °C for 5 days. The crude reaction mixture was concentrated *in vacuo*, redissolved in $CHCl_3$ (20 mL) and washed with aqueous NH_4OH/EDTA (20 mL x 2), and each aqueous layer was back extracted with $CHCl_3$ (10 mL) to minimise the loss of product. The combined organic layers were washed with brine (50 mL), dried over anhydrous $MgSO_4$, filtered and concentrated *in vacuo*. The product was purified by

preparative TLC (2:90:8 *v/v* CH_3OH:DCM:EtOAc) to give *m*-**2.6a·Zn** and *m*-**2.6b·Zn** as dark red solids.

m-**2.6a·Zn** Yield: 25.0 mg (30%).
^{1}H NMR (500 MHz, $CDCl_3$, 298 K) δ: 10.23 (s, 2H, H_1), 9.33 (d, J = 4.4 Hz, 4H, H_2), 8.95 (d, J = 4.4 Hz, 4H, H_3), 8.20 (m, 2H, H_5), 7.83 (s, 2H, H_9), 7.64 (t, J = 7.6 Hz, 2H, H_6), 7.56 (s, 1H, H_4), 7.51 (s, 1H, $H_{4'}$), 7.41 (d, J = 7.6 Hz, 2H, H_7), 7.19 (m, 12H, H_{13}), 7.10 (s, 1H, H_a), 7.04 (m, 12H, H_{14}), 6.97 (m, 4H, H_{12}), 6.60 (dd, J = 15.4, 7.7 Hz, 4H, H_{11}), 6.51 (m, 6H, $H_{b,e}$), 6.21 (dd, J = 12.9, 8.2 Hz, 4H, H_f), 5.47 (s, 4H, H_8), 4.65 (s, 2H, H_{10}), 4.54 (s, 2H, $H_{10'}$), 3.89 (d, J = 16.8 Hz, 4H, $H_{c,c'}$), 3.77 (d, J = 14.8 Hz, 4H, $H_{d,d'}$), 3.48 (dt, J = 10.0, 4.8 Hz, 4H, H_g), 3.30 (app. q, J = 4.8 Hz, 4H, H_h), 3.12 (app. q, J = 4.7 Hz, 4H, H_i), 3.01 (t, J = 4.7 Hz, 4H, H_j), 2.95 (s, 4H, H_k), 1.27 (d, J = 2.6 Hz, 54H, H_{15}) ppm.

^{13}C{^{1}H} NMR (126 MHz, $CDCl_3$, 298 K) δ: 157.9, 157.9, 157.1, 155.9, 155.8, 149.8, 149.5, 148.3, 144.2, 143.7, 143.5, 139.8, 136.7, 137.6, 134.1, 132.2, 131.9, 130.7, 129.4, 129.4, 129.0, 128.9, 127.1, 126.6, 124.1, 119.7, 114.0, 113.1, 106.2, 71.6, 71.5, 70.8, 70.3, 70.2, 69.2, 66.7, 63.1, 60.9, 60.7, 34.3, 31.4 ppm.

HR-ESI-MS *m/z* calculated for $[C_{145}H_{153}N_{11}O_{10}Zn]^+$, $[M+H]^+$, 2274.1199, found: 2274.1145.

m-**2.6b·Zn** Yield: 4.1 mg (8%).
^{1}H NMR (500 MHz, $CDCl_3$, 298 K) δ: 10.26 (d, J = 6.0 Hz, 2H, H_1), 9.35 (dd, J = 4.5, 2.1 Hz, 4H, H_2), 8.98 (t, J = 3.8 Hz, 4H, H_3), 8.17 (d, J = 7.5 Hz, 1H, H_5), 8.13 (d, J = 7.5 Hz, 1H, $H_{5'}$), 7.78 (s, 1H, H_9), 7.67 (s, 1H, $H_{9'}$), 7.62 – 7.55 (m, 3H, $H_{6,6',7}$), 7.53 (t, J = 7.7 Hz, 1H, H_a), 7.34 (d, J = 7.9 Hz, 1H, $H_{7'}$), 7.28 (t, J = 7.8 Hz, 1H, $H_{a'}$), 7.17 (dd, J = 20.5, 8.6 Hz, 14H, $H_{4,4',13,13'}$), 7.02 (dd, J = 21.1, 8.6 Hz, 14H, $H_{b,14,14'}$), 6.94 (d, J = 8.9 Hz, 2H, H_{12}), 6.88 (d, J = 8.8 Hz, 2H, $H_{12'}$), 6.82 (d, J = 8.6 Hz, 2H, $H_{b'}$), 6.71 (d, J = 11.1 Hz, 4H, H_e), 6.57 (dd, J = 11.1, 8.9 Hz, 6H, $H_{e',11}$), 6.46 (d, J = 8.9 Hz, 2H, $H_{11'}$), 6.36 (d, J = 8.2 Hz, 4H, H_f), 6.26 (d, J = 8.2 Hz, 4H, $H_{f'}$), 5.39 (d, J = 8.5 Hz, 4H, H_8), 4.56 (dd, J = 68.4, 34.8 Hz, 4H, $H_{10,10'}$), 4.23 – 3.78 (m, 16H, $H_{c,d}$), 3.69 – 3.04 (m, 40H, H_{g-h}), 1.26 (d, J = 10.5 Hz, 54H, H_{15}) ppm.

^{13}C NMR (126 MHz, $CDCl_3$, 298 K) δ: 158.4, 158.1, 158.0, 157.7, 157.4, 157.2, 156.1, 156.0, 149.9, 149.8, 149.5, 148.2, 148.2, 144.2, 144.2, 143.9, 143.1, 143.0, 139.5, 139.4, 136.9, 136.7, 134.1, 133.9, 133.8, 133.8, 132.6, 132.0, 131.9, 131.8, 130.7, 130.6, 129.9, 129.6, 129.5, 129.2, 129.1, 127.2, 127.1, 126.8, 124.2, 124.0, 124.0, 120.5, 120.0, 119.8, 119.2, 119.1, 114.5, 114.2, 114.1, 113.2, 113.1, 106.2, 72.0, 71.9, 71.7, 71.2, 71.0, 70.9, 70.7, 70.7, 70.3, 70.2, 69.6, 69.3, 69.2, 67.5, 66.9, 66.8, 63.0, 62.9, 61.3, 61.3, 34.3, 31.4 ppm.

HR-ESI-MS *m/z* calculated for $[C_{176}H_{192}N_{12}O_{18}Zn]^+$, $[M+H]^+$: 2827.3875, found: 2827.3808.

Meta-substituted Zn(II) Metalloporphyrin Axle ***m*-2.6c·Zn**

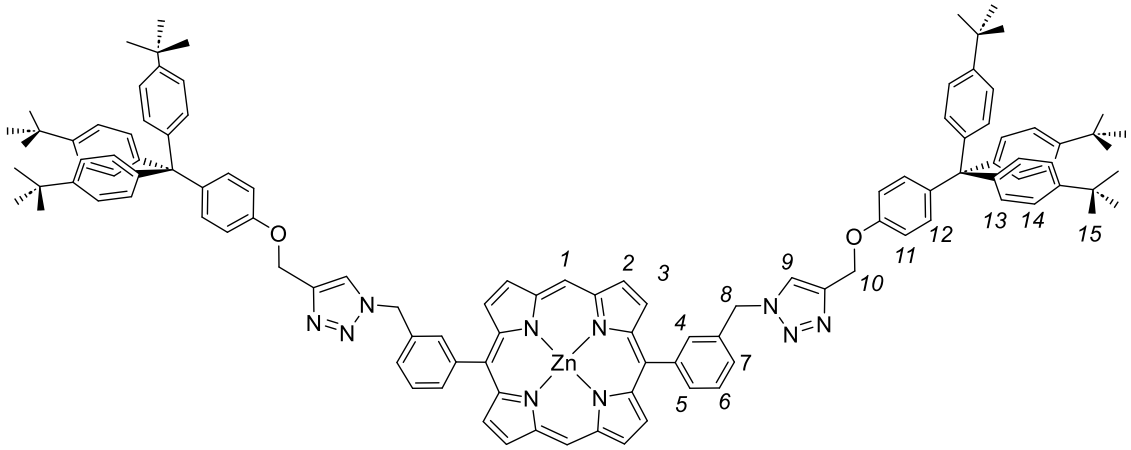

***m*-2.6c·Zn**

Bis-azido zinc(II) metalloporphyrin ***m*-2.2·Zn** (100 mg, 0.157 mmol) was dissolved in dry THF (3 mL) in a sealed flask and degassed for five minutes. TBTA (50 mg, 0.095 mmol) and $[Cu(MeCN)_4]PF_6$ (46.9 mg, 0.126 mmol) were added and the solution was degassed for a further five minutes. A solution of stopper alkyne (179 mg, 0.330 mmol)[10] in dry and degassed THF (2.0 mL) was prepared and added into the microwave vial before degassing for five minutes. The solution was stirred under positive pressure of N_2 for three days at room temperature. The reaction mixture was diluted with DCM (40 mL), washed with aqueous NH_4OH/EDTA (30ml x 2), H_2O (30 mL) and brine (30 mL), then dried over anhydrous $MgSO_4$ and filtered. The volatiles were removed *in vacuo* and the product purified by column chromatography (3:7 *v/v* hexane:DCM graded to 100% DCM and then to 1:9 *v/v* EtOAc:DCM). Yield: 116 mg (43%).

^{1}H NMR (500 MHz, $CDCl_3$, 298 K) δ: 9.96 (d, J = 5.4 Hz, 2H, H_1), 9.05 (d, J = 4.5 Hz, 4H, H_2), 8.66 (d, J = 4.5 Hz, 4H, H_3), 8.05 (t, J = 8.7 Hz, 2H, H_5), 7.62 (s, 2H, H_9), 7.44 (m, 2H, H_6), 7.29 – 7.21 (m, 12H, H_{13}), 7.14 – 7.06 (m, 12H, H_{14}), 7.05 (d, J = 8.8 Hz, 4H, H_{12}), 7.00 (d, J = 6.8 Hz, 2H, H_7), 6.86 (s, 2H, H_4), 6.32 (dd, J = 8.8, 4.1 Hz, 4H, H_{11}), 4.99 – 4.82 (m, 4H, H_8), 3.39 (s, 4H, H_{10}), 1.31 (d, J = 2.1 Hz, 54H, H_{15}) ppm.

$^{13}C\{^{1}H\}$ NMR (126 MHz, $CDCl_3$, 298 K) δ: 171.2, 155.6, 149.8, 149.5, 148.5, 144.2, 144.1, 143.1, 140.1, 135.0, 133.9, 132.3, 131.9, 130.9, 127.0, 126.3, 124.3, 121.6, 118.4, 113.1, 106.2, 63.2, 60.5, 60.0, 53.9, 34.5, 31.6 ppm.

HR-ESI-MS *m/z* calculated for $[C_{114}H_{114}N_{10}NaO_2Zn]^+$, $[M+Na]^+$: 1742.8344, found: 1742.8282.

Macrocycle **2.8**

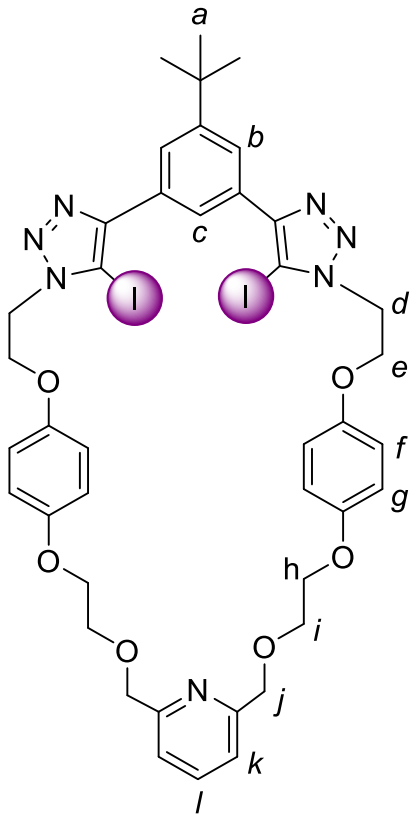

2.8

$[Cu(MeCN)_4]PF_6$ (93 mg, 0.25 mmol) and TBTA (66 mg, 0.12 mmol) were dissolved in dry, degassed DCM (250 mL). The solution was stirred at room temperature under N_2 for 20 min to allow the TBTA to pre-complex the copper catalyst. 2,6-Bis((2-(4-(2-azidoethoxy)phenoxy)ethoxy)methyl)pyridine (275 mg, 0.500 mmol)[12] and 1-(*tert*-butyl)-3,5-bis(iodoethynyl)benzene (217 mg, 0.500 mmol)[13] were added to a glass vial, and the vial purged with N_2. The solids were dissolved in degassed dry DCM (5 mL) and the resulting solution added dropwise to the copper solution. The reaction was stirred at

room temperature under N_2 and exclusion of light for 48 h. The reaction mixture was washed with an aqueous solution of EDTA/NH_4OH (2 x 150 mL) and washed with water (100 mL). The organic mixture was dried over $MgSO_4$ and the volatiles removed *in vacuo*. The residue was taken up in the minimum amount of 40:1:59 *v/v* MeCN:MeOH:DCM, loaded onto a silica column and eluted with the same solvent mixture to afford macrocycle **2.8** as a pale white solid. Yield: 158 mg (32%).

^{1}H NMR (400 MHz, $CDCl_3$, 298 K) δ: 8.24 (t, J = 1.6 Hz, 1H, H_l), 8.00 (d, J = 1.6 Hz, 2H, H_k), 7.60 (t, J = 7.7 Hz, 1H, H_c), 7.29 (d, J = 7.7 Hz, 2H, H_b), 6.82 – 6.68 (m, 8H, $H_{f, g}$), 4.85 (t, J = 5.3 Hz, 4H, H_h), 4.67 (s, 4H, H_j), 4.43 (t, J = 5.3 Hz, 4H, H_i), 4.10 (t, J = 4.4 Hz, 4H, H_e), 3.90 – 3.83 (t, J = 4.4 Hz, 4H, H_d), 1.42 (s, 9H, H_a) ppm.

^{13}C{^{1}H} NMR (101 MHz, $CDCl_3$) δ: 171.2, 157.7, 153.4, 152.3, 150.1, 137.2, 130.1, 125.3, 120.4, 115.9, 115.7, 74.1, 69.4, 68.2, 67.3, 60.4, 50.0, 35.2, 31.4 ppm. Undetected aromatic signal believed to be coincident.

HR-ESI-MS *m/z* calculated for $C_{41}H_{44}I_2N_7O_6$ $[M+H]^+$: 984.1442, found: 984.1437.

Heteroditopic Zn(II)-Metalloporphyrin [2]Rotaxane ***p*-2.11·Zn**

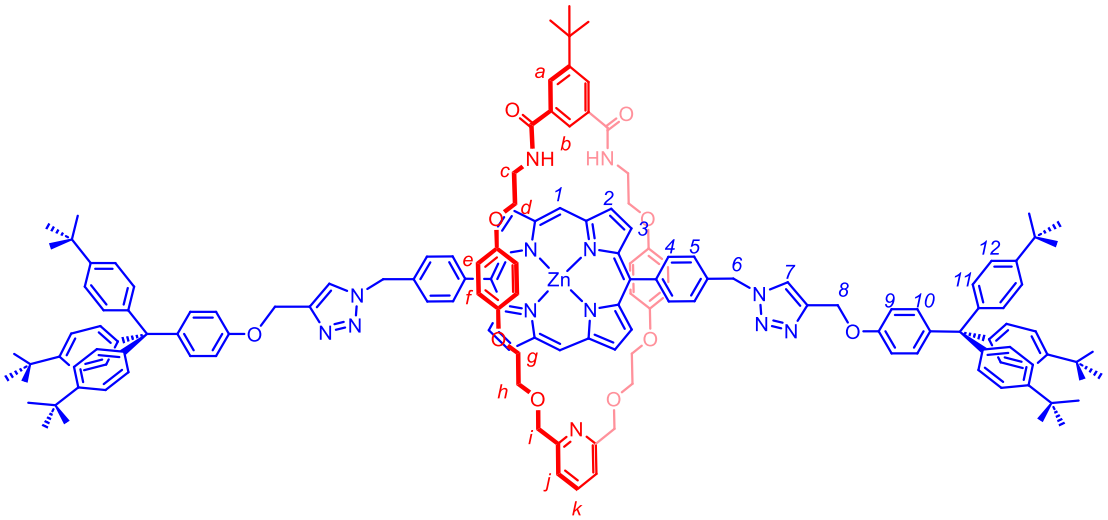

***p*-2.11·Zn**

Macrocycle **2.10** (14.2 mg, 0.021 mmol)[12] and $[Cu(MeCN)_4]PF_6$ (7.7 mg, 0.021 mmol) were added to degassed dry DCE (1.6 mL) in a sealed flask. The mixture was purged with N_2 for 10 min, and stirred at room temperature for 30 min. Stopper alkyne **2.4** (68.0

mg, 0.125 mmol)[10] and the *para*-metalloporphyrin bis-azide *p*-**2.1·Zn** (39.1 mg, 0.061 mmol) were dissolved in degassed dry DCE (3 mL) and the resulting solution purged with N_2 for 5 min. The porphyrin solution was added dropwise to the copper solution, and the reaction mixture heated to 60 °C for 3 days. The reaction was cooled to room temperature and the solvent removed *in vacuo*. The residue was taken up in DCM (30 mL) and washed with aqueous NH_4OH/EDTA (2 x 20 mL) and water (20 mL). The combined aqueous layers were re-extracted with further DCM (20 mL) and the combined organic layers dried over $MgSO_4$ and the volatiles removed *in vacuo*. *p*-**2.11·Zn** was obtained by preparative TLC (4% MeOH *v/v* in DCM, followed by 2:89:9 *v/v* MeOH:DCM:EtOAc) as a red solid. Yield: 36.9 mg (73%).

^{1}H NMR (500 MHz, $CDCl_3$, 338 K) δ: 10.22 (s, 2H, H_1), 9.37 (d, J = 4.4 Hz, 2H, H_2), 8.94 (broad s, 2H, H_3), 8.14 (d, J = 7.4 Hz, 4H, H_4), 7.85 (app s., 1H, H_k), 7.65 (m, 4H, $H_{a,\ j}$) 7.56-7.41 (m, 11H, $H_{5,7,10\ b}$), 7.29 (d, J = 8.7 Hz, 12H, H_{11}), 7.15 (d, J = 8.7 Hz, 12H, H_{12}), 6.82 (d, J = 8.5 Hz, 4H, H_9), 6.71 (d, J = 8.8 Hz, 4H, H_e), 6.64 (d, J = 8.8 Hz, 4H, H_f), 5.68 (s, 4H H_6), 5.44 – 5.36 (m, 2H, H_{NH}), 4.94 (s, 4H, H_8), 4.64 (s, 4H, H_i), 4.10 (s, 4H, H_d), 3.90-3.84 (m, 8H, $H_{g,h}$), 3.42 (s, 4H, H_c), 1.34 (s, 54H, $H_{stopper\ tBu)}$, 1.32 (s, 9H, H_{tBu}) ppm.

^{13}C{^{1}H} NMR (151 MHz, $CDCl_3$) δ: 167.9, 157.4, 155.8, 153.1, 152.4, 152.0, 149.7, 149.5, 148.4, 144.0, 143.6, 143.4, 140.4, 134.8, 133.6, 133.2, 132.4, 132.0, 131.8, 130.7, 127.9, 125.6, 124.1, 121.0, 118.5, 115.8, 115.5, 113.1, 106.2, 74.3, 69.9, 68.3, 66.5, 63.1, 39.3, 34.8, 34.3, 33.2, 31.9, 31.4 31.0, 29.7, 29.4 ppm. Undetected aromatic signals believed to be coincident.

HR-ESI-MS *m/z* calculated for $[C_{153}H_{160}O_{10}N_{13}Zn]^+$, $[M+H]^+$: 2403.1697, found: 2403.1703.

Heteroditopic Free-base Porphyrin [2]Rotaxane ***p*-2.11·H$_2$**

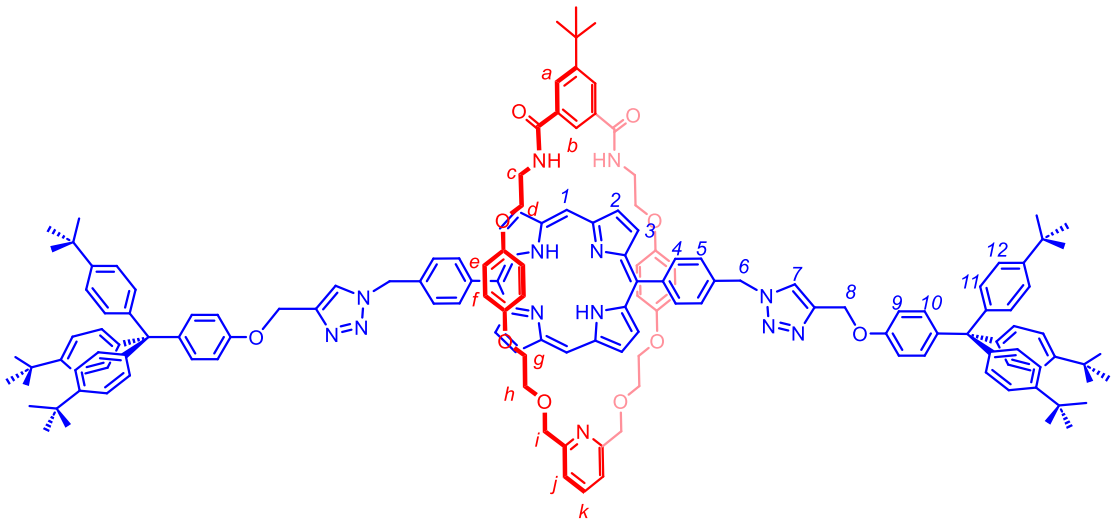

***p*-2.11·H$_2$**

Trifluoroacetic acid (0.05 mL, 0.66 mmol) was added dropwise to a solution of ***p*-2.11·Zn** (16 mg, 6.60 μmol) in dry DCM (5 mL) in a sealed flask before stirring for four hours at room temperature. Aqueous $NaHCO_3$ (1.0 M) was added to the reaction mixture until effervescence ceased, whereupon an additional 10 mL was added. The organic layer was collected and the aqueous layer further extracted with DCM (10 mL x 3). The combined organic layers were washed with 1.0 M $NaHCO_3$ (20 mL) and H_2O (30 mL x 4) and dried over $MgSO_4$. The solvent was removed *in vacuo* affording ***p*-2.11·H$_2$** afforded as a red solid. Yield: 13.3 mg (Quantitative).

^{1}H NMR (600 MHz, $CDCl_3$) δ: 10.32 (s, 2H, H_1), 9.39 (d, J = 4.5 Hz, 4H, H_2), 8.98 (d, J = 4.5 Hz, 4H, H_3), 8.31 (s, 1H, H_b), 8.21 (m, 6H, $H_{4,7}$), 7.64 (s, 2H, H_a), 7.58 (m, 6H, $H_{5,j}$), 7.33 (t, J = 7.6 Hz, 1H, H_k), 7.25 – 7.22 (d, J = 8.5 Hz, 12H, H_{11}), 7.15 (d, J = 8.3 Hz, 4H, H_{10}), 7.10 (d, J = 8.5 Hz, 12H, H_{12}), 6.81 (d, J = 8.3 Hz, 4H, H_9), 6.64 (d, J = 8.7 Hz, 4H $H_{e\ or\ f}$), 6.48 (d, J = 8.7 Hz, 4H $H_{e\ or\ f}$), 5.65 (s, 4H, H_6), 5.04 (s, 4H, H_8), 4.65 (s, 4H, H_i), 4.04 – 3.99 (m, 4H, H_d), 3.89 – 3.84 (m, 8H, $H_{g,\ h}$), 3.77 (m, 4H, H_c), 1.30 (s, 54H, $H_{stopper\ tBu}$), 1.26 (s, 9H, $H_{macrocycle\ tBu}$), -3.15 (s, 2H, H_{NH}) ppm.

^{13}C{^{1}H} NMR (151 MHz, $CDCl_3$) δ: 167.8, 157.7, 156.0, 153.0, 152.6, 152.5, 148.4, 146.9, 145.3, 144.7, 144.1, 142.0, 140.5, 137.1, 135.4, 134.1, 133.9, 132.4, 132.0, 130.9, 130.7, 128.8, 126.8, 123.4, 121.5, 118.0, 115.7, 115.4, 113.2, 105.6, 74.1, 69.7, 68.2, 66.9, 63.1, 61.7, 54.1, 53.4, 39.9, 35.0, 34.3, 31.2, 30.9, 29.7 ppm.

HR-ESI-MS *m/z* calculated for $[C_{153}H_{162}O_{10}N_{13}]^+$, $[M+H]^+$: 2341.2562, found: 2341.2562.

6.3 Synthesis and Characterisation of Novel Compounds in Chapter 3

Stopper Azide **3.3**

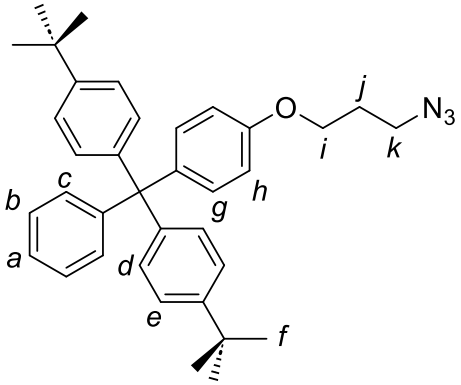

3.3

Stopper precursor alcohol (1.00 g, 2.22 mmol)[14] and 3-azidopropyl tosylate (1.13 g, 4.44 mmol)[15] were dissolved in MeCN (75 mL). K_2CO_3 (1.38 g, 10.0 mmol) was added and the mixture heated to reflux for 24 h. The resulting suspension was cooled to room temperature and neutralised with 1 M HCl (aq.) until effervescence ceased. The organic layer was collected, washed with brine (3 x 50 mL) and dried over $MgSO_4$. The volatiles were removed *in vacuo* and **3.3** obtained as a white solid by column chromatography (3:7 *v/v* hexane:DCM). Yield: 790 mg (67%).

^{1}H NMR (400 MHz, $CDCl_3$) δ: 7.26 – 7.13 (m, 7H, $H_{a,b,e}$), 7.13 – 7.05 (m, 8H, $H_{c,d,g}$), 6.76 (d, J = 8.9 Hz, 2H, H_h), 4.02 (t, J = 6.3 Hz, 2H, H_i), 3.51 (t, J = 6.3 Hz, 2H, H_k), 2.04 (p, J = 6.3 Hz, 2H, H_j), 1.30 (s, 18H, H_f) ppm.

13C{^{1}H} NMR (151 MHz, $CDCl_3$) δ: 156.5, 148.6, 148.3, 144.1, 143.5, 132.3, 130.7, 130.6, 130.6, 124.2, 124.0, 113.0, 65.5, 64.3, 48.3, 34.3, 31.4, 28.9 ppm.

HR-ESI-MS *m/z* calculated for $[C_{36}H_{41}ON_3]^+$, $[M+H]^+$: 532.3322, found: 532.2316.

P5A [2]Rotaxane **3.4** and Non-interlocked Axle

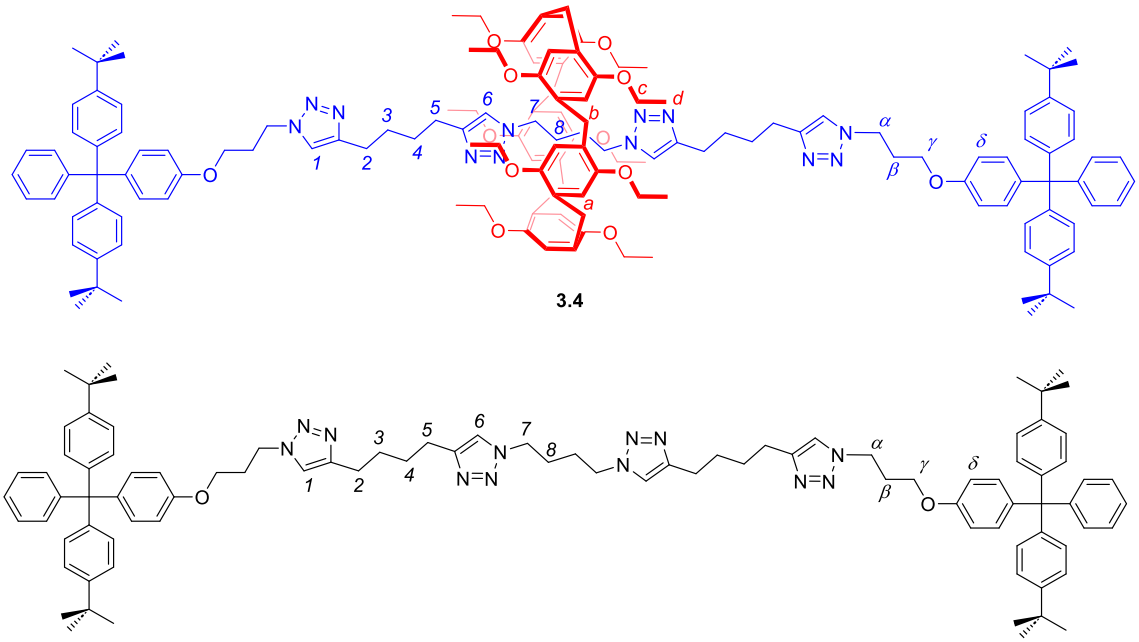

3.4

Axle precursor bis-alkyne **3.1** (7.5 mg, 0.023 mmol),[16] P5A **3.2** (95.7 mg, 0.108 mmol)[17] and stopper azide **3.3** (45.6 mg, 0.086 mmol) were dissolved in degassed anhydrous $CHCl_3$ (10 mL) and stirred at room temperature for 1 h, to enable pseudorotaxane formation between **3.1** and **3.2**. $[Cu(MeCN)_4]PF_6$ (4.1 mg, 0.011 mmol) and TBTA (5.8 mg, 0.011 mmol) were dissolved in degassed anhydrous $CHCl_3$ (2 mL) and the resulting solution added to the pseudorotaxane solution. The reaction mixture was stirred at room temperature for 24 h, diluted with DCM (20 mL) and washed with EDTA/NH_4OH (aq.) (2 x 20 mL) and water (20 mL). The combined aqueous layers were back-extracted with DCM (20 mL), and the combined organic layers dried over $MgSO_4$. The volatiles were removed *in vacuo* and **3.4** and **3.5** isolated by preparative TLC (3:2:95 *v/v* MeOH:EtOAc:DCM).

3.4 Yield: 14.3 mg (27%).
^{1}H NMR (400 MHz, $CDCl_3$) δ: 7.30 (s, 2H, H_6), 7.20 – 7.10 (m, 14H, $H_{stopperAr}$), 7.08 – 6.96 (m, 16H, $H_{stopperAr}$), 6.81 (s, 10H, H_a), 6.70 (d, J = 8.5 Hz, 4H, H_δ), 4.49 (t, J = 6.4 Hz, 4H, H_α), 3.91 (t, J = 6.4 Hz, 4H, H_γ), 3.72 – 3.62 (m, 30H, $H_{b,c}$), 2.74 (m, 8H, $H_{2,5}$), 2.36 (p, J = 6.4 Hz, 4H, H_β), 1.93 (broad s, 4H, H_3), 1.80 (broad s, 4H, H_4), 1.57 (broad s, 4H, H_7), 1.28 – 1.20 (m, 30H, H_d), -1.25 (broad s, 4H, H_8) ppm. H_1 not observed and is believed to lie below the residual protiosolvent peak.

^{13}C {^{1}H} NMR (151 MHz, $CDCl_3$) δ: 156.3, 149.7, 148.5, 147.9, 147.3, 146.3, 143.9, 140.0, 132.3, 131.1, 130.7, 128.8, 127.3, 125.7, 124.2, 121.1, 119.6, 114.7, 113.1, 64.0, 63.9, 63.5, 48.2, 47.1, 34.3, 31.9, 31.4, 30.3, 30.2, 29.7, 26.0, 25.6, 23.8, 22.7, 14.1 ppm.

HR-ESI-MS *m/z* calculated for $[C_{147}H_{181}O_{12}N_{12}]^+$, $[M+H]^+$: 2307.3899, found: 2307.3950.

Axle Yield: 20.5 mg (63%).
^{1}H NMR (400 MHz, $CDCl_3$) δ: 7.18 – 7.09 (m, 16H, $H_{6,\ stopperAr}$), 7.06 – 6.97 (m, 18H $H_{1,\ stopperAr}$), 6.67 (d, J = 8.6 Hz, 4H, H_δ), 4.46 (broad s, 4H, H_α), 4.24 (broad s, 4H, H_7), 3.86 (t, J = 5.7 Hz, 4H, H_γ), 2.66 (broad s, 8H, $H_{2,5}$), 2.29 (broad s, 4H, H_β), 1.82 (broad s, 4H, H_8), 1.69 – 1.51 (m, 8H, $H_{3,4}$), 1.22 (s, 36H, H_{tBu}) ppm.

^{13}C {^{1}H} NMR (151 MHz, $CDCl_3$) δ: 156.3, 148.5, 147.3, 143.9, 139.9, 132.3, 131.1, 130.7, 127.3, 125.7, 124.2, 113.1, 64.0, 63.5, 34.3, 31.9, 31.4, 30.1, 29.7, 29.7, 29.4, 27.1, 25.4, 22.7 ppm. Undetected aromatic signal likely coincident.

HR-ESI-MS *m/z* calculated for $[C_{92}H_{110}O_2N_{12}]^+$, $[M+H]^+$: 1415.8948, found: 1415.8969.

Triethyleneglycol Macrocycle **3.5**

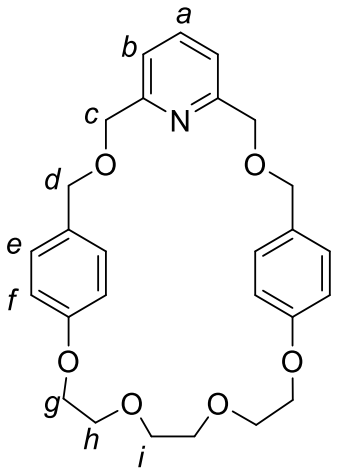

3.5

NaH (0.80 g, 19.92 mmol, 60% *w/w* dispersion) was suspended in anhydrous THF (100 mL) and stirred at 70 °C for 30 minutes. Separate solutions of 2,6-bis(bromomethyl)pyridine (1.19 g, 4.98 mmol) and the diol 1,8-bis[4-(hydroxymethyl)phenoxy]-3,6-dioxaoctane (1.80 g, 4.98 mmol),[18] each in THF (50 mL), were added dropwise to the refluxing solution over the course of 3 hours. Once the

addition was complete, the mixture was left to stir overnight at 70 °C. After which, the mixture was left to cool to room temperature and was carefully quenched by the addition of MeOH (50 mL). The resultant mixture was concentrated to dryness *in vacuo* and the crude reaction mixture partitioned between DCM (250 mL) and H_2O (250 mL). The organic phase was collected and washed with H_2O (250 mL), dried over $MgSO_4$ and the solvent removed *in vacuo*. The crude reaction mixture was purified by column chromatography (3:2:0.3 *v/v* DCM:EtOAc:MeOH) to afford **3.5** as a white solid. Yield: 0.90 g (39%).

^{1}H NMR (500 MHz, $CDCl_3$) δ: 7.67 (t, J = 7.7 Hz, 1H, H_a), 7.29 (d, J = 7.7 Hz, 2H, H_b), 7.23 – 7.17 (d, J = 8.0 Hz, 4H, H_e), 6.82 – 6.76 (d, J = 8.0 Hz, 4H, H_f), 4.57 (s, 4H, H_c), 4.54 (s, 4H, H_d), 4.10 – 4.05 (m, 4H, H_g), 3.87 – 3.81 (m, 4H, H_h), 3.72 (s, 4H, H_i) ppm.

^{13}C{^{1}H} NMR (126 MHz, $CDCl_3$) δ: 158.5, 157.7, 137.0, 130.1, 129.9, 121.2, 114.7, 71.9, 71.6, 71.0, 69.8, 67.6 ppm.

HR-ESI-MS *m/z* calculated for $[C_{27}H_{31}O_6NNa]^+$, $[M+Na]^+$: 488.2044, found: 488.2054.

Pyridyl [2]Rotaxane **3.6**

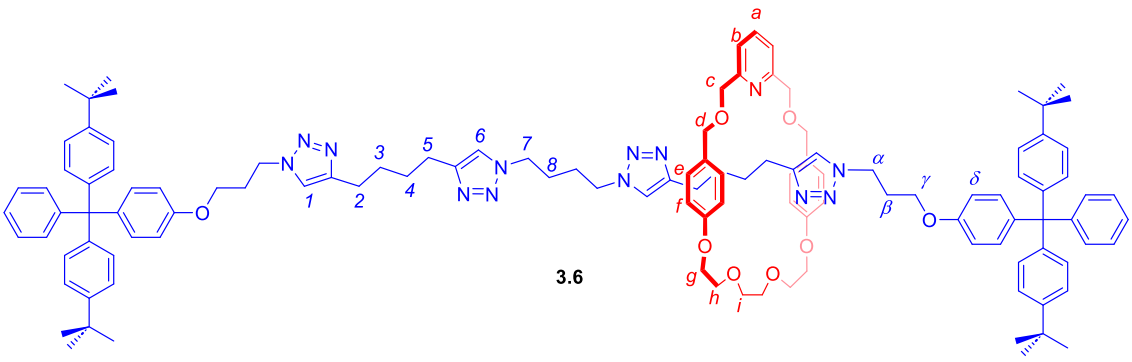

Axle precursor bis-alkyne **3.1** (7.6 mg, 0.021 mmol), P5A **3.2** (95.6 mg, 0.107 mmol) and stopper azide **3.3** (45.6 mg, 0.086 mmol) were dissolved in degassed anhydrous $CHCl_3$ (2.9 mL) and stirred at room temperature for 1 h, to enable pseudorotaxane formation between **3.1** and **3.2**. $[Cu(MeCN)_4]PF_6$ (4.1 mg, 0.011 mmol) and macrocycle **3.5** (20.0 mg, 0.043 mmol) were dissolved in degassed anhydrous $CHCl_3$ (1.4 mL) and the resulting

solution added to the pseudorotaxane solution. The reaction mixture was stirred at room temperature for 24 h, diluted with DCM (20 mL) and washed with NH_4OH/EDTA (aq.) (2 x 20 mL) and water (20 mL). The combined aqueous layers were back-extracted with DCM (20 mL), and the combined organic layers dried over $MgSO_4$. The volatiles were removed *in vacuo* and the interlocked products **3.4** and **3.6** isolated by preparative TLC (3:2:95 *v/v* MeOH:EtOAc:DCM). Yield 7.1 mg (18%).

^{1}H NMR (400 MHz, $CDCl_3$) δ: 7.64 (broad s, 1H, H_a), 7.30 – 7.28 (m, 6H, $H_{1,6,b}$) 7.24 – 7.15 (m, 14H, $H_{stopperAr}$), 7.15 – 7.06 (m, 16H $_{stopperAr}$), 6.99 (d, J = 8.0 Hz, 4H, H_e), 6.74 (d, J = 8.6 Hz, 4H, H_δ), 6.69 (d, J = 8.0 Hz, 4H, H_f), 4.45 (t, J = 6.8 Hz, 4H, H_α), 4.48 (s, 4H, H_c), 4.29 (m, 8H, $H_{7,\gamma}$), 3.94 (t, J = 5.7 Hz, 4H, H_5), 3.84 – 3.71 (m, 12 H, $H_{d,g,h}$), 3.62 (s, 4H, H_i), 2.72 (broad s, 4H, H_5), 2.66 (m, 4H, H_β) 2.35 (t, J = 6.0 Hz, 4H, H_2), 1.88 (broad s, 4H, H_8), 1.75 – 1.61 (m, 8H, $H_{3,4}$), 1.29 (s, 36H, H_{tBu}) ppm.

^{13}C {^{1}H} NMR (151 MHz, $CDCl_3$) δ: 158.4, 156.3, 148.5, 148.2, 147.9, 147.3, 143.9, 139.9, 139.8, 132.3, 131.1, 130.7, 130.6, 127.3, 125.7, 124.2, 121.2, 120.7, 114.2, 113.1, 113.1, 72.6, 70.7, 69.8, 67.2, 64.1, 64.0, 63.5, 49.1, 47.0, 34.3, 31.4, 30.1, 28.9, 28.9, 27.2, 25.4 ppm.

HR-ESI-MS *m/z* calculated for $[C_{119}H_{142}O_8N_{13}]^+$, $[M+H]^+$: 1881.1099, found: 1881.1129.

Bis-alkyne Axle Precursor **3.8**

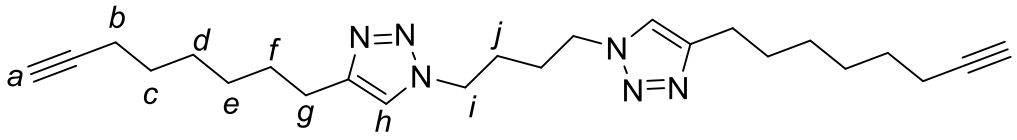

3.8

1,4-Diazidobutane (400 mg, 2.85 mmol) and deca-1,9-diyne (5.00 g, 37.7 mmol) were dissolved in degassed dry DCM (10 mL). $[Cu(MeCN)_4]PF_6$ (40 mg, 0.108 mmol) and TBTA (50.0 mg, 0.094 mmol) were dissolved in degassed dry DCM (2 mL) and the resulting solution added to the reaction mixture. The resulting solution was stirred at room temperature for 3 h and diluted with DCM (20 mL), washed with NH_4OH/EDTA (aq.) (3 x 20 mL) and the organic layer dried over $MgSO_4$. The volatiles were removed

in vacuo and **3.8** obtained as a white solid by column chromatography (1:1 *v/v* DCM:EtOAc). Yield 885 mg (76%).

^{1}H NMR (400 MHz, $CDCl_3$) δ: 7.23 (s, 2H, H_h), 4.33 (m, 4H, H_i), 2.71 (t, J = 8.1 Hz, 4H, H_g), 2.18 (td, J = 7.4 Hz, 2.9 Hz, 4H, H_b), 1.94 – 1.89 (m, 6H, $H_{a,j}$), 1.68 (q, J = 8.1 Hz, 4H, H_f), 1.53 (q, J = 7.4 Hz, 4H, H_c), 1.47 – 1.35 (m, 8H, $H_{d,e}$) ppm.

^{13}C{^{1}H} NMR (151 MHz, $CDCl_3$) δ: 148.6, 120.6, 84.6, 68.2, 49.2, 29.3, 28.7, 28.4, 28.3, 27.2, 25.6, 18.3 ppm.

HR-ESI-MS *m/z* calculated for $[C_{24}H_{37}N_6]^+$, $[M+H]^+$: 409.3074, found: 409.3096.

Inorganic [2]Rotaxane **3.10**

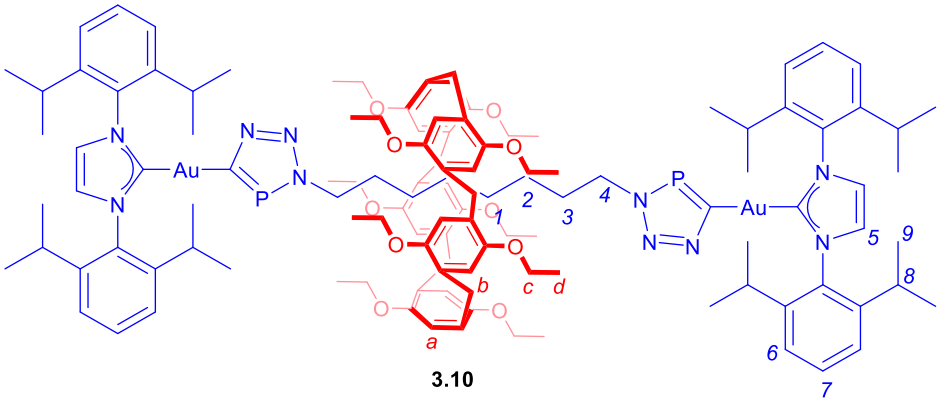

3.10

Per-methylated P5A **3.7** (103.0 mg, 0.115 mmol) and 1,8-diazidooctane (4.5 mg, 0.023 mmol) were dissolved in dry benzene (2 mL) and the mixture stirred for 15 min. Stopper phosphaalkyne precursor **3.9** (30.3 mg, 0.048 mmol)[19] was added and the solution stirred under an inert atmosphere overnight at room temperature. The volatiles were removed *in vacuo* and the crude product purified by column chromatography (1:1 *v/v* EtOAc:hexane) to afford **3.10** as a white powder. Crystals suitable for single crystal XRD studies were grown by slow diffusion of hexane into a saturated solution of **3.10** in toluene. Yield: 20.5 mg (38%).

^{1}H NMR (600 MHz, C_6D_6, 298 K) δ: 7.26 (s, 10H, H_a), 7.19 (m, 4H, H_7), 7.06 (m, 8H, H_6), 6.31 (s, 4H, H_5), 4.26 (broad s, 4H, H_4), 4.22 (s, 10H, H_b), 4.10 (m, 10H, H_c), 3.81 (m, 10H, H_c), 2.67 (sept., J = 6.9 Hz, 8H, H_8), 1.51 (dd, J = 6.9 Hz, 24 H, H_9), 1.33 (t, J

= 6.9 Hz, 30H, H_d), 1.10 (dd, J = 6.9 Hz, 24 H, H_9), 1.08 (q, J = 7.7 Hz, 4H, H_3), −0.44 (broad s, 4H, H_2), −1.19 (broad s, 4H, H_1) ppm.

^{13}C{^{1}H} NMR (151 MHz, C_6D_6, 298 K) δ: 206.4, 196.2, 150.3, 145.9, 145.8, 134.8, 130.7, 128.8, 124.3, 122.8, 114.5, 63.7, 52.5, 52.4, 29.9, 29.1, 28.6, 24.9, 24.0 15.8 ppm.

^{31}P NMR (253 MHz, C_6D_6, 298 K) δ: 198.6 ppm.

HR-ESI-MS *m/z* calculated for $[C_{119}H_{160}O_{10}Au_2N_{10}P_2]^{2+}$, $[M+2H]^{2+}$: 1173.0573, found: 1173.0557.

Inorganic Non-interlocked Axle **3.11**

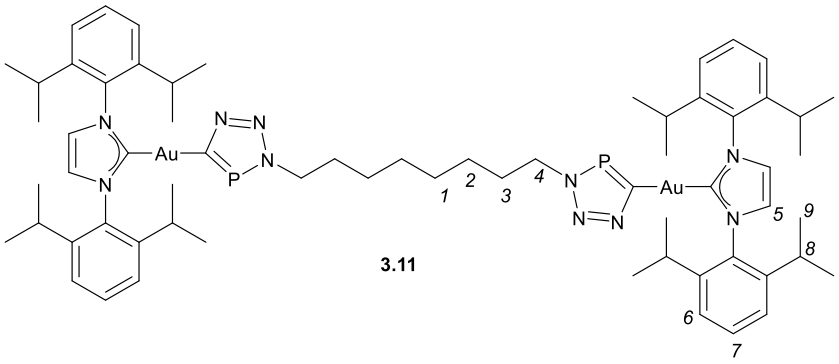

3.11

Stopper phosphaalkyne precursor **3.9** (29.6 mg, 0.047 mmol) and 1,8-diazidooctane (4.4 mg, 0.022 mmol) were dissolved in dry benzene (0.5 mL) and stirred overnight at room temperature, under an inert atmosphere. The solution was concentrated *in vacuo* and hexane (3 mL) added. The resulting crystals were isolated by cannula filtration and washed with hexane (3 x 1 mL) and pentane (3 x 1 mL). The resulting crystals were dried under high vacuum to afford **3.11**. Yield: 23.1 mg (71%).

^{1}H NMR (400 MHz, C_6D_6, 298 K) δ: 7.14 (m, 4H, H_7), 7.06 (d, J = 7.8 Hz, 8H, H_6), 6.34 (s, 4H, H_5), 4.16 (m, 4H, H_4), 2.69 (sept., J = 6.9 Hz, 8H, H_8), 1.53 (d, J = 6.9 Hz, 24H, H_9), 1.46 (q, J = 4.4 Hz, 4H, H_3), 1.10 (d, J = 6.9 Hz, 24H, H_9), 0.74 (m, 4H, H_2), 0.63 (m, 4H, H_1) ppm.

^{13}C{^{1}H} NMR (151 MHz, C_6D_6, 298 K) δ: 207.2, 196.4, 145.9, 134.8, 130.7, 124.3, 122.7, 51.5, 32.8, 29.2, 29.0, 26.7, 24.9, 24.0 ppm.

^{31}P NMR (253 MHz, C_6D_6, 298 K) δ: 199.9 ppm.

HR-ESI-MS *m/z* calculated for $[C_{64}H_{89}Au_2N_{10}P_2]^+$, $[M+H]^+$: 1453.6072, found: 1453.6032.

Bis-triazole Axle Precursor **3.13**

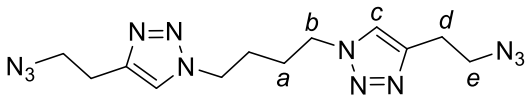

3.13

1,4-Diazidobutane (400 mg, 2.85 mmol), TBTA (56.0 mg, 0.11 mmol) and 4-bromobutyne (797 mg, 6.00 mmol) were dissolved in dry chloroform (10 mL), $[Cu(CH_3CN)_4]PF_6$ (40 mg, 0.105 mmol) was added and the reaction mixture stirred for 24 h at room temperature. The reaction mixture was poured onto hexane and the precipitate collected. The precipitate was redissolved in DMSO (20 mL), and NaN_3 (468 mg, 7.06 mmol) and trace NaI were added. The solution was stirred overnight at room temperature, diluted with H_2O (100 mL) and extracted with DCM (3 x 60 mL). The combined organic layers were washed with brine (3 x 60 mL) and dried over $MgSO_4$. The volatiles were removed *in vacuo* and the crude product purified by column chromatography (1:9 *v/v* MeOH:DCM) to afford **3.13** as a white powder. Yield: 324 mg (35%).

^{1}H NMR (400 MHz, $CDCl_3$) δ: 7.37 (s, 2H, H_c), 4.36 (m, 4H, H_b), 3.62 (t, J = 6.7 Hz, 4H, H_e), 3.00 (t, J = 6.7 Hz, H_d), 1.93 (t, J = 6.7 Hz, 4H, H_a) ppm.

^{13}C{^{1}H} NMR (151 MHz, $CDCl_3$) δ: 144.6, 121.9, 50.8, 49.4, 27.3, 26.0 ppm.

HR-ESI-MS *m/z* calculated for $[C_{12}H_{18}N_{12}]^+$, $[M+H]^+$: 331.1850, found: 331.1846.

Inorganic [2]Rotaxane **3.14**

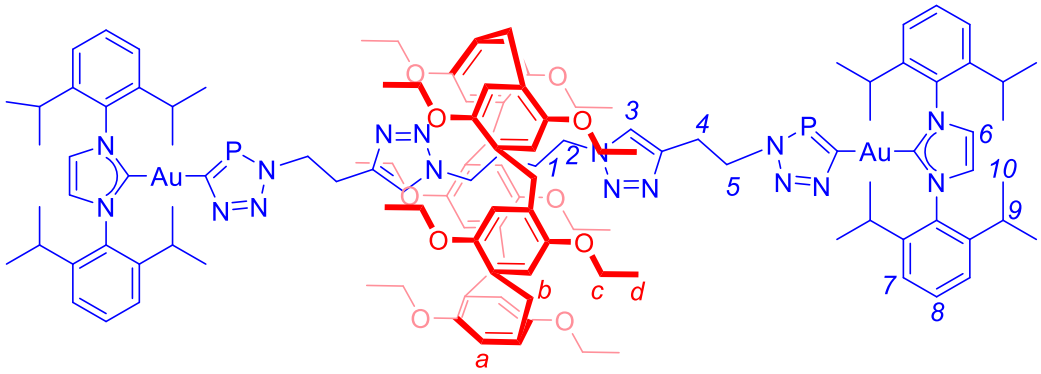

3.14

Per-methylated P5A **3.7** (40.6 mg, 0.045 mmol) and axle precursor **3.13** (14.9 mg, 0.045 mmol) were dissolved in benzene (2 mL) and the mixture stirred for 15 min. Stopper phosphaalkyne precursor **3.9** (56.6 mg, 0.090 mmol)[19] was added and the solution stirred under an inert atmosphere overnight at room temperature. The volatiles were removed *in vacuo* and the crude product purified by column chromatography (1:1 *v/v* EtOAc:hexane) to afford **3.14** as a white powder. Crystals suitable for single crystal XRD studies were grown by slow diffusion of hexane into a saturated solution of **3.14** in toluene. Yield: 72.9 mg (65%).

^{1}H NMR (400 MHz, C_6D_6) δ: 7.18 (m, 16H, $H_{a,\,3,\,8}$), 7.05 (m, 8H, H_7), 6.33 (s, 4H, H_6), 4.90 (dt, J = 7.3 Hz, 3.6 Hz, 4H, H_5), 4.15 (s, 10H, H_b), 3.86 (m, 10H, H_c), 3.69 (m, 10H, H_c), 3.30 (t, J = 7.3 Hz, 4H, H_4), 2.67 (sept., J = 6.9 Hz, 8H, H_9), 2.22 (m, 4H, H_2), 1.54 (d, J = 6.9 Hz, 24H, H_{10}), 1.28 (t, J = 6.9 Hz, 30H, H_d), 1.10 (d, J = 6.9 Hz, 24H, H_{10}), −0.79 (m, 4H, H_1) ppm.

^{13}C{^{1}H} NMR (151 MHz, C_6D_6) δ: 207.4, 196.0, 150.3, 145.8, 143.2, 134.7, 130.8, 129.2, 124.3, 122.8, 115.1, 64.1, 51.0, 48.6, 29.9, 29.8, 29.1, 25.1, 24.9, 24.0, 15.6 ppm. One aromatic environment believed to be coincident with solvent peak.

^{31}P NMR (253 MHz, C_6D_6, 298 K) δ: 201.3 ppm.

HR-ESI-MS *m/z* calculated for $[C_{123}H_{162}Au_2O_{10}N_{16}P_2]^{2+}$, $[M+2H]^{2+}$: 1240.0733, found: 1240.0743.

Inorganic Non-interlocked Axle **3.15**

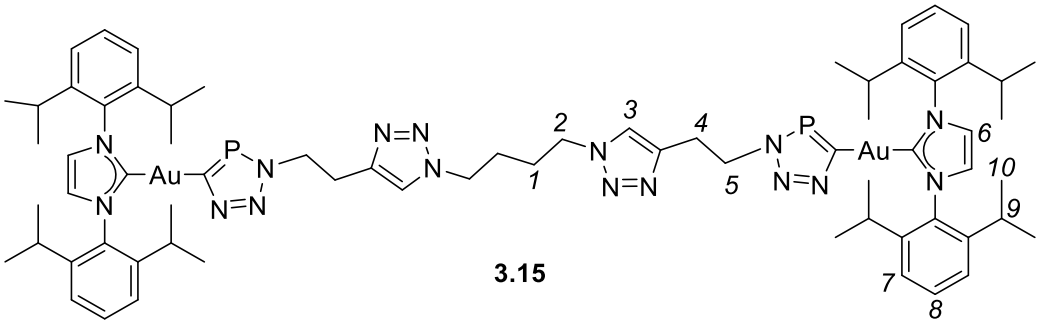

3.15

Stopper phosphaalkyne precursor **3.9** (19.5 mg, 0.031 mmol) and **3.13** (4.8 mg, 0.015 mmol) were dissolved in benzene (0.5 mL) and stirred overnight at room temperature, under an inert atmosphere. The solution was concentrated and stored at −35 °C for 7 days, affording yellow crystals of **3.15**. The supernatant was removed, and the crystals washed with pentane (3 x 1 mL) then dried under high vacuum. Yield 18.6 mg (78%).

^{1}H NMR (400 MHz, C_6D_6) δ: 7.22 (t, J = 7.8 Hz, 4H, H_8), 7.09 (d, J = 7.8 Hz, 8H, H_7), 6.34 (s, 4H, H_6), 6.08 (s, 2H, H_3), 4.51 (dt, J = 6.4, 3.8 Hz, 4H, H_5), 3.48 (m, 4H, H_2), 3.09 (t, J = 6.4 Hz, 4H, H_4), 2.67 (sept., J = 6.9 Hz, 8H, H_9), 1.51 (d, J = 6.9 Hz, 24H, H_{10}), 1.10 (d, J = 6.9 Hz, 24H, H_{10}), 1.04 (m, 4H, H_1) ppm.

^{13}C{^{1}H} NMR (151 MHz, C_6D_6) δ: 207.5, 195.8, 145.8, 144.1, 134.7, 130.9, 124.4, 122.8, 122.0, 51.0, 48.3, 29.4, 29.2, 26.5, 24.9, 24.0 ppm.

^{31}P NMR (253 MHz, C_6D_6, 298 K) δ: 201.9 ppm.

HR-ESI-MS *m/z* calculated for $[C_{66}H_{91}Au_2N_{16}P_2]^+$, $[M+H]^+$: 1587.6413, found: 1587.6388.

XB Bis-iodoalkyne P5A **3.16·XB**

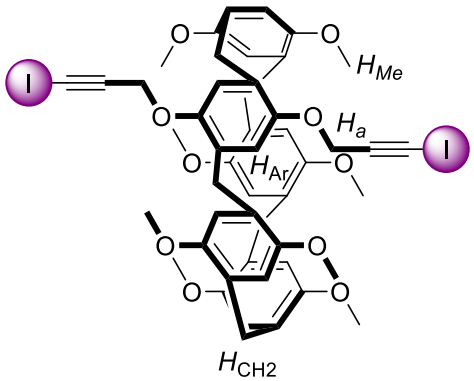

3.16·XB

3.16·HB (170 mg, 0.31 mmol)[20] and catalytic CuI (6 mg, 0.03 mmol) were dissolved in dry THF (2 mL). *N*-iodomorpholine hydroiodide (420 mg, 1.24 mmol) was added and the mixture stirred at room temperature, under exclusion of light, for 3 h, after which only one spot was visible by TLC (10% EtOAc *v/v* in hexane). The reaction mixture was diluted with DCM (50 mL) and poured onto a saturated DCM pad of neutral alumina. The pad was eluted with DCM until the solution ran clear and the organic layer decolourised with saturated $Na_2S_2O_3$ (aq.) (25 mL), and washed with H_2O (3 x 100 mL). The organic layer was dried over $MgSO_4$ and the volatiles removed *in vacuo*. The crude product was dry-loaded onto a silica column and eluted with 10% EtOAc *v/v* in hexane to afford **3.16·XB** as an off-white solid. The product was estimated by ^{1}H NMR to be 66% pure, with the contaminant identified as non-functionalised *per*-methoxypillar[5]arene, residual from the synthesis of **3.16·HB**. As the side product would not react in the subsequent step, **3.16·XB** was used without further purification. Yield: 329.1 mg (66%).

^{1}H NMR (400 MHz, $CDCl_3$) δ: 6.89 6.88 6.85 6.80 6.76 (5 s, 2H each, H_{Ar}), 4.79 (s, 4 H, H_a), 3.72 (m, 10H, H_{CH2}), 3.69-3.61 (m, 24H, H_{Me}) ppm.

^{13}C{^{1}H} NMR (151 MHz, $CDCl_3$) δ: 150.6, 150.4, 150.3, 148.7, 129.4, 128.7, 128.0, 127.7, 127.6, 116.2, 114.3, 113.8, 113.7, 113.4, 89.5, 57.7, 55.8, 55.7, 55.6, 55.5, 29.8,

29.7, 29.6, 29.0 ppm. Iodoalkyne environment is not observed, and is likely coincident with the $CDCl_3$ solvent resonance.

HR-ESI-MS: *m/z* calculated for $[C_{49}H_{48}I_2O_{10}Na]^+$, $[M+Na]^+$: 1073.1229, found: 1073.1272.

BODIPY-appended XB P5A Receptor **3.19·XB**

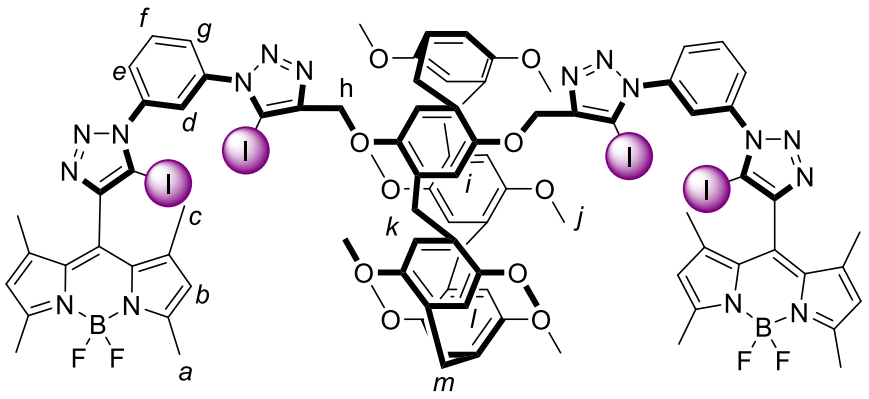

3.19·XB

$[Cu(MeCN)_4]PF_6$ (5.6 mg, 0.015 mmol) and TBTA (8.0 mg, 0.015 mmol) were placed in a 5 mL microwave vial and degassed for 10 minutes. The solids were dissolved in the minimum amount of degassed dry DCM (3 mL) and stirred at room temperature for 15 minutes. XB BODIPY precursor **3.18·XB** (40 mg, 0.072 mmol)[21] and P5A bis-iodoalkyne **3·16·XB** (19 mg, 0.018 mmol) were dissolved in the minimum amount of degassed dry DCM (2 mL) and the resulting solution added to the pre-complexed Cu^I/TBTA solution. The resulting solution was stirred at room temperature, under exclusion of light, for 12 h, after which the reaction mixture was diluted with DCM (15 mL) and washed with NH_4OH/EDTA (aq.) (2 x 20 mL) and H_2O (20 mL). All aqueous layers were back-extracted with DCM (10 mL) and the combined organic layers were dried over $MgSO_4$ and the volatiles removed *in vacuo*. **3.19·XB** was obtained by column chromatography of the resulting crude solid in acetone:DCM mixtures graded from *v/v* 0:100 to 3:97, as a purple solid. Yield 28.0 mg (72%).

^{1}H NMR (400 MHz, Acetone-d_6) δ: 8.17 (broad s, 2H, H_f), 8.08 (app. s, 6H, $H_{d,e,g}$), 7.23 (s, 2H, H_i), 6.91-6.86 (m, 8H, H_l), 6.23 (s, 4H, H_b), 5.16 (app. t, 4H, H_h), 3.81 – 3.64 (m, 34H, $H_{j,k,m}$), 2.55 (s, 12H, H_c), 1.64 (s, 12H, H_a) ppm.

^{13}C{^{1}H} NMR (151 MHz, Acetone-d_6) δ: 157.2, 150.5, 150.5, 150.4, 150.4, 150.0, 148.8, 146.4, 142.7, 138.1, 137.5, 132.1, 131.1, 129.4, 128.4, 128.3, 128.2, 128.2, 128.1, 128.0, 127.8, 124.3, 121.8, 121.8, 115.9, 113.7, 113.5, 113.4, 85.2, 83.5, 62.7, 55.3, 55.1, 55.1, 55.0, 13.9, 13.2 ppm.

HR-ESI-MS: *m/z* calculated for $[C_{91}H_{85}B_2F_4I_4N_{16}O_{10}]^+$, $[M+H]^+$: 2167.2930, found: 2167.2886.

BODIPY-appended HB P5A Receptor **3.19·HB**

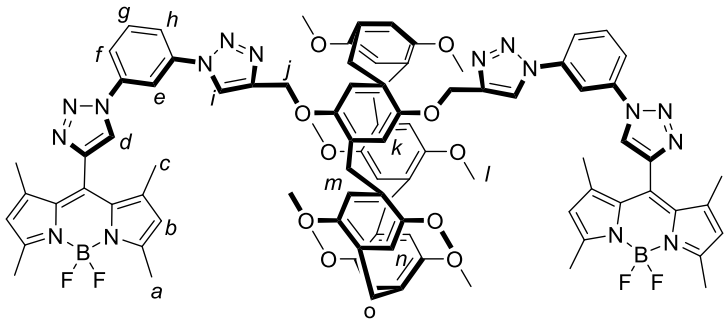

3.19·HB

$[Cu(MeCN)_4]PF_6$ (5.0 mg, 0.013 mmol) and TBTA (7.0 mg, 0.013 mmol) were placed in a 5 mL microwave vial and degassed for 10 minutes. The solids were dissolved in the minimum amount of degassed dry DCM (3 mL) and stirred at room temperature for 15 minutes. HB BODIPY precursor **3.18·HB** (25 mg, 0.058 mmol)[21] and P5A bis-alkyne **3.16·HB** (12 mg, 0.015 mmol) were dissolved in the minimum amount of degassed dry DCM (2 mL) and the resulting solution added to the pre-complexed Cu^I/TBTA solution. The resulting solution was stirred at room temperature for 12 h, after which the reaction mixture was diluted with DCM (15 mL) and washed with NH_4OH/EDTA (aq.) (2 x 20 mL) and H_2O (20 mL). All aqueous layers were back-extracted with DCM (10 mL) and the combined organic layers were dried over $MgSO_4$ and the volatiles removed *in vacuo*. **3.19·HB** was obtained by column chromatography of the resulting crude solid in

acetone:DCM mixtures graded from *v/v* 0:100 to 3:97, as a purple solid. Yield 11.5 mg (46%).

^{1}H NMR (400 MHz, Acetone-d_6) δ: 9.08 8.96 (2s, 2H each, $H_{d,i}$), 8.64 (t, J = 2.1 Hz, 2H, H_e), 8.17 (m, 4H, $H_{f,h}$), 7.94 (t, J = 8.2 Hz, H_g), 7.13 (s, 2H, H_k), 6.87-6.84 (m, 8H, H_n), 6.18 (broad s, 4H, H_b), 5.20 (m, 4H, H_j), 3.76 – 3.59 (m, 34H, $H_{m,l,o}$), 2.53 (s, 12H, H_c),1.62 (s, 12H, H_a) ppm.

^{13}C{^{1}H} NMR (151 MHz, Acetone-d_6) δ: 156.6, 150.5, 150.5, 150.5,149.8,145.7, 143.1, 140.6, 138.4, 138.1, 132.2, 131.7, 129.2, 128.9, 128.8, 128.2, 128.2, 128.1, 128.1, 128.1, 128.0, 127.9, 127.7, 123.4, 122.0, 120.1, 115.1, 113.7, 113.5, 113.4, 112.2, 75.4, 62.2, 55.1, 55.1, 55.1, 55.0, 13.6, 12.9 ppm.

HR-ESI-MS: *m/z* calculated for $[C_{91}H_{89}B_2F_4N_{16}O_{10}]^+$, $[M+H]^+$: 1663.7064, found: 1663.7053.

6.4 Synthesis and Characterisation of Novel Compounds in Chapter 4

Bis-azide Salen Ligand **4.1·H$_2$**

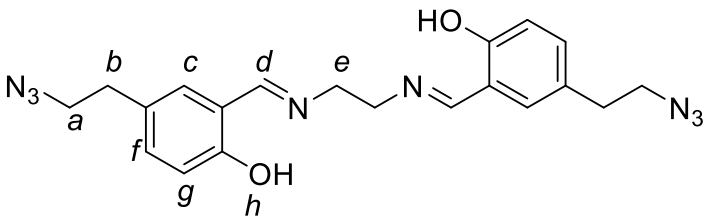

4.1·H$_2$

5-(2-Azidoethyl)-2-hydroxybenzaldehyde (0.94 g, 4.9 mmol)[22] was dissolved in dry toluene (5 mL). Ethylenediamine (0.18 mL, 2.7 mmol) was added to rapidly afford a yellow solution which was stirred at room temperature for 30 minutes. Hexane (20 mL) was added and the yellow precipitate filtered and washed with further hexane. The resulting yellow solid was used for subsequent synthesis without further purification. Yield: 0.90 g (80%).

^{1}H NMR (400 MHz, $CDCl_3$) δ: 13.08 (s, 2H, H_h), 8.33 (s, 2H, H_d), 7.14 (dd, J = 8.4 Hz, 2.3 Hz, 2H, H_f), 7.07 (d, J = 2.3 Hz, 2 Hz, H_c), 6.90 (d, J = 8.4 Hz, 2H, H_g), 3.95 (s, 4H, H_e), 3.45 (t, J = 7.1 Hz, 4H, H_a), 2.81 (t, J = 7.1 Hz, 4H, H_b) ppm.

$^{13}C\{^{1}H\}$ NMR (151 MHz, $CDCl_3$) δ: 166.3, 159.9, 132.8, 131.5, 128.1, 118.6, 117.3, 59.8, 52.6, 34.4 ppm.

HR-ESI-MS *m/z* calculated for $[C_{20}H_{23}O_2N_8]^+$, $[M+H]^+$: 407.1938, measured: 407.1937.

Bis-azide Ni(II) Complex **4.1·Ni**

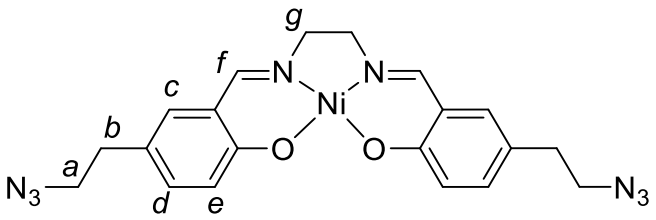

4.1·Ni

The Schiff base ligand **4.1·H₂** (300 mg, 0.793 mmol) was dissolved in methanol (15 mL). Nickel(II) acetate tetrahydrate (197 mg, 0.793 mmol) was added. A rapid colour change to a red solution was observed, indicating complex formation. Over the course of an hour, the product precipitated out of solution as a red semi-crystalline solid, which was isolated by filtration and washed with cold hexane. The product complex was used for subsequent synthesis without further purification. Yield: 366 mg (Quantitative).

^{1}H NMR (400 MHz, $CDCl_3$) δ: 7.32 (s, 2H, H_f), 7.08 (dd, J = 8.6, 2.3 Hz, 2H, H_d), 6.97 (d, J = 8.6 Hz, 2 Hz, H_e), 6.77 (d, J = 2.36 Hz, 2H, H_c), 3.47 (m, 8H, $H_{a,g}$), 2.74 (t, J = 7.1 Hz, 4H, H_b) ppm.

$^{13}C\{^{1}H\}$ NMR (151 MHz, $CDCl_3$) δ: 163.7, 161.5, 134.4, 131.8, 123.8, 121.7, 119.9, 58.5, 52.5, 34.1 ppm.

HR-ESI-MS *m/z* calculated for $[C_{20}H_{21}O_2N_8Ni]^+$, $[M+H]^+$: 463.1135, measured: 463.1135.

Macrocycle **4.3**

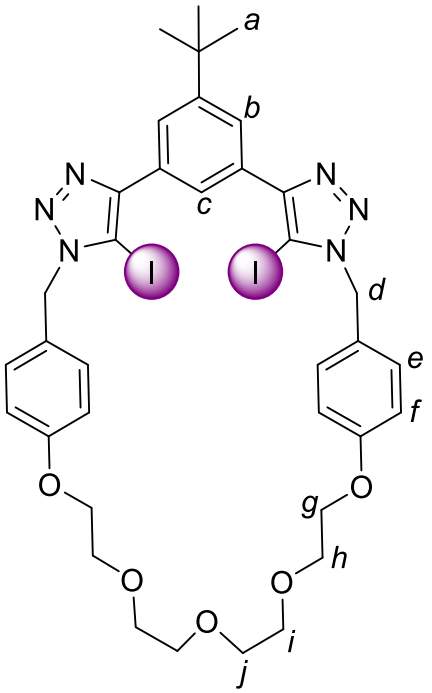

4.3

$[Cu(MeCN)_4]PF_6$ (111 mg, 0.299 mmol) and TBTA (80 mg, 0.299 mmol) were placed in a 250 mL round bottom flask and degassed for 10 minutes. The solid was dissolved in degassed dry DCM (200 mL) and stirred for 20 minutes. 1-*tert*-butyl-3,5-bis(iodoethynyl)benzene (260 mg, 0.599 mmol) and the bis-tosylated polyether precursor (226 mg, 0.599 mmol)[23] were dissolved in degassed dry DCM (5 mL) and the solution was added to the reaction mixture. The reaction was stirred in the dark at room temperature overnight. The combined organic fractions were dried over $MgSO_4$ and the volatiles removed *in vacuo* to afford a yellow oil which was loaded onto a silica column and eluted in 30:70 *v/v* EtOAc:DCM to afford an off-white solid. Yield: 223 mg (42%).

^{1}H NMR (400 MHz, $CDCl_3$) δ: 7.94 (d, J = 1.6 Hz, 2H, H_b), 7.81 (t, J =1.6 Hz, 1H, H_c), 7.19 (d, J = 8.8 Hz, 4H, H_e), 6.83 (d, J = 8.8 Hz, 4H, H_f), 5.61 (s, 4H, H_d), 4.07 (t, J = 5.2 Hz, 4H, H_g), 3.81 (t, J = 5.2 Hz, 4H, H_h), 3.67 (m, 8H, $H_{i,j}$), 1.43 (s, 9H, H_a) ppm.

^{13}C{^{1}H} NMR (151 MHz, $CDCl_3$) δ: 158.8, 152.5, 151.5, 132.4, 130.1, 129.4, 126.6, 125.8, 123.9, 114.8, 70.9, 70.7, 69.5, 67.5, 54.2, 35.1, 31.4 ppm.

HR-ESI-MS *m/z* calculated for $[C_{36}H_{41}O_5N_6I_2]^+$, $[M+H]^+$: 891.1222, measured 891.1215.

Ni(salen)-containing Non-interlocked Axle **4.4**

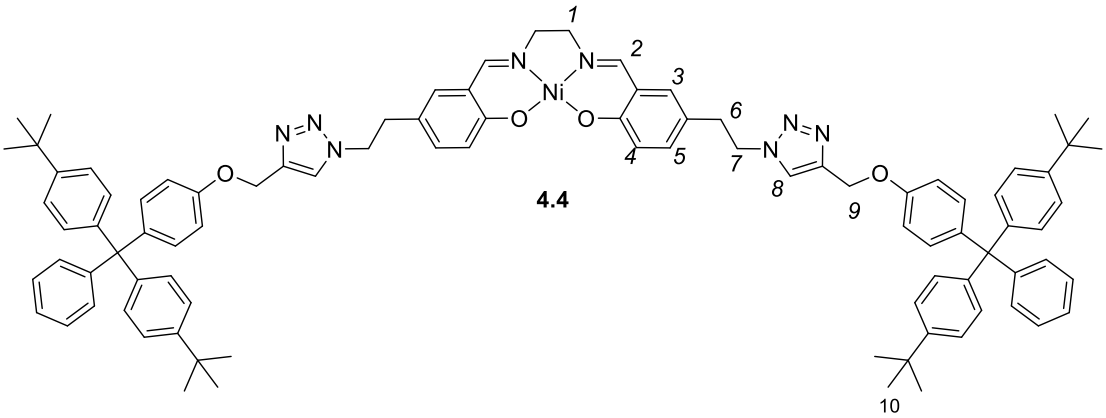

$[Cu(MeCN)_4]PF_6$ (8.08 mg, 0.0216 mmol) and TBTA (11.5 mg, 0.0216 mmol) were placed in a sealed 5 mL vial and degassed with N_2 for 10 minutes. Dry DCM (2 mL) was added and the solution stirred for 20 minutes at room temperature. Stopper alkyne **4.2** (153 mg, 0.324 mmol)[14] and bis-azido Ni(II) salen complex **4.1·Ni** (50.0 mg, 0.108 mmol) were placed in a sealed 10 mL vial and degassed with N_2 for 10 min. The precursors were dissolved in DCM (2 mL) and added to the Cu^I/TBTA solution. The resulting reaction mixture was stirred at room temperature for 4 hours before being opened to air and diluted with DCM (50 mL). The reaction mixture was washed with aqueous NH_4OH/EDTA (2 x 25 mL) and water (25 mL). The combined organic fractions were dried over $MgSO_4$ and the volatiles removed *in vacuo* to afford a red solid, which was purified by column chromatography (1:1 *v/v* EtOAc:DCM) to afford **4.4** as a red solid. Yield: 135 mg (89%).

^{1}H NMR (600 MHz, $CDCl_3$) δ: 7.46 (s, 2H, H_8), 7.32 (s, 2H, H_2), 7.24 – 7.19 (m, 10H, $H_{5,\ stopperAr}$), 7.17 (dt, J = 8.0, 2.2 Hz, 10H, $H_{stopperAr}$), 7.12 – 7.10 (m, 4H, $H_{stopperAr}$), 7.09 – 6.96 (m, 8H, $H_{stopperAr}$), 7.03 – 6.96 (m, 4H $H_{stopperAr}$), 6.92 – 6.87 (m, 2H, H_4), 6.60 (d, J = 2.2 Hz, 2H, H_3), 5.11 (s, 4H, H_9), 4.50 (t, J = 7.1 Hz, 4H, H_7), 3.22 (s, 4H, H_1), 3.05 (t, J = 7.1 Hz, 4H, H_6), 1.29 (s, 36H, H_{10}) ppm.

$^{13}C\{^{1}H\}$ NMR (151 MHz, $CDCl_3$) δ: 164.1, 161.6, 156.2, 148.5, 147.3, 143.9, 143.9, 140.0, 134.4, 132.3, 131.8, 131.1, 130.7, 127.3, 125.7, 124.2, 123.2, 123.0, 122.4, 119.7, 113.5, 63.5, 62.0, 58.3, 51.8, 35.6, 34.3, 29.7 ppm.

HR-ESI-MS *m/z* calculated for $[C_{92}H_{97}O_4N_8Ni]^+$, $[M+H]^+$: 1435.6884, measured 1435.6986.

Tetraethyleneglycol Macrocycle **4.5**

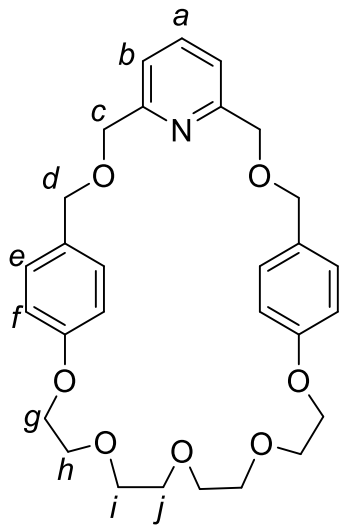

4.5

NaH (0.80 g, 19.92 mmol, 60% *w/w* dispersion) was suspended in anhydrous THF (100 mL) and stirred at 70 °C for 30 minutes. Separate solutions of 2,6-bis(bromomethyl)pyridine (1.19 g, 4.98 mmol) and 1,13-bis[4-(hydroxymethyl)benzyl]-1,4,7,10,13-pentaoxatridecane (2.02 g, 4.98 mmol),[24] each in THF (50 mL), were added dropwise to the refluxing solution over the course of 3 hours. Once the addition was complete, the mixture was left to stir overnight at 70 °C. After which the mixture was left to cool to room temperature and was carefully quenched by the addition of MeOH (50 mL). The resultant mixture was concentrated to dryness *in vacuo* and the crude reaction mixture was partitioned between DCM (250 mL) and H_2O (250 mL), the organic phase was collected and washed with H_2O (250 mL), dried over $MgSO_4$ and the solvent

removed *in vacuo*. The crude reaction mixture was purified by column chromatography (3:2:0.3 *v/v* DCM:EtOAc:MeOH) to afford the product **3.5** as a white solid. Yield: 1.29 g (51%).

^{1}H NMR (500 MHz, $CDCl_3$) δ: 7.67 (t, J = 7.7 Hz, 1H, H_a), 7.31 (d, J = 7.7 Hz, 2H, H_b), 7.21 (d, J = 8.3 Hz, 4H, H_e), 6.81 (d, J = 8.3 Hz, 4H, H_f), 4.56 (s, 4H, H_c), 4.51 (s, 4H, H_d), 4.08 (t, J = 5.7, 4H, H_g), 3.87 – 3.81 (m, 4H, H_h), 3.73 – 3.65 (m, 8H, $H_{i,j}$) ppm.

^{13}C{^{1}H} NMR (126 MHz, $CDCl_3$) δ: 158.5, 157.7, 137.0, 130.0, 130.0, 120.7, 114.5, 71.8, 71.7, 70.8, 70.8, 69.6, 67.6 ppm.

HR-ESI-MS *m/z* calculated for $[C_{29}H_{35}O_7N]^+$, $[M+H]^+$, 510.2486, found: 510.2505.

Ni(II) Salen [2]Rotaxanes **4.6·Ni** – **4.8·Ni**

General method

$[Cu(MeCN)_4]PF_6$ (8.08 mg, 0.022 mmol) and the appropriate macrocycle (0.022 mmol) were placed in a sealed 5 mL vial and degassed with N_2 for 10 minutes. Dry DCM (2 mL) was added and the solution stirred for 20 minutes at room temperature. Stopper alkyne (61.3 mg, 0.130 mmol) and the bis-azido Ni(II) salen complex **4.1·Ni** (30.0 mg, 0.065 mmol) were placed in a sealed 10 mL vial and degassed with N_2 for 10 min. The precursors were dissolved in DCM (2 mL) and added to the Cu^I/macrocycle solution. The resulting reaction mixture was stirred at room temperature for 48 hours before being opened to air and diluted with DCM (25 mL). The reaction mixture was washed with aqueous NH_4OH/EDTA (2 x 15 mL) and water (15 mL). The combined organic fractions were dried over $MgSO_4$ and the volatiles removed *in vacuo* to afford red solid, which was purified by preparative TLC (2:98 *v/v* MeOH:DCM) to afford the desired target [2]rotaxanes **4.6·Ni** – **4.8·Ni** as red solids.

4.6·Ni

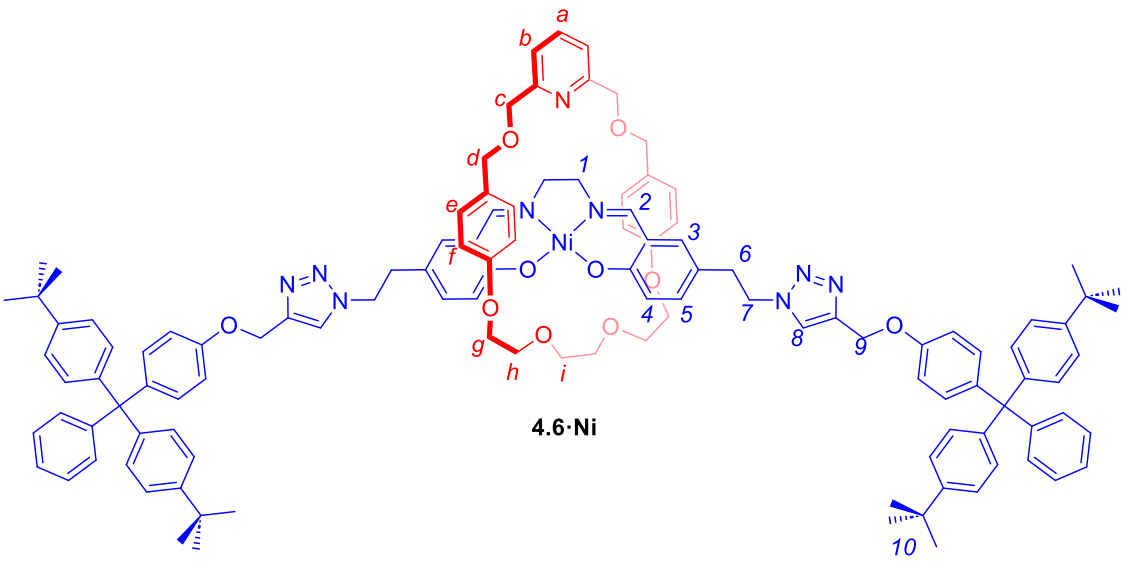

4.6·Ni

Yield: 5.8 mg (14%).

^{1}H NMR (400 MHz, $CDCl_3$) *δ:* 7.57 (t, *J* = 7.8 Hz, 1H, H_a), 7.49 (s, 2H, H_8), 7.42 (s, 2H, H_2), 7.28 (d, *J* = 7.8 Hz, 2H, H_b), 7.24 – 7.15 (m, 18H, $H_{5,\ stopperAr}$), 7.13 – 7.05 (m, 18H, $H_{stopperAr}$), 6.95 (m, 4H, H_e), 6.87 (d, *J* = 8.7 Hz, 2H, H_4), 6.65 (broad s, 2H, H_3), 6.32 (d, *J* = 8.2 Hz, 4H, H_f), 5.05 (s, 4H, H_9), 4.41 (s, 4H, H_c), 4.28 (s, 4H, H_d), 3.86 (t, *J* = 8.6 Hz, 4H, H_7), 3.70 (app. d, 12H, $H_{g,h,i}$), 3.29 (s, 4H, H_1), 2.67 (t, *J* = 8.6 Hz, 4H, H_6), 1.29 (s, 36H, $H_{stoppertBu}$) ppm.

^{13}C NMR{^{1}H} 162.7, 162.4, 158.4, 156.2, 155.9, 148.4, 147.4, 143.9, 143.7, 139.9, 137.2, 134.8, 132.3, 132.1, 131.1, 130.7, 130.2, 129.2. 127.4, 125.7, 124.2, 120.1, 114.6, 114.3, 113.4, 70.9, 70.7, 69.6, 67.5, 67.3, 63.5, 61.9, 35.5, 35.1, 34.3, 31.4 ppm. Undetected aromatic signals believed to be coincident.

HR-ESI-MS *m/z* calculated for $[C_{119}H_{128}O_{10}N_9Ni]^+$, $[M+H]^+$, 1901.9132, found: 1901.9127.

4.7·Ni

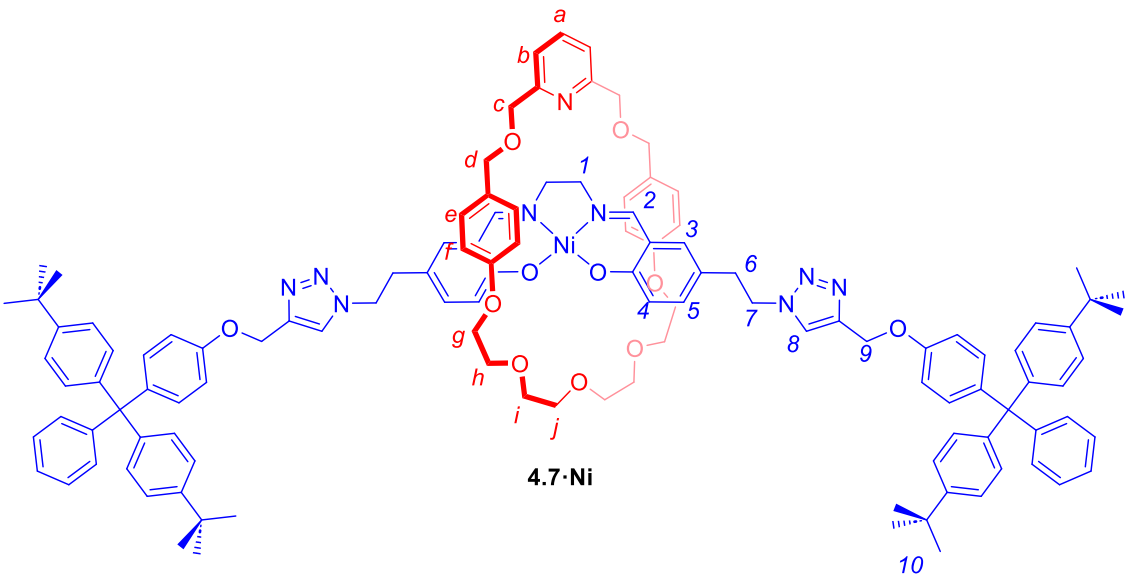

4.7·Ni

Yield: 7.2 mg (17%).

^{1}H NMR (400 MHz, $CDCl_3$) *δ:* 7.52 (t, *J* = 7.7 Hz, 1H, H_a), 7.47 (s, 2H, H_8), 7.43, (s, 2H, H_2), 7.28 (broad d, 2H, H_b), 7.24 – 7.16 (m, 18H, $H_{5,\ stopperAr}$), 7.13 – 7.00 (m, 18H, $H_{stopperAr}$), 6.89 (m, 4H, $H_{3,4}$), 6.82 (d, *J* = 8.6 Hz, 4H, H_e), 6.51, (d, *J* = 8.6 Hz, 4H, H_f), 5.07 (s, 4H H_9), 4.49 (s, 4H, H_c), 4.17 (broad m, 8H, $H_{d,7}$), 3.75 (m, 4H, H_g), 3.61 (m, 4H, H_h), 3.58 (app s., 8H, $H_{i,j}$), 3.30 (s, 4H, H_1), 2.77 (broad m, 4H, H_6) 1.29 (s, 36H, H_{10}) ppm.

^{13}C{^{1}H} NMR (126 MHz, $CDCl_3$) *δ*: 163.7, 162.9, 158.2, 157.5, 156.3, 148.4, 147.4, 143.9, 143.6, 139.9, 137.2, 135.0, 132.3, 131.8, 131.2, 130.7, 130.0, 129.0, 127.3, 125.7, 124.2, 123.4, 123.3, 121.9, 120.7, 119.8, 114.0, 113.4, 72.7, 71.6, 70.8, 69.7, 67.0, 63.5, 62.0, 58.2, 51.1, 34.6, 34.3, 31.4, 29.7 ppm.

HR-ESI-MS *m/z* calculated for $[C_{121}H_{132}O_{11}N_9Ni]^+$, $[M+H]^+$: 1944.9394, found: 1944.9394.

4.8·Ni

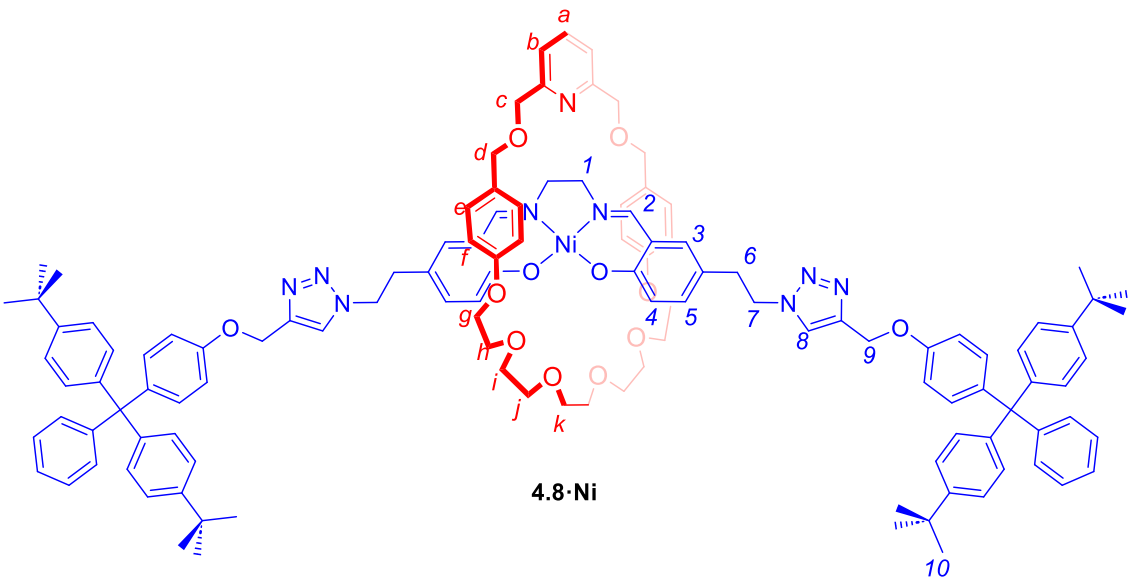

4.8·Ni

Yield: 7.7 mg (18%).

^{1}H NMR (400 MHz, $CDCl_3$) δ: 7.61 (t, J = 7.8 Hz, 1H, H_a), 7.53 (s, 2H, H_8), 7.41 (s, 2H, H_2), 7.29 (d, J = 7.8 Hz, 2H, H_b), 7.24 – 7.15 (m, 18H, $H_{5,\ stopperAr}$), 7.13 – 7.05 (m, 18H, $H_{stopperAr}$), 6.94 (m, 4H, H_e), 6.84 (d, J = 8.7 Hz, 2H, H_4), 6.54 (s, 2H, H_3), 6.38 (d, J = 8.2 Hz, 4H, H_f), 5.08 (s, 4H, H_9), 4.46 (s, 4H, H_c), 4.34 (s, 4H, H_d), 4.07 (t, J = 8.6 Hz, 4H, H_7), 3.67 (app. d, 8H, $H_{g,h}$), 3.61 (app. s, 12H, $H_{i,\ j,\ k}$), 3.29 (s, 4H, H_1), 2.62 (t, J = 8.6 Hz, 4H, H_6), 1.29 (s, 36H, $H_{stoppertBu}$) ppm.

^{13}C NMR (126 MHz, $CDCl_3$) δ: 163.8, 163.0, 158.3, 157.6, 156.4, 148.6, 147.5, 144.1, 143.8, 140.0, 135.1, 132.4, 131.9, 131.3, 130.8, 130.2, 129.2, 127.4, 125.9, 124.3, 123.5, 123.4, 122.0, 120.8, 120.0, 114.2, 113.5, 72.9, 71.7, 70.9, 69.9, 67.1, 63.6, 62.1, 58.3, 51.2, 35.0, 34.4, 32.1, 31.5 ppm. Undetected aromatic signals believed to be coincident.

HR-ESI-MS *m/z* calculated for $[C_{123}H_{136}O_{12}N_9Ni]^+$, $[M+H]^+$: 1989.9695, found: 1989.9278.

Bis-azide Co(III) Complex **4.9·Co^{III}·OAc**

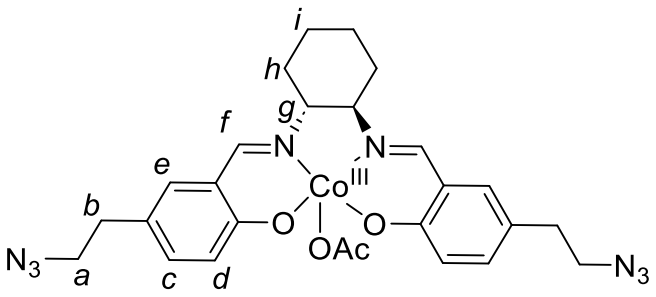

4.9·Co^{III}·OAc

5-(2-Azidoethyl)-2-hydroxybenzaldehyde (100 mg, 0.524 mmol)[22] was dissolved in degassed anhydrous methanol (20 mL) under an N_2 atmosphere. *Trans*-1,2-diaminocyclohexane (31.5 mL, 0.262 mmol) was added, affording a red solution in which a red precipitate rapidly formed. The solution was stirred for 20 min at room temperature, and a further 10 minutes with cooling in a water-ice bath. The solvent was removed by cannula filtration and the residue redissolved in DCM (20 mL) and glacial acetic acid added (1 mL) The reaction mixture was diluted with further DCM (30 mL) and washed with brine (2 x 25 mL) and water (25 mL). The combined organic fractions were dried over $MgSO_4$, filtered, and concentrated *in vacuo*. The resulting oil was suspended in pentane and sonicated for 15 minutes to afford a green-grey precipitate which was isolated by filtration under reduced pressure and washed with further pentane. The ^{1}H NMR spectrum in chloroform-*d* was indicative of aggregate formation, in DMSO-d_6, a readily interpretable spectrum was obtained at a sample concentration of 5 mg mL^{-1}. Yield: 151 mg (Quantitative).

^{1}H NMR (400 MHz, DMSO-d_6) δ: 7.97 (s, 2H, H_f), 7.51 (d, J = 2.3 Hz, 2H, H_e), 7.42 (d, J = 8.5 Hz, 2H, H_d), 7.33 (dd, J = 8.6, 2.3 Hz, 2H, H_c), 3.56 (t, J = 7.0 Hz, 4H, H_a), 3.03 (m, 2H, H_g), 2.81 (t, J = 7.0 Hz, 4H, H_b), 2.34 (s, 3H, H_{OAc}) 1.52 – 1.37 (broad m, 8H, $H_{h,i}$) ppm.

^{13}C{^{1}H} NMR spectroscopy was prohibited by complex aggregation at experimental concentration.

MALDI-ToF MS: *m/z* calculated for $[C_{24}H_{26}O_2CoN_8]^+$, $[M-OAc]^+$: 517.1644, found: 517.1505

p-Salicylaldehyde B15C5 **4.11**

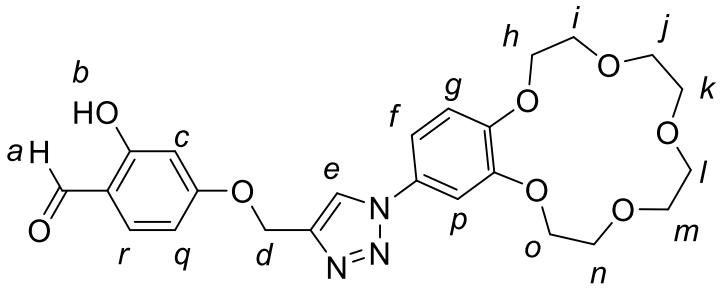

4.11

$[Cu(MeCN)_4]PF_6$ (85 mg, 0.227 mmol) was placed in a 25 mL round bottom flask and degassed for 10 minutes. The solid was dissolved in degassed dry DCM (15 mL) and *N*,*N*-diisopropylethylamine (0.1 mL, 0.575 mmol) was added to the resulting solution. 2-Hydroxy-4-(prop-2-yn-1-yloxy)benzaldehyde (200 mg, 1.14 mmol)[25] and 3-azidobenzo-15-crown-5 (350 mg, 1.14 mmol)[26] were added as solids and the resulting yellow suspension stirred overnight at room temperature. The reaction mixture was diluted with DCM (200 mL), washed with aqueous NH_4Cl (100 mL), NH_4OH/EDTA (2 x 100 mL) and water (100 mL). The combined organic fractions were dried over $MgSO_4$ and the volatiles removed *in vacuo* to afford a yellow oil which was loaded onto a silica column and eluted in 2% *v/v* methanol in DCM to afford the product as a white solid. Yield: 384 mg (69%).

^{1}H NMR (400 MHz, $CDCl_3$) δ: 11.46 (s, 1H, H_b), 9.74 (s, 1H, H_a), 7.97 (s, 1H, H_e), 7.47 (d, J = 8.7 Hz, 1H, H_r), 7.34 (d, J = 8.7 Hz, 1H, H_g), 7.15 (dd, J = 8.7, 2.5 Hz, 1H, H_f), 6.95 (d, J = 2.5 Hz, 1H, H_p), 6.66 (dd, J = 8.7, 2.4 Hz, 1H, H_q), 6.58 (d, J = 2.4 Hz, 1H, H_c), 5.32 (s, 2H, H_d), 4.20 (m, 4H, $H_{h,o}$), 3.94 (m, 4H, $H_{i,n}$), 4.20 (m, 8H, $H_{j,k,l,m}$) ppm.

^{13}C{^{1}H} NMR (151 MHz, $CDCl_3$) δ: 194.5, 165.3, 164.4, 150.0, 149.7, 143.5, 135.5, 130.7, 121.3, 115.7, 113.9, 113.0, 108.5, 107.2, 101.9, 71.1, 71.1, 70.4, 70.4, 69.4, 69.3, 69.3, 69.2, 62.3 ppm.

HR-ESI-MS *m/z* calculated for $[C_{24}H_{28}N_3O_8]^+$, $[M+H]^+$: 486.1876. Found: 486.2789.

Ni(II) Salen B15C5 Receptor *p*-Isomer **4.12·Ni**

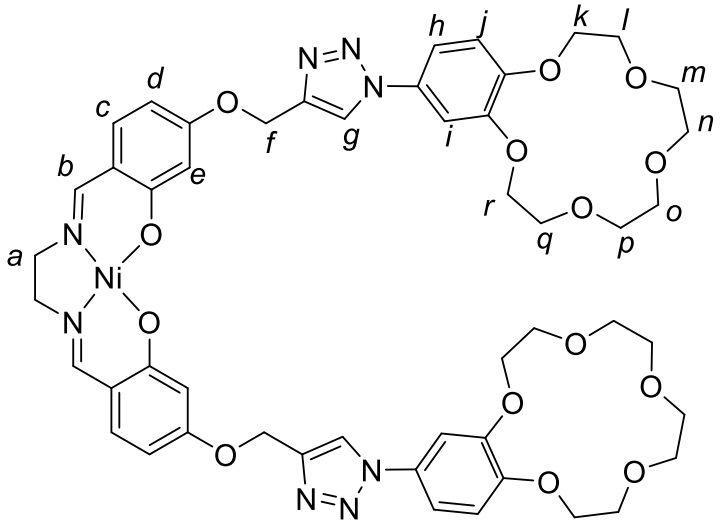

4.12·Ni

p-Salicylaldehyde B15C5 **4.11** (100 mg, 0.206 mmol) was added to methanol (15 mL) and the minimum amount of DCM added to fully solubilise the mixture (*c.* 3 mL). Ethylenediamine (6.9 mL, 0.103 mmol) was added and the reaction mixture stirred at room temperature for two hours. $Ni(OAc)_2 \cdot 4H_2O$ (28.0 mg, 0.113 mmol) was added and the reaction mixture stirred for a further 30 minutes, during which time the product precipitated as a red semi-crystalline solid, which was isolated by filtration and washed the solid with ice-cold methanol. Yield: 97 mg (88%).

^{1}H NMR (600 MHz, $CDCl_3$) δ: 7.97 (s, 2H, H_g), 7.37 (s, 2H, H_b), 7.33 (d, J = 2.5 Hz, 2H, H_i), 7.16 (dd, J = 8.6, 2.5 Hz, 2H, H_h), 6.99 (d, J = 8.8 Hz, 2H, H_c), 6.95 (d, J = 8.6 Hz, 2H, H_j), 6.64 (d, J = 2.4 Hz, 2H, H_e), 6.27 (dd, J = 8.8, 2.4 Hz, 2H, H_d), 5.21 (s, 4H, H_f), 4.24 – 4.16 (m, 4H, $H_{k,r}$), 3.93 (dq, J = 4.4, 2.4 Hz, 4H, $H_{l,q}$), 3.81 – 3.73 (m, 8H, $H_{m,n,o,p}$), 3.36 (s, 4H, H_a) ppm.

^{13}C NMR (151 MHz, $CDCl_3$) δ: 166.8, 163.2, 160.5, 149.8, 149.5, 144.1, 133.2, 130.8, 121.2, 114.7, 113.8, 113.0, 107.2, 106.8, 103.6, 71.1, 71.0, 70.4, 70.3, 69.4, 69.2, 69.1, 61.6, 58.3, 29.6 ppm.

HR-ESI-MS *m/z* calculated for $[C_{50}H_{56}O_{14}N_8NaNi]^+$, $[M+Na]^+$: 1073.3162, found: 1073.3149.

m-Salicylaldehyde B15C5 **4.13**

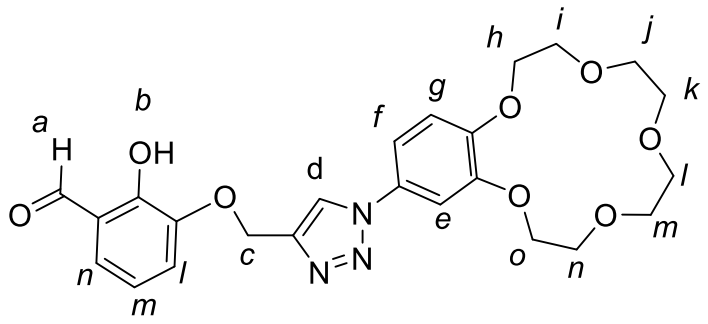

4.13

$[Cu(MeCN)_4]PF_6$ (85 mg, 0.227 mmol) was placed in a 25 mL round bottom flask and degassed for 10 minutes. The solid was dissolved in 15 mL degassed dry DCM and *N*,*N*-diisopropylethylamine (0.1 mL, 0.575 mmol) was added to the resulting solution. 2-Hydroxy-3-(prop-2-yn-1-yloxy)benzaldehyde (200 mg, 1.14 mmol)[25] and 3-azidobenzo-15-crown-5 (350 mg, 1.14 mmol)[26] were added as solids and the resulting yellow suspension stirred overnight at room temperature. The reaction mixture was diluted with DCM (200 mL) and washed with aqueous NH_4Cl (100 mL), NH_4OH/EDTA (2 x 100 mL) and water (100 mL). The combined organic fractions were dried over $MgSO_4$ and the volatiles removed *in vacuo* to afford a yellow oil which was loaded onto a silica column and eluted in 2% *v/v* methanol in DCM to afford the product as a white solid. Yield: 495 mg (89%).

^{1}H NMR (400 MHz, $CDCl_3$) δ: 11.15 (s, 1H, H_b), 9.90 (s, 1H, H_a), 8.04 (s, 1H, H_d), 7.36 (m, 1H, H_n), 7.30 (m, 1H, H_m), 7.22 (dd, J = 7.8, 1.5 Hz, 1H, H_f), 7.13 (dd, J = 8.6, 2.5 Hz, 1H, H_l), 7.01 – 6.89 (m, 2H, $H_{g,e}$), 5.22 (s, 2H, H_c) , 4.23 – 4.13 (m, 4H, $H_{h,o}$), 3.92 – 3.80 (m, 4H, $H_{i,n}$), 3.75 (app. s, 8H, $H_{j,k,l,m}$).

^{13}C{^{1}H} NMR δ: 194.9, 165.6, 150.3, 150.1, 143.8, 123.8, 122.6, 121.7, 116.0, 114.2, 113.4, 108.9, 107.6, 102.2, 71.5, 71.5, 70.8, 70.7, 69.8, 69.6, 69.6, 69.5, 62.6 ppm.

HR-ESI-MS *m/z* calculated for $[C_{24}H_{28}N_3O_8]^+$, $[M+H]^+$: 486.1876. Found: 486.2868.

Ni(II) Salen B15C5 Receptor *m*-Isomer **4.14·Ni**

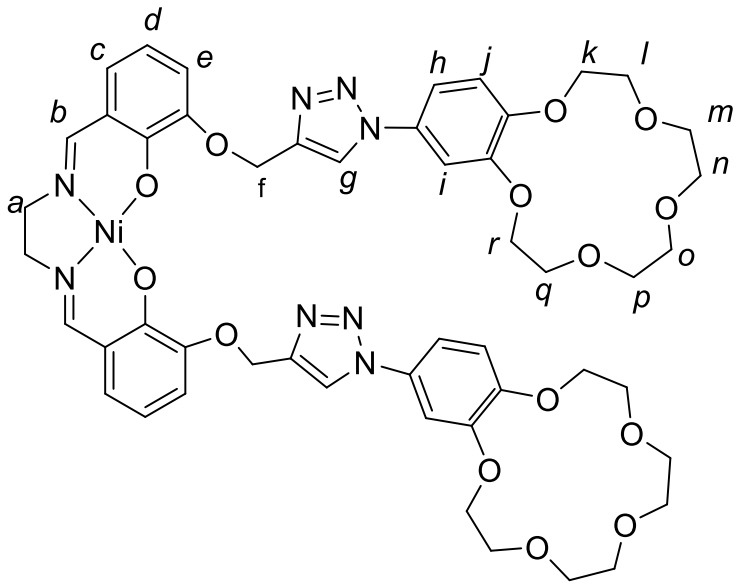

4.14·Ni

m-Salicylaldehyde B15C5 **4.13** (100 mg, 0.206 mmol) was added to methanol (15 mL) and the minimum amount of DCM added to fully solubilise the mixture (*c.* 3 mL). Ethylenediamine (6.9 mL, 0.103 mmol) was added and the reaction stirred at room temperature for two hours. $Ni(OAc)_2 \cdot 4H_2O$ (28.0 mg, 0.113 mmol) was added and the reaction mixture stirred for a further 30 minutes, during which time the product was precipitated as a red semi-crystalline solid, which was isolated by filtering the reaction mixture and washing the solid with ice-cold methanol. Yield: 110 mg (Quantitative).

^{1}H NMR (400 MHz, $CDCl_3$) δ: 8.37 (s, 2H, H_g), 7.42 (s, 2H, H_b), 7.29 (d, J = 1.8 Hz, 2H, H_i), 7.14 (dd, J = 8.6 Hz, 1.8 Hz, 2H, H_h), 6.92 (d, J = 7.5 Hz, 2H, H_d), 6.71 (dd, J = 7.5, 1.5 Hz, 2H H_e), 6.63 (d, J = 8.6 Hz, 2H, H_j), 5.08 (s, 4H, H_f), 4.10 (m, 8H. $H_{k,r}$), 3.94 – 3.82 (m, 8H, $H_{l,q}$), 3.76 (m, J = 6.8 Hz, 16H, $H_{m,n,o,p}$), 3.41 (s, 4H, H_a) ppm. H_c not observed, and believed to be coincident with residual protio solvent.

^{13}C{^{1}H} NMR (151 MHz, $CDCl_3$) δ: 161.7, 149.6, 149.0, 145.1, 130.9, 125.8, 120.9, 114.2, 113.9, 112.8, 106.5, 71.1, 71.0, 70.4, 70.4, 69.5, 69.3, 69.1, 68.9, 58.5, 29.8 ppm. Undetected aromatic signals believed to be coincident.

HR-ESI-MS *m/z* calculated for $[C_{50}H_{57}O_{14}N_8Ni]^+$, $[M+H]^+$: 1051.3342, found: 1051.3323.

Co(III) Salen B15C5 Potential Catalyst **4.15·Co^{III}·OAc**

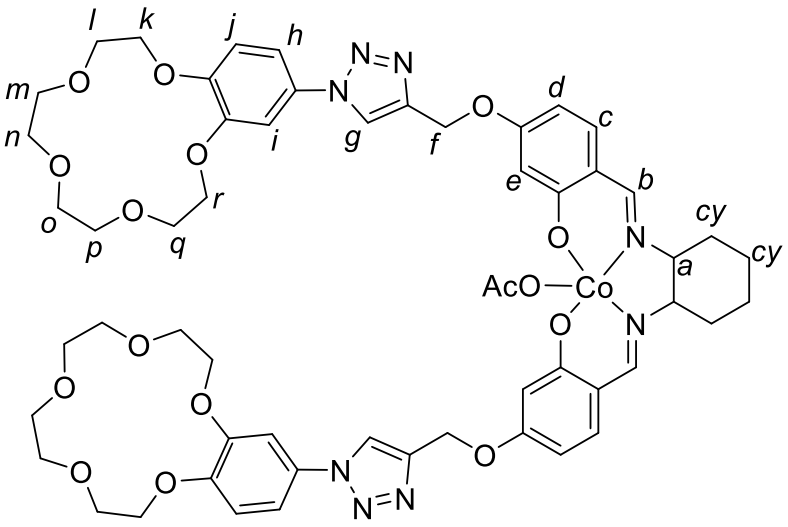

4.15·Co^{III}·OAc

p-Salicylaldehyde B15C5 **4.11** (50 mg, 0.103 mmol) was added to anhydrous degassed methanol (10 mL) under N_2 atmosphere and the minimum amount of degassed anhydrous DCM added to fully solubilise the mixture (*c.* 2 mL). *Trans*-1,2-diaminocyclohexane (3.1 mL, 0.026 mmol) was added and the reaction stirred at room temperature for 10 min under N_2 atmosphere. Anhydrous $Co(OAc)_2$ (17.7 mg, 0.100 mmol) was added and the reaction mixture stirred for a further 30 min after which the solvent was removed by cannula filtration and the resulting solid redissolved in DCM (10 mL) and glacial acetic acid (1 mL) added. The solution was stirred under exposure to air for 24 hours, after which the product was precipitated by addition of methanol (20 mL) and the product washed with ice-cold methanol. Yield: 56 mg (92%).

^{1}H NMR (400 MHz, DMSO-d_6) δ: 8.93 (s, 2H, H_g), 8.10 (s, 2H, H_b), 7.88 (broad s, 2H, H_d), 7.56 (d, J = 8.8 Hz, 2H, H_c), 7.49 (d, J = 2.5 Hz, 2H, H_e), 7.42 (dd, J = 8.4, 2.7 Hz, 2H, H_h), 7.17 (d, J = 2.7 Hz, 2H, H_i), 7.14 (d, J = 8.4 Hz, 2H, H_j), 6.41 (m, 2H, H_a) 5.34 (s, 4H, H_f), 4.15 (m, 8H, $H_{k,r}$), 3.80 (m, 8H, $H_{l,q}$), 3.63 (s, 16H, $H_{m,n,o,p}$), 1.98 (s, 3H, H_{OAc}), 1.86 – 1.57 (broad m, 8H, H_{cy}) ppm.

^{13}C{^{1}H} NMR spectroscopy was prohibited by complex aggregation at experimental concentration.

HR-ESI-MS *m/z* calculated for $[C_{56}H_{65}O_{16}CoN_8Na]^+$, $[M+H]^+$: 1187.3815, found: 1187.3784.

XB Iodoalkyne **4.16**

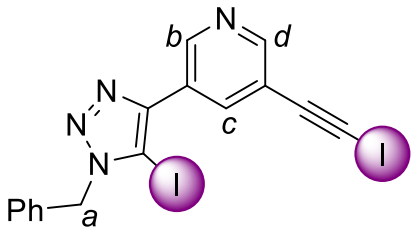

4.16

$[Cu(MeCN)_4]PF_6$ (25 mg, 0.066 mmol) and TBTA (35 mg, 0.066 mmol) were placed in a 25 mL round bottom flask and degassed for 10 minutes. The solid was dissolved in 15 mL of a mixture of 1:1 *v/v* degassed dry DCM and degassed dry THF. 3,5-Bis(iodoethynyl)pyridine (200 mg, 0.529 mmol)[27] was added in a single portion. Benzyl azide (35.2 mg, 0.265 mmol) was dissolved in 2 mL degassed dry DCM and the solution was added to the reaction mixture dropwise over 3 hours. The reaction was stirred in the dark at room temperature overnight. The reaction mixture was diluted with DCM (200 mL), washed with aqueous NH_4OH/EDTA (2 x 100 mL) and water (100 mL). The combined organic fractions were dried over $MgSO_4$ and the volatiles removed *in vacuo* to afford a yellow oil which was loaded onto a silica column and eluted in 5% *v/v* EtOAc in DCM to afford the product as a white solid. Yield: 118 mg (87%).

^{1}H NMR (400 MHz, $CDCl_3$) δ: 9.16 (broad s, 1H, H_b), 8.68 (broad s, 1H, H_d), 8.34 (broad s, 1H, H_c), 7.41-7.29 (broad m, 5H, H_{Ph}), 5.69 (s, 2H, H_a) ppm.

^{13}C{^{1}H} NMR (151 MHz, $CDCl_3$) δ: 151.8, 147.3, 146.6, 138.3, 138.1, 133.9, 129.0, 128.7, 127.9, 126.4, 120.7, 90.2, 54.6 ppm. Alkyne environment not observed and believed to overlap with the solvent peak.

HR-ESI-MS *m/z* calculated for $[C_{16}H_{11}I_2N_4]^+$, $[M+H]^+$: 512.9073, found 512.9068.

XB Pro-ligand **4.17**

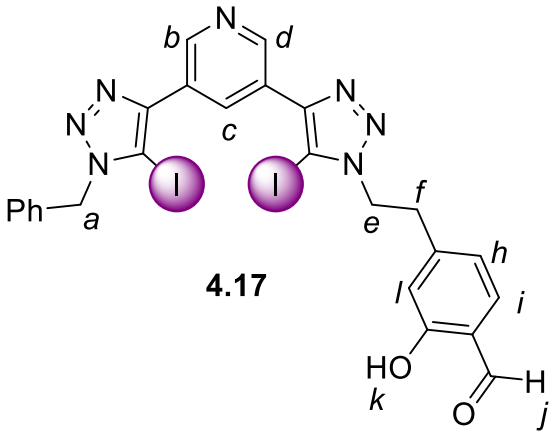

4.17

$[Cu(MeCN)_4]PF_6$ (7.26 mg, 0.019 mmol) and TBTA (10.37 mg, 0.019 mmol) were placed in a 25 mL round bottom flask and degassed for 10 minutes. The solid was dissolved in 10 mL of a mixture of 1:1 *v/v* degassed dry DCM and degassed dry THF and stirred for 20 minutes. **4.16** (40 mg, 0.078 mmol) was added in a single portion. 4-(2-Azidoethyl)-2-hydroxybenzaldehyde (14.9 mg, 0.086 mmol) was dissolved in 2 mL dry degassed DCM and the solution was added to reaction mixture. The reaction was stirred in the dark at room temperature overnight. The reaction mixture was diluted with $CHCl_3$ (300 mL), washed with aqueous NH_4OH/EDTA (2 x 100 mL) and water (100 mL). The combined organic fractions were dried over $MgSO_4$ and the volatiles removed *in vacuo* to afford a yellow oil which was loaded onto a silica column and eluted in 4:2:94 *v/v* MeOH:acetone:DCM. Yield: 38.4 mg (70%).

^{1}H NMR (400 MHz, $CDCl_3$) δ: 10.94 (s, 1H, H_k), 9.85 (s, 1H, H_j), 9.27 (s, 1H, $H_{b\text{ or }d}$), 9.22 (s, 1H, $H_{b\text{ or }d}$), 8.88 (s, 1H, H_c), 7.41—7.28 (m, 7H, $H_{Ph,l,i}$), 6.96 (d, J = 8.2 Hz, 1H, H_h), 5.71 (s, 1H, H_a), 4.61 (t, J = 7.3 Hz, 2H, H_e), 3.30 (t, J = 7.3 Hz, 2H, H_f) ppm.

^{13}C{^{1}H} NMR (151 MHz, $CDCl_3$) δ: 196.2, 160.9, 147.6, 147.2, 146.8, 137.5, 134.0, 133.7, 133.2, 133.1, 129.3, 129.1, 129.0, 128.7, 128.4, 127.9, 127.8, 126.5, 120.7, 118.4, 54.6, 51.9, 35.2 ppm.

HR-ESI-MS *m/z* calculated for $[C_{25}H_{20}I_2N_7O_2]^+$: 703.9768, found 703.9758.

XB-pendant Ni(II) Salen Complex **4.18·Ni**

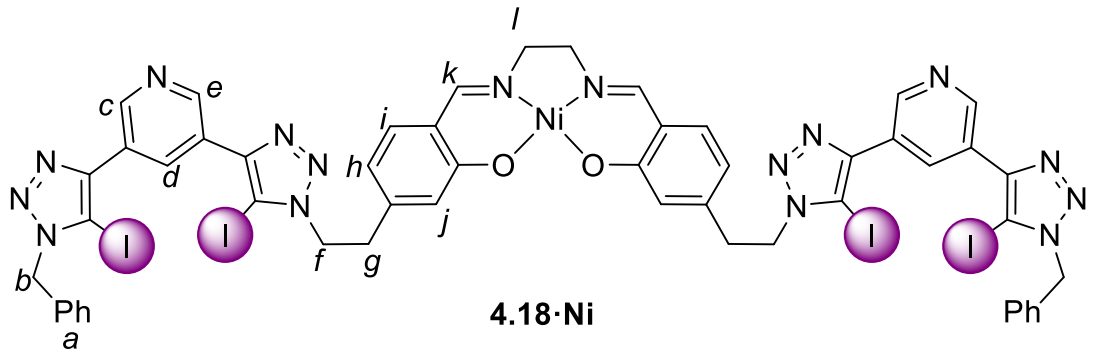

4.18·Ni

Pro-ligand **4.17** (80 mg, 0.114 mmol) was suspended in MeOH (15 mL) and $CHCl_3$ (2 mL) added. To the suspension was added 1,2-ethylenediamine (3.42 mg, 0.057 mmol) and the mixture stirred for 2 hours, forming a yellow suspension. To the resulting suspension, nickel(II) acetate tetrahydrate (14.15 mg, 0.057 mmol) was added and the mixture stirred for three hours. The resulting red suspension was fully solubilised in $CHCl_3$ (300 mL) and washed with water (3 x 100 mL). The combined organic layers were dried over $MgSO_4$ and loaded onto silica. The complex was eluted with 4% MeOH *v/v* in DCM. Yield: 73.5 mg (87%).

^{1}H NMR (400 MHz, DMSO-d_6) δ: 9.17 (d, J = 2.0 Hz, 2H, $H_{\text{c or e}}$), 9.10 (d, J = 2.0 Hz, 2H, $H_{\text{c or e}}$), 8.80 (apparent t, J = 2.0 Hz, 2H, H_{d}), 7.83 (s, 2H, H_{k}), 7.41—7.19 (m, 10H, H_{a}), 7.03 (d, J = 2.0 Hz, 2H, H_{j}), 6.88 (dd, J = 8.7, 2.0 Hz, 2H, H_{h}), 6.65 (d, J = 8.7 Hz, 2H, H_{i}), 5.75 (s, 4H, H_{b}), 4.63 (t, J = 6.6 Hz, 4H, H_{f}), 3.37 (s, 4H, H_{l}), 3.07 (t, J = 6.6 Hz, 4H, H_{g}) ppm.

^{13}C{^{1}H} NMR (126 MHz, DMSO-d_6) δ: 163.4, 162.9, 147.5, 147.4, 146.5, 146.0, 135.6, 135.0, 132.9, 131.9, 131.9, 129.3, 128.6, 127.9, 127.0, 126.8, 123.0, 120.6, 120.5, 83.6, 58.4, 54.1, 52.1, 35.0 ppm.

HR-ESI-MS *m/z* calculated for $[C_{52}H_4O_2N_{16}I_4Ni]^+$, $[M+H]^+$: 1486.9125, found 1486.9117.

Per-fluorobenzene XB Iodoalkyne **4.19**

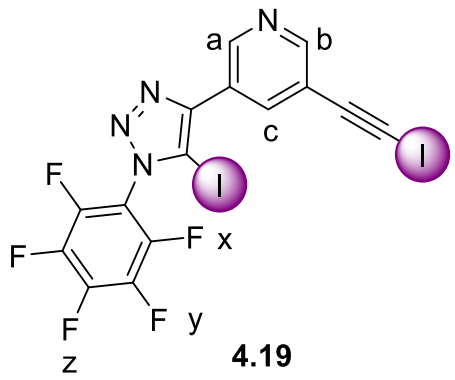

4.19

$[Cu(MeCN)_4]PF_6$ (25 mg, 0.066 mmol) and TBTA (35 mg, 0.066 mmol) were placed in a 25 mL round bottom flask and degassed for 10 minutes. The solid was dissolved in 1:1 *v/v* degassed dry DCM and degassed dry THF (15 mL). 3,5-Bis(iodoethynyl)pyridine (200 mg, 0.529 mmol)[27] was added in a single portion. *Per*-fluorophenyl azide (55.3 mg, 0.265 mmol)[28] was dissolved in 2 mL degassed dry DCM and the solution was added to the reaction mixture dropwise over 3 hours. The reaction was stirred in the dark at room temperature overnight. The reaction mixture was diluted with DCM (200 mL), washed with aqueous NH_4OH/EDTA (2 x 100 mL) and water (100 mL). The combined organic fractions were dried over $MgSO_4$ and the volatiles removed *in vacuo* to afford a yellow oil which was loaded onto a silica column and eluted in 3% *v/v* EtOAc in DCM afford the product as a white solid. Yield: 113 mg (73%).

^{1}H NMR (400 MHz, $CDCl_3$) δ: 9.24 (d, J = 1.8 Hz, 1H, H_a), 8.74 (d, J = 1.8 Hz, 1H, H_b), 8.40 (apparent t, J = 1.8 Hz, 1H, H_c) ppm.

^{19}F{^{1}H} NMR (376 MHz, $CDCl_3$) δ: -142.18 (m, 2F, F_x), -146.63 (1F, app. t, J = 21.5 Hz, F_z), -158.74 (m, 2F, F_y) ppm.

^{13}C{^{1}H, ^{19}F} NMR (151 MHz, $CDCl_3$) δ: 153.0, 147.3, 147.1, 144.5, 142.8, 137.8, 125.1, 120.7, 90.2, 81.0 ppm. Remaining environments undetected due to poor sample solubility.

HR-ESI-MS *m/z* calculated for $[C_{15}H_4F_5I_2N_4]^+$, $[M+H]^+$: 588.8440, found 588.8438.

Per-fluorobenzene XB Pro-ligand **4.20**

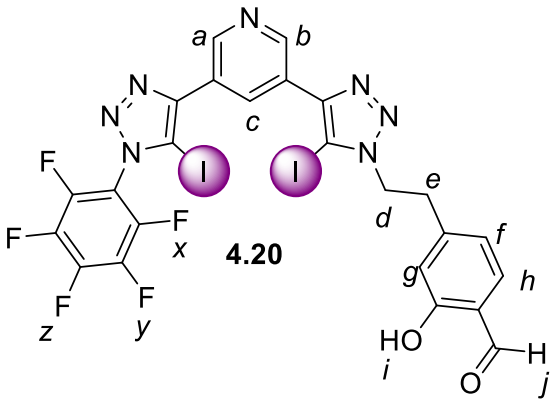

$[Cu(MeCN)_4]PF_6$ (7.26 mg, 0.019 mmol) and TBTA (10.37 mg, 0.019 mmol) were placed in a 25 mL round bottom flask and degassed for 10 minutes. The solid was dissolved in 10 mL of a mixture of 1:1 *v/v* degassed dry DCM and degassed dry THF and stirred for 20 minutes. **4.19** (135 mg, 0.173 mmol) was added in a single portion. 4-(2-Azidoethyl)-2-hydroxybenzaldehyde (43.9 mg, 0.229 mmol) was dissolved in 2 mL degassed dry DCM and the solution was added to reaction mixture which was stirred in the dark at room temperature overnight. The reaction mixture was diluted with $CHCl_3$ (300 mL), washed with aqueous NH_4OH/EDTA (2 x 100 mL) and water (100 mL). The combined organic fractions were dried over $MgSO_4$ and the volatiles removed *in vacuo* to afford a yellow oil which was loaded onto a silica column and eluted in 3:2:95 *v/v* methanol:acetone:DCM. Yield: 158 mg (89%).

^{1}H NMR (400 MHz, $CDCl_3$) δ: 10.94 (s, 1H, H_i), 9.85 (s, 1H, H_j), 9.27 (s, 1H, $H_{a\ or\ b}$), 9.22 (s, 1H, $H_{a\ or\ b}$), 8.88 (s, 1H, H_c), 7.35 (d, J = 1.4 Hz, 1H, H_g), 7.32 (dd, J = 8.2 Hz, J = 1.4 Hz, 1H, H_f), 6.96 (d, J = 8.2 Hz, 1H, H_h), 4.71 (t, J = 7.2 Hz, 2H, H_d), 3.31 (t, J = 7.2 Hz, 2H, H_e) ppm.

^{19}F{^{1}H} NMR (376 MHz, $CDCl_3$) δ: -142.13 (m, 2F, F_x), -146.68 (m, 1F, F_z), -158.75 (m, 2F, F_y) ppm.

^{13}C{^{1}H, ^{19}F} NMR (126 MHz, CDCl3) δ: 196.3, 160.9, 148.5, 147.9, 147.8, 146.7, 143.7, 143.6, 138.1, 137.6, 133.7, 132.9, 127.9, 120.7, 118.4, 81.1, 77.8, 51.9, 35.2 ppm. Remaining signals undetected due to poor sample solubility.

HR-ESI-MS *m/z* calculated for $[C_{24}H_{13}F_5I_2N_7O_2]^+$, $[M+H]^+$: 779.9135, found 779.9129.

Per-fluorobenzene XB Ni(salen) **4.21·Ni**

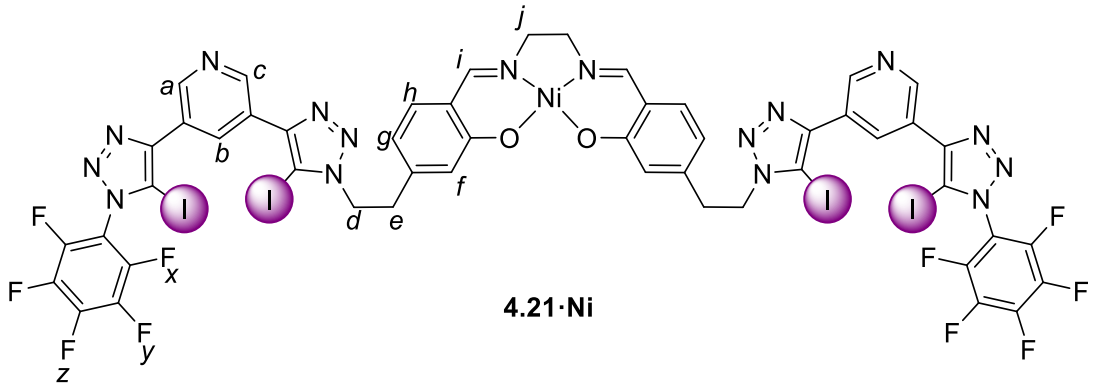

Pro-ligand **4.20** (89 mg, 0.114 mmol) was suspended in 15 mL MeOH and 2 mL $CHCl_3$ added. To the suspension was added 1,2-ethylenediamine (3.42 mg, 0.057 mmol) and the mixture stirred for 2 hours, forming a yellow suspension. To the resulting suspension, $Ni(OAc)_2{\cdot}4H_2O$ (14.15 mg, 0.057 mmol) was added and the mixture stirred for three hours. The resulting red suspension was fully solubilised in $CHCl_3$ (300 mL) and washed with water (3 x 100 mL). The combined organic layers were dried over $MgSO_4$ and loaded onto silica. The complex was eluted with 4% MeOH *v/v* in DCM. Yield: 78.5 mg (84%).

^{1}H NMR (400 MHz, DMSO-d_6) δ: 9.41 (broad s, 2H, $H_{a\text{ or }c}$), 9.20 (broad s, 2H, $H_{a\text{ or }c}$), 8.88 (broad s, 2H, H_b), 7.44 (s, 2H, H_i), 6.83 (broad s, 2H, H_f), 6.74 – 6.62 (m, 4H, $H_{g,\,h}$), 4.68 (t, J = 6.7 Hz, 4H, H_d), 3.41 (s, 4H, H_j), 3.18 (t, J = 6.7 Hz, 4H, H_e) ppm.

^{19}F NMR (377 MHz, DMSO-d_6) δ: -144.8 (m, 2F, F_x), -147.3 (s, 1F, F_y), -159.5 (m, 2F, F_z) ppm.

^{13}C{1H} NMR Poor sample solubility and ^{19}F coupling prevented the collection of an interpretable spectrum.

HR-ESI-MS *m/z* calculated for $[C_{50}H_{27}F_{10}I_4N_{16}O_2Ni]^+$, $[M+H]^+$: 1638.7870, found 1638.7842

6.5 Single Crystal X-ray Diffraction Data

X-ray diffraction data for the crystal structures presented in this thesis were collected and solved by Prof. Jose Goicoechea. The data are deposited in the CCDC database with the deposition numbers indicated below (Table 6.1).

	3.10·3C_6H_6	**3.14**
Formula	$C_{137}H_{176}Au_2N_{10}O_{10}P_2$	$C_{123}H_{164}Au_2N_{16}O_{10}P_2$
CCDC	2271341	2271342
Fw (g mol^{-1})	2578.74	2482.57
Crystal system	triclinic	monoclinic
Space group	*P*1	$P2_1/n$
a (Å)	12.5314(2)	12.3413(2)
b (Å)	14.0421(2)	43.5798(6)
c (Å)	19.8345(3)	12.7293(2)
α (°)	96.403(1)	90
β (°)	107.769(1)	95.536(2)
γ (°)	95.770(1)	90
V (Å^3)	3269.42(9)	6814.29(18)
Z	1	2
Radiation, λ (Å)	Cu Kα, 1.54184	Cu Kα, 1.54184
Temp (K)	150(2)	150(2)
ρ_{calc} (g cm^{-3})	1.310	1.210
μ (mm^{-1})	4.856	4.653
Reflections collected	79947	107442
Indep. reflections	25632	11989
Parameters	1267	927
R(int)	0.0449	0.0937
R1/wR2, I ≥ 2σI (%)	3.92/9.56	11.30/25.73
R1/wR2, all data (%)	4.89/10.37	12.42/26.07
GOF	1.057	1.134

Table 6.1. Selected x-ray data collection and refinement parameters for XRD studies presented in this thesis. GOF = Goodness of fit.

6.6 References

1. Agilent Technologies, *CrysAlisPro*.
2. G. Sheldrick, *Acta Crystallogr. A* . 1990, **46**, 467-473.
3. G. Sheldrick, *Acta Crystallogr. A* . 2008, **64**, 112-122.
4. http://supramolecular.org, *Bindfit v 0.5*.
5. D. Brynn Hibbert and P. Thordarson, *Chem. Commun.*, 2016, **52**, 12792-12805.
6. OriginLab Corporation, *OriginPro*, 2023.
7. M. Zengerle, F. Brandhuber, C. Schneider, F. Worek, G. Reiter and S. Kubik, *Beilstein J. Org. Chem.*, 2011, **7**, 1543-1554.
8. U. Burger and F. Dreier, *Tetrahedron*, 1983, **39**, 2065-2071.
9. P. Lucio Anelli, N. Spencer and J. F. Stoddart, *Tetrahedron Lett.*, 1988, **29**, 1569-1572.
10. V. Aucagne, K. D. Hänni, D. A. Leigh, P. J. Lusby and D. B. Walker, *J. Am. Chem. Soc.*, 2006, **128**, 2186-2187.
11. D. A. Roberts, T. W. Schmidt, M. J. Crossley and S. Perrier, *Chem. Eur. J.*, 2013, **19**, 12759-12770.
12. A. Brown, T. Lang, K. M. Mullen and P. D. Beer, *Org. Biomol. Chem.*, 2017, **15**, 4587-4594.
13. Y. C. Tse, A. Docker, Z. Zhang and P. D. Beer, *Chem. Commun.*, 2021, **57**, 4950-4953.
14. A. V. Leontiev, C. A. Jemmett and P. D. Beer, *Chem. Eur. J.*, 2011, **17**, 816-825.
15. J. M. Smith, J. R. Frost and R. Fasan, *Chem. Commun.*, 2014, **50**, 5027-5030.
16. T. Ogoshi, R. Iizuka, D. Kotera and T.-a. Yamagishi, *Org. Lett.*, 2015, **17**, 350-353.
17. T. Ogoshi, S. Kanai, S. Fujinami, T.-a. Yamagishi and Y. Nakamoto, *J. Am. Chem. Soc.*, 2008, **130**, 5022-5023.
18. J. E. Kickham, S. J. Loeb and S. L. Murphy, *Chem. Eur. J.*, 1997, **3**, 1203-1213.
19. A. Mapp, J. T. Wilmore, P. D. Beer and J. M. Goicoechea, *Angew. Chem. Int. Ed.*, 2023, **62**, e202309211.
20. J. Bi, X. Zeng, D. Tian and H. Li, *Org. Lett.*, 2016, **18**, 1092-1095.
21. A. J. Taylor, R. Hein, S. C. Patrick, J. J. Davis and P. D. Beer, *Angew. Chem. Int. Ed.*, 2024, **63**, e202315959.
22. A. Makarem, K. D. Klika, G. Litau, Y. Remde and K. Kopka, *J. Org. Chem.*, 2019, **84**, 7501-7508.
23. Y. Vida, E. Perez-Inestrosa and R. Suau, *Tetrahedron Lett.*, 2005, **46**, 1575-1577.
24. E. Perez-Inestrosa, J.-P. Desvergne, H. Bouas-Laurent, J.-C. Rayez, M.-T. Rayez, M. Cotrait and P. Marsau, *Eur. J. Org. Chem.*, 2002, **2002**, 331-344.
25. V. Selvarani, B. Annaraj, M. A. Neelakantan, S. Sundaramoorthy and D. Velmurugan, *Polyhedron*, 2013, **54**, 74-83.
26. T. Bunchuay, A. Docker, U. Eiamprasert, P. Surawatanawong, A. Brown and P. D. Beer, *Angew. Chem. Int. Ed.*, 2020, **59**, 12007-12012.
27. S. W. Robinson and P. D. Beer, *Org. Biomol. Chem.*, 2017, **15**, 153-159.
28. L.-M. Jin, X. Xu, H. Lu, X. Cui, L. Wojtas and X. P. Zhang, *Angew. Chem. Int. Ed.*, 2013, **52**, 5309-5313.